Magneto-Fluorescent Transition Metal Oxide Nanostructures For Biomedical Application

Thesis submitted for the Degree of

Doctor of Philosophy

in

Chemistry (Inorganic)

By

Indranil Chakraborty

Department of Chemistry

University of Calcutta

July, 2019

Dedicated to my beloved elder brother…

Acknowledgement

First of all I am grateful to my supervisor Prof. Kalyan Mandal who is a source of inspiration to me. His humble guidance, suggestions and help motivated me to carry out my research work in his laboratory. Without his support and help my research would not be continued.

I am thankful to S. N. Bose National Centre for Basic Sciences, Kolkata, India for providing a beautiful green campus, hostel facility, research environment, advanced instrumental facilities and financial supports.

I would like to thank our collaborators Dr. Gopinatha Suresh Kumar from IICB, Kolkata, Dr. Somenath Roy from CGCRI, Kolkata, and Dr. S. P. Sinha Babu, Visva-Bharati University, Santiniketan. I am grateful to them for allowing me to do experiments in their laboratory.

My sincere thanks to Dr. Urmila Saha, Dr. Deblina Majumder, and Dr. Suprabhat Mukherjee for their tremendous help to carry out some necessary experiments.

I am also obliged to the director of our institute, Mr. Samit Kumar Ray for his constant effort to increase the research facilities in our centre. I thank to all faculty members and staff members for their cooperation. I am thankful to our all technical staff members specially Mr. Samik Roy, Mrs. Urmi Chakraborty, Mr. Shakti nath Das, Mr. Joy Bandopadhyay, and Mr. Amit Kr. Chanda for their help in sample characterization.

I would like to acknowledge my seniors and labmates: Dr. Arup Ghosh, Dr. Rupali Rakshit, Mr. Souvanik Talukdar, Mahebub, Keshab, Subrata, Dipika, Priyanka, Dipanjan, Swarnali, and Anupam. I am also thankful to my seniors specially Dr. Biplab Bhattacharjee, Mr. Sumanta Kundu, Mr. Somnath Dutta, Mr. Arghya Das and Mr. Subhadip Chakraborti for encouraging me to do the research.

I am thankful to Dr. Monalisa Pal who guided me during my research work. Without her help, I could not get success in my research career.

I am grateful to my school teachers, private tutors, college teachers and my friends. I will never forget some teachers of my college: Dr. Aragya Varan Saha, Dr. Prasanta Ghosh and Dr. Bimal Kr. Sadhukha. They inspired me to do research through their way of teaching.

I must name some of my friends also: Krishnendu, Gobinda, Dibyo, Ranjit, Mukunda, Kaushik, Swarnakamal, Samrat, Suman, Avijit, Krishnendu, Dipendu, Rajdeep and Sudhir for their company.

I am also thankful to some monks of Ramakrishna Mission: Swami Suparnananda (Satyada), Swami Madhabeshananda (Monomoyda) and Swami Divyasudhabhananda (Arijitda) who always show me the right path to walk. I am blessed that I came in their contact during my college days.

Finally I express my gratitude to my beloved parents (Mrs. Snigdha Chakraborty and Mr. Asim Chakraborty) for their constant moral supports, inspiration and guidance. I am very much thankful to my elder brother Dr. Chandrachur Chakraborty who guides me always from my very early school days to till now. I am really lucky that I got an elder brother like him. I am also thankful to my sister-in-law Mrs. Shrabasti Bhattacharya for her moral support.

Indranil Chakraborty

List of Publications

1. **I. Chakraborty**, U. Saha, D. Mandal, S. Mukherjee, N. Joardar, S. P. S. Babu, G. S. Kumar, and K. Mandal
"Effect of bovine serum albumin on tartrate-modified manganese ferrite nano hollow spheres: spectroscopic and toxicity study"
Physical Chemistry Chemical Physics, 21 (2019) 10726-10737.

2. **I. Chakraborty**, U. Saha, R. Rakshit, S. Talukdar, K. Mandal, and G.S. Kumar
"Design and development of bioactive α-hydroxy carboxylate group modified $MnFe_2O_4$ nanoparticle: comparative fluorescence study, magnetism and DNA nuclease activity" **Materials Today Chemistry**, 5 (2017) 92-100.

3. **I. Chakraborty**, R. Rakshit, and K. Mandal
"Synthesis and functionalization of $MnFe_2O_4$ nano−hollow spheres for novel optical and catalytic properties"
Surfaces and Interfaces, 7 (2017) 106-112.

4. **I. Chakraborty**, D. Majumder, S. Roy, and K. Mandal
"Surface engineered magneto-fluorescent $MnFe_2O_4$ nanoparticles in the realm of biomedical applications"
Surfaces and Interfaces, 9 (2017) 154-159.

5. M. Alam, **I. Chakraborty,** and K. Mandal
"Microwave synthesis of surface functionalized $ErFeO_3$ nanoparticles for photoluminescence and excellent photocatalytic activity"
Journal of Luminescence, 196 (2018) 387-391.

6. D. Majumder, **I. Chakraborty**, S. Roy, and K. Mandal
"Facet-dependent photodegradation of mythelene blue using pristine CeO_2 nanostructures" **ACS Omega**, 4 (2019) 4243-4251.

Contents

Chapter 1

Introduction

This introductory chapter consists of literature review of various works that motivated me to work in this specific field. In addition, it contains a brief outline of the entire work and the theoretical aspects that helps to explain the findings.

1. Introduction

1.1. Nanomaterials

The prefix *nano* comes from the Greek word for *dwarf*, and hence nanoscience deals with the study of atoms, molecules and nanoscale particles. Although, beginning of nanomaterials (NMs) are unclear. The first nanotechnologists may have been glass workers. They used gold for making various glazes found on ancient and antique glasses. Later, on 1959, Professor Richard Feynman raises few questions and possibilities which opened a new door of modern origin of nanoscience. Nowadays, researchers witness the development and advancement of the new interdisciplinary scientific field−nanoscience. In the world of this field, researchers deal with the particles between 1 and 100 nanometres (nm) which is termed as nanomaterials. NMs have a great influence to interrelate chemistry, physics and biology field to develop a new fundamental knowledge. The new and significant improvement of various properties of NMs enriches the field comparing with bulk materials [1]. A bulk material has constant physical properties irrespective of size but at the nano-scale, size dependent properties are observed. The interesting and unexpected properties of NMs are often observed due to the large surface area to volume ratio which dominates the contribution made by the small bulk of the material. In fact, properties of NMs differ enormously when the size or morphology changes ranging from spheres, particle, cube, rod, disc, film and wire [2-7]. NMs significantly influence optical and magnetic properties, chemical reactivity, electronic excitation and conductivity depending on their size. Due to their novel properties, NMs have become promising candidate to solve challenges in the field of medicine, energy storage, catalysis, sensing and information technology [8-15].

1.2. Metal Oxide Nanomaterials

3d transition metal oxide based NMs play a very important role in interdisciplinary areas due to their unique physical and chemical properties resulting from the small size and a high density of corner or edge surface sites. Transition metal oxides like TiO_2, Fe_3O_4, MnO_2, CoO, NiO and CuO nanostructures have attracted key attention due to their cost effectiveness, high chemical stability, easy synthesis process, optical, electronic, magnetic, catalytic, and electrochemical properties [16-23].

1.3. Crystal Structures of Different Transition Metal oxides

Atoms in a solid try to organize themselves in such a way that the overall energy becomes minimize. Such arrangements may be extended over large distances. In a crystal, the smallest repeating pattern is known as unit cell. A unit cell is the repeat unit that can generate 3D crystal. Crystal structure is described in terms of the geometry of arrangement of particles in the unit cell. In general, metallic solids tend to adopt close-packed structures in which each atom has 12 surrounding nearest neighbors. Based on the arrangement and stacking of atoms in the layer, hexagonal close packing (hcp), cubic close packing (ccp) and face centered cubic (fcc) structures can be formed. For example, FeO possesses ccp structure where Fe^{2+} ions take place octahedral sites. Ferrite (Fe_3O_4) is a mixed oxide having cubic inverse spinel structure, where the oxide ions are in a face centered ccp array. The divalent Fe^{2+} ions occupy octahedral sites whereas the trivalent Fe^{3+} ions are equally occupying tetrahedral and octahedral sites. Other members of ferrite are developed replacing Fe^{2+} by other divalent cations such as Mn^{2+}, Co^{2+} and Ni^{2+} etc. The spinel structure is typical for a large number of metal oxides and sulfides of general stoichiometry AB_2X_4 where X = O or S. A is usually a cation of charge 2+ and B a cation of charge 3+ but other combinations are also known. When the A cations normally occupy one-eight of the tetrahedral sites and the B cations occupy half of the octahedral holes, the structure is called normal spinel which is represented as $A^{ted}B_2{}^{oh}X_4$. Figure 1.1 demonstrates crystal structure of normal spinel (AB_2O_4) where trivalent B ion and divalent A ion stay in octahedral and tetrahedral sites, respectively.

However, in some spinels, the coordination geometry of A and B cations are reversed. The A cations displace half of the B cations from their octahedral sites and the displaced B cations now enter the vacated tetrahedral sites. This is usually referred to as the inverse spinel structure which is represented as $B^{ted}(AB)^{oh}X_4$.

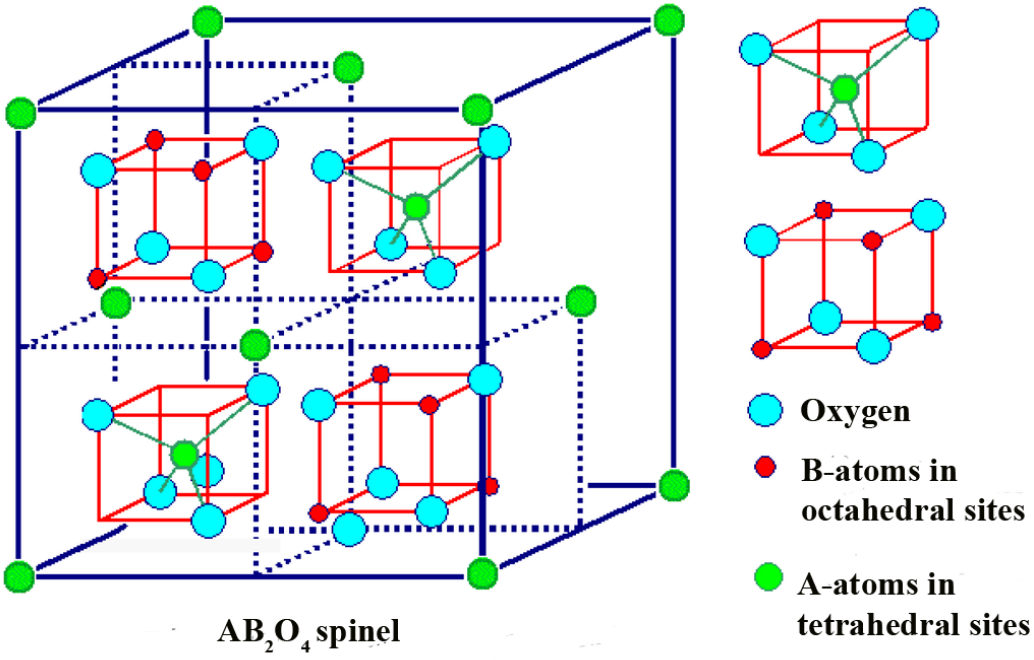

Figure 1.1. Crystal structure of AB_2O_4. (red ball is B^{3+}, green ball is A^{2+} and the blue ball is O^{2-}).(© chemwiki.ucdavis.edu)

Some spinels with inverse structure are the iron (III) oxide spinels like AFe_2O_4 where A may be Co^{2+}, Ni^{2+} or Mn^{2+}. During the synthesis of nanostructures (NSs), atoms arrange themselves in such a way that the growth of crystal along preferred orientation leads to the formation of different crystal phases and/or different shapes of same crystal structure with same elemental composition. Besides, NSs synthesis is highly dependent on temperature, pressure, time, nature and amount of capping agent.

1.4. Magnetic Properties

Some of the transition metal oxides like FeO, MnO, NiO and CoO show antiferromagnetism. Antiferromagnetism arises when the spins on different nuclei interact cooperatively but in such a way as to cancel out the magnetic moments. For example, ccp structure of CoO where several linear Co-O-Co arrangements exist. In each of this, the dz^2 orbital on the Co can overlap with the $2p_z$ on oxygen, leading to partial covalency. The oxide ion of Co-O bond has a closed shell and so there is another $2p_z$ electron, which must have opposite spin. This electron forms a partial bond with the next Co, as a consequence, the dz^2 on this Co pairs with the $2p_z$ electron of opposite spin. The net result is that adjacent Co ions have opposed spins. In this case, spins of electrons interact through the oxide ions and the spins align antiparallel through super exchange. Generally, in cubic spinel structure, ions on octahedral

sites interact directly with each other and their spins align parallel and they also interact with those on tetrahedral sites.

For molecular formula of AFe_2O_4 (where A^{2+} = divalent ions of Fe, Mn, Ni, Co etc.), the Fe^{3+} ions on tetrahedral sites are aligned antiparallel to those on octahedral sites, so that there is no net magnetization from these ions. A^{2+} ions, having unpaired electrons, tend to align their spins parallel with those of Fe^{3+} on adjacent octahedral sites and hence with those of other A^{2+} ions. This produces a resultant ferromagnetic interaction for ferrites where A^{2+} has unpaired electrons. Ferromagnetism is actually greatly enhanced paramagnetism due to close alignment of magnetic dipoles in the same direction. Magnetic properties of NMs depend on size and surface of the NMs which give rise to various special features. The dimensions of magnetic domains are about 10-1000 nm which are comparable to the size of NMs. So if the crystal size approaches to single domain dimension upon scaling down the particle size of ferromagnetic material, all the spins get aligned to each other, so the demagnetization becomes very much difficult. Superparamagnetism of NMs is a form of magnetism which appears in small ferromagnetic or ferromagnetic NMs. In sufficiently small NMs, magnetization can randomly flip direction under the influence of temperature. The typical time between two flips is called the Néel relaxation time. In the absence of an external magnetic field, when the time used to measure the magnetization of the NMs is much longer than the Néel relaxation time, their magnetization appears to be in average zero; they are said to be in the superparamagnetic state. In this state, an external magnetic field is able to magnetize the NMs, similarly to a paramagnet.

1.5. Surface Modification of Nanomaterials

Surface modification of NMs is necessary to tune the optical, magnetic and catalytic properties for different applications in the field of nanotechnology and biomedical field. There are different types of surface modification strategy such as chemical functionalization process, plasma assisted coating and scaling down the size of NMs to improve surface to volume ratio.

Chemical functionalization process is carried out for various purposes. For synthesis of NMs, different types of surfactants are used. Surfactants molecules bind to the surface of the NMs and stabilize the nuclei and large NMs against aggregation by a repulsive force. Surfactants also control the growth of the NMs in terms of rate and final size or geometric size. NMs can be functionalized with suitable ligands, so that they can be dispersed either in aqueous

medium or organic solvent due to hydrophilic and hydrophobic behavior respectively [24-26]. Polar molecules are soluble in aqueous medium. Tartrate, malate, citrate, amino acids and glucose are soluble in water medium as they have permanent dipole moment. Ligands with –COOH, −OH and $–NH_2$ groups are suitable for surface modification of NMs as they are able to interact further with macromolecules like DNA, RNA and proteins. This modification strategy is very helpful for biomedical applications of the NMs.

Nonpolar organic solvents like toluene, hexane and chloroform are used for fabrication of oil-soluble type NMs. The most common organic solvents are oleic acid and oleyamine, which have a C_{18} tail with a cis-double-bond in the middle, forming a kink. Such kinks are extremely necessary for effective stabilization of the NPs during the synthesis process. Some amphiphilic ligands like poly (ethylene glycol) (PEG), block copolymers (such as HAMAFA-b-DBAM) make the NMs soluble in a number of solvents with intermediate polarity [27-33]. To change the hydrophobic layer of the ligand over the surface of NMs to hydrophilic layer, ligand exchange method may be useful also. This process exchanges the hydrophobicity of the ligand. Ligand for surface functionalization of the NMs may be chosen on the basis of NMs. Carboxylic acid or hydroxyl groups are suitable candidate for surface functionalization of metal oxide NMs. Gold nanoparticles (NPs) prefer to bind with thiol, Trioctylphosphine (TOP) or its oxide (TOPO) binds preferentially to the zinc or cadmium quantum dots (QDs) [34-41]. Ligand molecules bind to the NPs by electrostatic interaction. Nowadays, researchers are interested to use biodegradable polymers like poly (aspartate), poly (saccharides), gelatin, starch, poly (acrylic acid), PEG, poly (D, L-lactide) (PLA), chitosan, and poly (methylmethacrylate) (PMMA) as a ligand for functionalization of magnetic nanomaterials (MNMs) [42-53]. Inorganic materials show absorption, fluorescence, phosphorescence properties and high magnetic moment which can be useful for various purposes. Coating of NMs with these ligands provides the stability of NMs and improves the optical properties, catalytic efficiency, bio labeling and bio imaging properties. Some inorganic materials (silica, Au, metal oxides etc.) help biological ligands in binding to the NMs surface. Chemically surface functionalization of MNPs and changing of surfactants tuned the magnetic and fluorescence properties of MNPs. Surface modification of MNMs with biocompatible ligand and dye makes modified MNMs suitable for imaging diagnosis, drug delivery, biomarker and therapy [54-64]. Also, MNMs coated with specific antibody help to target selectively tumor or cancer cells [65-69]. Another aspect for surface modification of MNMs is to increase surface to volume ratio. With increasing surface for the

same volume, the reactivity increases. Enhanced surface area plays valuable role in various technological applications (e.g. catalysis, adsorption, electrochemical performance etc.) [70].

1.6. Ligand Field Theory for Chemically Functionalized Metal Ions

According to valence bond theory, covalent bond formation occurs for overlapping of atomic orbitals (usually hybrid orbitals) of the metal and the ligand. This theory can explain the coordination number of a complex and hybridization state. Although this theory has many drawbacks; particularly it cannot explain the spectral properties and magnetism of a compound. To explain the color and magnetic properties of salts of metals, crystal field theory (CFT) was proposed based on purely electrostatic interaction between a metal ion and the ligands. The electrostatic interaction occurs between the positive nucleus of the metal and the negatively charged electrons of the ligands. Later modifications of the crystal field theory are sometimes referred to as the ligand field theory. This theory is now used in a broader sense which is a combination of CFT and molecular orbital theory. It describes the loss of degeneracy of metal d orbitals in transition metal complexes. Metal d orbitals split in the following fashion as shown in the Figure 1.2.

In octahedral field, ligands approach from the direction of axes resulting in destabilization of the orbitals along the axes ($d_{x^2-y^2}$ and d_{z^2}), and stabilization of the orbitals lying in between the axes (d_{xy}, d_{yz}, d_{xz}). In case of tetrahedral field d_{xy}, d_{yz}, d_{xz} orbitals are nearer to the direction of approach of the ligands than the $d_{x^2-y^2}$ and d_{z^2} orbitals, so the inverse arrangement is observed [71].

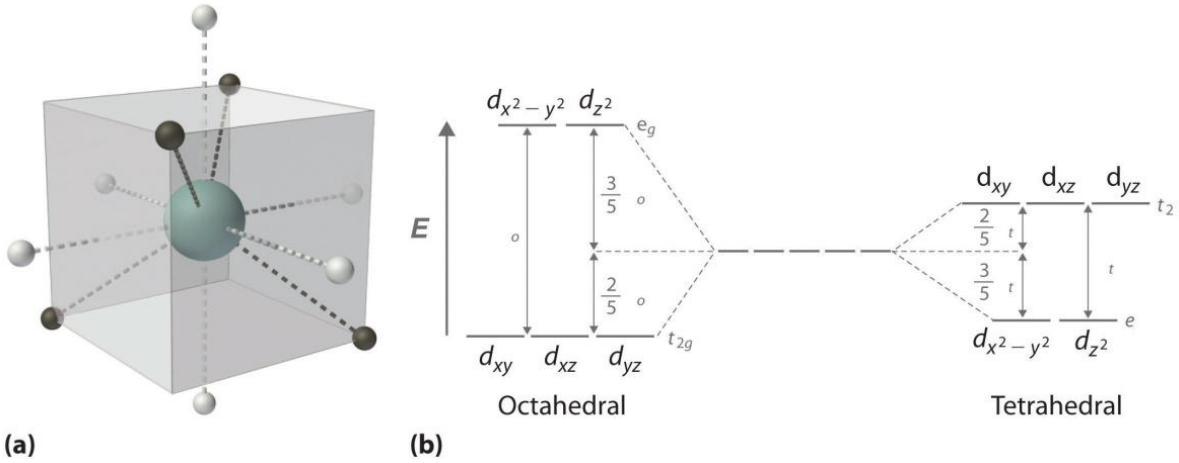

Figure 1.2. (a) White and black spheres indicate orientation of metal d orbitals in octahedral and tetrahedral coordination spheres, respectively. (b) Energy splitting of d orbitals in octahedral and tetrahedral field.

1.7. Spectrochemical Series

A spectrochemical series of the ligands is written as the increasing order of their splitting of the d orbitals (Δ) value or field strength in a given geometry. For a given ligand, Δ value is almost same in first transition series in the same oxidation state. The magnitude of Δ increases by about 30% to 50% on passing from the 1st transition series to the 3rd transition series, that is 3d<4d<5d. Δ value also increases with the oxidation state of the metal. For a given ligand, metal ions can be arranged according to increasing order of Δ:

$$Mn^{2+}<Ni^{2+}<Co^{+2}<Fe^{2+}<V^{2+}<Fe^{3+}<Cr^{3+}<V^{3+}<Co^{3+}$$

In this spectrochemical series of metal ions, magnitude of Δ gradually increases with the charge of metal ions which results in increased of metal−ligand interaction. The order of common ligands according to their increasing ligand field strength is:

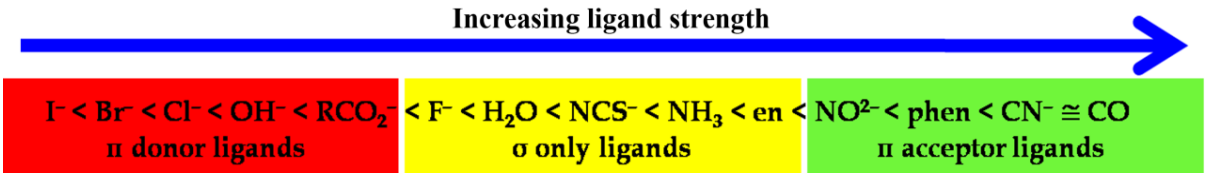

Figure 1.3. Spectrochemical series of various ligands in the increasing order of ligand strength.

In Figure 1.3, ligands arranged on the left end are weak field ligands and form high spin complexes. On the other hand, ligands lying at the right end are stronger field ligands and form low spin complexes. The order of spectrochemical series can also be classified by their donor and acceptor abilities. Ligands that have occupied p orbitals are Π donor ligands. They have tendency to donate Π electrons with the σ bonding electrons to the metal, exhibiting stronger metal-ligand interactions and an effective decrease of Δ. Π acceptor ligands having vacant Π* with comparable energy to metal d orbitals, can undergo Π back bonding, resulting in increase of Δ. The metal ions can also be arranged in order of increasing Δ.

1.8. Tanabe-Sugano Diagrams

Orgel diagram is suitable for high spin complexes. They show spin allowed transition only. In general, Orgel diagram is less informative. Tanabe-Sugano diagram is most widely used as this diagram is suitable for high and low spin complexes. This diagram shows both spin allowed and spin forbidden transitions. Tanabe–Sugano diagrams are used in inorganic chemistry to predict absorption in the UV, visible and IR electromagnetic spectrum of coordination chemistry. This diagram shows the energy of different states at various field strengths including low spin complexes. The state energies and 10 Dq (Dq = Ligand field splitting parameter) are both expressed in units of the Racah parameter B, denoting interelectronic repulsion. Since, energies are plotted in units of B, one Tanabe-Sugano diagram may be used for all members of an isoelectronic group. The energy of the ground state is considered as zero for all field strength and all energies of all other terms are plotted with respect to the ground term. Certain Tanabe–Sugano diagrams of d^4, d^5, d^6 and d^7 systems have a vertical line drawn at a specific Dq/B value, which corresponds with a discontinuity in the slopes of the excited states' energy levels. This pucker in the lines occurs when the spin pairing energy (P) is equal to the Dq. Complexes to the left of this line (lower Dq/B values) is high spin and to the right (higher Dq/B values) are low spin. There is no high spin or low spin designation for d^2, d^3 or d^8. For an example, Tanabe–Sugano diagram of d^4 system is demonstrated in Figure 1.4.

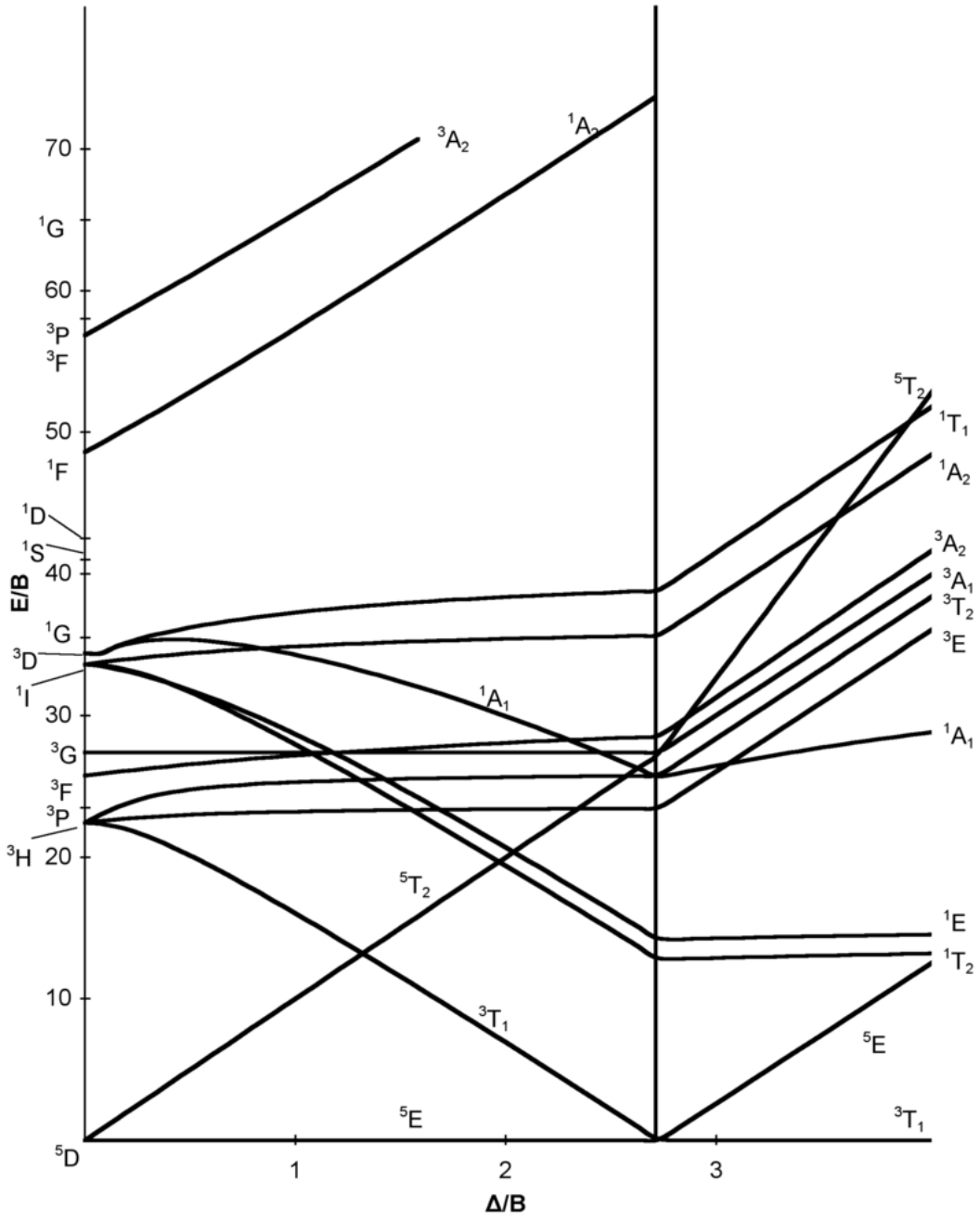

Figure 1.4. Tanabe–Sugano diagram of d^4 system.

1.9. Selection Rule

Laporte and spin are two types of selection rule for electronic transitions. In a centrosymmetric environment, an allowed transition must have orbitals of different symmetry with respect to an inversion centre, i.e., gerade (*g*) to ungerade (*u*) transitions or vice versa are allowed. $g \rightarrow g$ and $u \rightarrow u$ are forbidden. Alternatively, allowed transitions for an

electron will be $\Delta L = \pm 1$. That means, $d \rightarrow p$, $s \rightarrow p$ transitions are allowed but $d \rightarrow d$ or $s \rightarrow d$ transitions are not. Laporte rule is not applied for tetrahedral complexes as they don't have centre of inversion. Laporte rule may be relaxed if the centre of symmetry of octahedral complex is eliminated by some means. If the molecule vibrates asymmetrically, the centre of symmetry will be destroyed. Due to the vibronic coupling, mixing of orbitals results in electronic transition.

For the spin selection rule, transition is allowed between two energy states which have the same spin multiplicity. This means during the electronic transition, the change in the total number of unpaired electrons are spin forbidden. For a spin allowed transition: $\Delta S = 0$ and for spin forbidden transition: $\Delta S \neq 0$. For example, $^3A_{2g} \rightarrow {}^1E_g$ transition involving a change of multiplicity is much weaker than $^3A_{2g} \rightarrow {}^3T_{2g}$, where multiplicity remains unchanged. Like the Laporte rule, spin selection rule also is relaxed in some cases. During the spin-orbit coupling, spin selection rule breaks down.

1.10. Jahn-Teller Effect

Ligand field splitting of the five d orbitals produces degenerate group of five d states. One of these groups is neither half occupied nor full occupied by electrons. Jahn-Teller theorem states that any non-linear molecular system in a degenerate electronic state is unstable and will undergo distortion to remove the degeneracy and to lower the energy. The effect of Jahn–Teller distortion is more prominent when odd number of electrons occupies e_g orbitals of octahedral complexes. This situation arises in complexes with the configurations d^4 (high spin), d^7 (low spin) and d^9 complexes, which are doubly degenerate. Figure 1.5 shows the changes in Tanabe–Sugano diagram of Mn^{3+} complex due to Jahn–Teller distortion [72]. In octahedral complexes of d^4 system, the e_g orbitals point directly at the ligands. So, distortion of octahedral complexes causes destruction of degeneracy. As a result, large energetic stabilization occurs. This effect also occurs in t_{2g} orbital for d^1 and d^2 system as they both are triply degenerate. However, in such cases, the effect is not so prominent because repulsion is negligible to take ligands further away from the t_{2g} orbitals. In an octahedral ligand field, no Jahn-Teller distortion is expected for d^0, d^3, d^5 (high spin), low spin d^6, d^8 or d^{10} electron configurations; this means that repulsions between different ligands are all the same.

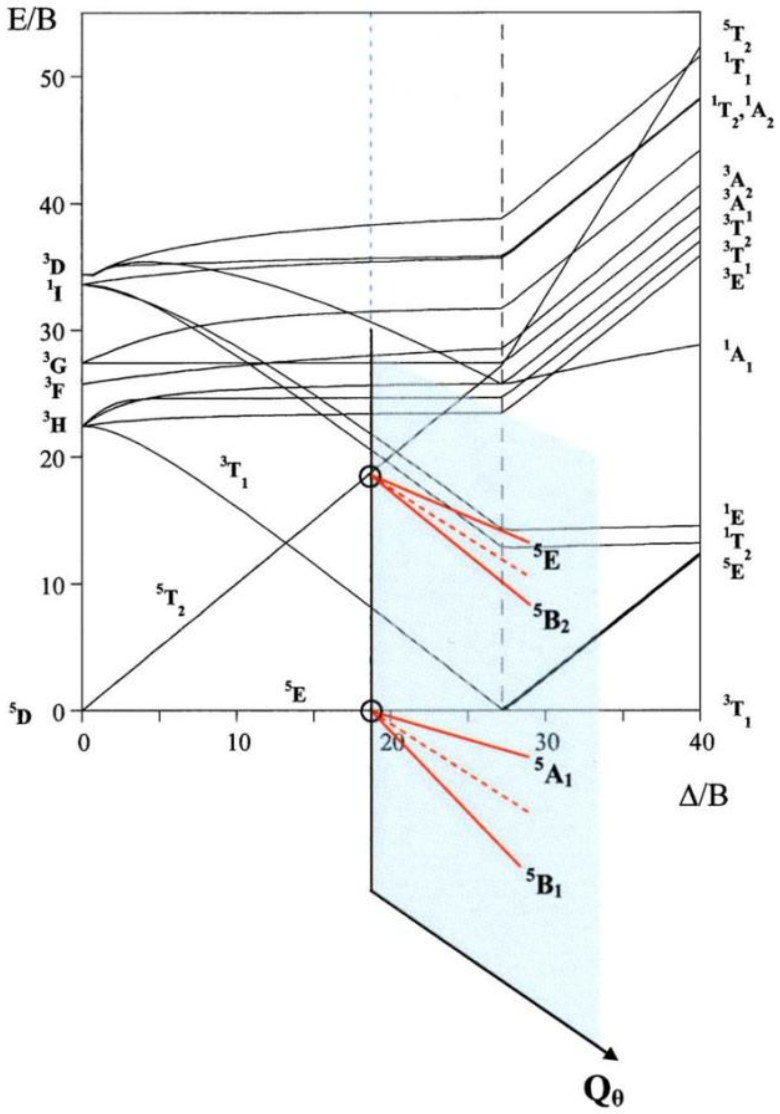

Figure 1.5. Tanabe-Sugano diagram for $3d^4$ ions due to Jahn–Teller effect. (©Aguado et.al *Phys. Rev. B* **2007,** 76, 094417).

1.11. Ligand to Metal and Metal to Ligand Charge Transfer Bands

Charge transfer transitions are basically movement of electrons from orbitals which have ligand character to orbitals which have metal character or vice versa. Ligand to metal charge transfer (LMCT) is common for both octahedral and tetrahedral complexes. LMCT is most common for the filled Π orbitals of the ligands. A simplified molecular orbital energy level diagram for octahedral complex is shown in Figure 1.6 where L stands for ligand. Ligand processes σ and Π orbitals. When ligand binds with the metal, Π → Π* and Π → σ* transitions are expected.

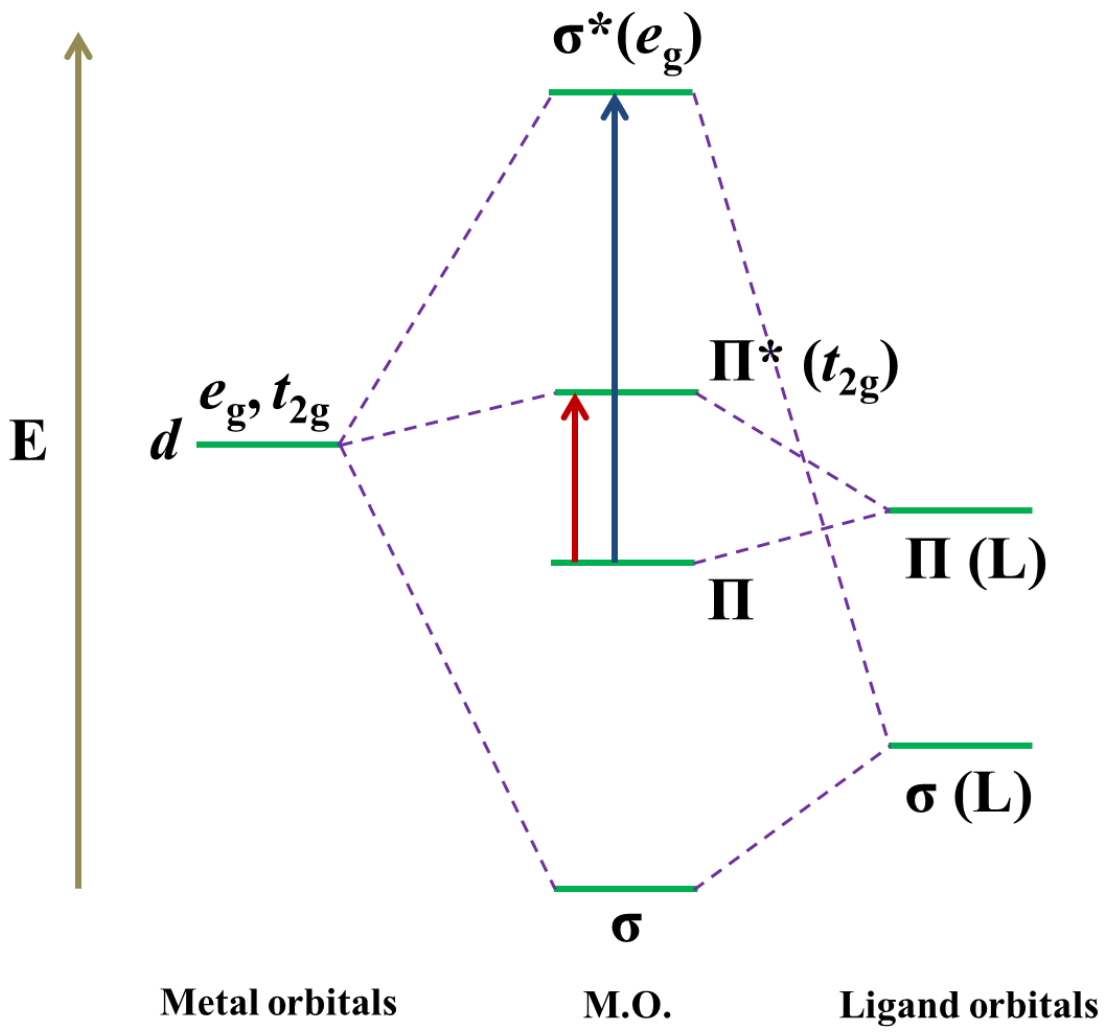

Figure 1.6. Simplified molecular orbital diagram showing charge transfer transitions in an octahedral complex.

If the metal is in a low oxidation state (electron rich) and the ligand possesses low-lying empty orbitals then a metal to ligand charge transfer (MLCT) transition may occur. As for example; CO, CN^- ligands have vacant Π* orbitals which can give rise to such charge transfer bands. Hence, MLCT transitions are common for Π acceptor ligands. Upon the absorption of light, electrons in the metal orbitals are excited to the ligand Π* orbitals.

1.12. Catalytic Activity of Nanomaterials

Catalysts are essential components for chemical synthesis. A catalyst increases the rate of the reaction and helps to achieve the desired product. Nanocatalysts are consisting of NMs of a noble metal that is well dispersed onto an oxide support. The use of nanocatalysts in catalysis

field is increasing rapidly due to the smaller size (1-100 nm) of the NMs. The active metal atoms are exposed to the surface and thus minimize the specific cost per function [73-75]. In past few decades, the growth of nanocatalysis has increased exponentially. Generally, two types of catalysis are used for various reaction purposes. One is homogeneous catalysis in solution and another is heterogeneous catalysis in which the NMs are supported on a substrate.[63] Homogeneous catalysts are used in the same medium as the reactants. For NMs, it means a solution or suspension of NMs in the solvent. The dispersed NMs in the solvent are stabilized by surfactants, ligands, polymers, block copolymers and dendrimers [76-79]. NMs have a natural tendency to attract each other in the solution medium. Nanocatalysts are designed in such a way that it can prevent aggregation of the NPs. Otherwise; NMs will clump together and form a larger particle. To stabilize NMs in the solution medium, generally long chain molecules are used. Long chain molecules are attached to the surface of the NMs and stabilize. Sometimes, they can reduce the catalytic activity of the NMs due to the blocking of surface area. Recovery of the catalysis is also a main concern. If NMs are used for at least 3 or 4 times, it can be beneficial for our ecosystem. The more environmentally friendly catalysis is heterogeneous catalysis. This catalysis is in the different phase to the reactants. The catalyst is usually solid and immobilized on a solid inert matrix. Heterogeneous catalysts are preferred over homogeneous catalysts because with the former the reaction products can be separated and recover easily. NMs are supported on various substrates like carbon, silica, alumina, titanium dioxide and polymers by chemical methods, grafting, lithography etc. [80-86]. Nanoporous materials are manufactured by growing the solid material around a molecular template. Catalytic activities greatly depend on their shape and size of NMs. Surface modification of MNMs is a strategic way to make a bridge between heterogeneous and homogeneous catalysis due to their easy preparation, active surface for adsorptions or immobilization of metals and ligands and controlled separation by applied magnetic field the completing the reaction. The impact on nanocatalysis is graphically shown in Figure 1.7. Key features of nanocatalysis research are to increase selectivity, activity, minimize energy consumption and enhance lifetime of catalysts by controlling pore size and particle characteristics. This can be achieved only by precisely controlling the size, shape, spatial distribution, surface composition and electronic structure and thermal and chemical stability of the individual NMs. In can be conclude that nanocatalysts are a crucial part of the modern chemical industry and are used in a huge number of chemical processes. Researchers are constantly pushing to improve the performance and lifetime of the new catalysts which are profitable in chemical manufacturing industries.

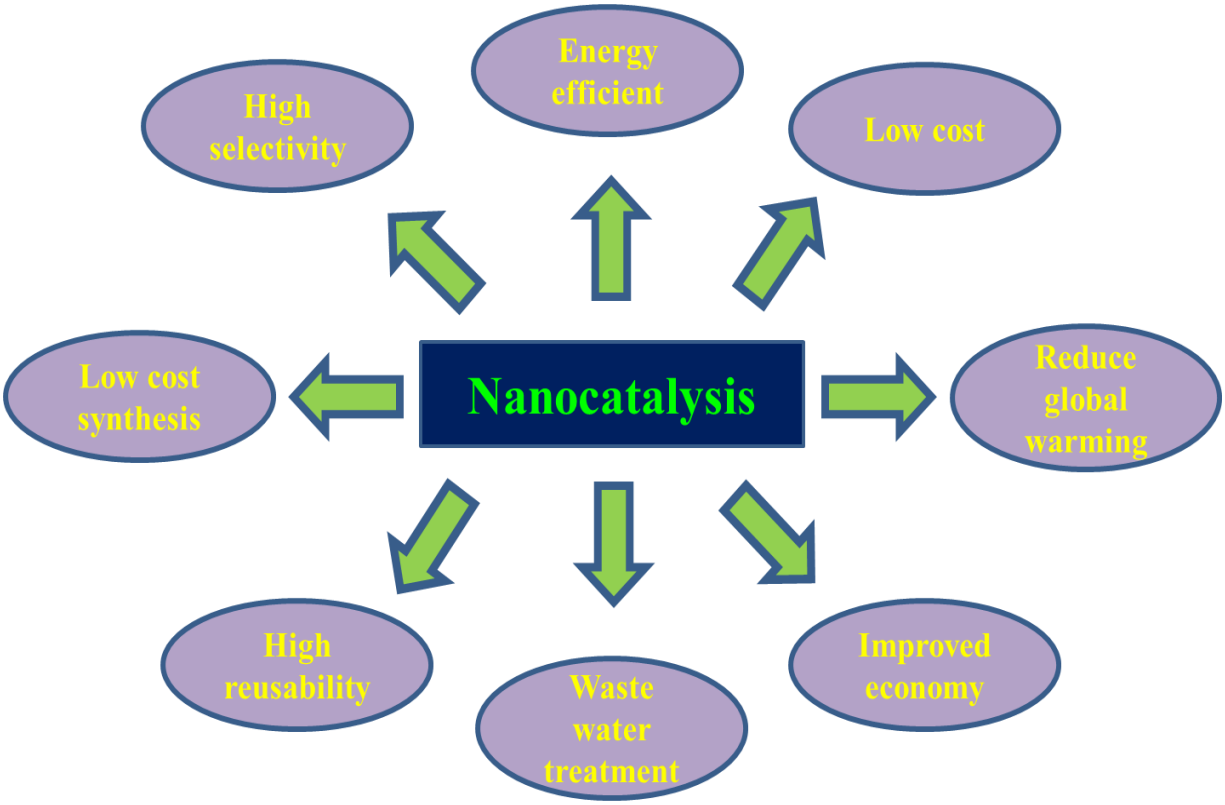

Figure 1.7. Graphical representation of impact of nanocatalysis.

1.13. Surface Functionalization of Nanomaterials

NMs are a new generation of innovative materials, which have advanced applications in diverse field of nanotechnology. Mainly, biomedical diagnosis and therapy is innovative and emerging field which can be traced back through several decades. The proper functionalization of MNMs has received a great advantage of consideration owing to their enhanced properties compared to their base counterparts. Functionalized MNMs rises many opportunity in the field of biomedical applications. In the realm of multifunctional MNMs, magnetic metal based system suspended in organic or inorganic liquid has got significant focus. Also, there are several approaches to construct biocompatible MNMs with desired functional ligands. Most of the biological functions take place at the molecular level that have a size range of less than 100 nm. Functionalized MNMs exhibit unique surface properties which can be used for biomedical applications. Size tunability of MNMs from few nanometres to tens of nanometres and functionalization with biocompatible ligand enable them to match with the biomacromolecules (DNA, RNA and protein etc.). The conjugation of a ligand to the surface of MNMs is a new tool to recognize antigen and antibody.

Multifunctional MNMs are fabricated either by chemically with small ligands like proteins, surfactants, DNA, RNA, antibodies and dyes etc. or by forming nanocomposites with other functional nanoprobes such as, metal NPs, QDs etc. Colloidal MNMs can be applied in early detection, disease diagnosis noninvasive treatment and also in disease prevention. Some other applications include: targeting dug delivery to a specific site with the help of external magnetic field, facilitate the enhancement of the MRI contrast, gene therapy, hyperthermia, fluorescence imaging and MRI contrast agent [87-91]. NMs are solid in nature. Sometimes, it is difficult to use the NMs for biological purposes. The outer surface modification of NMs with water soluble ligands makes the NMs disperse and stable in the water medium. Further, depending on the type of applications; DNA, protein, fluorophore, drug and antibody can be attached to the functional group of ligand [92-97]. Very recently, significant attention has been given to develop MNMs as sustainable nanocatalyst for specific chemical reactions having both economic and environmental significance.

1.13.1. Determination of Association Constant (K_{BH})

The association constant (K_{BH}) is determined to reaction equilibrium that form one-to-one complex, such as host (H)-guest (M) molecular complexation. For the following equilibrium:

$$H + M \leftrightarrows HM \qquad (1.1)$$

Where M denotes the concentration of guest.

The equilibrium constant for the above equation is,

$$K = \frac{[c]}{([H]-[c])([M]-[c])} \qquad (1.2)$$

Where, c is the molar concentration of the complex. Since, [M] >> [c], we replace [M]-[c] with [M].

From the Beer-Lambert law, we know

$$\log_{10}\left(\frac{I_0}{I}\right) = \varepsilon.c.l \qquad (1.3)$$

Where, ε is the molar extinction coefficient.

Now, we can eliminate [c] from equation (1.1) and (1.3) and rearranging the resulting equation, we obtain the following equation which is known as Benesi-Hildebrand (B-H) equation

$$\frac{1}{\Delta A} = \frac{1}{\Delta A_{max}} + \frac{1}{(\Delta A_{\max}) K_{BH}} X \frac{1}{[M]} \qquad (1.4)$$

To determine the association constant for binding of DNA with the NPs, we used this equation where ΔA denotes the difference in absorbance and [M] is the DNA concentration.

Although this equation is related with the absorption spectra of UV-vis spectroscopy, later modification have been made that allow B–H equation to be applied to the fluorescence spectroscopy. The modified B-H equation is as follows:

$$\frac{1}{\Delta F} = \frac{1}{\Delta F_{max}} + \frac{1}{(\Delta F_{max})\, K_{BH}} \times \frac{1}{[M]} \qquad (1.5)$$

1.13.2. Determination of Binding Constant Using Ingersoll and Strollo Method

Fluorescence anisotropy (*r*) is a useful experiment to know how the surrounding environment imposes motional restriction on the fluorophore. With lower the anisotropy value, rotational diffusion becomes faster and the vice versa. Anisotropy measurements are made by exciting the fluorophore with polarized light and measuring the fluorescence intensity both parallel and perpendicular to the excitation polarization. Specifically, the sample is excited with vertically polarized light and the vertical and horizontal emission components (I_{VV} and I_{VH}) are measured. Anisotropy (*r*) is defined by the following equation:

$$r = \frac{I_{VV} - G I_{VH}}{I_{VV} + 2G I_{VH}} \qquad (1.6)$$

Where, *G* is the intensity ratio of the vertical (V) to horizontal (H) components of the emission.

The measured anisotropy (*r*) is also represented as follows:

$$r = f_F r_F + f_B r_B \qquad (1.7)$$

where f_F and f_B are the fractional fluorescence contributions of the free and bound forms of the fluorophore, respectively, and r_F and r_B are the corresponding anisotropy values.

Rearranging equation (1.7) and incorporating a correction factor (R), the f_B is calculated as follows:

$$f_B = \frac{r - r_F}{R(r_B - r) + (r - r_F)} \quad (1.8)$$

Notice that if there is no change in intensity upon binding, R is equal to one.

Considering the equilibrium for the binding of NHSs to BSA,

$$NHSs + BSA \leftrightarrows NHSs - BSA \quad (1.9)$$

The binding constant can be expressed as

$$K_b = \frac{NHSs - BSA}{[NHSs][BSA]} \quad (1.10)$$

and the dissociation constant, $K_d = 1/K_b$. The equilibrium expression is related to the fraction of f_B

$$f_B = \frac{[BSA]}{[BSA] + K_d} \quad (1.11)$$

or

$$\frac{1}{f_B} = 1 + \frac{1}{K_b[\mathrm{BSA}]} \quad (1.12)$$

1.14. Motivation and Objective of Thesis

The surface functionalization of NMs has attracted an attention because particle surface chemistry determines their interactions with the drug, DNA, RNA and protein. These interactions not only play a key role in colloidal stability but also control assembly process, targeting, drug delivery and sensing capabilities. Therefore, long term research has been focused on the morphology controlled synthesis and functionalization of metal oxides for advanced physiological properties and technological applications. Magnetic NPs as well as nano hollow spheres (NHSs) gain enormous attention due to their long range applications from data storage, energy sector, catalysis to biomedical field [98-103].

Moreover, outer surface fabricated NPs and NHSs exhibits improved optical, magnetic and electrical properties compared to their bulk counterparts. In recent years, the performance of various NPs and NHSs has been improved. MNMs are coated with thiols, silica, titania and polymer etc. In general, all of them are classified within three routes: ligand exchange, ligand modification and deposition of additional layers. Unfortunately, the coated materials do not show any fluorescent colours. Some fluorescent dyes that can be combined with the surface

of the MNMs, is used for different biological purposes. Application of these probes including levelling of cells, proteins, diagnosis, therapy and measurement of enzyme activity. Fluorescent nanomaterials with versatile optical properties provide unique advantages for fluorescence due to their size, composition and surface modification. Fluorescent MNMs are attractive for bio sensing and bioimaging. For huge applications of the MNMs in biomedical field, incorporation of intrinsic fluorescence property to the magnetic NMs is highly desirable.

To develop new drugs in the active area of medical research, DNA has been targeted extensively. MNMs can interact with the DNA by electrostatic interaction or intercalation between the base pairs. Similarly, bovine serum albumin (BSA) is a model globular protein to study the interaction of protein with the NMs. The interaction largely depends on microenvironment of the system. The interaction study of NMs with the protein or DNA is very essential for drug development and many other investigations. BSA can interact with many biological molecules like fatty acids, vitamins, salts and hormones.

The key focus of the thesis is:

- ✓ We have synthesized $MnFe_2O_4$ NPs and NHSs by wet chemical and solvothermal method respectively.
- ✓ We have functionalized NPs and NHSs with small organic ligands like disodium tartrate (T), disodium DL-malate hydrate (M) and trisodium citrate dihydrate (C) to disperse them in water medium which is an essential criterion for biomedical applications.
- ✓ We have studied the optical properties of the ligand functionalized NPs and NHSs. Interestingly functionalized NPs and NHSs show intrinsic multicolour fluorescence.
- ✓ We have explained the origin of multicolour fluorescence of the ligand functionalized NPs and NHSs using several spectroscopic techniques.
- ✓ We have studied the catalytic efficiency of functionalized nanostructures in degradation of bilirubin and methylene blue which are biologically and environmentally harmful respectively.
- ✓ We have studied the interaction of calf thymus DNA with the NPs and the DNA nuclease activity through systematic study by various spectroscopic tools.

- ✓ We have studied the interaction of human serum albumin (HSA) with the citrate functionalized NPs.
- ✓ We have studied the effect of tartrate functionalized NHSs to the BSA by several spectroscopic techniques.
- ✓ We have measured the toxicity of the functionalized NHSs. RAW 264.7 cell line and Wister rat model were used for *in vitro* and *in vivo* toxicity analysis respectively.

1.15. Organization of Thesis

The entire thesis has been divided into seven different chapters. A brief sketch of the chapters is given below.

Chapter 1 gives a brief introduction about the 3d transition metal oxide based nanostructures, their crystal structures and magnetic properties. Here we have also discussed the necessity of surface functionalization of NMs for their biomedical application and better catalytic activity. To explain the multifluorescent color of modified NMs, we discussed crystal field theory, ligand field theory, spectrochemical series and Tanabe-Sugano diagram in this chapter. Moreover, the motivation of the thesis work and the outline is also included here.

Chapter 2 provides the synthesis procedures of different NSs, their different characterization techniques including instrumental details and experimental methods.

Chapter 3 demonstrates the comparative nature of fluorescence intensities due to the presence of different α-hydroxy carboxylate group in the outer surface of the NPs. Here, we have functionalized $MnFe_2O_4$ NPs with tartrate, malate and citrate. We successfully explained the reason for getting different fluorescence intensities. Detailed study unveils that α-hydroxy carboxylate moiety of the ligands plays key role to generate intrinsic fluorescence in functionalized $MnFe_2O_4$ NPs through the activation of ligand to metal charge transfer transitions, associated with ligand-Mn^{2+}/Fe^{3+} interactions along with d-d transition corresponding to d-orbital energy level splitting of Fe^{3+} ions on NPs surface. Further, $MnFe_2O_4$ NPs show a maximum 140.88% increase in coercivity and 97.95% decrease in magnetization compared to its bare one upon functionalization. The ligands that induce smallest crystal field splitting of d-orbital energy level of transition metal ions are found to result in strongest ferromagnetic activation of the NPs. Moreover, we noticed that tartrate

functionalized NPs binds very easily with calf thymus DNA and it cleaves the supercoiled pBR322 plasmid DNA.

Chapter 4 describes the synthesis of $MnFe_2O_4$ NPs by wet chemical method. To disperse NPs in water medium, surface functionalization has been done with citrate ligand by cyclomixing. The systematic spectroscopic analysis regarding UV-visible absorption and steady state fluorescence emission and excitation reveal that the citrate functionalized $MnFe_2O_4$ (C-$MnFe_2O_4$) NPs are capable of emerging multicolor fluorescence starting from blue, green to red are due to the LMCT and d-d transitions. C-$MnFe_2O_4$ NPs also interact with HSA and show catalytic activity towards methylene blue, a water contaminant and bilirubin, a pigment responsible for jaundice.

Chapter 5 exhibits the synthesis of $MnFe_2O_4$ NHSs by solvothermal process. We have successfully prepared NHSs of diameter of 100 nm. The outer surface modification of NHSs with tartrate ligand makes the nano complex fluorescent. The bright multicolor fluorescence has been explained on the basis of LMCT and d-d transitions over the metal ions. The magnetic measurements through vibrating sample magnetometer demonstrate that room temperature superparamagnetic nature of $MnFe_2O_4$ NHSs remains unaltered after surface modification. We noticed that due to the larger surface area, tartrate functionalized $MnFe_2O_4$ NHSs are more efficient for waste water treatment.

Chapter 6 unveils the interaction of BSA with the tartrate modified $MnFe_2O_4$ NHSs using several spectroscopic techniques which suggest that the interaction occurs by an electrostatic mechanism. BSA enhances the charge transfer transition from tartrate ligand to the metal ions along with d-d transition of Fe^{3+} ions on NHSs surfaces at different pH. A very strong salt bridge formation occurs between the BSA and the surface modified NHSs at pH 10 which is followed by pH 3 and pH 7. Fluorescence microscopic analysis suggests that the BSA significantly enhances the contrast of T-$MnFe_2O_4$ NHSs in UV and blue light excitation because of extended charge transfer from BSA to T-$MnFe_2O_4$ NHSs. Furthermore, *in vitro* toxicity analysis using RAW 264.7 cell line and *in vivo* studies on Wister rat reveales that the T-$MnFe_2O_4$ NHSs are benign. Furthermore, T-$MnFe_2O_4$ NHSs are also appearing to be an antimicrobial agent.

Chapter 7 concludes the thesis with an idea about the scope for future work in this direction.

Bibliography

(1) K. Schwirn, L. Tietjen, I. Beer, Why are nanomaterials different and how can they be appropriately regulated under REACH?, *Environ. Sci. Eur*. **2014**, 26, 4.

(2) A. S. Arico, P. Bruce, B. Scrosati, J. -M. Tarascon, W. van Schalkwijk, Nanostructured Materials for Advanced Energy Conversion and Storage Devices, *Nat. Mater.* **2005,** 4, 366-377.

(3) N. Yang, J. Zhai, D. Wang, Y. Chen, L. Jiang, Two-Dimensional Graphene Bridges Enhanced Photoinduced Charge Transport in Dye-Sensitized Solar Cells, *ACS Nano* **2010,** 4, 887-894.

(4) Z. -S. Wu, W. Ren, L. Wen, L. Gao, J. Zhao, Z. Chen, G. Zhou, F. Li, H. -M. Cheng, Graphene Anchored with Co_3O_4 Nanoparticles as Anode of Lithium Ion Batteries with Enhanced Reversible Capacity and Cyclic Performance, *ACS Nano* **2010,** 4, 3187-3194.

(5) X. Yao, X. Xin, Y. Zhang, J. Wang, Z. Liu, X. Xu, Co_3O_4 Nanowires as High Capacity Anode Materials for Lithium Ion Batteries, *J. Alloys Compd.* **2012,** 521, 95-100.

(6) A. Gowda, S. Kumar, Recent Advances in Discotic Liquid Crystal-Assisted Nanoparticles, *Materials* **2018**, 11, 382.

(7) S. Rahong, T. Yasui, N. Kaji, Y. Baba, Recent developments in nanowires for bio-applications from molecular to cellular levels, *Lab Chip*. **2016**, 16, 1126-1138.

(8) Y. Fan, Y. Huang, The Effective Peroxidase-like Activity of Chitosan-functionalized $CoFe_2O_4$ Nanoparticles for Chemiluminescence Sensing of Hydrogen Peroxide and Glucose, *Analyst* **2012,** 137, 1225-1231.

(9) Q. Cao, Z. Liu, R. Che, Ordered Mesoporous $CoFe_2O_4$ Nanoparticles: Molten-salt-assisted Rapid Nanocasting Synthesis and the Effects of Calcining Heating Rate, *New J. Chem.* **2014,** 38, 3193-3198.

(10) S. Sun, H. Zeng, D. B. Robinson, S. Raoux, P. M. Rice, S. X. Wang, G. Li, Monodisperse MFe_2O_4 (M = Fe, Co, Mn) Nanoparticles, *J. Am. Chem. Soc.* **2003,** 126, 273-279.

(11) M. Pal, A. Kundu, R. Rakshit, K. Mandal, Ligand-Induced Evolution of Intrinsic Fluorescence and Catalytic Activity from Cobalt Ferrite Nanoparticles, *ChemPhysChem* **2015,** 16, 1627-1634.

(12) X. Ren, L. Tong, X. Chen, H. Ding, X. Yang, H. Yang, Deposition of Luminescent Y_2O_3:Eu^{3+} on Ferromagnetic Mesoporous $CoFe_2O_4$@mSiO_2 Nanocomposites, *Phys. Chem. Chem. Phys.* **2014,** 16, 10539-10547.

(13) H. L. Andersen, M. Christensen, In Situ Powder X-ray Diffraction Study of Magnetic $CoFe_2O_4$ Nanocrystallite Synthesis, *Nanoscale* **2015,** 7, 3481-3490.

(14) A. Giri, N. Goswami, M. S. Bootharaju, P. L. Xavier, R. John, N. T. K. Thanh, T. Pradeep, B. Ghosh, A. K. Raychaudhuri, S. K. Pal, Emergence of Multicolor Photoluminescence in $La_{0.67}Sr_{0.33}MnO_3$ Nanoparticles, *J. Phys. Chem. C* **2012**, 116, 25623-25629.

(15) M. R. Willner, P. J. Vikesland, Nanomaterial enabled sensors for environmental contaminants, *J. Nanobiotechnol*. **2018**, 16, 95.

(16) S. K. Nune, P. Gunda, P. K. Thallapally, Y. –Y. Lin, M. L. Forrest, C. J. Berkland, Nanoparticles for biomedical imaging, *Expert Opin Drug Deliv*. **2009**, 6, 1175-1194.

(17) F. Kiessling, M. E. Mertens, J. Grimm, T. Lammers, Nanoparticles for Imaging: Top or Flop?, *Radiology* **2014**, 273, 10-28.

(18) X. Han, K. Xu, O. Taratula, K. Farsad, Applications of nanoparticles in biomedical imaging, *Nanoscale* **2019**, 11, 799-819.

(19) M. M. Mahan, A. L. Doiron, Gold Nanoparticles as X-Ray, CT, and Multimodal Imaging Contrast Agents: Formulation, Targeting, and Methodology, *J. Nanomater*. **2018**, 2018, 15.

(20) R. Bosetti, Cost–effectiveness of nanomedicine: the path to a future successful and dominant market?, *Nanomedicine* **2015**, 10, 1851-1853.

(21) Z. Cheng, A. A. Zaki, J. Z. Hui, V. R. Muzykantov, A. Tsourkas, Multifunctional Nanoparticles: Cost versus benefit of adding targeting and imaging capabilities, *Science* **2012**, 338, 903-910.

(22) I. A. Stenina, P.A. Nikiforova, T. L. Kulova, A. M. Skundin, A. B. Yaroslavtsev, Electrochemical Properties of $Li_2ZnTi_3O_8$/C Nanomaterials, *Nanotechnol Russia* **2017**, 12, 605-612.

(23) K. Jagiello, B. Chomicz, A. Avramopoulos, A. Gajewicz, A. Mikolajczyk, P. Bonifassi, M. G. Papadopoulos, J. Leszczynski, T. Puzyn, Size-dependent electronic properties of nanomaterials: How this novel class of nanodescriptors supposed to be calculated?, *Struct. Chem*. **2017**, 28, 635–643.

(24) H. T. Uyeda, I. L. Medintz, J. K. Jaiswal, S. M. Simon, H. Mattoussi, Synthesis of Compact Multidentate Ligands to Prepare Stable Hydrophilic Quantum Dot Fluorophores, *J. Am. Chem. Soc.* **2005**, 127, 3870-3878.

(25) I. Fratoddi, Hydrophobic and Hydrophilic Au and Ag Nanoparticles. Breakthroughs and Perspectives, *Nanomaterials* **2018**, 8, 11.

(26) I. Kaur, L. -J. Ellis, I. Romer, R. Tantra, M. Carriere, S. Allard, M. M. L'Hermite, C. Minelli, W. Unger, A. Potthoff, S. Rades, E. V. Jones, Dispersion of Nanomaterials in Aqueous Media: Towards Protocol Optimization, *J. Vis. Exp.* **2017**, 130, 56074.

(27) S. Yang, D. Chen, N. Li, X. Mei, X. Qi, H. Li, Q. Xu, J. Lu, A Facile Preparation of Targetable pH-sensitive Polymeric Nanocarriers with Encapsulated Magnetic Nanoparticles for Controlled Drug Release, *J. Mater. Chem. C* **2012**, 22, 25354-25361.

(28) W. Wu, Z. Wu, T. Yu, C. Jiang, W. -S. Kim, Recent progress on magnetic iron oxide nanoparticles: synthesis, surface functional strategies and biomedical applications, *Sci. Technol. Adv. Mater*. **2015**, 16, 023501.

(29) J. S. Suk, Q. Xu, N. Kim, J. Hanes, L. M. Ensign, PEGylation as a strategy for improving nanoparticle-based drug and gene delivery, *Adv Drug Deliv Rev*. **2016**, 99, 28-51.

(30) Beatriz Pelaz, P. del Pino, P. Maffre, R. Hartmann, M. Gallego, S. R. Fernández, J. M. dela Fuente, G. U. Nienhaus, W. J. Parak, Surface Functionalization of Nanoparticles with Polyethylene Glycol: Effects on Protein Adsorption and Cellular Uptake, *ACS Nano* **2015**, 9, 6996-7008.

(31) Y. Okada, K. Ishikawa, N. Maeta, H. Kamiya, Understanding the Colloidal Stability of Nanoparticle–Ligand Complexes: Design, Synthesis, and Structure–Function Relationship Studies of Amphiphilic Small-Molecule Ligands, *Chem.: Eur. J.* **2018**, 24, 1853-1858.

(32) J. -E. Park, M. Seo, E. Jang, H. Kim, J. S. Kim, S. J. Park, Vesicle-like assemblies of ligand-stabilized nanoparticles with controllable membrane composition and properties, *Nanoscale* **2019**, 11, 1837-1846.

(33) H. -Y. Lee, S. H. R. Shin, A. M. Drews, A. M. Chirsan, S. A. Lewis, K. J. M. Bishop, Self-Assembly of Nanoparticle Amphiphiles with Adaptive Surface Chemistry, *ACS Nano* **2014**, 8, 9979-9987.

(34) A. P. Alivisatos, Perspectives on the Physical Chemistry of Semiconductor Nanocrystals. *J. Phys. Chem.* **1996**, 100, 13226-13239.

(35) C. S. Weisbecker, M V. Merritt, G. M. Whitesides, Molecular Self-Assembly of Aliphatic Thiols on Gold Colloids, *Langmuir* **1996,** 12, 3763-3772.

(36) P. M. Shem, R. Sardar, J. S. Shumaker-Parry, One-Step Synthesis of Phosphine-Stabilized Gold Nanoparticles Using the Mild Reducing Agent 9-BBN, *Langmuir* **2009**, 25, 13279-13283.

(37) M. K. Corbierre, R. B. Lennox, Preparation of Thiol-Capped Gold Nanoparticles by Chemical Reduction of Soluble Au(I)−Thiolates, *Chem. Mater.* **2005**, 17, 5691-5696.

(38) G. H. Woehrle, L. O. Brown, J. E. Hutchison, Thiol-Functionalized, 1.5-nm Gold Nanoparticles through Ligand Exchange Reactions: Scope and Mechanism of Ligand Exchange, *J. Am. Chem. Soc*. **2005**, 12, 2172-2183.

(39) T. J. Macdonald, K. Wu, S. K. Sehmi, S. Noimark, W. J. Peveler, H. du Toit, N. H. Voelcker, E. Allan, A. J. MacRobert, A. Gavriilidis, I. P. Parkin, Thiol-Capped Gold Nanoparticles Swell-Encapsulated into Polyurethane as Powerful Antibacterial Surfaces Under Dark and Light Conditions, *Sci. Rep*. **2016**, 6, 39272.

(40) P. Zhang, A. Y. -C. Chu, T. -K. Sham, Y. Yao, S. -T. Lee, Chemical synthesis and structural studies of thiol-capped gold nanoparticles, *Can. J. Chem*. **2009**, 87, 335-340.

(41) V. Spampinato, M. A. Parracino, R. L. Spina, F. Rossi, G. Ceccone, Surface Analysis of Gold Nanoparticles Functionalized with Thiol-Modified Glucose SAMs for Biosensor Applications, *Front Chem*. **2016**, 4, 8.

(42) J. Liu, Y. Zeng, S. Shi, L. Xu, H. Zhang, J. L. Pathak, Y. Pan, Design of polyaspartic acid peptide-poly (ethylene glycol)-poly (ε-caprolactone) nanoparticles as a carrier of hydrophobic drugs targeting cancer metastasized to bone, *Int. J. Nanomedicine* **2017**, 12, 3561-3575.

(43) H. J. Lee, Y. Bae, Cross-Linked Nanoassemblies from Poly(ethylene glycol)-poly(aspartate) Block Copolymers as Stable Supramolecular Templates for Particulate Drug Delivery, Biomacromolecules **2011**, 12, 2686-2696.

(44) N. R. Jana, N. Erathodiyil, J. Jiang, J. Y. Ying, Cysteine-Functionalized Polyaspartic Acid: A Polymer for Coating and Bioconjugation of Nanoparticles and Quantum Dots, *Langmuir* **2010**, 26, 6503-6507.

(45) G. Settanni, J. Zhou, T. Suo, S. Schottler, K. Landfester, F. Schmid, V. Mailänder, Protein corona composition of poly(ethylene glycol)- and poly(phosphoester)-coated nanoparticles correlates strongly with the amino acid composition of the protein surface, *Nanoscale* **2017**, 9, 2138-2144.

(46) K. -O. Doh, Y. Yeo, Application of polysaccharides for surface modification of nanomedicines, *Ther. Deliv*. **2012**, 3, 1447–1456.

(47) M. Swierczewska, H. S. Han, K. Kim, J. H. Park, S. Lee, Polysaccharide-based Nanoparticles for Theranostic Nanomedicine, *Adv. Drug Deliv. Rev*. **2016**, 99, 70–84.

(48) A. C. Henry, T. J. Tutt, M. Galloway, Y. Y. Davidson, C. S. McWhorter, S. A. Soper, R. L. McCarley, Surface Modification of Poly(methyl methacrylate) Used in the Fabrication of Microanalytical Devices, *Anal. Chem*. **2000**, 72, 5331-5337.

(49) H. Wang, L. Yang, G. L. Rempel, Preparation of poly(methyl methacrylate)/polystyrene/poly(acrylonitrile-*co*-butadiene) tri-layer core–shell nanoparticles and their postpolymerization modification *via*catalytic latex hydrogenation, *RSC Adv.* **2015,** 5, 44483-44491.

(50) M. Schmitt, J. Zhang, J. Lee, B. Lee, X. Ning, R. Zhang, A. Karim, R. F. Davis, K. Matyjaszewski, M. R. Bockstaller, Polymer ligand–induced autonomous sorting and reversible phase separation in binary particle blends, *Sci Adv.* **2016**, 2, 1601484.

(51) E. H. Alsharaeh, Polystyrene-Poly(methyl methacrylate) Silver Nanocomposites: Significant Modification of the Thermal and Electrical Properties by Microwave Irradiation, *Materials* **2016**, 9, 458.

(52) A. Kotal, T. K. Mandal, D. R. Walt, Synthesis of gold–poly(methyl methacrylate) core–shell nanoparticles by surface-confined atom transfer radical polymerization at elevated temperature, *J. Polym. Sci. A* **2005**, 43, 3631-3642.

(53) B. Lu, X. Lv, Y. Le, Chitosan-Modified PLGA Nanoparticles for Control-Released Drug Delivery, *Polymers*, **2019**, 11, 304.

(54) S. Dürr, C. Janko, S. Lyer, P. Tripal, M. Schwarz, J. Zaloga, R. Tietze, C. Alexiou, Magnetic nanoparticles for cancer therapy, *Nanotechnol. Rev.* **2013**, 2, 395-409.

(55) M. Wu, S. Huang, Magnetic nanoparticles in cancer diagnosis, drug delivery and treatment, *Mol Clin Oncol*. **2017**, 7, 738–746.

(56) A. J. Giustini, A. A. Petryk, S. M. Cassim, J. A. Tate, I. Baker, P. J. Hoopes, Magnetic Agentic Nanoparticle hyperthermia in cancer treatment, *Nano LIFE*, **2010**, 1, 17-32.

(57) O. Veiseh, J. W. Gunn, M. Zhang, Design and fabrication of magnetic nanoparticles for targeted drug delivery and imaging, *Adv. Drug Deliv. Rev.* **2010**, 62, 284-304.

(58) C. Sun, J. S. H. Lee, M. Zhang, Magnetic nanoparticles in MR imaging and drug delivery, *Adv. Drug Deliv. Rev***. 2008**, 60, 1252-1265.

(59) S. C. McBain, H. H. P. Yiu, J. Dobson, Magnetic nanoparticles for gene and drug delivery, *Int J. Nanomedicine* **2008**, 3, 169–180.

(60) A.K. Gupta, A.S.G. Curtis, Surface modified superparamagnetic nanoparticles for drug delivery: Interaction studies with human fibroblasts in culture**,** *J. Mater. Sci. Mater. Med***. 2004**, 15, 493-496.

(61) M. Arruebo, R. Fernández-Pacheco, M. R. Ibarra, J. Santamaría, Magnetic nanoparticles for drug delivery, *Nano Today* **2007**, 2, 22-32.

(62) X. Mou, Z. Ali, S. Li, H. Nongyue, Applications of Magnetic Nanoparticles in Targeted Drug Delivery System, *J. Nanosci. Nanotechnol***. 2015**, 15, 54-62.

(63) M. Liong, J. Lu, M. Kovochich, T. Xia, S. G. Ruehm, A. E. Nel, F. Tamanoi, J. I. Zink, Multifunctional Inorganic Nanoparticles for Imaging, Targeting, and Drug Delivery, *ACS Nano* **2008**, 2, 889-896.

(64) S. Kayal, R. V. Ramanujan, Doxorubicin loaded PVA coated iron oxide nanoparticles for targeted drug delivery, *Mater. Sci. Eng. C***. 2010**, 30, 484-490.

(65) M. Arruebo, M. Valladares, A. González-Fernández, Antibody-Conjugated Nanoparticles for Biomedical Applications, *J. Nanomater*. **2009**, 2009, 24.

(66) C. C. Gonzalez, C. A. M. Pérez, A. M. Martínez, I. O. Armendáriz, O. Z. Tapia, A. Martel-Estrada, P. E. García-Casillas, Development of Antibody-Coated Magnetite Nanoparticles for Biomarker Immobilization, *J. Nanomater*. **2014**, 2014, 7.

(67) H. Xu, Z. P. Aguilar, L. Yang, M. Kuang, H. Duan, Y. Xiong, H. Wei, A. Wang, Antibody Conjugated Magnetic Iron Oxide Nanoparticles for Cancer Cell Separation in Fresh Whole Blood, *Biomaterials* **2011**, 32, 9758–9765.

(68) Y. Liu, A. Thomas, S. Sohrabi, W. Shi, J. Xu, J. Yang, Antibody-coated nanoparticles are promising molecular probes for microscopic analysis of cell behavior, *Nanomedicine* **2016**, 11, 2383-2386.

(69) R. Marega, L. Karmani, L. Flamant, P. G. Nageswaran, V. Valembois, B. Masereel, O. Feron, T. V. Borght, S. Lucas, C. Michiels, B. Gallez, D. Bonifazi, Antibody-functionalized polymer-coated gold nanoparticles targeting cancer cells: an *in vitro* and *in vivo*study, *J. Mater. Chem.* **2012**, 22, 21305-21312.

(70) J. Requejo-Isidro, R. del Coso, J. Solis, J. Gonzalo, C. N. Afonso, Role of Surface-to-volume Ratio of Metal Nanoparticles in Optical Properties of Cu:Al_2O_3 Nanocomposite Films, *Appl. Phys. Lett.* **2005,** 86, 193104.

(71) J. E. Huheey, E. A. Keiter, R. L. Keiter, O. K. Medhi, *Inorganic Chemistry: Principles of Structure and Reactivity*. Pearson Education **2006**.

(72) F. Aguado, F. Rodriguez, P. Núñez, Pressure-induced Jahn-Teller Suppression and Simultaneous High-spin to Low-spin Transition in the Layered Perovskite $CsMnF_4$, *Phys. Rev. B* **2007,** 76, 094417.

(73) M. B. Gawande, P. S. Branco, R. S. Varma, Nano-magnetite (Fe_3O_4) as a Support for Recyclable Catalysts in the Development of Sustainable Methodologies, *Chem. Soc. Rev.* **2013,** 42, 3371-3393.

(74) L. M. Rossi, N. J. S. Costa, F. P. Silva, R. Wojcieszak, Magnetic nanomaterials in catalysis: advanced catalysts for magnetic separation and beyond, *Green Chem.* **2014**, 16, 2906-2933.

(75) M. Neamtu, C. Nadejde, V. -D. Hodoroaba, R. J. Schneider, L. Verestiuc, U. Panne, Functionalized magnetic nanoparticles: Synthesis, characterization, catalytic application and assessment of toxicity, *Sci. Rep.* **2018**, 8, 6278.

(76) S. N. Sidorov, I. V. Volkov, V. A. Davankov, M. P. Tsyurupa, P. M. Valetsky, L. M. Bronstein, R. Karlinsey, J. W. Zwanziger, V. G. Matveeva, E. M. Sulman, N. V. Lakina, E. A. Wilder, R. J. Spontak, Platinum-Containing Hyper-Cross-Linked Polystyrene as a Modifier-Free Selective Catalyst for l-Sorbose Oxidation, *J. Am. Chem. Soc.* **2001,** 123, 10502-10510.

(77) A. Borsla, A. M. Wilhelm, H. Delmas, Hydrogenation of Olefins in Aqueous Phase, Catalyzed by Polymer-protected Rhodium Colloids: Kinetic Study, *Catal. Today* **2001,** 66, 389-395.

(78) Y. Li, M. A. El-Sayed, The Effect of Stabilizers on the Catalytic Activity and Stability of Pd Colloidal Nanoparticles in the Suzuki Reactions in Aqueous Solution, *J. Phys. Chem. B* **2001,** 105, 8938-8943.

(79) K. Esumi, R. Isono, T. Yoshimura, Preparation of PAMAM− and PPI−Metal (Silver, Platinum, and Palladium) Nanocomposites and Their Catalytic Activities for Reduction of 4-Nitrophenol, *Langmuir* **2004,** 20, 237-243.

(80) Z. Liu, X. Y. Ling, X. Su, J. Y. Lee, Carbon-Supported Pt and PtRu Nanoparticles as Catalysts for a Direct Methanol Fuel Cell, *J. Phys. Chem. B* **2004,** 108, 8234-8240.

(81) D. A. Bulushev, I. Yuranov, E. I. Suvorova, P. A. Buffat, L. Kiwi-Minsker, Highly Dispersed Gold on Activated Carbon Fibers for Low-temperature CO Oxidation, *J. Catal.* **2004,** 224, 8-17.

(82) C. Bianchini, V. D. Santo, A. Meli, S. Moneti, M. Moreno, W. Oberhauser, R. Psaro, L. Sordelli, F. Vizza, A Comparison Between Silica-immobilized Ruthenium(II) Single Sites

and Silica-supported Ruthenium Nanoparticles in the Catalytic Hydrogenation of Model Hetero- and Polyaromatics Contained in Raw Oil Materials, *J. Catal.* **2003,** 213, 47-62.

(83) H. Lang, R. A. May, B. L. Iversen, B. D. Chandler, Dendrimer-Encapsulated Nanoparticle Precursors to Supported Platinum Catalysts, *J. Am. Chem. Soc.* **2003,** 125, 14832-14836.

(84) I. Balint, A. Miyazaki, K. -I. Aika, Effect of Platinum Morphology on Lean Reduction of NO with C_3H_6. *Phys. Chem. Chem. Phys.* **2004,** 6, 2000-2002.

(85) L. Li, C. Han, D. Xu, J. -Y. Xing, Y. -H. Xue, H. Liu, Polymer-grafted nanoparticles prepared *via* a grafting-from strategy: a computer simulation study, *Phys. Chem. Chem. Phys.* **2018**, 20, 18400-18409.

(86) M. Asai, D. Zhao, S. K. Kumar, Role of Grafting Mechanism on the Polymer Coverage and Self-Assembly of Hairy Nanoparticles, *ACS Nano* **2017**, 11, 7028-7035.

(87) J. Gao, G. Liang, J. S. Cheung, Y. Pan, Y. Kuang, F. Zhao, B. Zhang, X. Zhang, E. X. Wu, B. Xu, Multifunctional yolk−shell nanoparticles: a potential MRI contrast and anticancer agent, *J. Am. Chem. Soc.* **2008,** 130, 11828-11833.

(88) J. Yang, E. -K. Lim, H. J. Lee, J. Park, S. C. Lee, K. Lee, H. -G. Yoon, J. -S. Suh, Y. -M. Huh, s. Haam, Fluorescent Magnetic Nanohybrids as Multimodal Imaging Agents for Human Epithelial Cancer Detection, *Biomaterials* **2008,** 29, 2548-2555.

(89) J. Gao, W. Zhang, P. Huang, B. Zhang, X. Zhang, B. Xu, Intracellular Spatial Control of Fluorescent Magnetic Nanoparticles, *J. Am. Chem. Soc.* **2008,** 130, 3710-3711.

(90) H. Kim, M. Achermann, L. P. Balet, J. A. Hollingsworth, V. I. Klimov, Synthesis and Characterization of Co/CdSe Core/Shell Nanocomposites: Bifunctional Magnetic-Optical Nanocrystals, *J. Am. Chem. Soc.* **2004,** 127, 544-546.

(91) M. Johannsen, U. Gneveckow, L. Eckelt, A. Feussner, N. Waldofner, R. Scholz, S. Deger, P. Wust, S. A. Loening, A. Jordan, Clinical Hyperthermia of Prostate Cancer Using Magnetic Nanoparticles: Presentation of a New Interstitial Technique, *Int. J. Hyperther.* **2005,** 21, 637-647.

(92) G. Tian, Z. Gu, X. Liu, L. Zhou, W. Yin, L. Yan, S. Jin, W. Ren, G. Xing, S. Li, Y. Zhao, Facile Fabrication of Rare-Earth-Doped Gd_2O_3 Hollow Spheres with Upconversion Luminescence, Magnetic Resonance, and Drug Delivery Properties, *J. Phys. Chem.* **C 2011**, 115, 23790–23796.

(93) B. Palazzo, M. Iafisco, M. Laforgia, N. Margiotta, G. Natile, C.L. Bianchi, D. Walsh, S. Mann, N. Roveri, Biomimetic Hydroxyapatite–Drug Nanocrystals as Potential Bone Substitutes with Antitumor Drug Delivery Properties, *Adv. Funct. Mater***. 2007**, 17, 2180–2188.

(94) Y. Si, M. Chen, L. Wu, Syntheses and biomedical applications of hollow micro-/nano-spheres with large-through-holes, *Chem. Soc. Rev***. 2016**, 45, 690-714.

(95) R. Lv, S. Gai, Y. Dai, N. Niu, F. He, P. Yang, Highly Uniform Hollow GdF_3 Spheres: Controllable Synthesis, Tuned Luminescence, and Drug-Release Properties, ACS Appl. Mater. Interfaces **2013**, 5, 10806-10818.

(96) R. K. DeLong, C. M. Reynolds, Y. Malcolm, A. Schaeffer, T. Severs, A. Wanekaya, Functionalized gold nanoparticles for the binding, stabilization, and delivery of therapeutic DNA, RNA, and other biological macromolecules, *Nanotechnol Sci Appl*. **2010**, 3, 53–63.

(97) M. Proupin-Perez, R. Cosstick, L. M. Liz-Marzan, V. Salgueiriño-Maceira, M. Brust, Studies on the attachment of DNA to silica-coated nanoparticles through a Diels-Alder reaction, *Nucleos. Nucleot. Nucl*. **2005,** 24, 1075-1079.

(98) P. V. Kamat, Meeting the Clean Energy Demand: Nanostructure Architectures for Solar Energy Conversion, *J. Phys. Chem. C* **2007**, 111, 2834-2860.

(99) Z. S. Wang, H. Kawauchi, T. Kashima, H. Arakawa, Significant influence of TiO_2 photoelectrode morphology on the energy conversion efficiency of N719 dye-sensitized solar cell, *Coord. Chem. Rev*. **2004**, 248, 1381-1389.

(100) M. G. Hosseini, R. Mahmoodi, Improvement of energy conversion efficiency and power generation in direct borohydride-hydrogen peroxide fuel cell: The effect of Ni-M core-shell nanoparticles (M = Pt, Pd, Ru)/Multiwalled Carbon Nanotubes on the cell performance, *J. Power Sources* **2017**, 370, 87-97.

(101) Y. -G. Guo, J. -S. Hu, L. -J. Wan, Nanostructured Materials for Electrochemical Energy Conversion and Storage Devices, *Adv. Mater*. **2008**, 20, 2878–2887.

(102) T. Hyeon, Chemical Synthesis of Magnetic Nanoparticles, *Chem. Commun*. **2003,** 8, 927-934.

(103) J. W. Lee, A. S. Hall, J. -D. Kim, T. E. Mallouk, A Facile and Template-Free Hydrothermal Synthesis of Mn_3O_4 Nanorods on Graphene Sheets for Supercapacitor Electrodes with Long Cycle Stability, *Chem. Mater*. **2012,** 24, 1158-1164.

Chapter 2

Experimental Details

In this chapter we have discussed about the different synthesis procedures of nanomaterials and different techniques for their characterization.

2. Material Synthesis and Characterization Techniques

2.1. Preamble

In this chapter, we described two experimental procedures such as wet chemical and solvothermal methods to synthesize 3d transition metal oxide based magnetic nanoparticles (NPs) and nano hollow spheres (NHSs).

The phase and morphology of the synthesized NPs and NHSs are studied using X-ray Diffraction (XRD), Field Emission Scanning Electron Microscope (FESEM), Transmission Electron Microscope (TEM), High Resolution Transmission Electron Microscope (HRTEM), Energy Dispersive X-ray Analysis (EDX) and Selected Area Electron Diffraction (SAED). Optical analyses are carried out using UV-visible spectrophotometer, Fourier transformed infrared spectrometer (FTIR), fluorescence microscope, steady state and time resolved fluorometer and circular dichroism (CD) spectroscopy. The magnetic characterizations are carried out employing Vibrating Sample Magnetometer (VSM). The melting temperature of CT-DNA is determined by UV-visible spectrophotometer equipped with Peltier controller. DNA cleavage study is carried out by agarose gel electrophoresis.

2.2. Synthesis of Nanomaterials

There are diverse techniques to prepare different nanostructured materials and all of them can be categorized into two simple groups, (1) top-down (i.e. bulk to nano) and (2) bottom-up (i.e. atom to nano) approaches.

2.2.1. Top-Down Approach

Top–down approach involves successive fragmentation of a bulk material. This is essentially the breaking down of a system to gain insight into its compositional sub-systems. This method includes high energy ball milling, etching, electro explosion, sonication etc. Nanostructures can be made by a top-down approach from a variety of macro-sized particles, and their actions depend on chemical composition and the size and/or shape of the particles as well as their chemical characteristics. The main disadvantages of this process are polydispercity of the final particles, the introduction of many defects (including contamination by the material used to make the grinding machinery) and imperfection in surface structures, such as broad size distribution, undefined shape, impurities, and defects.

2.2.2. Bottom-up Approach

Bottom up approach involves to the building up of a material from the bottom: atom by atom, molecule by molecule or cluster by cluster. The ability to assemble nanoscale functional building blocks is useful and modular way to design valuable materials with specific physical and chemical properties. Wet chemical synthesis, self-assembly, molecular fabrication, and electrodeposition are all examples of bottom-up techniques. It is easier and more economical for forming NSs of smaller geometry. When it is more important to minimize the product cost and increase component availability, bottom-up approach would be taken. However, there are some challenges in fabricating complex, robust nanostructured materials using bottom-up approaches [1].

2.3. Formation of Nanoparticles

Supersaturation refers to the formation of homogeneous nucleation during the uniform growth of nuclei throughout the parent phase. This condition can be achieved by controlling the reaction conditions such as solvent, capping agents, temperature etc. The homogeneous nuclei formation process can be achieved thermodynamically by considering the total free energy (ΔG) of NPs as a sum of surface free energy and bulk free energy. The overall free energy changes (ΔG) associated with the homogeneous nucleation process, which is the total change in free energy between a small solid particle of a solute and the solute in solution. The excess surface free energy, ΔG_S, is the excess surface energy between the NPs and the corresponding bulk material. Excess volume free energy, ΔG_V, is the excess free energy between a very large particle and the solute in the solution. Dependence of ΔG_S and ΔG_V on particle size with radius (r) can be observed from Equation 2.1 and also depicted in Figure 2.1 [2].

$$\Delta G = \Delta G_S + \Delta G_V = 4\pi r^2\gamma + (^4/_3)\pi r^3 \Delta G_V \qquad (2.1)$$

Where, ΔG_V is the free energy change per unit volume and γ is the interfacial tension between the growing NPs surface and the supersaturated solution.

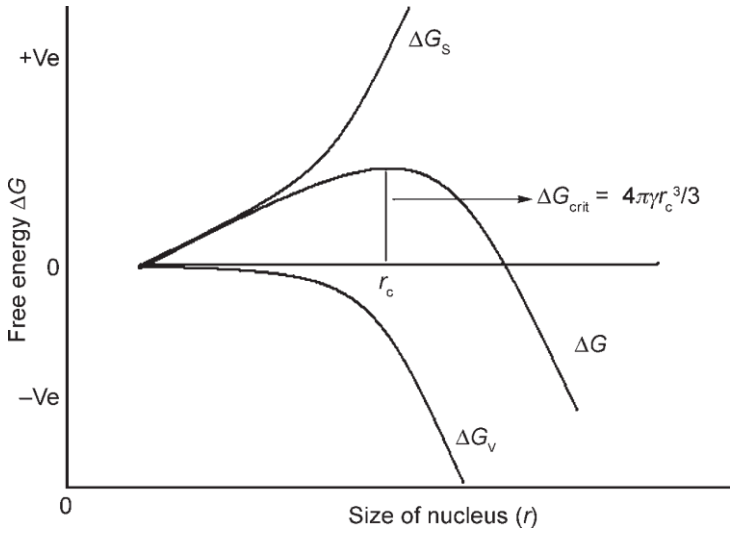

Figure 2.1. Free-energy diagram for nucleation process. (© Kumar et al. *Small* **2006,** *2* (3), 316-329).

As ΔG_S is always positive and ΔG_V is always negative, it is possible to find a ΔG for a stable nucleus having an optimum size (critical radius, r_c) by differentiating ΔG with respect to r and setting it to zero, which gives a critical free energy, as shown in Equation 2.2. The critical radius is defined in Equation 2.3. It is evident from Figure 2.1, that the total excess free energy, ΔG, passes through a maximum, ΔG_{crit}, corresponding to the critical nucleus size, r_c,

$$\frac{d(\Delta G)}{dr} = 8\pi r_c\gamma + 4\pi r_c^2 \Delta G_V = 0, \text{ where } r = r_c \qquad (2.2)$$

$$\Rightarrow r_c = -\frac{2\gamma}{\Delta G_V} \qquad (2.3)$$

From equations (2.1) and (2.3), we can obtain the critical value of ΔG as

$$\Delta G = \Delta G_{crit} = \frac{16\pi\gamma^3}{3(\Delta G_V)^2} = \frac{4\pi\gamma r_c^2}{3}, \text{ where } r = r_c \quad (2.4)$$

i.e. the minimum energy barrier that a nucleation process must overcome is ΔG_{crit}, which corresponds to the minimum size of a stable spherical nucleus (r_c). This critical radius corresponds to the minimum size at which a particle can survive in solution without being redissolved. Crystal structure, size and morphology of the growing particles mainly depend on the system and reaction parameter. The growth of NPs is dependent on two mechanisms: the surface reaction and the monomer's diffusion to the surface.

Different theories have been proposed to explain the nucleation and growth mechanism of various reactions [3]. Such as, in the LaMer mechanism, the process of nucleation and growth is divided into three portions. Firstly, a rapid increase in the concentration of free monomers in solution. Secondly, the monomer undergoes "burst nucleation" which significantly reduces the concentration of free monomers in solution. The rate of nucleation is described as "effectively infinite" and after this point, nucleation almost stops due to the low concentration of monomers; in third stage growth occurs under the control of the diffusion of the monomers through solution. Ostwald and digestive ripening mechanism say that, growth is caused by the change in solubility of NPs dependent on their size. According to Ostwald ripening, due to the high solubility and surface energy of smaller particles within solution, these redissolve and in turn allow the larger particles to grow even more. Digestive ripening, described by Lee et al., is effectively the inverse of Ostwald ripening, where smaller particles grow at expense of the larger ones by surface energy controlled process [4]. The Finke-Watzky two step mechanism is a process of nucleation and growth where both steps happen simultaneously [5]. The first is a slow continuous nucleation, (shown in Equation 2.5) and the second is the autocatalytic surface growth which is not diffusion controlled, (shown in Equation 2.6).

$$A \rightarrow B \qquad (2.5)$$

$$A + B \rightarrow 2B \qquad (2.6)$$

Shape of the crystallites occurs either in order to minimize the surface energy of the particles or because of the kinetics of the growth. If kinetics dominates, the shape is then determined by the rate at which different crystal faces grow. In thermal equilibrium, crystal shape is determined by minimization of surface energy.

2.3.1. Wet Chemical Process

Wet chemical is a group of synthesis method used for producing nano and ultra-dispersed inorganic powders from aqueous and non-aqueous solutions [6]. This method includes sol-gel process, cryochemical synthesis, hydrothermal synthesis, and aerosol spray pyrolysis etc. The main advantage of this process is that smaller grains can be prepared. Moreover, lower temperature and shorter duration of phase formation is required. Mainly "bottom-up" method is followed to synthesize NPs by chemical reduction of metal salts, electrochemical trails or through controlled decomposition of different metastable organometallic compounds. This process is more precise in controlling size and shape of NPs.

2.3.2. Formation of Metal Oxides by Refluxing Organometallic Compounds

Figure 2.2. Setup for refluxing.

Reflux is a technique to prepare chemical products involving the condensation of vapors and return of this condensate to the system. This process assures the supply of energy in the form of heat for a period of time. This process is simple and low cost which gives the desired product precisely controlling reaction parameters. This method is very helpful to prepare nanoparticles, nanorods, nanowires, nanourchins, and hierarchical nanostructures [7]. This method one can control the size, morphology, and crystallinity of the materials by changing parameters such as the reaction time, concentration of precursors, and the type of solvent employed in the reaction system. An optimization of order of addition of precursors, the time of the reflux, and the cooling rate is very essential to obtain the desired phase and morphology of the nanostructures. In this process, after the initial nucleation, grain growth, and the phase formation take place simultaneously. Incomplete phase can be formed if the reaction is stopped early. On the other hand, if the reaction time is over, it leads to a larger grain size and hence bulk crystals will be obtained. Therefore reaction time should be

optimized for obtaining pure phase nanostructure. The refluxing setup used in our laboratory is shown in Figure 2.2. $MnFe_2O_4$ NPs were prepared by template free wet chemical process following a previous report with some modification [6] which involves the high-temperature (270 °C) reflux of metal ion salts like Iron (III) acetylacetonate ($Fe(acac)_3$) and Manganese (II) acetate ($Mn(ac)_2$) with proper molar ratio. Diphenyl ether was used as an organic solvent with the capping agents like cetyl alcohol ($C_{16}H_{33}OH$), oleylamine ($CH_3(CH_2)_7CH=CH(CH_2)_8NH_2$), and oleic acid ($CH_3(CH_2)_7CH=CH(CH_2)_7COOH$).

2.3.3. Solvothermal Method

Solvothermal method is used for preparing a variety of materials such as metals, semiconductors, ceramics and polymers. In this method solvent is used under moderate to high pressure (typically between 1 atm and 10,000 atm) and temperature (typically between 100 °C and 1000 °C) that facilitates the interaction of precursors during synthesis. If water is used as a solvent instead of organic solvents, the method is called hydrothermal synthesis. This synthetic strategy is important for the preparation of nano hollow spheres (NHSs) in non-aqueous medium by controlling pressure, temperature, capping agent, chemical composition, and reaction time. Different non-polar solvents like benzene, ethylene glycol, ethylenediamine are used under high pressure and temperature. Temperature above the normal boiling point of solvent is generally maintained during the reaction. A sealed reaction vessel is used for the reaction and within the vessel pressure is increased dramatically with temperature. Other experimental factors such as the percentage fill of the vessel, any dissolved salts, and capping agents are also important. As for example, the viscosity of water decreases with increasing temperature under ambient conditions. Thus it is evident that the mobility of dissolved ions and molecules in the solvent is higher under solvothermal conditions than the ambient temperature and pressure. Similarly, the dielectric constants of solvents are considerably reduced above the critical pressure and temperature. This can have major implications on the solubility of solid components under reaction conditions.

In this method, precursors are dissolved in the solvent under the stirring condition or sonication and the homogenous solution is transferred into the teflon lined stainless steel autoclave chamber. Figure 2.3 shows the schematic diagram of an autoclave and a teflon chamber which is used for solvothermal synthesis [8]. The autoclave is sealed and heated to a desired temperature for several hours. When the reaction is over, the system is allowed to cool down to the room temperature. The sample is washed with water and alcohols to

remove impurities and then dried into inert atmosphere to obtain final product. Various nanostructures like nanoparticles, wires, hollow spheres, and spindles are prepared by this method [8]. The main advantage of this method is that almost any material can be dissolved in the solvent by increasing the temperature and pressure to its critical point, isolation of metastable phases not seen at high temperature and the control of crystal form makes this method suitable for synthesis.

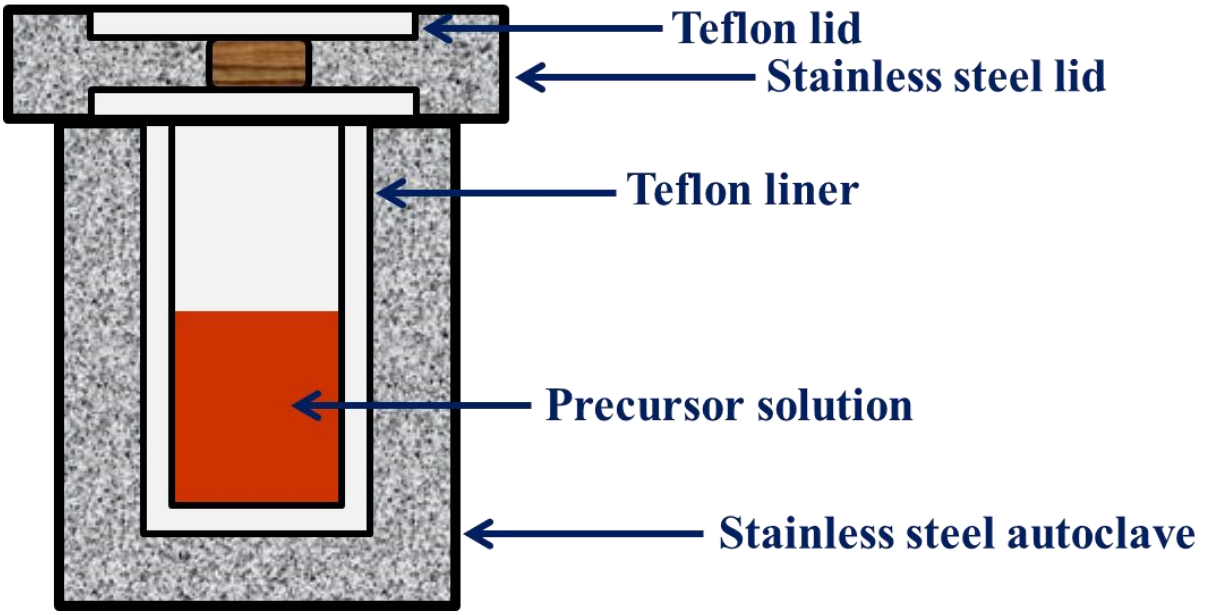

Figure 2.3. Schematic diagram of an autoclave and a teflon chamber used in solvothermal synthesis. (© R. I. Walton, Chem. Soc. Rev. **31**, 230 (2002)).

We have synthesized $MnFe_2O_4$ nano hollow spheres (NHSs) by solvothermal route where 0.30 g of $MnCl_2.6H_2O$ and 0.80 g of $FeCl_3.6H_2O$ were mixed together into a 30 ml solvent mixture of ethylene glycol and ethanol in 2:1 ratio and after that we have added 0.53 g of urea as base and 3 ml of oleylamine as capping agent in the mixture. The mixture was stirred for about 10 min to form homogeneous slurry. Then the suspension was transferred into a 50 ml teflon lined autoclave and heated at 200 °C for 24 h.

2.3.4. Functionalization Procedure of Nanostructures

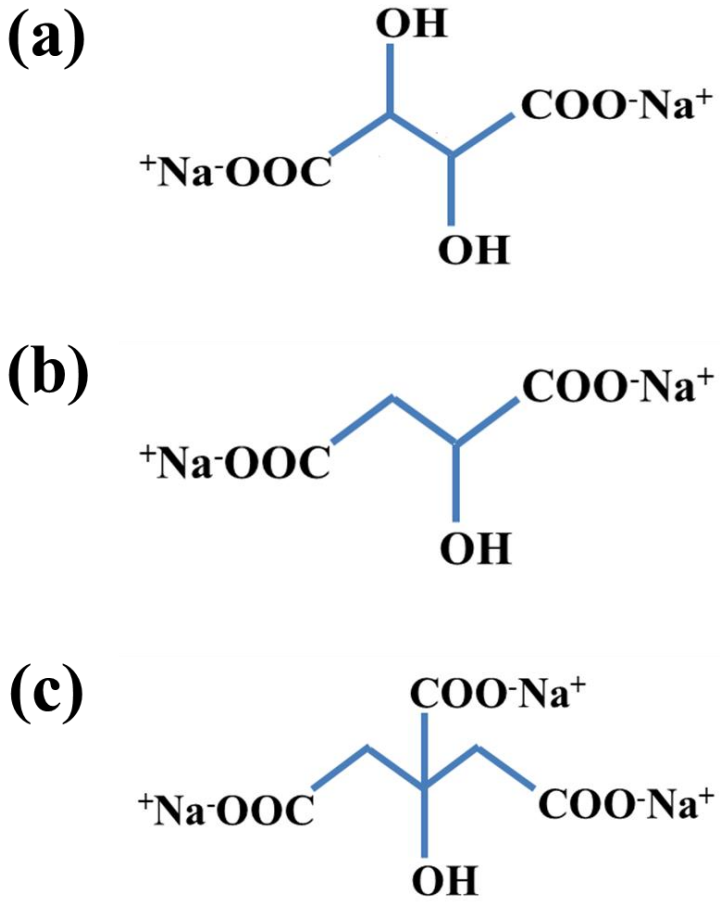

Figure 2.4. Chemical structures of a (a) tartrate (b) malate and (c) citrate molecules respectively.

As-prepared nanostructures were cyclomixed with small hydrophilic organic ligands like tartrate, malate and citrate. 0.5 M solution of different ligands was prepared in Milli-Q water at pH ~ 7. Figure 2.4 shows the structure of tartrate, malate and citrate. The nonfunctionalized larger nanostructures were filtered out with a syringe filter of 0.22 μm diameter. The as obtained filtrate was tartrate, malate, and citrate functionalized nanostructures i.e. T-$MnFe_2O_4$, M-$MnFe_2O_4$, and C-$MnFe_2O_4$ respectively. Sometimes, to amplify the optical response, pH of the solution increases to ~ 12 by drop wise addition of NaOH. Further the solutions were heated at about 65 °C for several hours depending on the requirement. Heating at higher pH turns the color of the solution darker and showed intense fluorescence under UV light irradiation. For FTIR and magnetic measurement (VSM), powered sample was prepared by dialysis and lyophilization of the functionalized nanostructures solution (to remove excess ligands) followed by drying over a water bath.

2.4. Phase and Morphology Characterization Techniques

2.4.1. X-ray Diffraction (XRD)

X-ray diffraction (XRD) is an analytical technique used for phase identification of a crystalline material and can provide information on unit cell dimensions.

This method is based on constructive interference of monochromatic X-rays and a crystalline sample. These X-rays are generated by a cathode ray tube, filtered to produce monochromatic radiation and directed toward the sample.

Now, measuring the intensity and angle of the diffracted beams, a three dimensional idea of the density of electrons within the specified crystal can be understood. The density of electrons varies due to the random orientation of the electrons in the material. Considering all possible diffraction directions of the lattice, mean position of the atoms can be determined.

According to Figure 2.5, monochromatic beam of X-rays collimated and directed onto a sample. The interaction of incident rays with the sample produces constructive interference when the sample satisfies Bragg's Law (Equation 2.7):

$$n\lambda = 2d\ sin\theta \qquad (2.7)$$

Where, n is a positive integer, λ is the wavelength of the incident wave, d is the interplanar spacing and θ is the diffraction angle.

The angles and intensities of the diffracted beams are recorded electronically using a detector, resulting in intensity vs. 2θ plot for a specific sample.

The grain size (D) of particle of crystal can be calculated by using Debye-Scherrer equation (Equation 2.8)

$$D = \frac{0.9\lambda}{\beta cos\theta} \qquad (2.8)$$

where, β is the full width at the half maximum intensity of the diffraction peak at a diffraction angle of 2θ. XRD patterns of our samples were recorded by Rigaku miniflex II diffractometer equipped with Cu Kα (λ ~ 1.54 Å) radiation (at 40 mA and 40 kV) applying a scanning rate of 0.02° s^{-1} in the 2θ range from 20° to 80°.

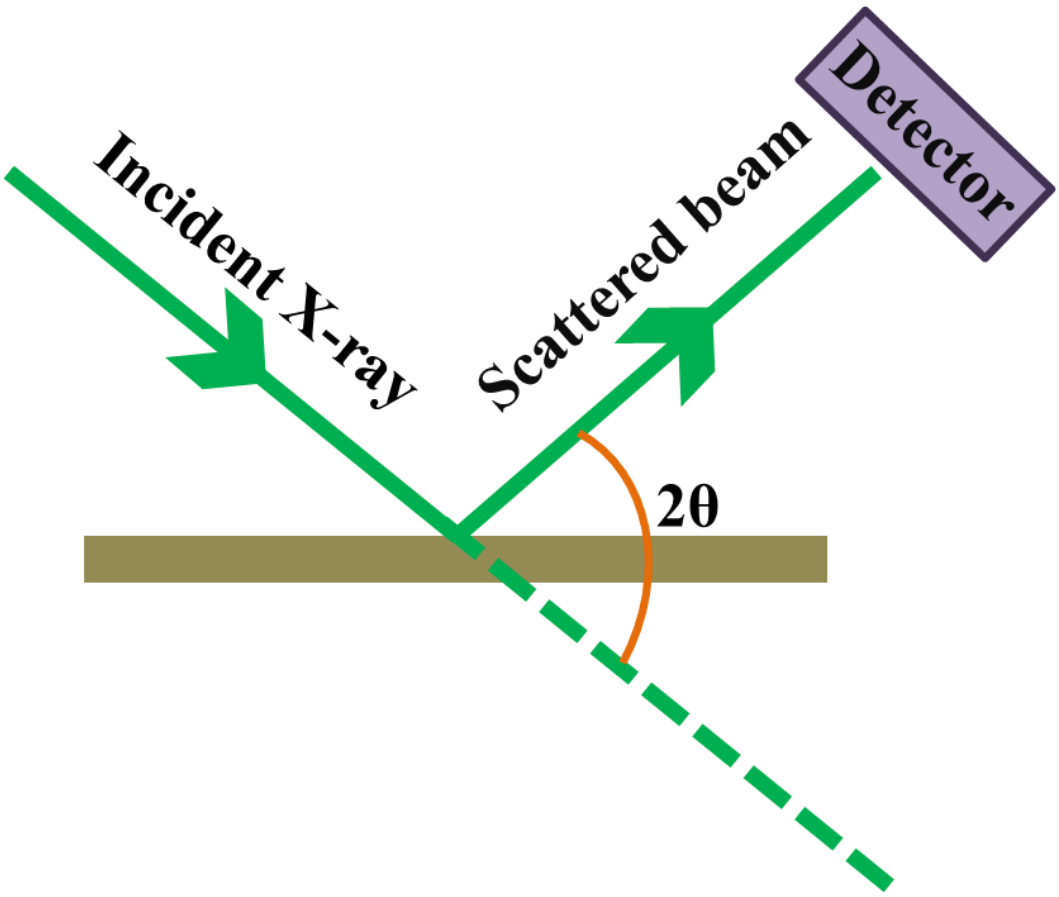

Figure 2.5. Schematic diagram of X-ray diffractometer.

2.4.2. Electron Microscopes

In electron microscope, electron is used to image the objects. Advantage of using electrons is that their wavelength can be tuned to a very small value, just by changing their energies so that the resolution can be increased. There are two types of electron microscopes i.e. Scanning Electron Microscope (SEM) and Transmission Electron Microscope (TEM) which we have used to analyze our samples as described below:

2.4.2.1. Scanning Electron Microscope (SEM)

In a SEM, backscattered electrons or secondary electrons are detected. The electron beam can be focused to a very small portion using electrostatic lenses [9]. The fine beam is scanned on the surface of the sample using a scan generator and back scattered electrons are collected by

a detector. Signal from the scan generator along with detector from the electron collector generates the image of sample surface. To avoid the oxidation, contamination of filament, and collisions between air molecules and electrons; filament and sample is kept in a vacuum chamber. Surface morphology, topology, and composition can be obtained from SEM. For imaging, 2 to 50 kV of voltage is used in this microscope. The interactions between electrons and ions in solids results into back scattering of electrons (BSEs), production of secondary electrons (SEs), X-rays, Auger electrons, visible light, and cathadoluminescence etc. depending upon the energy of electrons, type, and thickness of sample. Inelastic events occur when an incident beam electrons interact with the electric field of sample atom electrons, resulting transfer of energy leading to potential expulsion of an electron from that atom as a SE. SEs by definition are less than 50 eV. If the vacancy due to the formation of a SE is filled from a higher level orbital, an X-ray characteristic of that energy transition is produced. Elastic events occur when a beam electron interacts with the electric field of the nucleus of a specimen atom, resulting in change of direction of electrons without altering energy of the electron significantly (< 1eV). Among the elastically scattered electrons which are deflected backward are called BSE. BSEs have energy in between 50 eV to the energy of incident beam. Generally, the image displayed by a SEM is a mapping of the varying intensity of the signal produced by the SEs into the image in a position corresponding to the exact position of the beam on the specimen. Whereas the characteristic X-rays are used to obtain the composition of sample using a technique known as Energy Dispersive Analysis of X-rays (EDX). Morphology of our samples was tested by field emission scanning electron microscope (FESEM, FEI QUANTA FEG-250) operating at 5-10 kV.

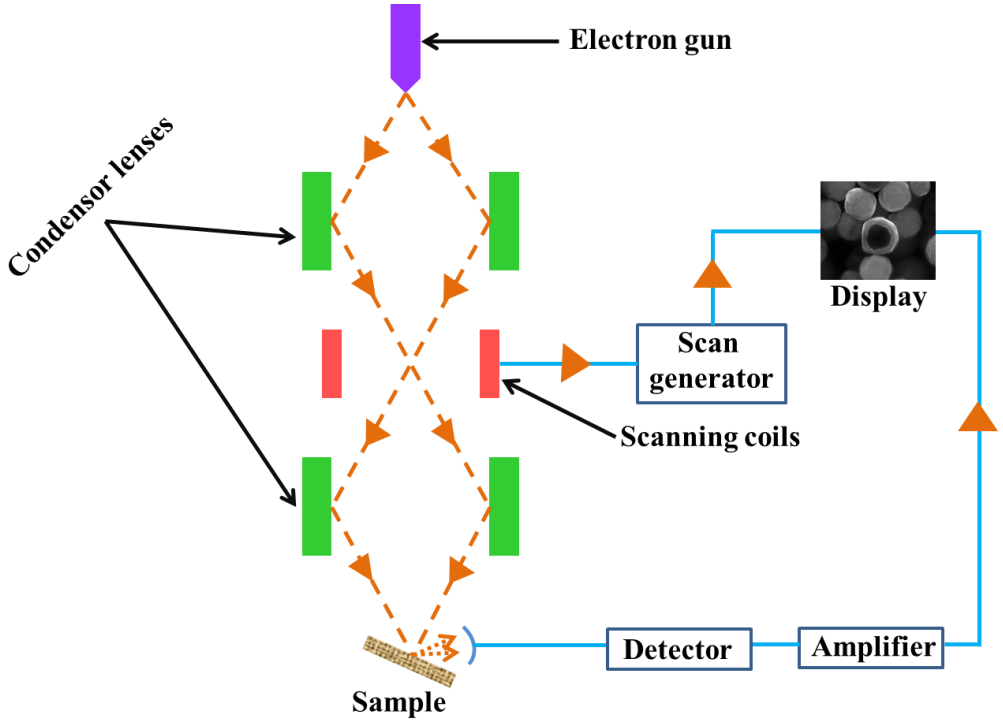

Figure 2.6. A typical sketch of a scanning electron microscope.

2.4.2.2. Transmission Electron Microscope (TEM)

TEM is suitable for investigating NSs due to the very high resolution of this instrument. Electrons of very high energy (typically > 50 keV) are transmitted through the specimen and a series of magnetic lenses. Interaction of electrons with matter is illustrated in Figure 2.7. The transmission of unscattered electrons is inversely proportional to the specimen thickness. The thick area of the specimen will have fewer transmitted unscattered electrons and will appear darker. On the other hand, the thinner areas will have more transmitted and thus will appear lighter. This mode of operation to grow contrast in image is known as bright field imaging mode.

TEM has the advantage that one can not only obtain the images of the specimen but diffraction patterns also. Diffraction pattern helps to analyze detailed crystal structure of the sample.

Electron beam undergoes Bragg scattering in accordance with the Bragg's law (Equation 2.7). All incident electrons enter the specimen perpendicularly with the same energy to its surface. Now, the scattered electrons by the same set of parallel planes can be collected using magnetic lenses to form a pattern of spots. Each spot is corresponding to a specific atomic

spacing or crystalline plane. This pattern bears information about the orientation, atomic arrangements, and phases present in the area being examined.

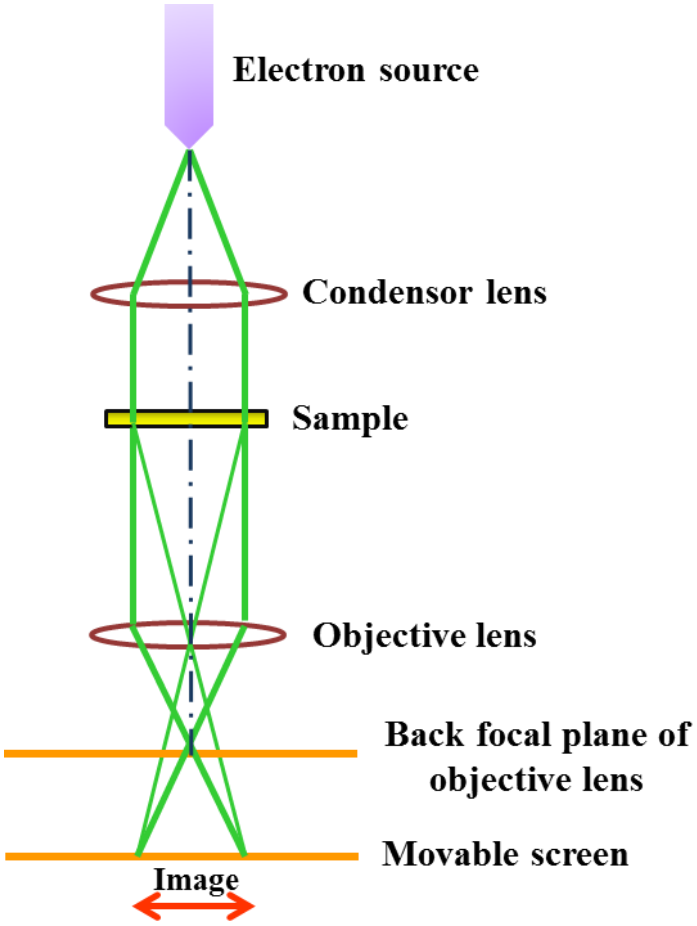

Figure 2.7. Schematic diagram of a transmission electron microscope.

In case of high resolution TEM (HRTEM) mode, we can achieve a resolution around 0.2 nm which is very efficient in observing the lattice fringes of the specimen. When the electron beam is transmitted through the thin section, a number of transmitted electrons, elastically and inelastically scattered (energy-loss) electrons, SEs, BSEs, auger electrons, and X-ray photons produce. TEM-based elemental analysis techniques use X-ray photons in EDX and inelastically scattered electrons or the "energy-loss" electrons in electron energy-loss spectroscopy (EELS) and Energy filtered transmission electron microscopy (EFTEM).

In case of TEM, samples are prepared by drop casting NSs in ethanol or water on 300-mesh carbon coated copper grid and dried overnight in air. Particle size was calculated from TEM micrographs and elemental analysis was carried out from EDX spectrum recorded by a FEI Tecnai TF-20 field-emission high resolution transmission electron microscope operating at 200 kV.

2.5. Magnetic Characterization Techniques

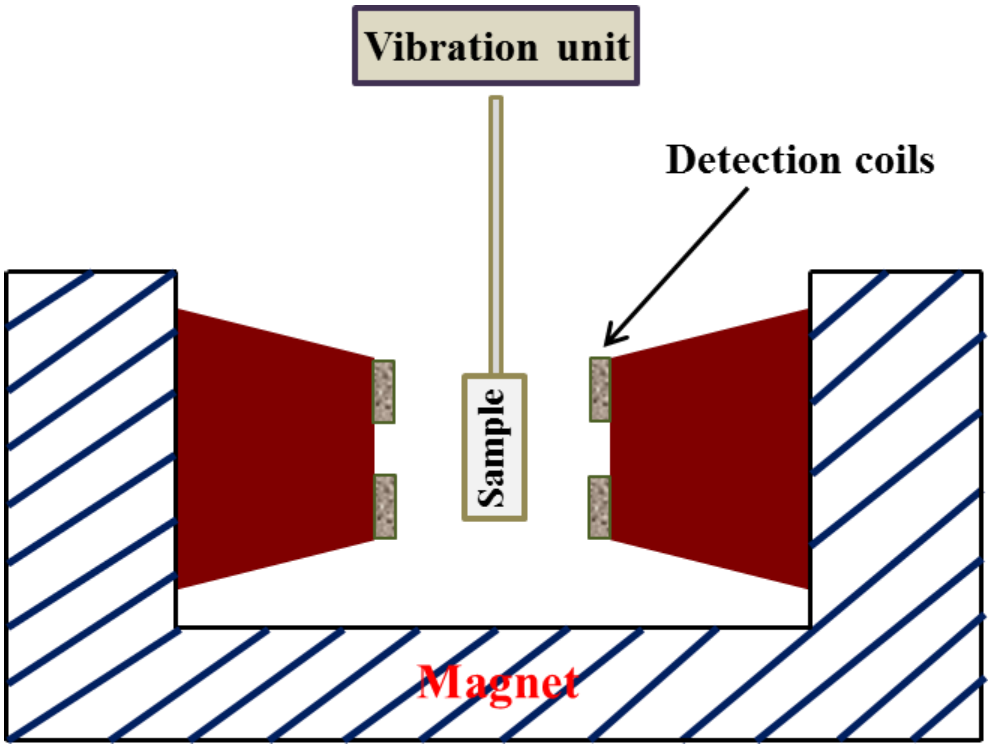

Figure 2.8. Schematic diagram of VSM.

Vibrating Sample Magnetometer (VSM) is a technique to determine magnetization of a sample in presence of magnetic field. VSM is based on the principle that an oscillatory magnetic field is created by vibrating a magnetic sample. A uniform magnetic field is applied to the sample to induce magnetization in the sample. The induced changes in the magnetic field are detected by a search coil. Although applied magnetic field is quite large, but it is not detected by search coil. Generally the constant magnetic field is not really constant but slowly varying magnetic field as compared to vibrating field (Hz). Figure 2.8 shows the schematic diagram of a typical VSM. In most of the instrument, a large electromagnet with 0 to 2.5 tesla field is used. For the magnetic measurement of our sample, a Lake Shore VSM equipped with an electromagnet, capable of generating field of up to 1.6 T at 300 K was used.

2.6. Optical Characterization Techniques

2.6.1. UV-visible Absorption Spectrometer

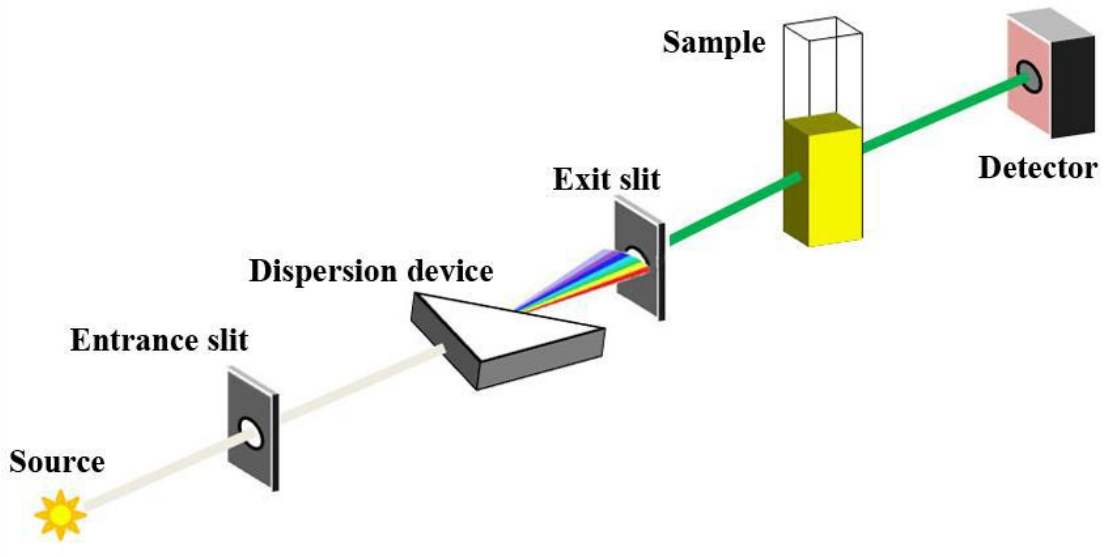

Figure 2.9. Schematic diagram of a UV-visible absorption spectrometer.

Absorptions in the UV-vis absorption spectrometer are associated with electronic transitions from the ground level to an excited state. This technique is often used to calculate the concentration of an absorbing species in solution using Beer-Lambert law:

$$A = \log_{10}(I_0/I) = \varepsilon.c.l \qquad (2.9)$$

Where, A is the absorbance of the sample, I_0 is the intensity of the incident light at a given wavelength, I is that for the transmitted light, l is the path length of light covered through the sample, c is the concentration of the absorbing species, and ε is the molar absorptivity or molar extinction coefficient that is characteristics of a particular absorber and constant at a particular wavelength. The schematic diagram of the UV-visible spectrometer is demonstrated in Figure 2.9. UV-visible absorbance spectra of our samples were obtained from a Shimadzu Model UV-2600 spectrophotometer using a quartz cuvette of 1 cm path length. We have studied catalytic and photocatalytic activities of our samples by using UV-visible spectrophotometer.

2.6.1.1. Optical Melting Study

Melting studies of CT-DNA and CT-DNA-NPs complex were carried out on a Shimadzu Pharmaspec 1700 unit equipped with the Peltier controlled TMSPC-8 model accessory (Shimadzu Corporation) (Figure 2.10). In this experiment, NPs of different concentrations were added to 5 mM CT-DNA solutions and mixed well in an eight partitioned micro optical cuvette of 10 mm path length. The absorbance change for CT-DNA at 260 nm was monitored with increasing temperature at a heating rate of 0.5°C/min. The melting temperature (T_m) was detected as the midpoint of the melting transition from the differential of the absorbance versus temperature plots.

Thermal stability of nucleic acid is an important factor that controls the structure, hybridization, and functions of nucleic acids; therefore, thermal stability analysis of nucleic acid (T_m analysis) is indispensable in these fields. Below is a simple description of nucleic acid thermal stability analysis (T_m analysis). Here, it is assumed that there is a state of equilibrium between the 2 different single-stranded (A_1, A_2) and double-stranded (A_1A_2) states, and that the concentrations of $A_1$and A_2 are the same.

$$A_1 + A_2 \Leftrightarrow A_1A_2 \qquad (2.10)$$

If the double-stranded molar fraction is α, and the total nucleic acid concentration is C_t, the equilibrium constant K for the system is expressed as follows:

$$K = \frac{[A_1A_2]}{[A_1][A_2]} = \frac{2\alpha}{(1-\alpha)^2 C_t} \qquad (2.11)$$

The observed absorbance (A_{obs}) at 260 nm is expressed as follows

$$A_{OBS} = (\varepsilon_{ds}\alpha + \varepsilon_{ss}(1-\alpha))C_t L \qquad (2.12)$$

ε_{ds}, ε_{ss} and L express the double-strand molar absorption coefficient, single-strand molar absorption coefficient and path length respectively. ε_{ds} and ε_{ss} are temperature-dependent. Since the absorbance changes linearly to a greater extent in the low-temperature, pre-transition region (region prior to large absorption change) and high-temperature post-

transition region as compared to during the transition region itself (region of large absorption change), ε_{ds} and ε_{ss} are expressed as follows, where T represents temperature.

$$\varepsilon_{ds} = a_{ds} + b_{ds}T \qquad (2.13)$$

$$\varepsilon_{ss} = a_{ss} + b_{ss}T \qquad (2.14)$$

The temperature becomes T_m when $\alpha = 1/2$, and this is what is used to determine T_m (melting temperature) from the melting curve. The baseline is determined with respect to the pre-transition region and post-transition region. Next, the median of the 2 baselines is drawn, and the temperature (T_m) at which this line intersects with the melting curve is obtained.

Figure 2.10. Temperature controlled cell holder.

2.6.2. Fluorescence Spectroscopy

Fluorescence spectroscopy is a widely used scientific tool in biophysics, biochemistry and in material science as in last few years several new applications based on fluorescence have been developed.

In this instrument, a specimen is excited with a particular wavelength of light. Absorbing the light, the excited photons of particular energy emit with different energies. Quantum mechanically, this can be described as excitation of an electron to a higher energy state by absorbing photons and then return to a lower energy state with the emission of photons. The period between absorption and emission is very short, in the order of 10 nanoseconds. Schematic diagram of the fluorescence spectrometer is shown in Figure 2.11. Steady state fluorescence emission and excitation spectra of different samples were recorded on Horiba Jobin Yvon Model Fluorolog fluorometer.

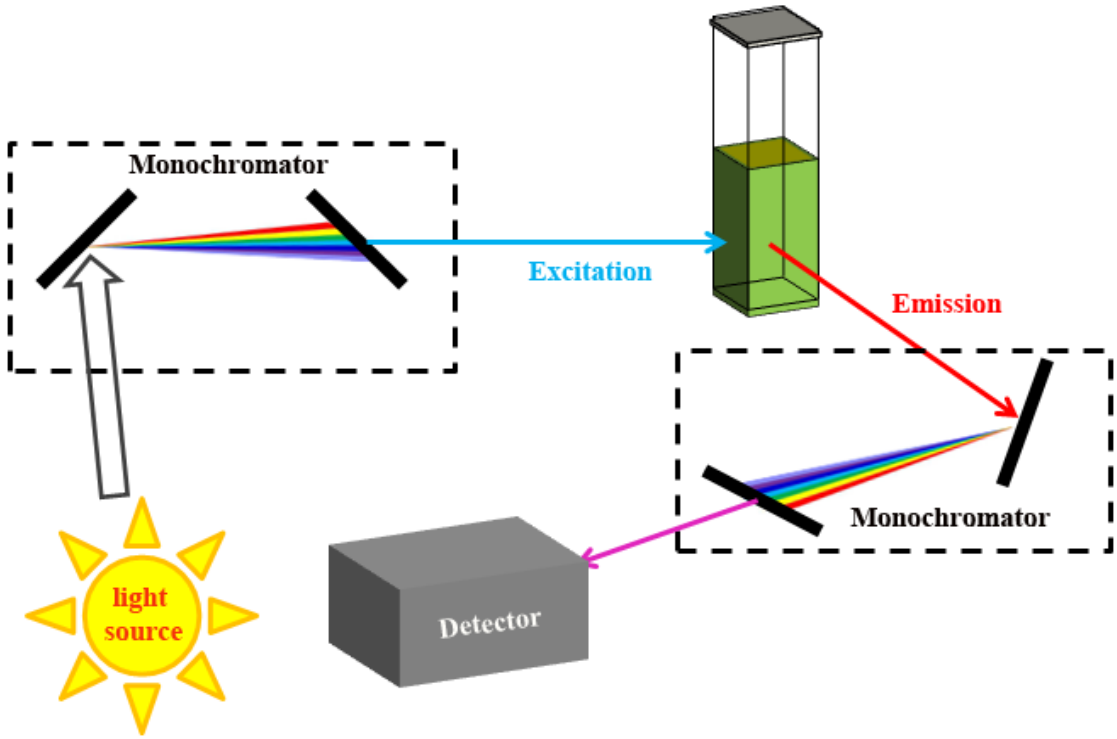

Figure 2.11. Schematic diagram of photoluminescence spectrometer.

2.6.3. Fluorescence Microscope

A fluorescence microscope is similar to the conventional light microscope with added features to enhance its capabilities where fluorescence can be used as a label or tag when preparing specific biological probes. The fluorescence microscope uses visible light with very high intensity light source (Xenon or Mercury arc-discharge lamp) to illuminate fluorochromes in a sample of interest. Fluorochromes in turn emit a lower energy light of a longer wavelength that produces the magnified image instead of the original light source. In fluorescence microscope, several light filtering components are used. Specific filters are used to isolate the excitation and emission wavelengths of a fluorochrome. First, the microscope

has a filter that only lets through radiation with the specific wavelength that matches the fluorescing material. A dichroic beam splitter (partial mirror) isolates the emitted light from the excitation wavelength by reflecting shorter wavelengths of light and allowing longer wavelengths to pass. To become detectable (visible to the human eye) the fluorescence emitted from the sample is separated from the much brighter excitation light in a second filter (Figure 2.12). This works because the emitted light is of lower energy and has a longer wavelength than the light that is used for illumination. Most of the fluorescence microscopes used in biology. Fluorescence micrographs of NPs were captured using an Olympus BX61 fluorescence microscope employing UV, blue, and green filters.

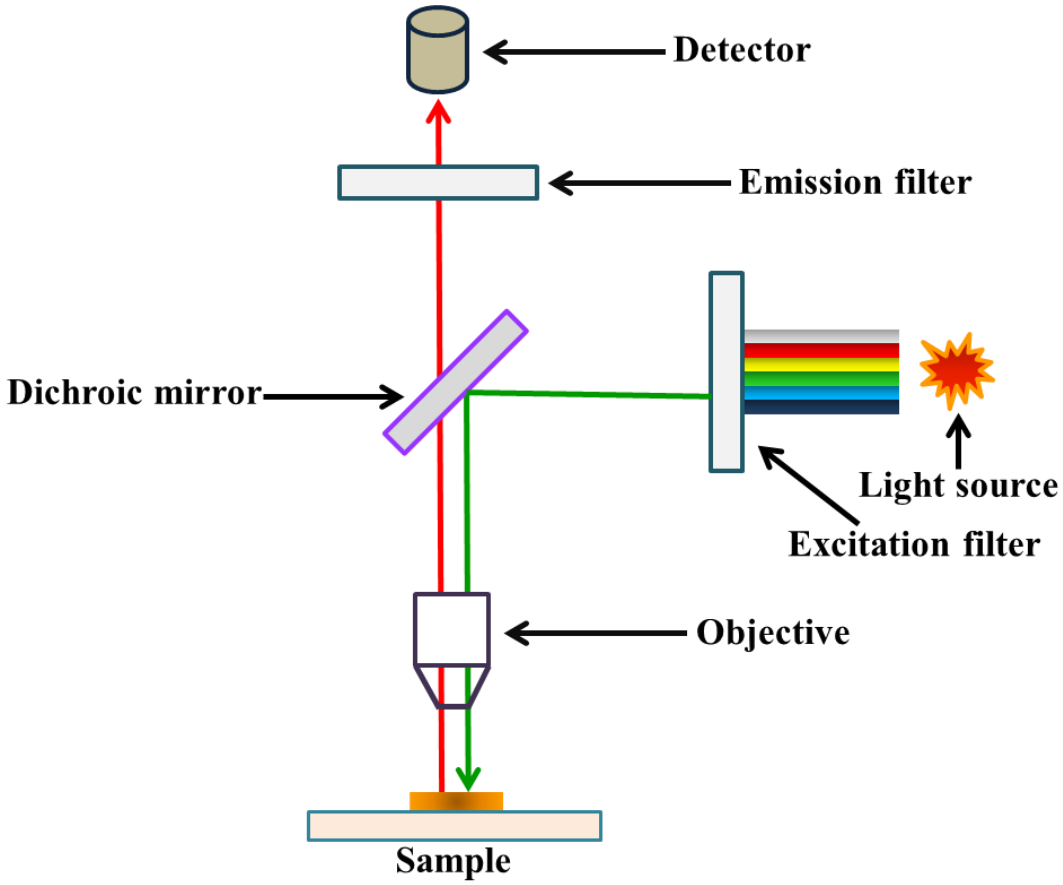

Figure 2.12. Schematic diagram of a fluorescence microscope.

2.6.4. Time Correlated Single Photon Counting (TCSPC)

Time-resolved fluorescence spectra were recorded using a commercially available spectrophotometer (LifeSpec-ps) from Edinburgh Instruments, UK. For the 320 nm laser

source, the instrument response function (IRF) was 90 ps. The data were fitted using Igor Pro 6.34A data analysis software. The emitted light from sample was collected at a right angle to the direction of the excitation beam maintaining magic angle polarization (54.7°) with a band pass of 2 nm. All the optical studies were performed at room temperature (298 K). The schematic block diagram of a TCSPC system is shown in Figure 2.13. The LED sends an excitation pulse to the sample and at the same time sends an electrical start signal to the time-to-amplitude-converter (TAC) which is responsible for analog-to-digital conversion (ADC) of the final signal. Now the sample absorbs the excitation pulse and after a short period of time re-emit photons in the direction of the detector. These photons pass through a monochromator and detected by a photomultiplier tube (PMT). In short, a photon of light generates a free electron inside of the PMT. The electron is then multiplied to become many electrons which are received at the TAC/ADC as the stop signal for the experiment. The TAC/ADC, which is essentially just a highly accurate stop-watch, begins building a voltage when it receives the start signal and stops building the voltage when it receives the stop signal from the PMT. The voltage built during the absorption, re-emission and detection processes is the correlated to a time and plotted as one count (one photon) at the correlated time that is recorded by the TAC/ADC. Based on the repetition rate (up to 1 MHz), this photon counting is repeated many times per second generating a plot of the number of photons counted at each time interval.

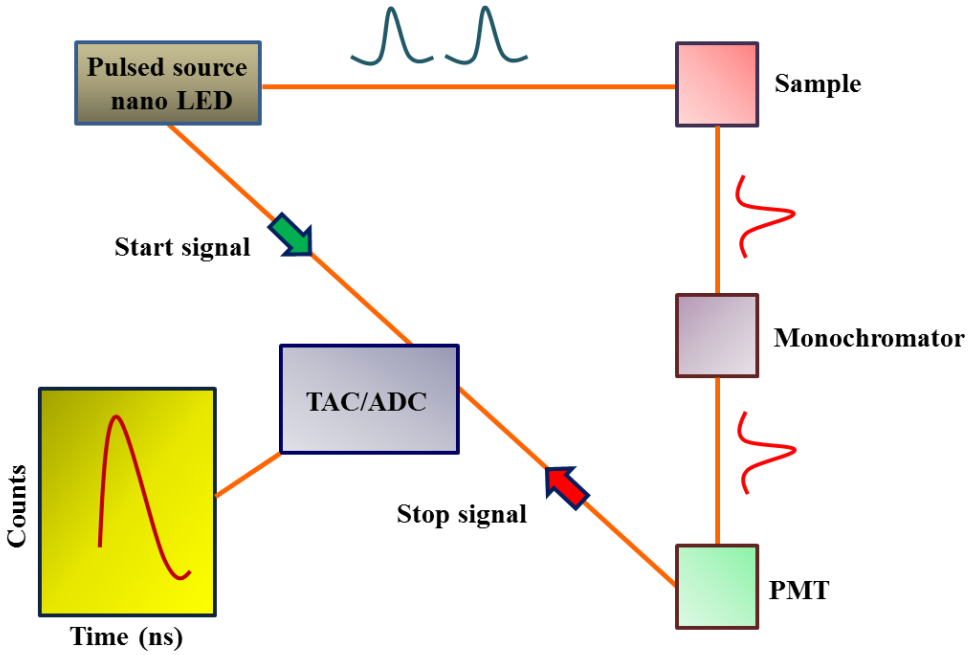

Figure 2.13. Schematic block diagram of a TCSPC system.

2.6.5. Fourier Transformed Infrared Spectroscopy (FTIR)

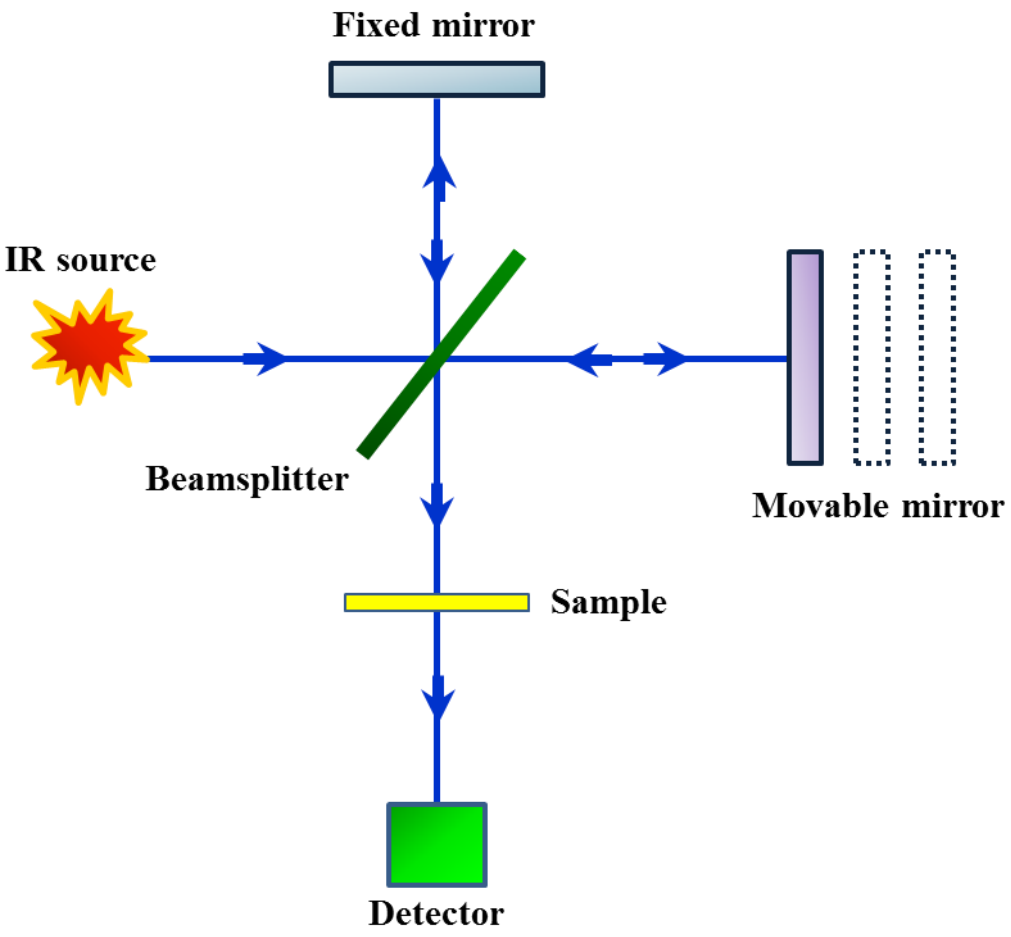

Figure 2.14. Schematic sketch of the essential features of a Fourier transform infrared (FTIR) spectrometer.

FTIR is a powerful tool to identify functional groups and chemical bonds within a molecule, is called molecular fingerprint. When the frequency of a polar vibrational mode of a bond matches with the incident IR frequency then due to absorbance of IR, FTIR signal is obtained. Additionally, the peaks get shifted or broadened due to interaction of functional groups with solvent molecules or NSs surface. Figure 2.14 shows the basic components of FTIR instrument and schematically show how to generate the spectroscopic information. Radiation from a polychromatic source collides into a beam splitter and is divided into two beams: one of them is reflected to a fixed mirror while the other is reflected to a moving mirror (the exact position of this movable mirror is measured with a mini-laser on the internal compartment of the instrument). After being reflected at each mirror, the beam recombines, producing constructive or destructive interference depending on the separation distance

between the movable mirror and the static mirror. This process produces again two beams: one returning back to the source of power and the other that goes towards the sample and is measured by the detector. This information accumulates as an interferogram in the memory of the computer. Due to the speed (usually less than 1 s) and high-accuracy throughout the process, hundreds or thousands of interferograms can be accumulated, and then added and converted through a Fourier transform in a conventional transmittance (or absorbance) spectra against wavenumbers. A JASCO FTIR-6300 spectrometer was used to carry out FTIR studies. For the FTIR measurements, powdered samples were mixed with KBr powder and pelletized. The background correction was made using a reference pure KBr pellet before every measurement.

2.6.6. Circular Dichroism (CD) Spectroscopy

CD is observed when refraction indices as well as absorption coefficients are different for left and right circularly polarized light. Figure 2.15 shows the schematic diagram of a CD spectroscopy where CD is measured by passing left circularly polarized light (LCPL) and right circularly polarized light (RCPL) consecutively through the sample and subtracting the observed intensities. The difference in left and right polarized absorbance is usually in the range of 0.0001, corresponding to an ellipticity of approximately 0.01°. CD is a very sensitive method to study molecular conformation, in particular for analyzing secondary structures of protein and nucleic acids in solution. Because different conformations have their characteristic CD spectra, the CD spectrum of a protein gives quantitative information about each kind of secondary structure. Moreover, CD is suited to a study of the rate of structural changes and it can probe interactions such as protein-ligand, protein-protein or protein-nucleic acid.

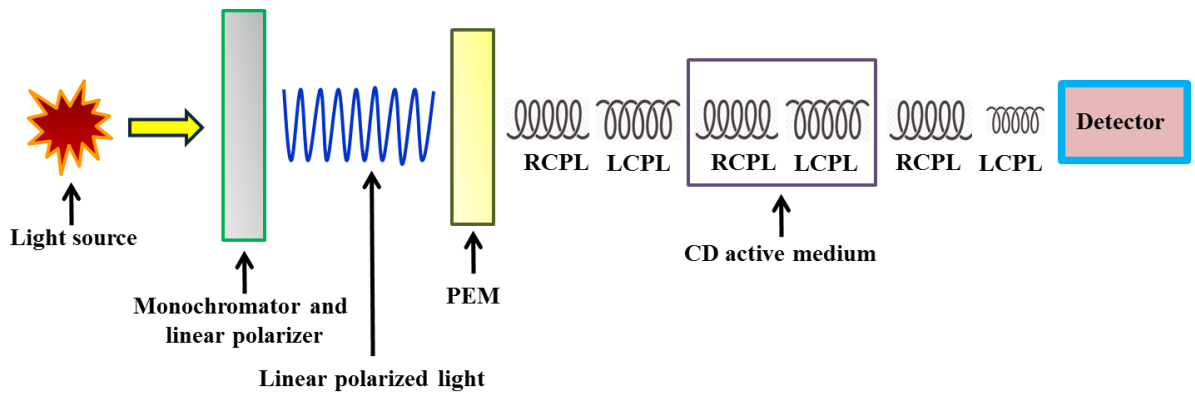

Figure 2.15. Schematic diagram of a CD spectroscopy.

2.7. Catalysis

Bilirubin (BR) is a yellow-orange breakdown product of normal heme catabolism in mammalian systems [10]. We have chosen this harmful pigment for catalytic study. Chemical structure of BR ($C_{33}H_{36}N_4O_6$) is demonstrated in Figure 2.16. Both antioxidant and toxic properties have been attributed to BR, which is normally conjugated with glucuronic acid and then excreted in the bile. However, when its conjugation with glucuronic acid is inhibited, as in neonatal jaundice and in hereditary forms of congenital jaundice, excess BR bind and deposit to various tissues, giving rise to severe hyperbilirubinemia and neurotoxicity. During the study of catalysis, aqueous NSs solution were added in the aqueous solution of BR kept in a quartz cuvette in the dark maintaining the pH of the solution ~ 7, with stirring condition. After few minutes, we measured absorbance of BR in the reaction mixture in an interval of time by the UV-visible spectrophotometer.

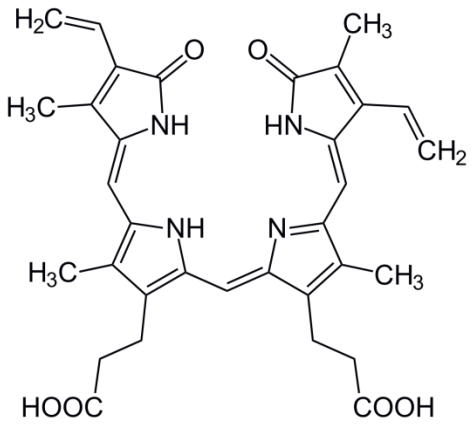

Figure 2.16. Chemical structure of bilirubin.

2.7.1. Photocatalysis

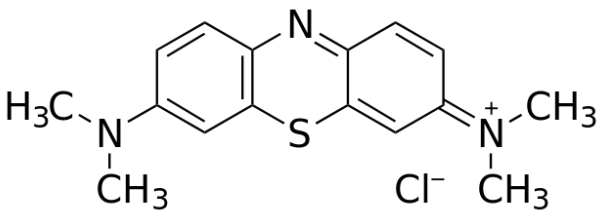

Figure 2.17. Chemical structure of methylene blue.

Methylene blue (MB) ($C_{16}H_{18}ClN_3S$) is a heterocyclic aromatic chemical compound which is used in different fields. It is an odorless, dark green powder which yields a blue solution when dissolved in water. It is also a water contaminant. So, we have chosen MB for photocatalytic degradation study [11]. Its structure is given in Figure 2.17. When MB is dissolved in water, three absorption peaks are observed at 246, 291 and 663 nm. The maximum absorption (λ_{max}) at 663 nm was used for analyzing of decolorization of MB dye. During the study of photocatalysis, we used an 8 W UV lamp as UV light and a 100 W incandescent light bulb as visible light source from Philips. Aqueous solution of MB and aqueous NSs solution were homogeneously mixed for 1 h in a quartz cuvette in the dark maintaining the pH of the solution ~ 3. Then the cuvette was kept ~ 2 cm apart from the light source and the absorbance of MB in the reaction mixture was recorded time to time by the UV-visible spectrophotometer.

Bibliography

(1) Y. Min, J. Kwak, A. Soon, U. Jeong, Nonstoichiometric Nucleation and Growth of Multicomponent Nanocrystals in Solution, *Acc. Chem. Res.* **2014,** 47, 2887-2893.

(2) S. Kumar, T. Nann, Shape Control of II–VI Semiconductor Nanomaterials, *Small* **2006,** 2, 316-329.

(3) N. T. K. Thanh, N. Maclean, S. Mahiddine, Mechanisms of Nucleation and Growth of Nanoparticles in Solution, *Chem. Rev.* **2014,** 114, 7610-7630.

(4) W. –R. Lee, M. G. Kim, J. –R. Choi, J. -I. Park, S. J. Ko, S. J. Oh, J. Cheon, Redox−Transmetalation Process as a Generalized Synthetic Strategy for Core−Shell Magnetic Nanoparticles, *J. Am. Chem. Soc.* **2005,** 127, 16090-16097.

(5) M. A. Watzky, R. G. Finke, Nanocluster Size-Control and "Magic Number" Investigations. Experimental Tests of the "Living-Metal Polymer" Concept and of Mechanism-Based Size-Control Predictions Leading to the Syntheses of Iridium(0) Nanoclusters Centering about Four Sequential Magic Numbers, *Chem. Mater.* **1997,** 9, 3083-3095.

(6) S. Sun, H. Zeng, D. B. Robinson, S. Raoux, P. M. Rice, S. X. Wang, G. Li, Monodisperse MFe_2O_4 (M = Fe, Co, Mn) Nanoparticles, *J. Am. Chem. Soc.* **2004,** 126, 273-279.

(7) S. K. Aditha, A. D. Kurdekar, L. A. A. Chunduri, S. Patnaik, V. Kamisetti, Aqueous based reflux method for green synthesis of nanostructures: Application in CZTS synthesis, *MethodsX*, **2016**, 3, 35-42.

(8) R. I. Walton, Subcritical Solvothermal Synthesis of Condensed Inorganic Materials, *Chem. Soc. Rev.* **2002**, 31, 230-238.

(9) T. R. Groves, H. C. Pfeiffer, T. H. Newman, F. J. Hohn, EL3 System for Quarter-micron Electron Beam Lithography, *J. Vac. Sci. Technol. B* **1988**, 6, 2028-2032.

(10) S. Sarkar, A. Makhal, S. Baruah, M. A. Mahmood, J. Dutta, S. K. Pal, Nanoparticle-Sensitized Photodegradation of Bilirubin and Potential Therapeutic Application, *J. Phys. Chem. C* 2012, 116, 9608-9615.

(11) R. S. Dariani A. Esmaeili, A. Mortezaali, S. Dehghanpour, Photocatalytic reaction and degradation of methylene blue on TiO_2 nano-sized particles, *Optik* **2016**, 127, 7143-7154.

Chapter 3

Surface Functionalization of $MnFe_2O_4$ Nanoparticles with Three Different Ligands for Comparative Fluorescence Study and DNA Nuclease Activity

In this chapter we have explained why the tartrate ligand functionalized $MnFe_2O_4$ nanoparticles show highest fluorescence intensity but lowest saturation magnetization comparing with malate and citrate ligand functionalized $MnFe_2O_4$ nanoparticles. Besides, we have noticed that tartrate functionalized $MnFe_2O_4$ nanoparticles bind calf thymus DNA by intercalative mode and cleave pBR322 plasmis DNA.

3. Design and Development of Bioactive α-hydroxy Carboxylate Group Modified $MnFe_2O_4$ Nanoparticle: Comparative Fluorescence Study, Magnetism and DNA Nuclease Activity

3.1. Preamble

3d-Transition metal oxide based magnetic nanoparticles (MNPs) have gained tremendous research interest due to their several applications in different growing fields ranging from magnetic resonance imaging (MRI) [1], AC magnetic field assisted hyperthermia [2], targeted drug and gene delivery [3,4], biosensor for clinical diagnosis [5], cell labeling and tracking [6], and tissue engineering [7] owing to their unique characteristics, including efficient contrast effect, biocompatibility, chemical stability, non-toxicity, inexpensive and simple preparation method, versatile surface capability, and controlled manipulation under external magnetic field. Among them, inverse spinel type ferromagnetic manganese ferrite ($MnFe_2O_4$) nanoparticles (NPs) have attracted enormous concern because of their highest saturation magnetization which strengthens their activity as magnetic probes. Further, the size tunability of $MnFe_2O_4$ NPs from a few to tens of nanometres helps to enhance their effective interaction with different biological entities having similar size dimension. However, the agglomerative nature and insolubility of MNPs restrict their biomedical application which can be easily overcome through proper surface coating or functionalization with non-toxic and biocompatible ligand.

Properly functionalized MNPs can provide highly water-soluble and well-dispersed MNPs which can facilitate their penetration through cell and tissue barriers and offer organ-specific therapeutic and diagnostic modalities [8]. Pal and her research group have developed $MnFe_2O_4$ NPs as a biocompatible novel multifunctional biological probe through their surface functionalization with small organic tartrate ligand. The tartrate modified $MnFe_2O_4$ NPs are found to exhibit simultaneously superparamagnetism as well as intrinsic bright multicolour fluorescence covering from cyan, green to red in addition to water solubility which improves the efficiency of MNPs for their application in non-invasive biomedical diagnosis [9]. In recent years, generation of novel property through judicious surface functionalization of MNPs has been the subject of key research and opens up new

opportunity on the study of metaleligand interaction which is found to significantly depend on the size, shape, surface chemistry of MNPs as well as the nature of surface binding ligands. For example, Lee et al. [10] demonstrated the effect of citric acid and various citrates on the formation of different ZnO structures based on pH of the solution. Zhang et al. [11] described the magnetic behaviour of AOT functionalized Mn doped ZnO nanorods on the basis of ligand to metal charge transfer (LMCT) effect and ligand field multiplet theory. In spite of numerous reports on the effect of ligands on NPs, the studies regarding microscopic origin of ligand modified novel properties of nearly monodispersed $MnFe_2O_4$ NPs through systematic variation of surface co-ordinating ligands are scarce in the extant articles.

Recently, engineered MNPs represent a cutting-edge tool in medicine and have found immense applications in DNA binding and delivery in vitro [12], gene therapy [13], and nanomedicines [14]. DNA is well studied macromolecule which is the key target for anticancer and antiviral therapies. A long term research unfolds that fluorescence and chemiluminescence are the beneficial tools for DNA detection [15-17]. Due to non-fluorescent nature of DNA [18,19], it becomes very essential to employ extrinsic fluorescent probes for identifying DNA [20-22]. The enhancement of emission intensity in fluorescence spectra of a given probe in the presence of DNA is more advantageous than the radioactive labelling for detecting DNA [23-25]. In recent years, so many researchers have shown the binding of gold (Au) or silver (Ag) NPs with macromolecular DNA [26-28] where these noble NPs are found to highly interact with nucleotides through the functionalization of stabilizing capping layer with fluorescent moieties. Furthermore, numerous researches on the interaction of nanostructured materials such as carbon NPs [29] and MNPs [30] with DNA have been started for exploring novel pathogenic bacteria detection, imaging, biosensor, and drug delivery applications. The structure and compositions of NPs, the pH at which DNA interacts with the NPs, and the functionalization of NPs are found to play significant role in determining the nature of interaction between DNA and NPs and have become a main area of research interest.

In view of aforementioned advantageous aspects of MNPs, we focus on the synthesis as well as functionalization of $MnFe_2O_4$ NPs by systematic variation of the nature of surface-binding ligands, named disodium tartrate dihydrate (T), disodium DL-malate hydrate (M), and trisodiumcitrate dihydrate (C) which help to solubilize and disperse the as-prepared $MnFe_2O_4$ NPs in aqueous medium as well as generate multiple intrinsic fluorescence. We have explained the optical response of functionalized $MnFe_2O_4$ NPs in the context of LMCT

transition from ligand to the lowest unoccupied energy level of Mn^{2+} or Fe^{3+} of NPs and d-d transition, centred over Fe^{3+} ions of $MnFe_2O_4$ NPs. We have been able to explain the origin of subtle changes in the optical and magnetic responses of functionalized $MnFe_2O_4$ NPs by rational variation of functional groups and steric hindrance of the ligand. Finally, we report the nuclease activity and the DNA-binding properties of structurally characterized tartrate functionalized $MnFe_2O_4$ NPs with maximum optical response in order to have a broad understanding of their binding mode with DNAs as well as for exploring new anticancer agents, biomolecular modification and detection agents.

3.2. Experimental Section

3.2.1. Materials Used

Iron(III) acetylacetonate [$Fe(acac)_3$], manganese(II) acetate [$Mn(ac)_2$], oleylamine and sodium hydroxide were purchased from Sigma Aldrich whereas oleic acid, cetyl alcohol, ethanol, disodium tartrate dihydrate, trisodium citrate dihydrate and the solvent diphenyl ether were obtained from Loba Chemie. Disodium DL-malate hydrate was purchased from TCI, Japan. Calf thymus (CT) DNA (sodium salt, type XI, 42 mol % GC content) and ethidium bromide (EB) were purchased from Sigma Chemical Company, USA, whereas supercoiled (SC) plasmid pBR322 DNA was obtained from Bangalore Genei (Bangalore, India). The whatman syringe and millipore membrane filters of 0.22 mM pore size were purchased from Sigma Aldrich and Millipore, India Pvt. Ltd., Bangalore, India, respectively. All the reagents are of analytical grade and used without further purification.

3.2.2. Synthesis and Functionalization of $MnFe_2O_4$ NPs

$MnFe_2O_4$ NPs were synthesized by wet chemical method [31], involving the high temperature of 270 °C reflux of $Fe(acac)_3$ and $Mn(ac)_2$ salts in presence of diphenyl ether, oleic acid, cetyl alcohol, and oleylamine for 1 h. The as-prepared NPs were vigorously cyclomixed with 0.5 M Na-tartrate, Na-malate, and Na-citrate solutions in separate vessels for 12 h at room temperature. In order to remove non solubilized larger $MnFe_2O_4$ NPs, three different solutions were passed through separate syringe filters of 0.22 mm diameter and the filtrates were termed as tartrate functionalized $MnFe_2O_4$ (T-$MnFe_2O_4$), malate functionalized $MnFe_2O_4$ (M-$MnFe_2O_4$), and citrate functionalized $MnFe_2O_4$ (C-$MnFe_2O_4$) NPs solution.

3.2.3. DNA

3.2.3.1. Structure of DNA

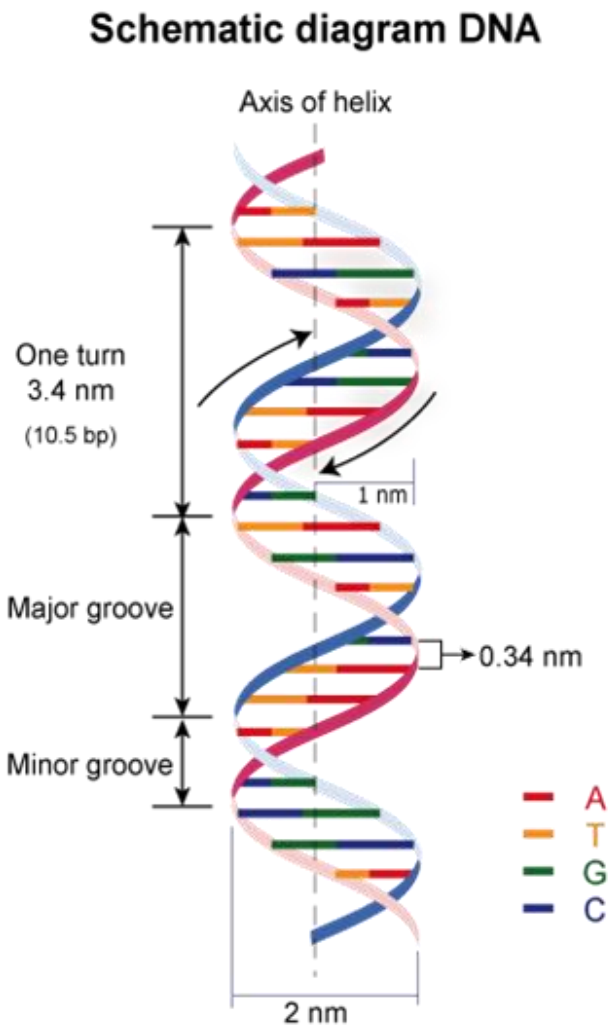

Figure 3.1. DNA double helix (Diagrammatic).

Nucleic acid is present within the nucleus. Nucleic acids are of two types: DNA and RNA. There are three major components in the nucleus: pentose sugar (deoxyribose), phosphoric acid and nitrogen bases (adenine, guanine, cytosine and thymine).

DNA is the most important chemical compound of living organisms, it is the blue print of life carrying hereditary information from generation to generation. It carries all the important information for controlling all the biological activities like growth, cell division and protein synthesis.

The DNA is a long double stranded macromolecule where each strand is made up of 4 types of nucleotides joined end to end and twisted in plectonemic fashion (Figure 3.1). The orientation of the two strands is antiparallel. The arrangement of the DNA double helix is like a spiral staircase, where the railings are formed by joining of alternate molecules of deoxyribose sugar and phosphoric acid, the steps are formed by joining of purine and pyrimidine bases. Adenine (A) is joined to thymine (T) with the help of two hydrogen bonds while guanine (G) is joined to cytosine (C) by three hydrogen bonds. The distance between two stands is fixed (2 nm). Each base pair forms an angle of 36° with the previous one, so in a complete turn of 360°, there will be 10 base pairs, separated by a distance of 0.34 nm. The helical distance of DNA in a 360° complete turn is 3.4 nm.

3.2.3.2. De-proteinization of DNA

DNA was de-proteinized by phenol-chloroform extraction method [32] followed by precipitation using ethanol. Initially, the dried DNA sample was dissolved in 10 mM CP buffer at pH 7 which was filtered through millipore membrane filters of 0.22 μM pore size. The filtrate was then sonicated in order to have uniform size of about 280 ± 50 base pairs of DNA by using a Labsonic 2000 sonicator (B. Braun, Germany) with a titanium ultrasonic needle probe (4 mm in diameter, 127 mm long) [33]. The sonicated DNA sample was dialysed several times against the experimental buffer under sterile conditions in order to free DNA sufficiently from protein contamination. The characteristic UV absorption spectra of DNA with A_{260}/A_{280} ratio between 1.88 and 1.92 and A_{260}/A_{230} ratio between 2.12 and 2.22 confirm the absence of protein from DNA and the concentration of the DNA sample was calculated from absorption spectroscopy by using the molar absorption coefficient value of 13200 M^{-1} cm^{-1} (base pairs). All experiments were performed at 25 ± 0.5 °C.

3.3. Results and Discussions

3.3.1. Phase, Morphology and Crystallinity Studies of $MnFe_2O_4$ NPs

Figure 3.2.(a) shows the XRD pattern of $MnFe_2O_4$ NPs, where all the diffraction peaks match with the cubic inverse spinel structure of $MnFe_2O_4$ NPs as reported in the literature [31]. The EDX analysis of $MnFe_2O_4$ NPs as shown in Figure 3.2.(b), confirms the presence of manganese (Mn), iron (Fe) and oxygen (O). The TEM study has been carried out to

understand the morphology of $MnFe_2O_4$ NPs as shown in Figure 3.2.(c), indicating their almost spherical shape with average size of 14 nm. Figure 3.2.(d) shows the high resolution TEM image where the calculated inter-planar distance between the lattice fringes is found to be 0.253 nm, which corresponds to the distance between the (311) planes of $MnFe_2O_4$ crystal lattice. The corresponding selected area electron diffraction (SAED) pattern is shown in Figure 3.2.(e), confirming the poly-crystallinity of the as-prepared NPs.

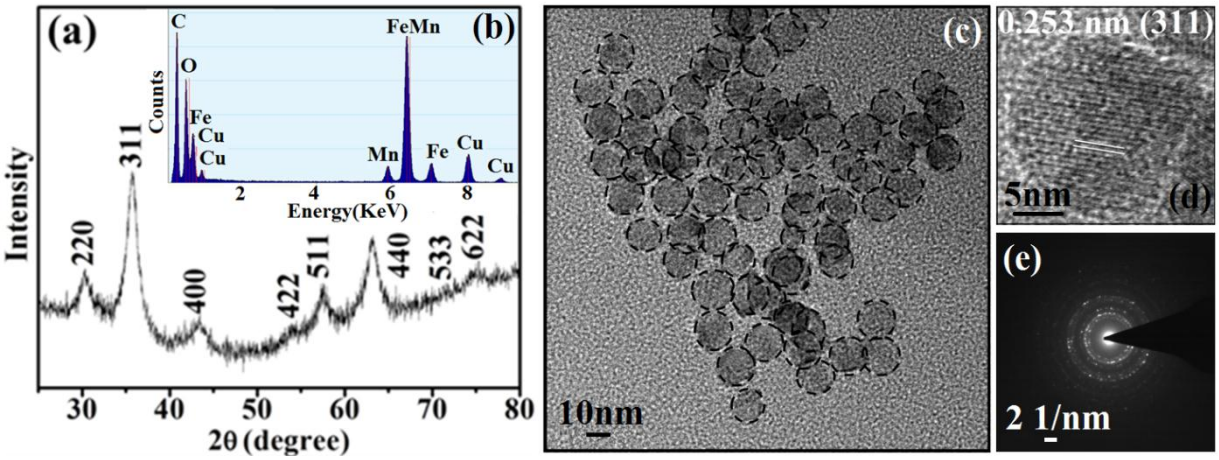

Figure 3.2. (a) XRD pattern, (b) EDX spectrum indicating the presence of Mn, Fe, and O, (c) TEM image, (d) high resolution TEM image of lattice fringes, indicating high crystallinity, and (e) SAED pattern of as-prepared $MnFe_2O_4$ NPs.

3.3.2. UV-vis Absorption Study of Functionalized $MnFe_2O_4$ NPs

It is well known that the surface modification of nanostructured materials has extensive impact on their surface electronic structures and may give rise to many novel optical, electrical, and magnetic properties which are completely absent in its bare form [36,37]. We have carried out surface functionalization of $MnFe_2O_4$ NPs with three different naturally occurring organic ligands which are tartrate, malate, and citrate as shown in Figure 3.3.(a)-(c) where the tartrate ligand is found to have two α-hydroxy carboxylate groups and both malate and citrate ligand have only one α-hydroxy carboxylate group. However, citrate ligand is found to be more steric in nature than the malate due to the presence of three carboxyl group in citrate. Three different ligands having varieties of α-hydroxy carboxylate moiety and steric effect have been employed in order to identify the exact functional group which is responsible for strong optical response from the functionalized NPs. In order to investigate the change in optical response of $MnFe_2O_4$ NPs upon attachment with tartrate, malate, and

citrate ligands, we have carried out UV-vis absorption spectra of T-$MnFe_2O_4$, M-$MnFe_2O_4$, and C-$MnFe_2O_4$ NPs at pH ~ 7 along with bare $MnFe_2O_4$ NPs, tartrate, malate, and citrate as shown in Figure 3.3.(d). From the UV-vis spectra, a clear broad absorption band at around 300−400 nm is observed for all functionalized $MnFe_2O_4$ NPs where the bare ligands including $MnFe_2O_4$ NPs do not show any absorption spectra within that wavelength range of analysis which completely support the interaction of ligands with the NPs. The comparative absorption spectra show the maximum absorption for T-$MnFe_2O_4$ NPs followed by M-$MnFe_2O_4$ and C-$MnFe_2O_4$ NPs. The broad absorption is due to the LMCT from the highest occupied energy level of the ligands to the lowest unoccupied energy level of the surface dangled metal ions (Mn^{2+} and Fe^{3+}) and d-d transitions centered over Fe^{3+} ions in the NPs [9,38]. Different absorption spectra of tartrate, malate, and citrate modified NPs imply that the structural differences of individual ligands have notable impact on the electronic structure of surface transition metal ions of $MnFe_2O_4$ NPs. It is found that the tartrate having two α-hydroxy carboxylate group exhibits maximum absorption with distinct absorption feature upon attachment with $MnFe_2O_4$ NPs than two other ligands, malate and citrate with one α-hydroxy carboxylate group. Interestingly, C-$MnFe_2O_4$ NPs show minimum absorption spectrum comparing with absorption spectra of T-$MnFe_2O_4$, M-$MnFe_2O_4$ NPs with no distinguishable peak in spite of having one α-hydroxy carboxylate group. It can be explained in the context of steric effect offered by bulky ligand. Chen and his research group have demonstrated that the steric influence of ligand can design new complexes with optimized properties since it affects structure, reactivity and selectivity of reactions significantly [39]. Therefore, big size effect of citrate ligand due to the presence of three carboxylate ($-COO^-$) groups causes more steric hindrance for the interaction of ligand with the surface metal ions of $MnFe_2O_4$ NPs, leading to obscure LMCT transition. The comparative study reveals that the presence of a α-hydroxy carboxylate moiety in the ligands plays key role for the optical response of functionalized $MnFe_2O_4$ NPs through activation of LMCT, associated with Mn^{2+}/Fe^{3+} -ligand interactions along with d-d transitions corresponding to the d-orbital energy level splitting of Fe^{3+} ions on the NPs surface.

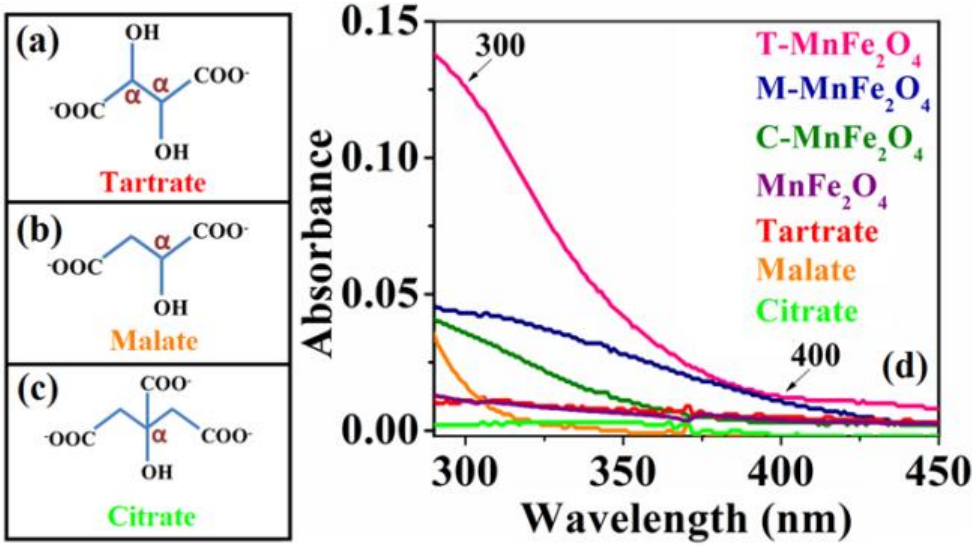

Figure 3.3. Schematic diagrams of the chemical structure of (a) tartrate, (b) malate and (c) citrate. (d) UV-vis absorption spectra of T-$MnFe_2O_4$, M-$MnFe_2O_4$, C-$MnFe_2O_4$ NPs along with tartrate, malate and citrate.

3.3.3. Photoluminescence Study of Functionalized $MnFe_2O_4$ NPs

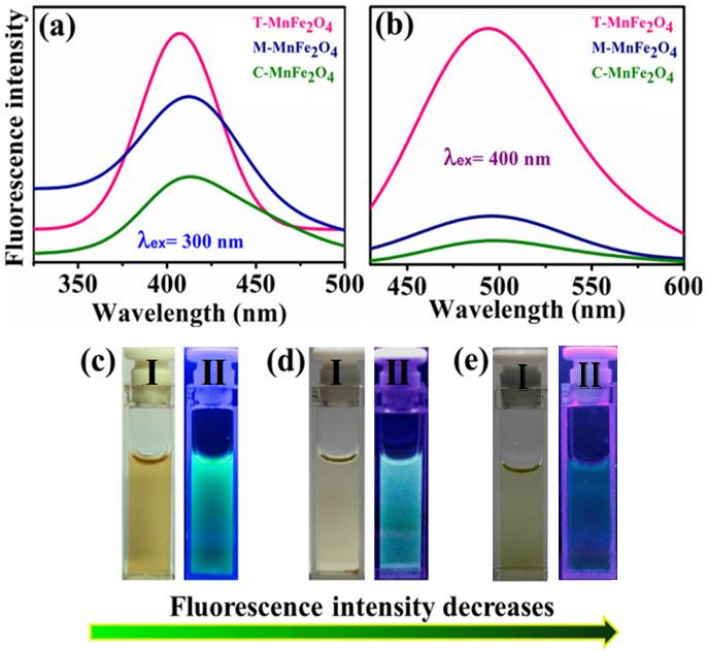

Figure 3.4. Fluorescence emission spectra of T-$MnFe_2O_4$, M-$MnFe_2O_4$ and C-$MnFe_2O_4$ NPs after excitation at (a) λ_{ex} = 300 nm and (b) λ_{ex} = 400 nm, respectively. The photographs of aqueous (c) T-$MnFe_2O_4$, (d) M-$MnFe_2O_4$ and (e) C-$MnFe_2O_4$ NPs solution under visible (I) and UV light (II).

Excellent results in the UV-vis absorption spectra of T-$MnFe_2O_4$, M-$MnFe_2O_4$, and C-$MnFe_2O_4$ NPs lead to carry out fluorescence study in order to get additional evidence regarding the origin of their optical properties. Figure 3.4.(a) and (b) show the emission study upon exciting T-$MnFe_2O_4$, M-$MnFe_2O_4$ and C-$MnFe_2O_4$ NPs at 300 and 400 nm, respectively. Upon exciting three different functionalized NPs at λ_{ex} = 300 nm, the emission in the wavelength (λ_{em}) range of 407−411 nm proves the fluorescence property of the samples. Different peak intensities of different metale ligand complexes are found to be consistent with the obtained results of UV-vis absorption spectra. Photoluminescence peak arising at λ_{em} = 407−411 nm assigns the involvement of LMCT transition from HOMO (Highest occupied molecular orbital) of the ligand to the LUMO (Lowest unoccupied molecular orbital) centered over metal ions i.e. Mn^{2+}/Fe^{3+}. When the functionalized NPs are excited against λ_{ex} = 400 nm, the emission spectra at λ_{em} ~ 493−497 nm with different peak intensities, similar as UV-vis absorption demonstrate one of the d-d transitions of surface Fe^{3+} ions. Although the d-d transitions of Fe^{3+} ($3d^5$) containing materials are formally dipole and spin forbidden transitions; however it can have considerable strength due to the relaxation of selection rules by octahedral distortion and spin-orbit coupling [40,41]. Further, identical intensity difference was obtained in the photographs of aqueous solutions of T-$MnFe_2O_4$, M-$MnFe_2O_4$, and C-$MnFe_2O_4$ NPs under visible and UV light, as shown in Figure 3.4.(c)-(e). The distinct absorption features from UV-vis absorption spectra and its corresponding emission intensities from fluorescence spectra clearly indicate that the strength of interaction between α-hydroxy carboxylate group of the ligand and the surface transition metal ions of the NPs plays key role in developing novel optical response in functionalized $MnFe_2O_4$ NPs.

3.3.4. FTIR Study of Functionalized $MnFe_2O_4$ NPs

The recorded FTIR spectra for one of the ligand functionalized $MnFe_2O_4$ NPs, as shown in Figure 3.5.(a) confirm the attachment of the functional group of tartrate to the $MnFe_2O_4$ NPs surface. In case of tartrate, two sharp peaks at 1068 and 1112 cm^{-1} are due to the stretching vibration of C−OH bond. Another two peaks at 1411 and 1617 cm^{-1} arise due to the symmetric and asymmetric stretching vibrations of $-COO^-$ groups, respectively [42,43]. The −OH stretching vibration at 3400 cm^{-1} is perturbed significantly along with other bands for T-$MnFe_2O_4$ NPs assuring the attachment of the functional groups of the tartrate ligand to the NPs surface. In a similar way, FTIR of the ligands (malate and citrate) having similar

functional groups attach to the NPs as the tartrate ligand are shown in Figure 3.5.(b) and Figure 3.5.(c) respectively. For disodium DL malate dihydrate, the characteristic peaks at 1400 and 1585 cm^{-1} are correspond to the symmetric and asymmetric stretching vibrations of $–COO^-$ group. A broad absorption band at around 3400 cm^{-1} is due to the –OH stretching vibration. When $MnFe_2O_4$ NPs are modified with malate, symmetric and asymmetric stretching modes become red shifted. This clearly confirms the attachment of malate to the NPs. For trisodium citrate, three peaks at 1391, 1590 and 3454 cm^{-1} are due to the symmetric, antisymmetric stretching of COO^- and stretching vibration of –OH respectively. In citrate modified NPs, all the bonds are perturbed through red shifting of symmetric and asymmetric stretching modes of $–COO^-$ group, confirming the functionalization of $MnFe_2O_4$ NPs with citrate.

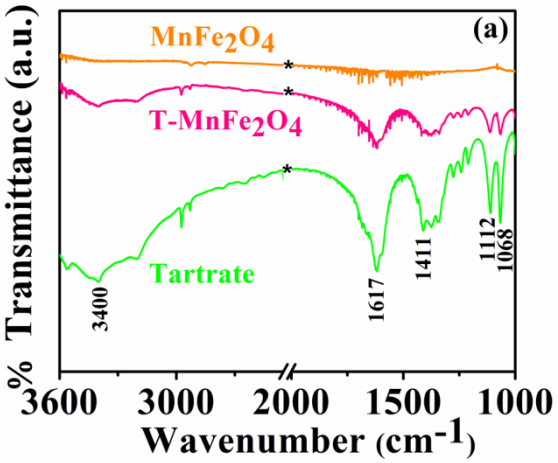

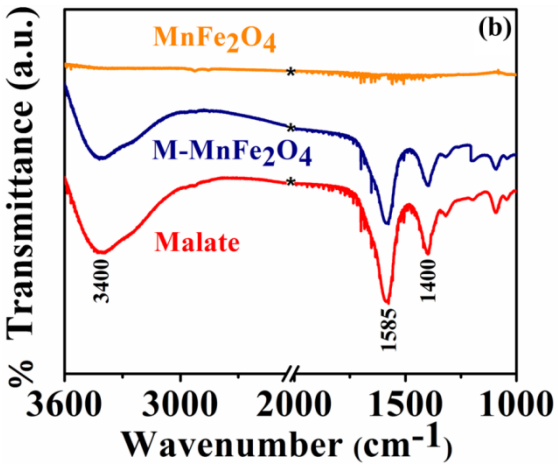

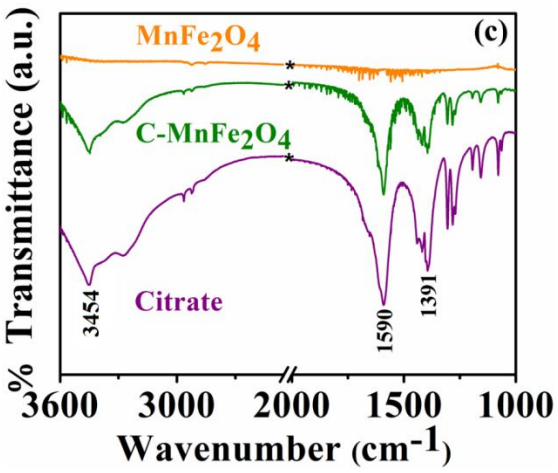

Figure 3.5. FTIR spectra of (a) T-$MnFe_2O_4$, Na-tartrate, (b) M-$MnFe_2O_4$ NPs, Na-malate and (c) C-$MnFe_2O_4$ NPs, Na-citrate along with as prepared $MnFe_2O_4$ NPs in each cases.

3.3.5. Magnetic Analyses of Bare and Functionalized $MnFe_2O_4$ NPs

Figure 3.6.(a) and (b) show the room temperature magnetic measurements of as-prepared $MnFe_2O_4$ and T-$MnFe_2O_4$, M-$MnFe_2O_4$, and C-$MnFe_2O_4$ NPs, respectively. The insets of Figure 3.6.(a) and (b) show the zoomed image which helps to calculate the coercivity of $MnFe_2O_4$ and functionalized $MnFe_2O_4$ NPs accurately. The hysteresis loops of as-prepared and all functionalized NPs indicate their ferrimagnetic nature and Table 3.1 indicates the change in coercivity and magnetization of functionalized $MnFe_2O_4$ NPs with reference to the bare NPs. The coercive fields for as-prepared $MnFe_2O_4$, T-$MnFe_2O_4$, M-$MnFe_2O_4$, and C-$MnFe_2O_4$ NPs are found to be 30.62, 61.97, 69.62, and 73.76 Oe, respectively whereas some their magnetizations are not found to reach their saturation values (M_{sat}) within the applied magnetic field range. The maximum magnetization (M_{max}) values of as-prepared $MnFe_2O_4$ and C-$MnFe_2O_4$ NPs at 12 kOe are found to be 31.93 and 2.72 emu/g whereas M_{sat} values of the T-$MnFe_2O_4$ and M-$MnFe_2O_4$ NPs are found to be 0.82 and 1.14 emu/g, respectively at 12 kOe. It is found that the functionalization of $MnFe_2O_4$ NPs with different ligands has a notable impact on the ferrimagnetic properties of bare $MnFe_2O_4$ NPs at room temperature.

Table 3.1. List of coercivity and maximum magnetization at 1500 Oe of as-prepared and C-$MnFe_2O_4$, M-$MnFe_2O_4$ and T-$MnFe_2O_4$ NPs.

Sample	Coercivity (Oe)	Maximum Magnetization at 12 kOe
$MnFe_2O_4$ NPs	30.62	31.93
C-$MnFe_2O_4$ NPs	73.76	2.72
M-$MnFe_2O_4$ NPs	69.62	1.14
T-$MnFe_2O_4$ NPs	61.97	0.82

The ligand co-ordination with the NPs causes a very strong pinning to the surface unpaired magnetic moments of Mn^{2+} ions, leading to a strong surface anisotropy which therefore enhances the coercivity of functionalized nano-system with reference to bare NPs [44]. Moreover, the surface binding of ligand leads to quenching of unpaired magnetic moments of surface Mn^{2+} ions due to LMCT and causes to significant reduction of magnetization of modified NPs with respect to the bare one [45]. Moreover, the distinct changes in magnetic properties of functionalized $MnFe_2O_4$ NPs are found to exhibit a profound dependence on the nature of surface binding ligands.

According to ligand field theory (LFT), there is a LMCT from HOMO of the ligand to the LUMO centered over metal ions i.e. Mn^{2+}/ Fe^{3+} upon interaction with the ligand where the field strengths as well as the number of functional ligands are found to play significant role in determining the magnitude of LMCT [46]. Among the three ligands, tartrate has two α-hydroxy carboxylate groups whereas both malate and citrate have single α-hydroxy carboxylate group. The enhanced ligand-metal interaction in case of T-$MnFe_2O_4$ NPs favours the quenching of orbital magnetic moments of 3d-transition metal ions and subsequently reduces both its magnetization as well as spin-orbit coupling more in comparison to M-$MnFe_2O_4$ and C-$MnFe_2O_4$ NPs. According to Stoner-Wohlfarth theory, the magnetocrystalline anisotropy energy (E_A) of single-domain MNPs extensively depends on its spin-orbit coupling (K) which can be expressed as, $E_A = KV\sin^2\theta$ with V as volume of the NP and θ, the angle between magnetization direction and easy axis of NP. Therefore, maximum reduction of spin-orbit coupling causes huge decrease in EA or the coercivity of T-$MnFe_2O_4$ NPs. In between C-$MnFe_2O_4$ and M-$MnFe_2O_4$ NPs, the functional groups of smaller ligands can interact with surface ions of the NP more efficiently than larger counterpart. Therefore, greater interaction of functional groups of malate ligand results in its

higher crystal field splitting energy (CFSE) of d-orbital energy levels of transition metal ions and causes more decrease in both coercivity and magnetization than the citrate one.

Having developed magneto-fluorescent $MnFe_2O_4$ NPs through surface functionalization, we are interested to exploit their broad optical response throughout the UV-vis region for non-invasive biomedical applications. In general, MNPs are broadly used in diagnostic immunoassays and various reactions involving enzymes, proteins, and DNA due to their advantages of easy isolation from biological materials. For instance, Shan et al. [47] have demonstrated an isolation of genomic DNA present in urine sample at a concentration of 50 x 10^{-6} mol/L using carboxylated MNPs as adsorbent. Gersting et al. [48] have reported the delivery of plasmid DNA to human respiratory epithelial cells using superparamagnetic particles, indicating gene therapy using nucleic acid-MNP nanocomposites which is a good alternative to viral vectors with no risk of immune response and development of infective diseases. Therefore, in order to investigate the efficiency of biocompatible multifunctional $MnFe_2O_4$ NPs for improving diagnosis and therapy of disease, we have chosen T-$MnFe_2O_4$ NPs with maximum fluorescence intensity upon specific wavelength excitation and carried out DNA binding study with CT-DNA and nuclease activity study with SC plasmid pBR322 DNA for exploring their biomedical applications as a DNA detector as well as anticancer drug.

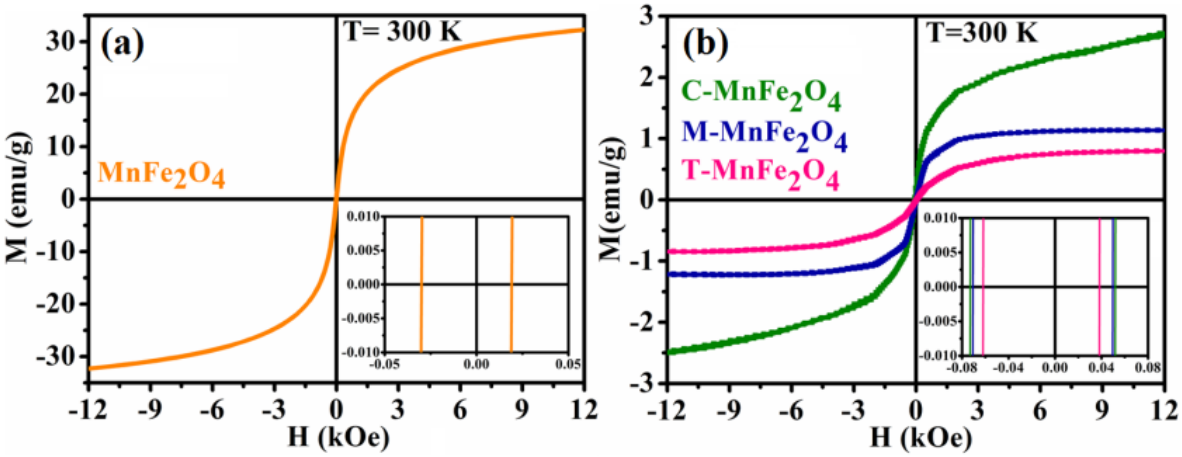

Figure 3.6. Room temperature magnetization versus applied magnetic field (M-H) curve of (a) $MnFe_2O_4$ NPs and (b) C-$MnFe_2O_4$, M-$MnFe_2O_4$ and T-$MnFe_2O_4$ NPs. Inset shows the zoomed image indicating the coercivity of bare and respective functionalized NPs.

3.3.6. Spectroscopic Studies on DNA Binding

The binding of T-$MnFe_2O_4$ NPs with DNA was investigated through spectrophotometric and spectrofluorometric titrations where the interaction is revealed by changes in the absorbance and fluorescence spectra. The electronic absorption of T-$MnFe_2O_4$ NPs was monitored in presence and absence of CT-DNA as shown in Figure 3.7.(a). An isosbestic point at 285 nm as pointed by an arrow mark in Figure 3.6.(a) was observed indicating a strong interaction of T-$MnFe_2O_4$ NPs with CT-DNA. There is a considerable increase of 252 nm band and decrease in the absorption band at around 370−400 nm due to the addition of CT-DNA. The association constant of the [CT-DNA]−[T-$MnFe_2O_4$ NPs] complex species was obtained from Benesi-Hildebrand (BH) plot as shown in Figure 3.7.(b) and calculated to be (8.71 ± 0.02) x 10^6 M^{-1}. The association constant of T-$MnFe_2O_4$ NPs is comparable to other classical intercalators and metal complex intercalators [49]. In recent past, Bouffier et al. [50] have shown Fe_3O_4 MNPs (average size of 24 nm) sequentially functionalized with trimethoxysilylpropyldiethylene- triamine and 9-chloro-4H-pyrido[4,3,2-kl]acridin-4-one as a DNA interacting agent with the binding affinity of 2.8 x 10^5 M^{-1} which imply that our developed T-$MnFe_2O_4$ NPs play excellent role in DNA binding. Evidence for the association of NPs to CT-DNA was also derived from fluorometric titration. The T-$MnFe_2O_4$ NPs are found to exhibit fluorescence maxima at 495 nm when excited at 400 nm. The steady state fluorescence of the NPs in the range 450-490 nm increased remarkably upon addition of CT-DNA as shown in Figure 3.7.(c). This kind of spectral pattern was observed due to the complexation of T-$MnFe_2O_4$ NPs with CT-DNA. Modified Benesi-Hildebrand (BH) plot as shown in Figure 3.7.(d) is used for the calculation of the binding constant between NPs and CT-DNA. The binding affinity value was estimated to be (6.18 ± 0.02) x 10^6 M^{-1}, which was in good agreement with the binding constant evaluated from the data of absorption spectroscopic analysis.

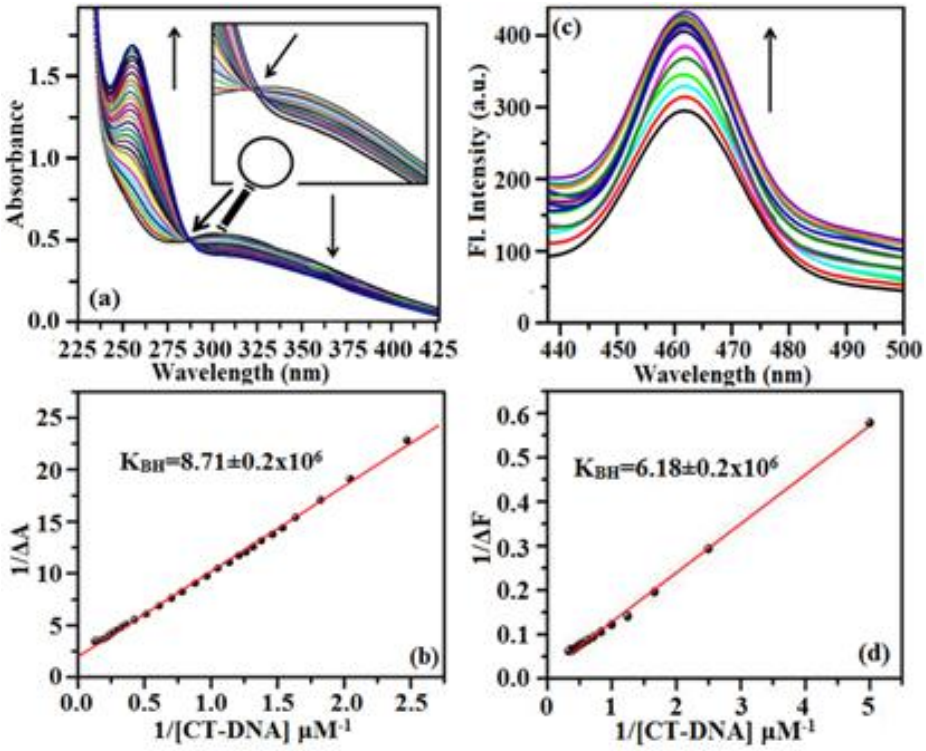

Figure 3.7. (a) Absorbance titration profile of T-$MnFe_2O_4$ NPs complex with increasing concentration of CT-DNA (molar ratio [DNA]/[NPs complex] = 0.2-2.5) (b) Modified Benesi-Hildebrand plot for the complexation of DNA with NPs from absorbance titration (c) Fluorescence titration of NPs complex with increasing concentration of CT-DNA (molar ratio [DNA]/[NPs complex] = 0.2-2.5) and (d) Modified Benesi-Hildebrand plot for the complexation of DNA with NPs from fluorescence data.

3.3.7. Ethidium Bromide Displacement Assay

In order to establish the binding mode of T-$MnFe_2O_4$ NPs with CT-DNA, the fluorimetric measurements using ethidium bromide (EB) were carried out. Ethidium bromide emits intense fluorescence in the presence of DNA due to its strong intercalation between the adjacent DNA base pairs [51,52]. This enhanced fluorescence can be quenched by the addition of a third molecule which can bind DNA by intercalative mode through displacement of EB [53,54]. The emission spectra of EB bound to DNA in the absence and presence of the T-$MnFe_2O_4$ NPs are presented in Figure 3.8.(a). The addition of T-$MnFe_2O_4$ NPs to DNA pre-treated with EB causes a gradual quenching in emission intensity, indicating that the T-$MnFe_2O_4$ NPs compete with EB in binding DNA and lead to a quenching in fluorescence intensity of EB-DNA complex system. Further, the increase in concentration of T-$MnFe_2O_4$ NPs gradually quenches the fluorescence intensity of EB-DNA complex system

which further confirms the displacement effect properly. Significant decrease in fluorescence intensity lends strong support in favour of intercalation of T-$MnFe_2O_4$ NPs into CT-DNA double helix by displacing EB. Fluorescence quenching study in presence of the T-$MnFe_2O_4$ NPs was analyzed further by Stern-Volmer equation: $I_0/I = 1 + K_{SV}$ [Q] [55]; where I_0 and I are the fluorescence intensities in the absence and presence of the quencher (T-$MnFe_2O_4$ NPs), respectively; [Q] is the concentration of the quencher, K_{SV} is the Stern-Volmer quenching constant, which is obtained from the slope of plot of I_0/I vs. [Q]. A plot of I_0/I vs. [T-$MnFe_2O_4$ NPs]/[EB-DNA] appears linear as shown in Figure 3.8.(b) and the Stern-Volmer quenching constant (K_{SV}) was found to be (6.31 ± 0.02) x 10^6 M^{-1} at 37 °C. This data is also in agreement with the value obtained by electronic spectral studies. The inset of Figure 3.8.(b) indicates the stages of T-$MnFe_2O_4$ NPs binding with the CT-DNA where clear replacement of EB from the base pairs of EB-DNA complex is presented by the T-$MnFe_2O_4$ NPs.

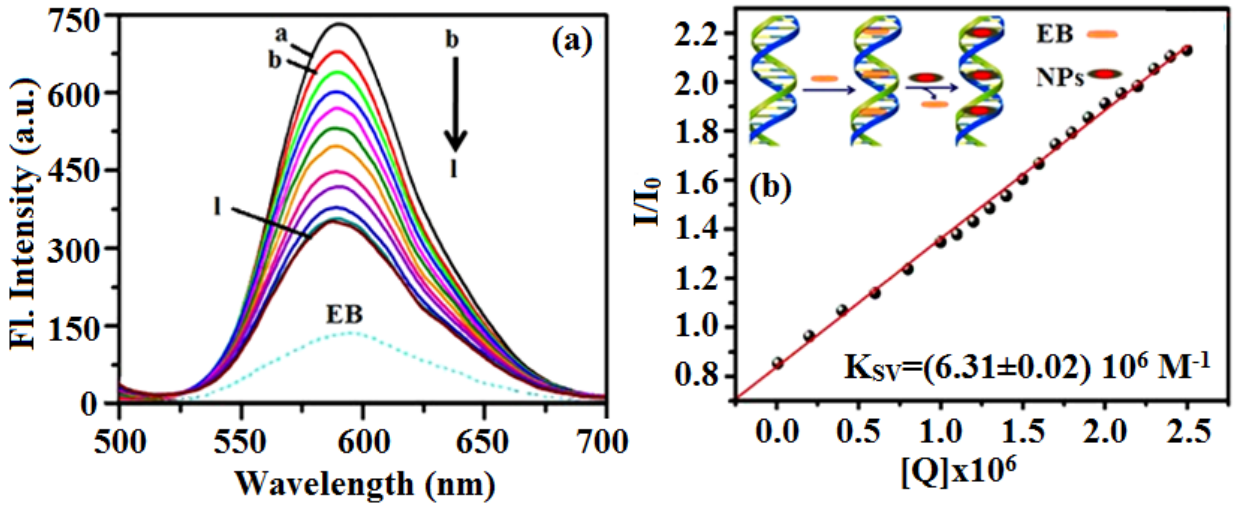

Figure 3.8. (a) Fluorescence emission spectra of the EB-DNA complex in the presence of EB of 15 mM and CT-DNA of 10 mM; (a-l) the ratio of [T-$MnFe_2O_4$ NPs]/[EB-DNA] = 0.2-2.5. Herein, the excitation wavelength = 490 nm. (b) Plot of I_0/I vs. [T-$MnFe_2O_4$ NPs]. Inset indicates the schematic diagram of EB replacement by T-$MnFe_2O_4$ NP at the base position of CT-DNA.

3.3.8. Optical Melting Study with CT-DNA

Optical melting study of CT-DNA in the presence of T-$MnFe_2O_4$ NPs can give the information about the stability of the complex when the temperature is increased, as well as the strength of interactive forces existing between T-$MnFe_2O_4$ NPs and DNA. The intercalative interaction of different types of natural or synthesized organic and metallo-

intercalators generally results due to considerable increase in melting temperature [56-58]. The melting curves of CT-DNA in the absence and presence of T-$MnFe_2O_4$ NPs are presented in Figure 3.9. Here, the thermal denaturation experiment for DNA in absence of T-$MnFe_2O_4$ NPs revealed the melting temperature (T_m) value of 65.41 (±0.2 °C) under the experimental conditions, whereas the observed T_m of DNA in the presence of T-$MnFe_2O_4$ NPs in turn increased to 82.81 (±0.2 °C). Addition of T-$MnFe_2O_4$ NPs to DNA resulted in a significant increase in melting temperature by 17.4 ± 0.2 °C which revealed that the binding of T-$MnFe_2O_4$ NPs to CT-DNA occurs through an intercalation binding mode [59].

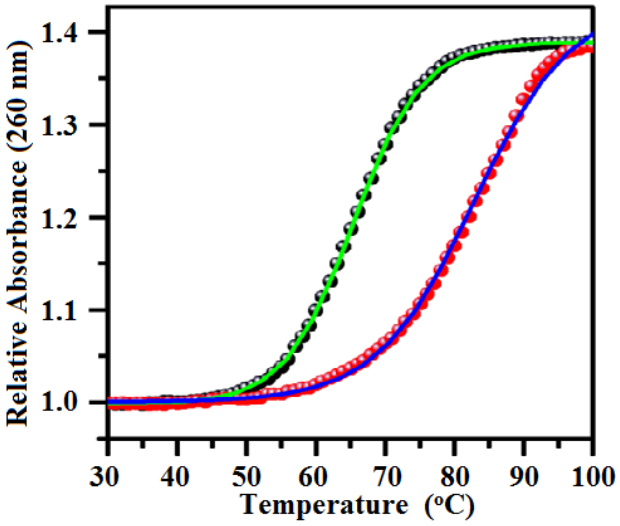

Figure 3.9. Melting profile of free CT-DNA (black curve) and in the presence of T-$MnFe_2O_4$ NPs (red curve).

3.3.9. DNA Cleavage Studies Using Agarose Gel Electrophoresis

The DNA nuclease activity of any molecule is assessed by monitoring the relaxation of supercoiled circular form I (SC) of pBR322 plasmid DNA into the nicked circular form II (NC) and the linear form III (LC). The double-stranded plasmid pBR322 DNA exists in a compact supercoiled (SC) form. The gel electropherogram reveals that if one strand is cleaved, the super coiled form will relax to produce a relatively slow moving nicked circular form, while if both the strands are cleaved, a linear form will be produced which will migrate between SC and NC [60]. The ability of the T-$MnFe_2O_4$ NPs to induce DNA cleavage was studied by gel electrophoresis using super coiled pBR322 DNA in Tris-HCl buffer (pH ~ 7). The breakage of DNA strands, induced by various concentrations of T-$MnFe_2O_4$ NPs (as shown in Figure 3.10) was quantified by the appropriate software; the results are presented in

Table 3.2. Controlled experiment suggests that untreated DNA (lane 1) has 85% form I (SC) and 15% form II (NC), whereas T-$MnFe_2O_4$ NPs induce nicking from 29 to 53% (lanes 2-5). Li and his group have demonstrated the effects of various NPs (Au, Ag, ZnO, CeO_2, Fe_2O_3, SiO_2) on DNA replication in vitro indicating their less nuclease activity than our developed T-$MnFe_2O_4$ NPs [61].

Table 3.2. Results of the cleavage of pBR322 DNA determined by gel electrophoresis study.

Lane	**Amount of T-$MnFe_2O_4$ NPs in DNA**	**Form I (% SC)**	**FormII (%NC)**	**FormIII (%LC)**
Lane 1	control DNA	85	15	0
Lane 2	DNA+T-$MnFe_2O_4$ NPs (4 µM)	71	18	11
Lane 3	DNA+T-$MnFe_2O_4$ NPs (6 µM)	65	22	13
Lane 4	DNA+T-$MnFe_2O_4$ NPs (8 µM)	53	29	18
Lane 5	DNA+T-$MnFe_2O_4$ NPs (10 µM)	47	32	21

Multifunctional magnetic-fluorescent $MnFe_2O_4$ NPs are found to be a promising biological probe for the vast area of research in nanobiotechnology. We have found that the mode of binding of T-$MnFe_2O_4$ NPs with CT-DNA exhibits intercalation interaction with the base pairs present in DNA whereas the DNA cleavage activity in presence of T-$MnFe_2O_4$ NPs indicates that the nuclease activity occurs through breakage of DNA strands which can contribute significantly to the design and development of new advanced biomedical applications such as DNA detection, gene therapy, and anticancer drug agents etc.

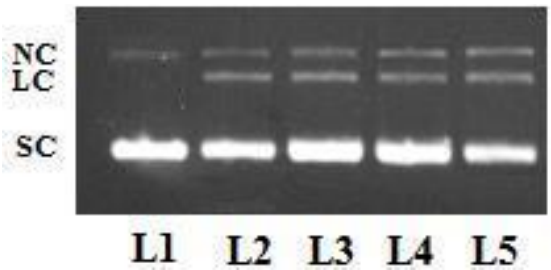

Figure 3.10. Cleavage of super coil pBR322 DNA by T-$MnFe_2O_4$ NPs in CP buffer (pH 7). Lane 1: DNA control, lanes 2-5: DNA + T-$MnFe_2O_4$ NPs (4-10 µM). SC: super coil, NC: nicked coil and LC: linear coil.

3.4. Conclusion

We have carried out surface modification of $MnFe_2O_4$ NPs with three small organic ligands, named tartrate, malate, and citrate having different number of α-hydroxy carboxylate group along with steric effect for studying the effects of surface chemistry on the optical/magnetic responses of the NPs. It is found that tartrate modified $MnFe_2O_4$ NPs show better fluorescence property comparing with malate and citrate modified $MnFe_2O_4$ NPs due to the presence of maximum number of α-hydroxy carboxylate group in tartrate ligand, indicating α-hydroxy carboxylate moiety plays key role to generate intrinsic fluorescence in functionalized $MnFe_2O_4$ NPs through activation of LMCT transitions, associated with ligand-Mn^{2+}/Fe^{3+} interactions along with d-d transition corresponding to the d-orbital energy level splitting of Fe^{3+} ions on the NP surface. Moreover, the comparative magnetic study of T-$MnFe_2O_4$, M-$MnFe_2O_4$ and C-$MnFe_2O_4$ NPs reveals that the ligand that induces largest splitting of d-orbital energy levels of surface transition metal ions results in nethermost enhancement of coercivity and upmost decrement of magnetization of bare $MnFe_2O_4$ NPs. Finally, we have utilized our developed biocompatible, multifluorescent, and magnetic probe for DNA binding and nuclease activity studies which clearly indicate that T-$MnFe_2O_4$ NPs bind and stabilize the DNA helix due to intercalation and induce cleavage on plasmid DNA. This may be taken into account for designing new biomolecular detection agents and anti-cancer drug which can open up a new door toward diverse non-invasive biomedical applications.

Bibliography

(1) C. W. Jung, P. Jacobs, Physical and Chemical Properties of Superparamagnetic Iron Oxide MR Contrast Agents: Ferumoxides, Ferumoxtran, Ferumoxsil, *Magn. Reson. Imaging* **1995**, 13, 661−674.

(2) A. Ito, H. Honda, T. Kobayashi, Cancer Immunotherapy Based on Intracellular Hyperthermia Using Magnetite Nanoparticles: a Novel Concept of "Heat-Controlled Necrosis" with Heat Shock Protein Expression, *Cancer Immunol. Immunother.* **2006**, 55, 320−328.

(3) J. Zhang, R. D. K. Misra, Magnetic Drug-targeting Carrier Encapsulated with Thermosensitive Smart Polymer: Core-shell Nanoparticle Carrier and Drug Release Response, *Acta Biomater*. **2007**, 3, 838−850.

(4) S. Khiati, D. Luvino, K. Oumzil, B. Chauffert, M. Camplo, P. Barthelemy, Nucleoside-Lipid-Based Nanoparticles for Cisplatin Delivery, *ACS Nano* **2011**, 5, 8649−8655.

(5) J. Oh, J. Lee, Salt Concentration-Induced Dehybridisation of DNA−Gold Nanoparticle Conjugate Assemblies for Diagnostic Applications, *Chem. Commun.* **2010**, 46, 6382−6384.

(6) D. Horak, M. Babic, P. Jendelová, V. Herynek, M. Trchová, Z. Pientka, E. Pollert, M. Hájek, E.-D. Syková, Mannose-Modified Iron Oxide Nanoparticles for Stem Cell Labeling, *Bioconjugate Chem.* **2007**, 18, 635−644.

(7) A. Ito, M. Kamihira, Tissue engineering using magnetite nanoparticles, *Prog Mol Biol Transl Sci*. **2011**, 104, 355−395.

(8) J. R. McCarthy, K. A. Kelly, E.Y. Sun, R. Weissleder, Targeted delivery of multifunctional magnetic nanoparticles, *Nanomed.* **2007**, 2, 153–167.

(9) M. Pal, R. Rakshit, K. Mandal, Surface Modification of $MnFe_2O_4$ Nanoparticles to Impart IntrinsicMultiple Fluorescence and Novel Photocatalytic Properties, *ACS Appl. Mater. Interfaces* **2014**, 6, 4903−4910.

(10) S. Cho, J. W. Jang, S. H. Jung, B. R. Lee, E. Oh, K. H. Lee, Precursor Effects of Citric Acid and Citrates on ZnO Crystal Formation, *Langmuir* **2009**, 25, 3825–3831.

(11) L. Zhang, J. Q. Wang, J. Li, S. Zhang, Z. Jiang, J. Zhou, J. Cheng, T. Hu, W. Yan, X. Wei, Z. Wu, Regulation of Magnetic Behavior and Electronic Configuration in Mn-Doped ZnO Nanorods through Surface Modifications, *Chem. Mater.* **2012**, 24, 1676–1681.

(12) V. I. Shubayev, T. R. Pisanic, S. H. Jin, Magnetic Nanoparticles for Theragnostics, *Adv. Drug Delivey. Rev.* **2009**, 61, 467−477.

(13) M. De, P. S. Ghosh, V.M. Rotello, Applications of Nanoparticles in Biology, *Adv. Mater*. **2008**, 20, 4225–4241.

(14) L. H. Reddy, J. L. Arias, J. Nicolas, P. Couvreur, Magnetic Nanoparticles: Design and Characterization, Toxicity and Biocompatibility, Pharmaceutical and Biomedical Applications, *Chem. Rev.* **2012**, 112, 5818–5878.

(15) W. Y. Li, J. G. Xu, X. Q. Guo, Q. Z. Zhu, Y. B. Zhao, A Novel Fluorometric Method For DNA and RNA Determination, *Anal. Lett.* **1997**, 30, 527–536.

(16) C. V. Kumar, E. H. Asuncion, DNA binding studies and site selective fluorescence sensitization of an anthryl probe, *J. Am. Chem. Soc*. **1993**, 115, 8547–8553.

(17) M. Wu, W. Wu, X. Lian, X. Lin, Z. Xie, Molecular and Biomolecular Spectroscopy, *Spectrochim. Acta Part A* **2008**, 71, 1333–1340.

(18) H. C. Borresen, *Acta Chem. Scand*. **1963**, 17, 921.

(19) S. Udenfriend, P. Zaltzman, Fluorescence characteristics of purines, pyrimidines, and their derivatives: Measurement of guanine in nucleic acid hydrolyzates, *Anal. Biochem*. **1962**, 3, 49–59.

(20) B. Qiu, L. Guo, W. Wang, G. Chen, Synthesis of a novel fluorescent probe useful for DNA detection, *Biosens. Bioelectron.* **2007,** 22, 2629–2635.

(21) G. W. Musheush, G. Yonuschot, *J. Lumin*. **1983**, 28, 233.

(22) J. B. Le Pecq, C. Paoletti, *Anal. Biochem*. **1966**, 14, 100.

(23) M. Khorasani-Motlagh, M. Noroozifar, S. Mirkazehi-Rigi, Fluorescence and DNA-binding properties of neodymium(III) and praseodymium(III) complexes containing 1,10-phenanthroline, *Spectrochim. Acta Part A* **2011**, 79, 978–984.

(24) B. Wang, Z. Y. Yang, Q.Wang, T. Cai, P. Crewdson, Synthesis, characterization, cytotoxic activities, and DNA-binding properties of the La(III) complex with Naringenin Schiff-base, *Bioorg. Med. Chem*. **2006**, 14, 1880–1888.

(25) C. Chen, J. Zhang, Y. Zhang, Z. Yang, H. Wu, G. Pan, Y. Bai, Gadolinium(III) and dysprosium(III) complexes with a Schiff base bis(*N*-salicylidene)-3-oxapentane-1,5-diamine: synthesis, characterization, antioxidation, and DNA-binding studies, *J. Coord. Chem*. **2015**, 68, 1054–1071.

(26) X. Zhang, M. R. Servos, J. Liu, Fast pH-Assisted Functionalization of Silver Nanoparticles with Monothiolated DNA, *Chem. Commun.* **2012**, 48, 10114–10116.

(27) H. Li, L. Rothberg, Colorimetric Detection of DNA Sequences Based on Electrostatic Interactions with Unmodified Gold Nanoparticles, *Proc. Natl. Acad. Sci. U. S. A.* **2004**, 101, 14036–14039.

(28) S. Pramanik, S. Chatterjee, A. Saha, P. S. Devi, G. S. Kumar, Unraveling the Interaction of Silver Nanoparticles with Mammalian and Bacterial DNA, *J Phys Chem B* **2016**, 120, 5313–5324.

(29) H. An, Q. Liu, Q. Ji, B. Jin, DNA binding and aggregation by carbon nanoparticles, *Biochemical and Biophysical Research Communications* **2010**, 393, 571–576.

(30) Z. Heger, N. Cernei, S. Krizkova, M. Masarik, P. Kopel, P. Hodek, O. Zitka, V. Adam, R. Kizek, Paramagnetic Nanoparticles as a Platform for FRET-Based Sarcosine Picomolar Detection, *Scientific Reports* **2015**, 5, 8868.

(31) S. Sun, H. Zeng, D. B. Robinson, S. Raoux, P. M. Rice, S. X. Wang, G. Li, Monodisperse MFe_2O_4 (M = Fe, Co, Mn) nanoparticles, *J. Am. Chem. Soc.* **2004**, 126, 273–279.

(32) M. Thomas, R. F. Moreno, L. L. Tilzer, DNA extraction with organic solvents in gel barrier tubes, *Nucleic acids research* **1989**, 17, 5411.

(33) R. Sinha, M. M. Islam, K. Bhadra, G. S. Kumar, A. Banerjee, M. Maiti, The binding of DNA intercalating and non-intercalating compounds to A-form and protonated form of poly(rC).poly(rG): spectroscopic and viscometric study, *Bioorg. Med. Chem.* **2006**, 14, 800–814.

(34) K. Bhadra, M. Maiti, G. S. Kumar, Molecular recognition of DNA by small molecules: AT base pair specific intercalative binding of cytotoxic plant alkaloid palmatine, *Biochim. Biophys. Acta* **2007**, 1770, 1071–1080.

(35) H. A. Benesi, J. H. Hildebrand, A Spectrophotometric Investigation of the Interaction of Iodine with Aromatic Hydrocarbons, *J. Am. Chem. Soc.* **1949**, 71, 2703–2707.

(36) Y. Fang, G. Ning, D. Hu, J. Lu, Synthesis and solvent-sensitive fluorescence properties of a novel surface-functionalized chitosan film: potential materials for reversible information storage, *J. Photoch. Photobio. A.* **2000**, 135, 141–145.

(37) S. C. Ray, A. Saha, N. R. Jana, R. Sarkar, Fluorescent Carbon Nanoparticles: Synthesis, Characterization, and Bioimaging Application, *J. Phys. Chem. C* **2009**, 113, 18546–18551.

(38) M. Pal, R. Rakshit, K. Mandal, Facile functionalization of Fe_2O_3 nanoparticles to induce inherent photoluminescence and excellent photocatalytic activity, *Appl. Phys. Lett.* **2014**, 104, 233110.

(39) C. Chen, S. M. Bellows, P. L. Holland, Tuning steric and electronic effects in transition-metal β-diketiminate complexes, *Dalton Trans*. **2015**, 44, 16654–16670.

(40) X. S. Xu, T. V. Brinzari, S. Lee, Y. H. Chu, L. W. Martin, A. Kumar, S. McGill, R. C. Rai, R. Ramesh, V. Gopalan, S. W. Cheong, J. L. Musfeldt, Optical properties and magnetochromism in multiferroic $BiFeO_3$, *Phys. Rev. B* **2009**, 79, 134425.

(41) J. H. Jung, M. Matsubara, T. Arima, J. P. He, Y. Kaneko, Y. Tokura, Optical Magnetoelectric Effect in the Polar $GaFeO_3$ Ferrimagnet, *Phys. Rev. Lett*. **2004**, 93, 037403.

(42) N. Kaneko, M. Kaneko, H. Takahashi, Infrared and Raman spectra and vibrational assignment of some metal tartrates, *Spectrochim. Acta Part A* **1984**, 40, 33–42.

(43) V. Ramakrishnan, J. M. T. Maroor, IR and Raman studies of gel grown manganese tartrate, *Infrared Phys.* **1988**, 28, 201–204.

(44) F. Bodker, S. Morup, S. Linderoth, Surface effects in metallic iron nanoparticles, *Phys. Rev. Lett*. **1994**, 72, 282–285.

(45) C. R. Vestal, Z. J. Zhang, Effects of surface coordination chemistry on the magnetic properties of $MnFe_2O_4$ spinel ferrite nanoparticles, *J. Am. Chem. Soc.* **2003**, 125, 9828–9833.

(46) B. N. Figgis, M. A. Hitchman, Ligand Field Theory and Its Applications, *Wiley-VCH, New York*, **2000**.

(47) Z. Shan, Z. Zhou, H. Chen, Z. Zhang, Y. Zhou, A. Wen, K. D Oakes, M. R. Servos, PCR-ready human DNA extraction from urine samples using magnetic nanoparticles, *J. Chromatogr. B* **2012**, 63, 881–882.

(48) S. W. Gersting, U. Schillinger, J. Lausier, P. Nicklaus, C. Rudolph, C. Plank, D. Reinhardt, J.J. Rosenecker, *Gene Med*. **2004**, 6, 913.

(49) T. Biver, N. Eltugral, A. Pucci, G. Ruggeri, A. Schena, F. Secco, M. Venturini, Synthesis, characterization, DNA interaction and potential applications of gold nanoparticles functionalized with Acridine Orange fluorophores, *Dalton Trans.* **2011**, 40, 4190–4199.

(50) L. Bouffier, H. H. P. Yiu, M. J. Rosseinsky, Chemical Grafting of a DNA Intercalator Probe onto Functional Iron Oxide Nanoparticles: A Physicochemical Study, *Langmuir* **2011**, 27, 6185–6192.

(51) J. Olmsted, D. R. Kearns, Mechanism of ethidium bromide fluorescence enhancement on binding to nucleic acids, *Biochemistry* **1977**, 16, 3647–3654.

(52) D. E. Graves, L. M. Velea, Intercalative binding of small molecules to nucleic acids, *Curr. Org. Chem*. **2000**, 4, 915–929.

(53) D. L. Boger, B. E. Fink, S. R. Brunette, W. C. Tse, M. P. Hedric, A simple, high-resolution method for establishing DNA binding affinity and sequence selectivity, *J. Am. Chem. Soc*. **2001**, 123, 5878–5891.

(54) W. K. Mudasir, E. T. Wahyuni, N. Yoshioka, H. Inoue, Salt-dependent binding of iron(II) mixed-ligand complexes containing 1,10-phenanthroline and dipyrido[3,2-*a*:2′,3′-*c*]phenazine to calf thymus DNA, *Biophys. Chem*. **2006**, 121, 121 44–50.

(55) T. Biver, F. Secco, M. R. Tine, M. Venturini, Kinetics and equilibria for the formation of a new DNA metal-intercalator: the cyclic polyamine Neotrien/copper(II) complex, *J. Inorg. Biochem*. **2004**, 98, 33–40.

(56) N. C. Harris, C. -H. Kiang, Defects Can Increase the Melting Temperature of DNA−Nanoparticle Assemblies, *J. Phys. Chem. B* **2006**, 110, 16393–16396.

(57) D. Murphy, R. Eritja, G. Redmond, Monitoring denaturation behaviour and comparative stability of DNA triple helices using oligonucleotide–gold nanoparticle conjugates, *Nucleic Acids Research* **2004**, 32, 65.

(58) D. Bhowmik, G. Fiorillo, P. Lombardi, G. S. Kumar, Recognition of human telomeric G-quadruplex DNA by berberine analogs: effect of substitution at the 9 and 13 positions of the isoquinoline moiety, *J. Mol. Recognit.* **2015**, 28, 722–730.

(59) A. Basu, P. Jaisankar, G. S. Kumar, Synthesis of novel 9-*O*-*N*-aryl/aryl–alkyl amino carbonyl methyl substituted berberine analogs and evaluation of DNA binding aspects, *Bioorg. Med. Chem*. **2012**, 20, 2498–2505.

(60) R. Gaur, L. Mishra, Synthesis and Characterization of Ru(II)–DMSO–Cl–Chalcone Complexes: DNA Binding, Nuclease, and Topoisomerase II Inhibitory Activity, *Inorg. Chem*. **2012**, 51, 3059−3070.

(61) K. Li, X. Zhao, B. K. Hammer, S. Du, Y. Chen, Nanoparticles Inhibit DNA Replication by Binding to DNA: Modeling and Experimental Validation, *ACS nano* **2013**, 7, 9664–9674.

Chapter 4

Citrate Modified $MnFe_2O_4$ Nanoparticles: Optical Property, Protein Adsorption and Catalytic Activity

In this chapter we have demonstrated chemical functionalization strategy of $MnFe_2O_4$ nanoparticles with a small organic ligand (citrate) to induce inherent fluorescence property, protein absorption ability and catalytic activity.

4. Surface Engineered Magneto-Fluorescent $MnFe_2O_4$ nanoparticles in the Realm of Biomedical Applications

4.1. Preamble

The tremendous application of 3d transition metal oxide based magnetic nanoparticles (MNPs) in diverse fields like energy storage [1], catalysis [2], sensing [3], they have grabbed a wide research interest for long. Due to biocompatibility, non-toxicity, chemical and mechanical stability in addition to control transport property, they rise their opportunities in the biomedical fields also. However, insolubility and agglomerative nature of these MNPs in aqueous medium restrict their application in biomedical field. Proper functionalization and/or surface coating of MNPs with biocompatible ligand helps to overcome these problems and find tremendous application as a magnetic resonance imaging (MRI) contrast and hyperthermia agents and drug delivery vehicles [4–7].

In recent years, the development of magneto-fluorescent composite nanoparticles (NPs) has attracted immense attention to the current researchers due to an increasing demand of nanomaterial based molecular markers for tumor diagnostics [8]. The optical property, in addition to magnetism of magneto-fluorescent NPs, provides the capability of remote vectorization and sensitive detection through light. The usual architecture consists of core-shell structures where an inorganic magnetic core is surrounded by fluorescent units. However, main limitations of these systems generally rely on spatial dilution of the active units, photobleaching of fluorescent dye in addition to their non-biocompatibility.

Therefore, it was necessary to develop an approach to make a well dispersed, water soluble MNPs with intrinsic fluorescence for their application in biological imaging. Superparamagnetic materials especially with intrinsic multifluorescence, have drawn gamut of attention in the use of MRI. Beside the magnetic saturation of the MRI particles, the bio compatibility of the material is of pre-eminent importance. It majorly depends on the size, shape and protein absorption. Reportedly, particles of greater than diameter 200 nm are generally taken up by the macrophages resulting in decrease in blood circulation time while particles with diameters ~10 nm are removed through renal clearance, suggesting that the particles ranging from 10–200 nm are suitable for MRI application. After the intrusion of the MRI nanoparticles, blood, containing thousands of different proteins, is the first physiological

environment they go an interaction for. Thus, the absorption of abandoned proteins on the nanomaterials (NMs) is very like to take place which in turn reduces the efficiency of the said material. Surface functionalization of the nanoparticles plays a very significant role here to reduce the protein absorption on the particle surface. Reportedly, ferrite NPs are found to be a good catalytic agent for selective chemical reactions, both economically and environmentally benign in terms of their low cost, great stability, high activity, easy preparation method, and controlled separation technique using an external magnetic field [9–12].

Considering the aforementioned advantageous aspects of ferrite nanostructures, we have focused on the synthesis and surface functionalization of $MnFe_2O_4$ NPs for the generation of intrinsic fluorescence. Interestingly, citrate modified $MnFe_2O_4$ NPs found to exhibit multicolor fluorescence at room temperature starting from blue, green to red. A detailed explanation regarding the occurrence of aforesaid is given in the light of ligand-to-metal charge transfer (LMCT) and Jahn-Teller (J-T) distortion concept. The citrate modification on $MnFe_2O_4$ NPs is found to be beneficial for the MRI application due to the less protein adsorption on its surface than the pristine $MnFe_2O_4$. In addition, we have inspected the catalytic efficiency of C-$MnFe_2O_4$ towards the methylene blue (MB) and bilirubin (BR) for wastewater as well as therapeutic treatment.

4.2. Experimental Section

4.2.1. Materials Used

Iron(III) acetylacetonate, manganese(II) acetate, oleylamine, sodium hydroxide, Na_2HPO_4, NaH_2PO_4 and human serum albumin (HSA) were purchased from Sigma Aldrich whereas oleic acid, cetyl alcohol, ethanol, trisodium citrate dihydrate and the solvent diphenyl ether were obtained from Loba Chemie. All the reagents are of analytical grade and used without further modification.

4.2.2. Synthesis and Functionalization of $MnFe_2O_4$ Nanoparticles

Synthesis of $MnFe_2O_4$ NPs following a previous report [13] has been discussed thoroughly in the experimental section of chapter 3. The as-prepared NPs were then cyclomixed with 0.5 M Na-citrate solution for 12 h at room temperature, resulted a pale yellow colored solution containing citrate functionalized $MnFe_2O_4$ (C-$MnFe_2O_4$), named as fl. modified C-$MnFe_2O_4$ NPs. In order to remove the nonsolubilized larger $MnFe_2O_4$ NPs, it is passed through a

syringe filter of 0.22 μm diameter. To manifest the fluorescence property of the functionalized NPs, continuous heating was performed for 15 h at 70 °C.

4.2.3. Human Serum Albumin (HSA)

HSA is the primary protein present in human blood plasma which constitutes about half of serum protein. It binds to water, cations (such as Ca^{2+}, Na^{+} and K^{+}), fatty acids, hormones, bilirubin, thyroxine (T4) etc. Albumin transports hormones, fatty acids, buffers pH and maintains oncotic pressure. Human albumin is a small globular protein (molecular weight: 66.5 kDa), consisting of a single chain of 585 amino acids organized in three repeated homolog domains (sites I, II and III). Each domain comprises two separate sub-domains (A and B) which are shown in Figure 4.1.

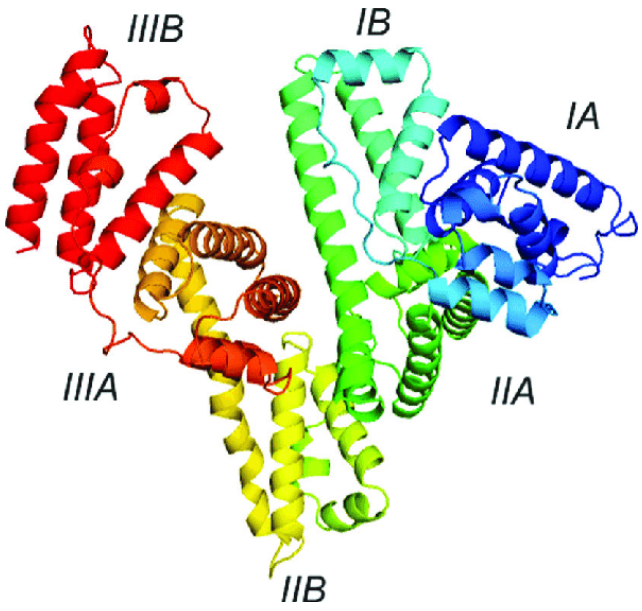

Figure 4.1. The ribbon model of the HSA.

4.2.3.1. HSA Adsorption

To deploy the superparamagnetic and fluorescent ferrite materials for MRI application, the preliminary protein adsorption test was performed using HSA. 0.1 g of HSA was dissolved in distilled and deionized water under mild shaking and stored at 4 °C. Both $MnFe_2O_4$ and C-$MnFe_2O_4$ NPs at varying concentrations (50, 100, 200, 250, 500, 1000 μg/ml) were dispersed into 15 ml of PBS at a fixed temperature of 37 °C and a shaking rate of 150 rpm. 5 ml of the prepared HSA solution was added to the solutions containing different concentration of NPs

as mentioned above. For each concentration of particle three batches of experiments were performed. After the incubation for 2 h, the mixed solutions were centrifuged and supernatants were collected. The concentrations of residual HSA were determined from the absorbance of the mentioned upper clear solutions at 278 nm. HSA adsorbed on nanoparticles were calculated using the equation:

$$q = (C_i – C_f)\ V/m$$

where 'C_i' and 'C_f' are the initial HSA and final HSA concentrations in solutions before and after HSA adsorption, respectively; 'V' is the total solution volume (20 ml); 'm' is the weight of NPs added into the solution.

4.2.4. Photocatalysis

For photocatalytic study of MB, an 8 W UV lamp and a 100 W incandescent light bulb were purchased from Philips as the UV and visible light sources respectively. An aqueous solution of MB (5 μM) and C-$MnFe_2O_4$ NPs (50 μL, containing 0.60 mg NPs) were mixed homogeneously for 1 h in a quartz cuvette in the dark, maintaining pH ~ 3 of the solution. Then, the cuvette was kept approximately 2 cm away from the light source and the absorbance of MB in the reaction mixture was recorded periodically using the UV-vis spectrophotometer. Similarly, for studying the catalysis of BR, C-$MnFe_2O_4$ NPs (50 μL, containing 0.60 mg NPs) were added to a 13.4 μM aqueous solution of BR and kept it in the dark in a quartz cuvette maintaining the pH ~ 7 under the stirring condition. The absorbance of BR in the reaction mixture was measured time to time.

4.3. Results and Discussion

The crystallographic study of the prepared materials is presented in Figure 4.2 where all the diffraction peaks match the cubic inverse spinel structure of $MnFe_2O_4$ NPs [14].

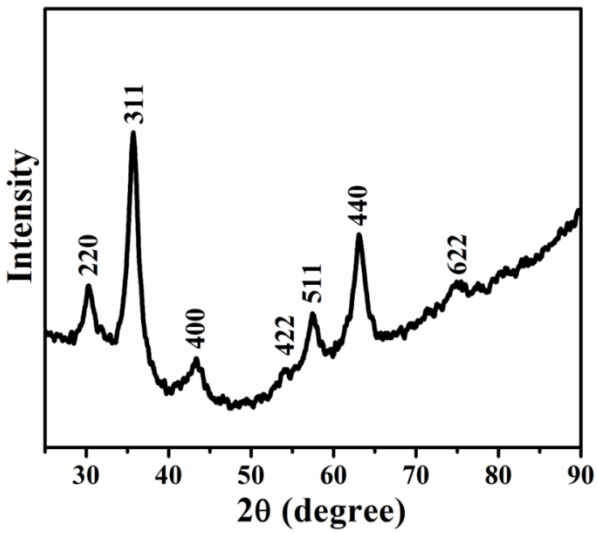

Figure 4.2. XRD pattern of $MnFe_2O_4$ nanoparticles.

The well dispersity of $MnFe_2O_4$ NPs is seen in TEM micrograph (Figure 4.3.(a)). In Figure 4.3.(b), the high resolution TEM (HRTEM) image shows the interplanar distance between the lattice fringes is 0.253 nm, upon calculation which corresponds to the distance between the (311) planes of $MnFe_2O_4$ crystal lattice. The corresponding selected area electron diffraction (SAED) pattern in inset of Figure 4.3.(b) confirms the polycrystallinity of as-prepared NPs.

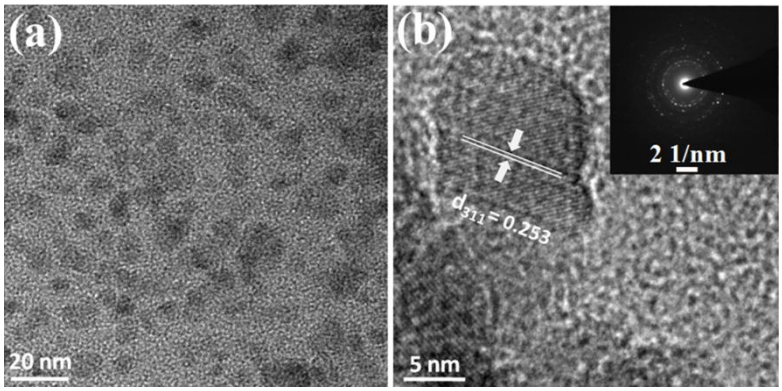

Figure 4.3. (a) TEM image of well dispersed $MnFe_2O_4$ NPs of the range of 10–12 nm, (b) lattice fringes (SAED inset) of the nanocrystals.

The EDX analysis of $MnFe_2O_4$ NPs as shown in Figure 4.4.(a) confirms the presence of manganese (Mn), iron (Fe) and oxygen (O). The presence of the elemental fingerprints of Mn, Fe and O are also obtained from EDAX mappings are shown in Figure 4.4.(b-e).

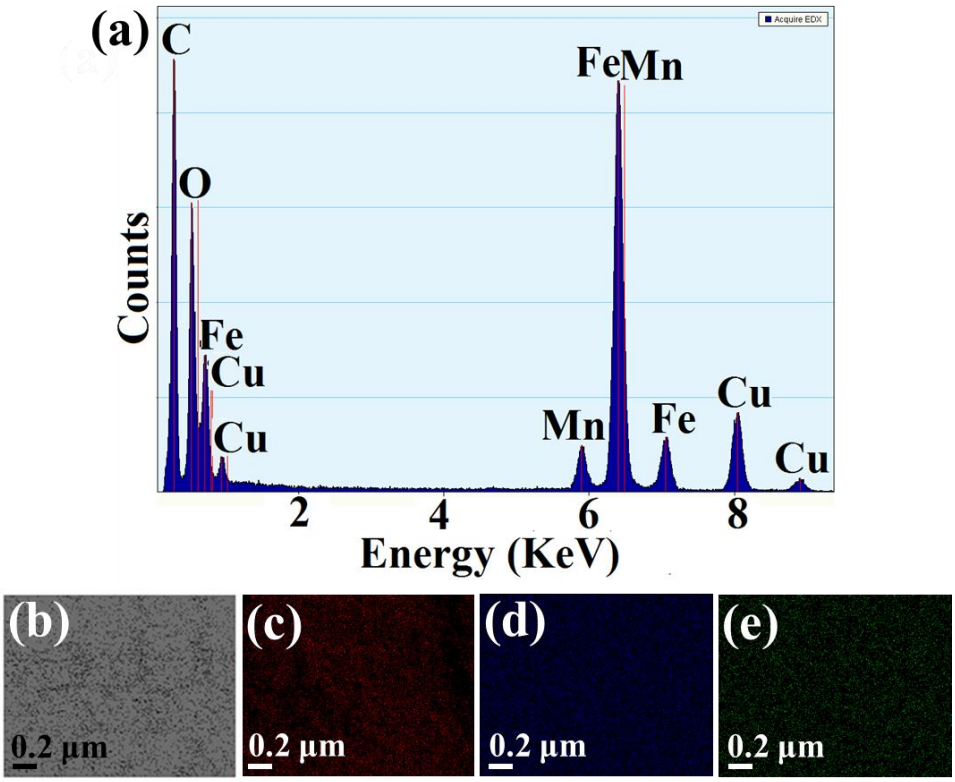

Figure 4.4. (a) EDAX spectrum indicating the presence of Mn, Fe and O. (b) SEM microghaph of the $MnFe_2O_4$ nanoparticles for the EDAX elemental mapping of O, Fe and Mn, shown in (c), (d) and (e) respectively.

Figure 4.5 shows the UV-vis absorption spectra of citrate, C-$MnFe_2O_4$, and fl. Mod. C-$MnFe_2O_4$ NPs, indicating the presence of absorption band in C-$MnFe_2O_4$ NPs which is completely absent in sole citrate ligand. To enhance the intensity of the absorption spectra of C-$MnFe_2O_4$ NPs, it is further modified through heat treatment at 70 ºC for 15 h at pH ~ 12. At this pH all the –COOH groups convert into $–COO^-$ group. The fl. Modified C-$MnFe_2O_4$ NPs is found to exhibit absorption peaks at 310, 425, and 454 nm, indicating a significant variation in the electronic structure of the NPs surface upon modification with citrate ligand.

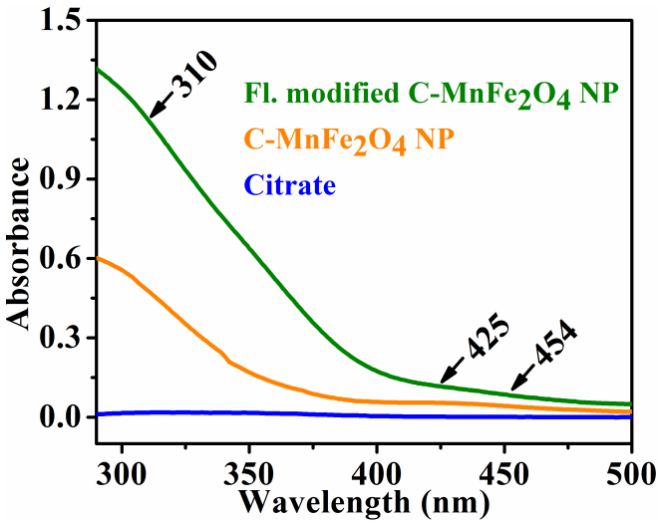

Figure 4.5. UV-vis absorption spectra of citrate, C-$MnFe_2O_4$, and fl. Mod. C-$MnFe_2O_4$ NPs.

Figure 4.6.(a) shows the normalized multicolor fluorescence emission spectra acquired upon exciting the fl. Mod. C-$MnFe_2O_4$ NPs at λ_{ex} = 310, 425, 454, and 494 nm which give rise to fluorescence at λ_{em} = 413, 495, 516 and 595 nm respectively whereas Figure 4.6.(b) shows the corresponding excitation spectra. The observed fluorescence at λ_{em} = 413 nm, may be attributed to the ligand to metal charge transfer (LMCT) transition where charge is transferring from the highest occupied energy level of citrate to the lowest unoccupied energy levels of $Mn^{2+/3+}$ or Fe^{3+} metal ion centers on the NPs' surface [15]. Origin of additional three peaks (495, 516, and 595 nm) might be due to the d-d transitions involving $Mn^{2+/3+}$ or Fe^{3+} metal ions in the fl. Mod. C-$MnFe_2O_4$ NPs surface. However, the possibility of d-d transitions in the case of both Fe^{3+} (d^5) and Mn^{2+} (d^5) ions is forbidden for Laporte and spin according to the selection rule of fundamental atomic spectroscopy [16,17]. In general, 3+ oxidation state of Mn ion is absent in $MnFe_2O_4$ NPs, however, under pH ~ 12, it is possible to form 3+ oxidation state of Mn ion [18]. As Mn^{3+} is d^4 system and in the high spin octahedral field, there is two-fold degeneracy in e_g level but degeneracy could be lost due to Jahn-Teller (J-T) distortion. Therefore, these three bands (495, 516, and 595 nm) can be explained on the basis of spectroscopic term symbols, involving the transitions of $5B_{1g} \rightarrow 5E_g$, $5B_{1g} \rightarrow 5B_{2g}$ and $5B_{1g} \rightarrow 5A_{1g}$ respectively [19]. The fluorescence images of fl. Mod. C-$MnFe_2O_4$ NPs are shown in Fig. 4.6.(c)–(e), indicating fluorescent colors such as blue, green and red upon exciting the NPs using proper filters.

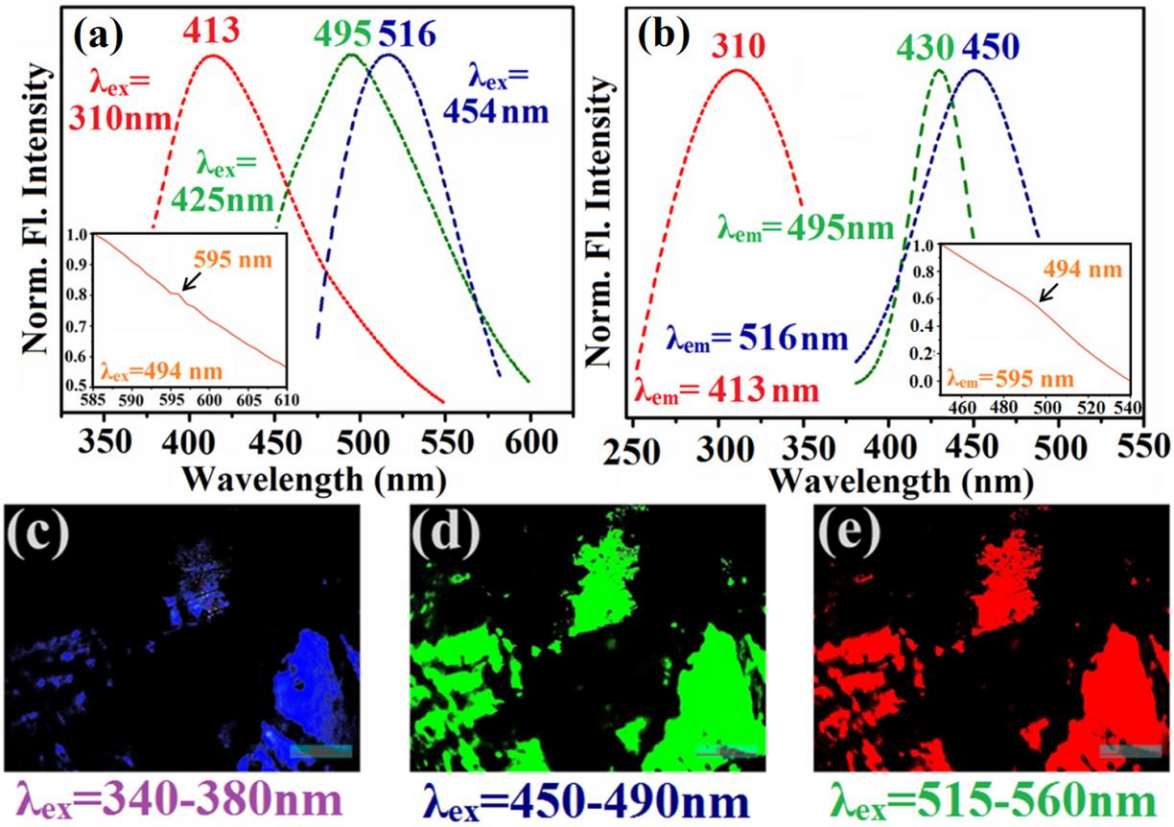

Figure 4.6. (a) Normalized steady-state fluorescence emission spectra at four different excitation wavelengths of 310, 425, 454, and 494 nm, (b) fluorescence excitation spectra at four different emission wavelengths of 413, 495, 516, and 595 nm of fl. Mod. C-$MnFe_2O_4$ NPs. Fluorescence microscopic images of the same NPs powder under (c) UV (d) blue and (e) green light irradiation. The scale bars in all the images are 500 μm.

We performed the comparative FTIR study of bare $MnFe_2O_4$, C-$MnFe_2O_4$ NPs along with Na-citrate ligand to confirm the attachment of the ligand to the NPs. As shown in Figure 4.7, for trisodium citrate, two strong characteristic peaks at 1590 and 1391 cm^{-1} correspond to the symmetric and asymmetric stretching of carboxylate group (COO^{-}) respectively and a peak at 3400 cm^{-1} is due to the stretching vibration of hydroxyl group (OH) [20,21]. The peak at 617 cm^{-1} proves the presence of alkyl group of citrate. All these different peaks are perturbed significantly for C-$MnFe_2O_4$, which imply the attachment of citrate to the $MnFe_2O_4$ NPs.

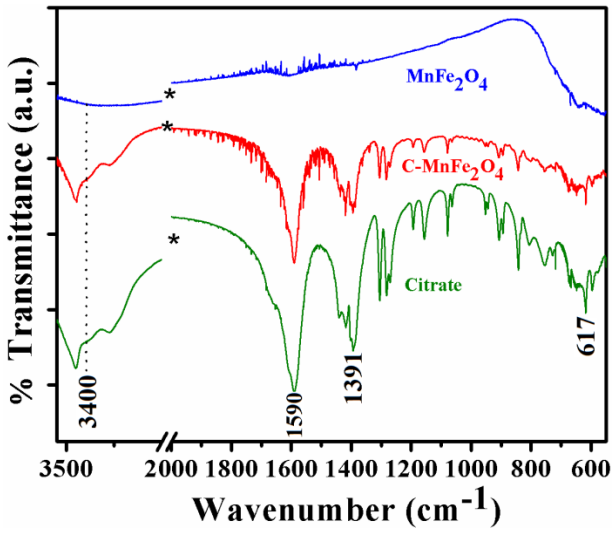

Figure 4.7. FTIR spectra of $MnFe_2O_4$ NPs, C-$MnFe_2O_4$ and citrate.

To study the effect of ligand on the magnetic properties of bare $MnFe_2O_4$ NPs, we measured M-H curve of $MnFe_2O_4$ as well as C-$MnFe_2O_4$ NPs at room temperature. The inset of Figure 4.8 indicates super paramagnetic nature of bare $MnFe_2O_4$ NPs. The saturation magnetization of bare $MnFe_2O_4$ is 28 emu/gm. Superparamagnetic natures remained unchanged in case of C-$MnFe_2O_4$ NPs with a huge decrease in saturation magnetization (0.14 emu/gm) due to LMCT, leading to reduction in the numbers of unpaired d-electrons of the surface ions [22].

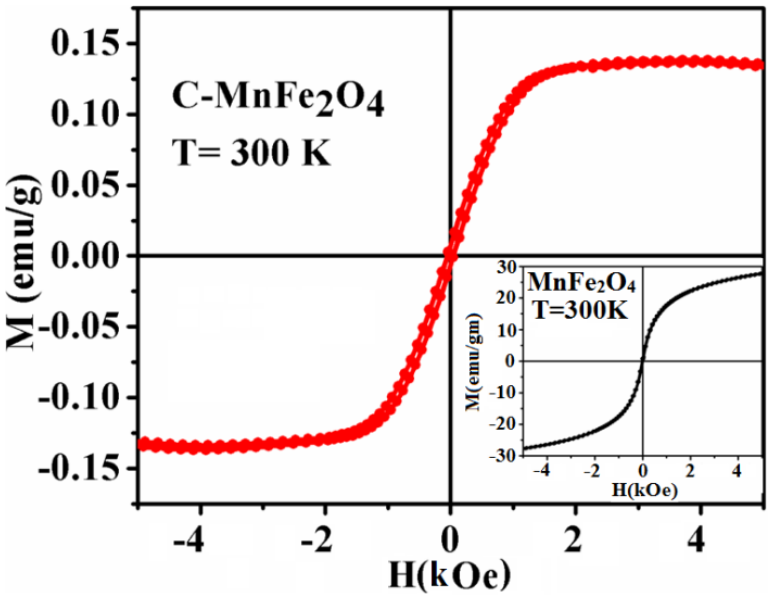

Figure 4.8. Field dependent magnetization (M-H) at room temperature of C-$MnFe_2O_4$ NPs. Inset shows M-H plot of bare $MnFe_2O_4$ NPs.

Figure 4.9.(a) and (b) show the representative UV-vis absorption spectra of HSA in the supernatant of different concentrations (batch 1) of $MnFe_2O_4$ NPs and C-$MnFe_2O_4$ NPs respectively. For the $MnFe_2O_4$ NPs, lower absorbance peak is observed comparing with C-$MnFe_2O_4$ NPs. That means HSA is more adsorbed on the surface of bare $MnFe_2O_4$ NPs than the surface of C-$MnFe_2O_4$ NPs. The same results are observed for batch II and III of samples which are provided in Figure 4.9.(c, d) and (e, f) respectively.

The adsorbed amount of HSA on both $MnFe_2O_4$ NPs and C-$MnFe_2O_4$ NPs with of different concentrations is represented in Figure 4.10.(a) and (b) respectively which also reveals that the HSA adsorption is more for $MnFe_2O_4$ NPs comparing to C-$MnFe_2O_4$ NPs. A linear increase of the amount of adsorbed HSA is found with the increase in particle concentration. Comparing the amount of adsorbed HSA for both $MnFe_2O_4$ and C-$MnFe_2O_4$ NPs, it is found that the amount of adsorbed HSA is reduced by three times in citrate functionalized $MnFe_2O_4$ than the pristine $MnFe_2O_4$ NPs (Figure 4.11). The bulk citrate ligand plays a very significant role to reduce the protein adsorption on the surface of C-$MnFe_2O_4$ NPs exercising its steric hindrance.

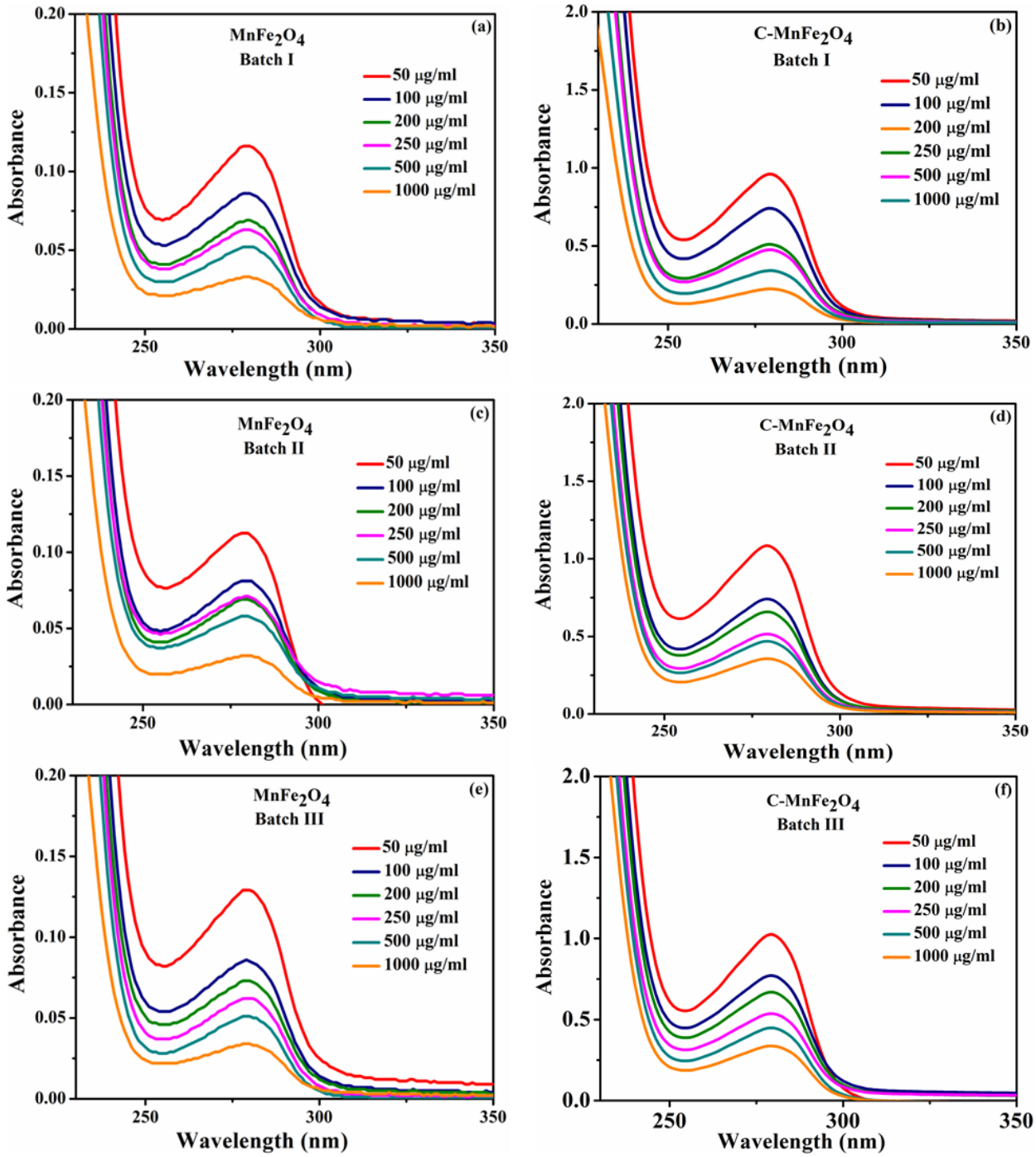

Figure 4.9. UV-vis absorption spectra of HSA in the supernatant solutions of (a, c, e) $MnFe_2O_4$ and (b, d, f) C-$MnFe_2O_4$ for batch I, II, III respectively where the concentration of the particles are of 50, 100, 200, 250, 500 and 1000 µg/ml.

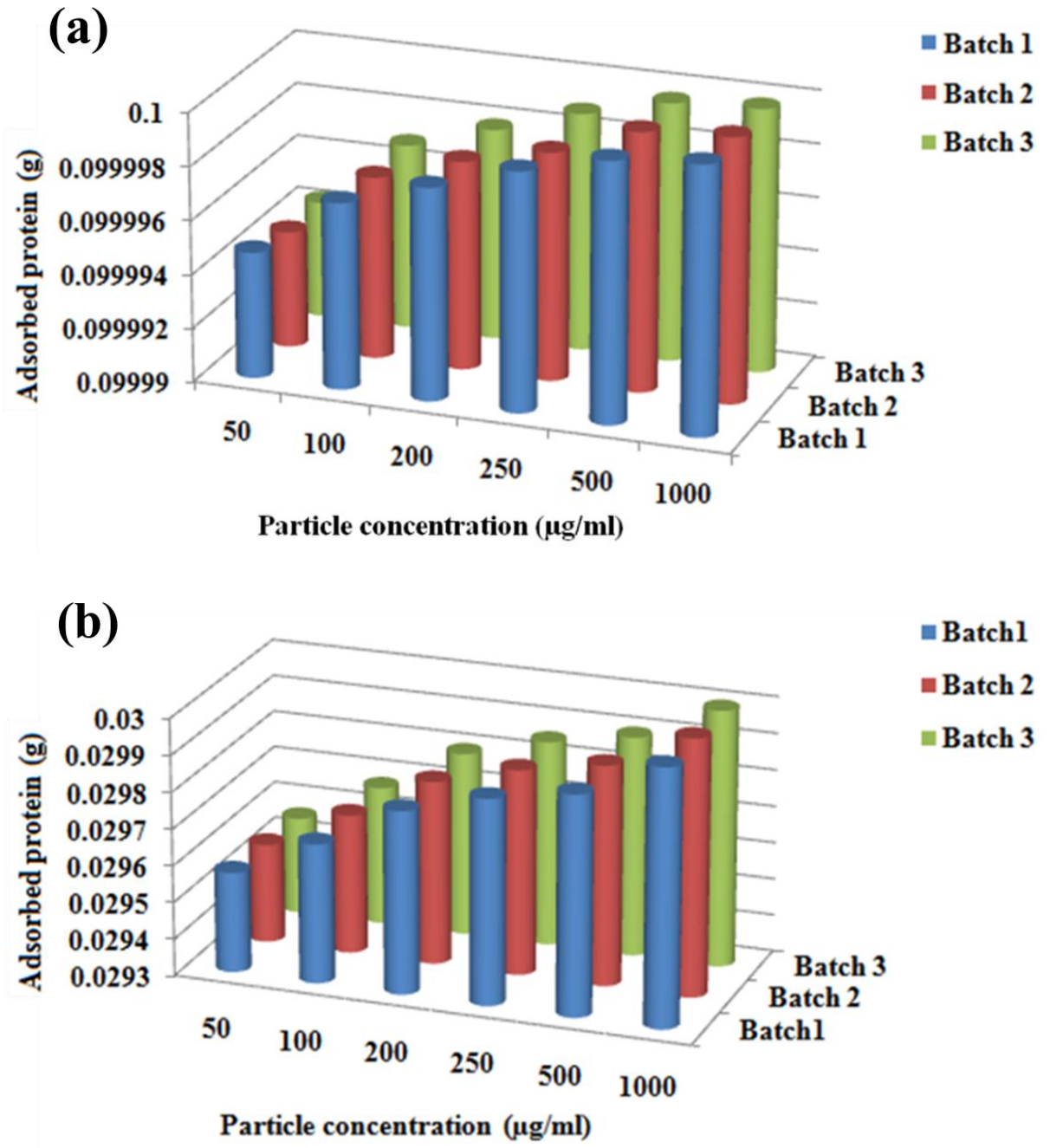

Figure 4.10. (a) and (b) represent the amount of adsorbed HSA on the surface of $MnFe_2O_4$ and C-$MnFe_2O_4$ NPs of different concentrations.

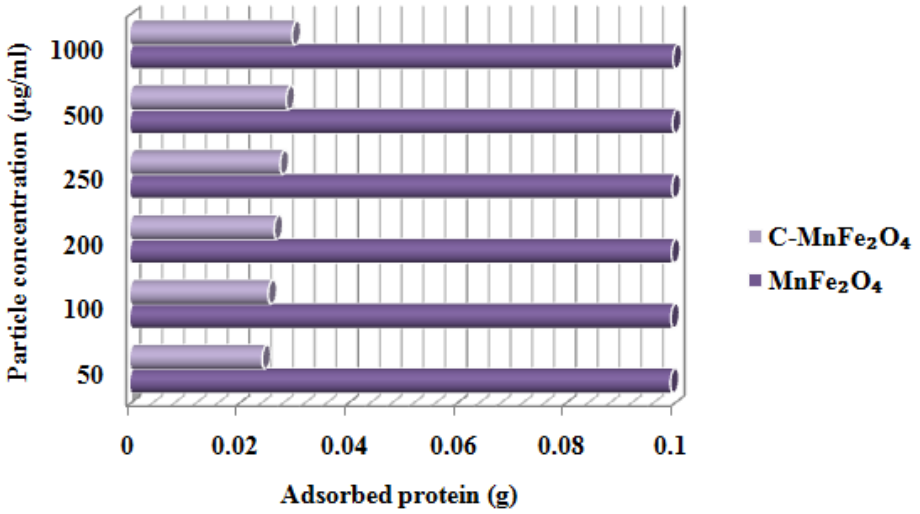

Figure 4.11. Comparative representation of amount of adsorbed HSA on $MnFe_2O_4$ and C-$MnFe_2O_4$

After studying the multiple fluorescence properties of C-$MnFe_2O_4$ NPs, we tried to utilize its UV absorption band in the degradation of environmentally harmful dye, methylene blue (MB) under UV irradiation. Figure 4.12.(a) shows that the absorption peak of MB at 663 nm drops with time and it takes almost 75 min to degrade completely at pH ~ 3 with a first order rate equation of kinetics rate constant (k) of 5.68 x 10^{-2} min^{-1}. The comparative rate of degradation of MB in presence of citrate and C–$MnFe_2O_4$ is shown in Figure 4.12.(b). Photoluminescence study of C–$MnFe_2O_4$ NPs already reveals the emergence of blue fluorescence under UV light irradiation, indicating the excitation of electrons from their valance band to the conduction band. Therefore, these excited electrons get the opportunity to react with the surface O_2 and H_2O of C–$MnFe_2O_4$ NPs solution to generate superoxide anions ($O_2^{\cdot -}$) and hydroxyl ions ($OH^{\cdot}$) respectively which are responsible for the degradation of MB present in the aqueous solution of C–$MnFe_2O_4$ NPs. The proposed reaction mechanism is as follows:

$$C\text{–}MnFe_2O_4 + h\gamma \rightarrow e_{CB}^{-} + h_{VB}^{+}$$

$$e_{CB}^{-} + O_2 \rightarrow O_2^{\cdot -}$$

$$O_2^{\cdot -} + MB \rightarrow Product$$

$$h_{VB}^{+} + H_2O \rightarrow HO^{\cdot} + H^{+}_{aq}$$

$$HO^{\cdot} + MB \rightarrow Product$$

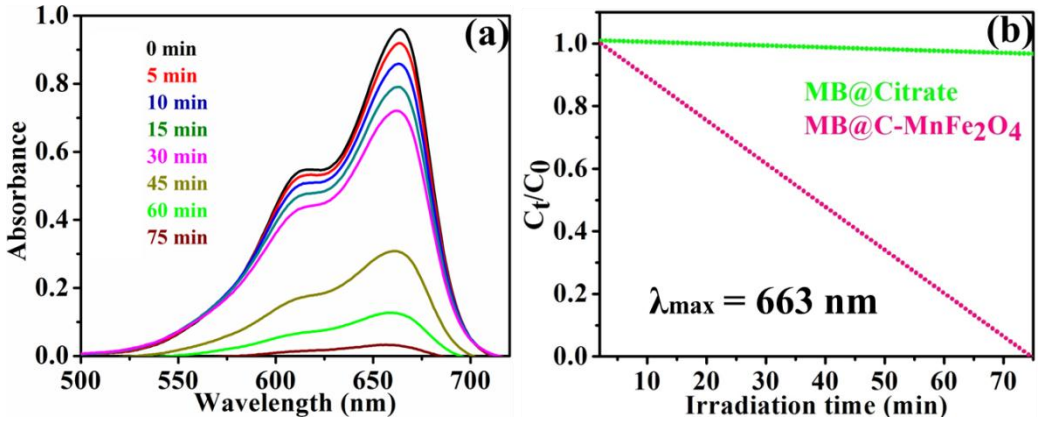

Figure 4.12. (a) C-$MnFe_2O_4$ promoted the degradation of MB under UV light over time in UV-vis spectroscopy and (b) rate of degradation of MB in UV light in presence of citrate and C-$MnFe_2O_4$ NPs.

After successful degradation of MB, we tried to see the degradation of an organic dye, bilirubin (BR) whose presence in higher concentration in blood leads to jaundice. The degradation of BR (pH ~ 7) with time at 435 nm proves the excellent catalytic efficiency of C-$MnFe_2O_4$ NPs at room temperature, as shown in Figure 4.13.(a) with a first order rate equation of kinetics rate constant (k) of $1.3x10^{-2}$ min^{-1}. Figure 4.13.(a) indicates that an increase in absorbance at 352 nm with a continuous decrease in BR absorbance at 435 nm over time, leading to an isosbestic point, observed at 370 nm. The absorbance peak at 352 nm arises due to the formation of methylvinylmaleimide (MVM), a photo oxidation product of BR in aqueous medium [23]. The rate of degradation of BR in presence of citrate and C-$MnFe_2O_4$ NPs are shown in Figure 4.13.(b).

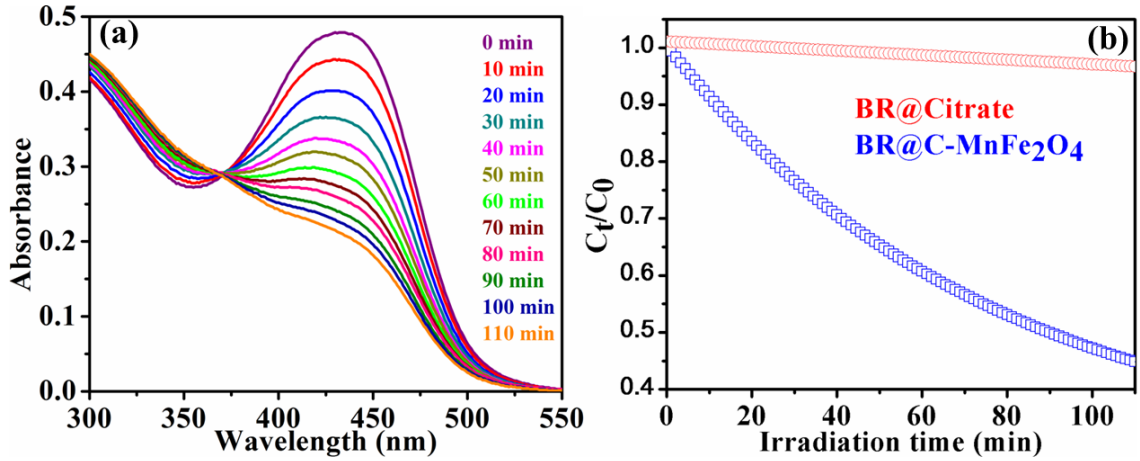

Figure 4.13. (a) C-$MnFe_2O_4$ promoted degradation of BR under stirring condition over time in UV-vis spectroscopy and (b) rate of degradation of BR in presence citrate and C-$MnFe_2O_4$ NPs.

4.4. Conclusion

Surface modification of $MnFe_2O_4$ NPs with trisodium citrate enlightens the scope of studying the surface electronic structures. Using the spectroscopic technique, the optical properties of the material are thoroughly ventured. We have also explored the origin of multicolor fluorescence properties through LMCT transition from the citrate ligand to the lowest unoccupied energy level of Mn ions and d-d transitions over Mn ions present in the NPs. The pristine and surface modified magneto fluorescent Mn_2FeO_4 nanoparticles are tested against protein adsorption for future biomedical application and satisfactory results are obtained. The catalytic activities of citrate functionalized $MnFe_2O_4$ NPs for the degradation of MB (a model water contaminant under UV light) and BR (a biologically harmful pigment) are investigated and competent performance is observed. We believe that the multifunctional citrate modified $MnFe_2O_4$ NPs will open up a new door for bio-imaging, drug delivery, wastewater decontamination and for the treatment of hyperbilirubinemia.

Bibliography

(1) D. R. Rolison, J. W. Long, J. C. Lytle, A. E. Fischer, C. P. Rhodes, T. M. McEvoy, M. E. Bourga, A. M. Lubers, Multifunctional 3D nanoarchitectures for energy storage and conversion, *Chem. Soc. Rev.* **2009**, 38, 226-252.

(2) Y. Zhu, J. Shen, K. Zhou, C. Chen, X. Yang, C. Li, Multifunctional Magnetic Composite Microspheres with in Situ Growth Au Nanoparticles: A Highly Efficient Catalyst System, *J. Phys. Chem. C* **2011**, 115, 1614-1619.

(3) Y. Wang, B. Li, L. Zhang, P. Li, L. Wang, J. Zhang, Multifunctional Magnetic Mesoporous Silica Nanocomposites with Improved Sensing Performance and Effective Removal Ability toward Hg(II), *Langmuir* **2012**, 28, 1657-1662.

(4) H.W. Shim, A.H. Lim, J.C. Kim, E. Jang, S.D. Seo, G.H. Lee, T.D. Kim, D.W. Kim, Scalable One-pot Bacteria-templating Synthesis Route toward Hierarchical, Porous-Co_3O_4 Superstructures for Supercapacitor Electrodes, *Sci. Rep.* **2013**, 3, 2325.

(5) S. Xiong, C. Yuan, X. Zhang, B. Xi, Y. Qian, Controllable Synthesis of Mesoporous Co_3O_4 Nanostructures with Tunable Morphology for Application in Supercapacitors, *Chem. Eur. J.* **2009**, 15, 5320-5326.

(6) Y. Xiao, S. Liu, F. Li, A. Zhang, J. Zhao, S. Fang, D. Jia, Hierarchical Nanoarchitectures: 3D Hierarchical Co_3O_4 Twin-Spheres with an Urchin-Like Structure: Large-Scale Synthesis, Multistep-Splitting Growth, and Electrochemical Pseudocapacitors, *Adv. Funct. Mater*. **2012**, 22, 4051.

(7) G. Wang, X. Shen, J. Horvat, B. Wang, H.L iu, D. Wexler, J Yao, Hydrothermal synthesis and optical, magnetic, and supercapacitance properties of nanoporous cobalt oxide nanorods, *J. Phys. Chem. C* **2009**, 113, 4357-4361.

(8) F. Corsi, DePalma C, M. Colombo, R. Allevi, M. Nebuloni, S. Ronchi, G. Rizzi, A. Tosoni, E. Trabucchi, E. Clementi, D. Prosperi, Towards ideal magnetofluorescent nanoparticles for bimodal detection of breast-cancer cells, *Small* **2009**, 5, 2555-2564.

(9) Y. Li, H. Tan, X.Y. Yang, B. Goris, J. Verbeeck, S. Bals, P. Colson, R. Cloots, G. V. Tendeloo, B.L. Su, Well Shaped Mn_3O_4 Nano-octahedra with Anomalous Magnetic Behavior and Enhanced Photodecomposition Properties, *Small* **2011**, 7, 475-483.

(10) P. Zhang, Y. Zhan, B. Cai, C. Hao, J. Wang, C. Liu, Z. Meng, Z. Yin, Q. Shape-controlled synthesis of Mn_3O_4 nanocrystals and their catalysis of the degradation of methylene blue, *Nano. Res.* **2010**, 3, 235-243.

(11) M.B. Gawande, P.S. Branco, R.S. Varma, Nano-magnetite (Fe_3O_4) as a support for recyclable catalysts in the development of sustainable methodologies, *Chem. Soc. Rev.* **2013**, 42, 3371-3393.

(12) H. Gu, K. Xu, Z. Yang, C.K. Chang, B. Xu, Synthesis and cellular uptake of porphyrin decorated iron oxide nanoparticles—a potential candidate for bimodal anticancer therapy, *Chem. Commun.* **2005**, 34, 4270-4272.

(13) U.R. Genger, M. Grabolle, S.C. Jaricot, R. Nitschke, T. Nann, Quantum dots versus organic dyes as fluorescent labels, *Nat. Methods* **2008**, 5, 763-775.

(14) S Sun, H. Zeng, D. B. Robinson, S. Raoux, P. M. Rice, S. X. Wang, G. Li, Monodisperse MFe_2O_4 (M = Fe, Co, Mn) Nanoparticles, *J. Am. Chem. Soc.* **2004**, 126, 273-279.

(15) M. E. Bodini, L. A. Willis, T. L. Riechel, D. T. Sawyer, Electrochemical and spectroscopic studies of manganese(II), -(III), and -(IV) gluconate complexes. 1. Formulas and oxidation-reduction stoichiometry, *Inorg. Chem.* **1976**, 15, 1538-1543.

(16) J.E. Huheey, E.A. Keiter, R.L. Keiter, *Inorganic chemistry*, Pearson Edu., 4, **2006**.

(17) T. Takashima, K. Hashimoto, R. Nakamura, Mechanisms of pH-Dependent Activity for Water Oxidation to Molecular Oxygen by MnO_2 Electrocatalyst, *J. Am. Chem. Soc*. **2012**, 134, 1519-1527.

(18) M. Matzapetakis, N. Karligiano, A. Bino, M. Dakanali, C.P. Raptopoulou, V. Tangoulis, A. Terzis, J. Giapintzakis, A. Salifoglou, Manganese Citrate Chemistry: Syntheses, Spectroscopic Studies, and Structural Characterizations of Novel Mononuclear, Water-Soluble Manganese Citrate Complexes, *Inorg. Chem*. **2000**, 39, 4044-4051.

(19) F. Aguado, F. Rodriguez, P. Núñez, Pressure-induced Jahn-Teller suppression and simultaneous high-spin to low-spin transition in the layered perovskite $CsMnF_4$, *Phys Rev. B* **2007**, 76, 094417.

(20) S. Sasidharan, A Jayasree, S Fazal, M. Koyakutty, S.V. Nair, D. Menon, Ambient temperature synthesis of citrate stabilized and biofunctionalized, fluorescent calcium fluoridenanocrystals for targeted labeling of cancer cells, *Biomater. Sci*. **2013**, 1, 294-305.

(21) X. Zou, E. Ying, S. Dong, Seed-mediated synthesis of branched gold nanoparticles with the assistance of citrate and their surface-enhanced Raman scattering properties, *Nanotechnology* **2006**, 17, 4758-4764.

(22) Q. He, J. Zhang, J. Shi, The effect of PEGylation of mesoporous silica nanoparticles on nonspecific binding of serum proteins and cellular responses, *Biomaterials* **2010**, 31, 1085-1092.

(23) W.E. Kurtin, Spectroscopy and Photochemistry of bilirubin Photoproducts. I. methylvinylmaleimide, *Photo. Chem. Photobiol* **1978**, 27, 503-509.

Chapter 5

$MnFe_2O_4$ Nano-Hollow Spheres: Surface Modification with Tartrate and Novel Catalytic Property

In this chapter we have synthesized $MnFe_2O_4$ nano-hollow spheres and functionalized with disodium tartrate ligand to induce inherent fluorescence property and catalytic activity.

5. Synthesis and Functionalization of $MnFe_2O_4$ Nano−Hollow Spheres for Novel Optical and Catalytic Properties

5.1. Preamble

An ancient but fascinating $MnFe_2O_4$ is a mixed valance (Mn^{+2} − Fe^{+3}) metal oxide with highest saturation magnetization which facilitates many applications such as magnetic resonance contrast agents [1], magnetic drug targeting [2], sensing [3], catalysis [4], and etc. $MnFe_2O_4$ strikingly differs from other ferrites, for example $CoFe_2O_4$ and $NiFe_2O_4$ which are highly resistive in nature. The electrical transport of cubic spinel type $MnFe_2O_4$ arises due to electron transfer between Mn and Fe ions on octahedral sites (Mn^{+2}+Fe^{+3} ↔ Mn^{+3}+Fe^{+2}) through Verway hopping [5], leading to its efficient catalytic activity. Recently, nano−sized spinel hollow ferrites have gained enormous attention among diversified morphologies such as thin films, nanoflakes, nanowires because of their low density, high effective surface area, large pore volume, and enhanced coercivity [6] which raise their performance in hyperthermia, drug delivery, electromagnetic wave absorption, waste water treatment, and catalysis [7] compared to their solid counterpart. A general strategy for the convenient high yield synthesis of $MnFe_2O_4$ nano−hollow spheres (NHSs) is either hard or soft template mediated approach where microemulsion droplet, liquid drop, polymer micelle, and vesicle are treated as soft templates [8] whereas polymeric microsphere and silica sphere are commonly used as the hard ones [9]. However, template mediated approach does not meet the criteria of biocompatibility and nontoxicity for their application in biomedical field. One step self−templated solvothermal/hydrothermal synthesis of $MnFe_2O_4$ hollow structures with narrow size distribution based on novel mechanism, Ostwald ripening [10] is the best way to get rid of this problem. In addition, solvothermal/hydrothermal approach is very powerful for synthesizing nanostructures with high uniformity, well−controlled morphology, size, and crystallization in a scalable and cost effective way which is still absent in the extant literatures for fabricating $MnFe_2O_4$ NHSs.

For biological and environmental applications, it is essential to have solubilised as well as well−dispersed magnetic particles in an aqueous medium. Due to high reactivity and high saturation magnetization [11] of magnetic nanostructures, it is very difficult to avoid their agglomeration which can be easily overcome through proper surface

coating/functionalization using organic/inorganic ligands. However, organic surfactant molecules with long hydrophobic tail used for stabilizing and individuating the nanoparticles (NPs) are insoluble in water, restricting their biomedical applications [12]. In particular, silanization of magnetic NPs has shown great success in preventing direct contact between the magnetic NPs and since the decoration of silica surface with functional groups including thiol, amine, and carboxylate groups is very easy, it in turn facilitates the solubility of these spheres in different solvents [13]. Despite of intrinsic water solubility, inorganic SiO_2 coating over magnetic NPs incorporates the properties like biocompatibility, non-cytotoxicity, high stability in biological buffer, high fluorescence activity, and photo stability in addition to controlled transport property [14]. Therefore, designing of an appropriate surface modification/functionalization strategy to obtain exact facilities like SiO_2 coating along with intrinsic water solubility is highly desirable to expedite the diverse biological applicability of magnetic NHSs.

Herein, we report a solvothermal approach to fabricate $MnFe_2O_4$ NHSs of average diameter of 100 nm followed by their rational surface modification through tartrate ligand which is an environmentally benign, biocompatible, and highly soluble in water and are found to exhibit many novel optical properties such as intrinsic fluorescence and enhanced photocatalytic activities. We believe that highly luminescent biocompatible magnetic tartrate functionalized $MnFe_2O_4$ (T−$MnFe_2O_4$) NHSs can serve as luminescent markers and can broaden novel application scopes in biolabelling, bioseparation, immunoassay, target imaging, pathogenic detections in addition to drug encapsulation within the nano−cavity of NHSs for drug delivery.

5.2. Experimental Section

5.2.1. Materials Used

The salts such as $MnCl_2.6H_2O$, $FeCl_3.6H_2O$ and the capping agent−oleylamine are purchased from Sigma Aldrich whereas the solvents−ethylene glycol and ethanol, the base−urea were purchased from Loba Chemie. Sodium hydroxide (NaOH) is obtained from Merck. Methylene blue (MB), a cationic dye for photocatalysis is purchased from Sigma Aldrich. All the reagents are of analytical grade.

5.2.2. Synthesis, Formation Mechanism and Functionalization of $MnFe_2O_4$ NHSs

In a typical synthesis of $MnFe_2O_4$ NHSs of average diameter 100 nm, we have incorporated 0.30 g of $MnCl_2$, $6H_2O$ and 0.80 g of $FeCl_3$, $6H_2O$ as salts into a 30 ml solvent mixture of ethylene glycol and ethanol in 2:1 ratio and after that we have added 0.53 g of urea as base and 3 ml of oleylamine as capping agent in the mixture. Finally, the homogeneous solution was transferred into a teflon lined autoclave and heated to 200°C for 24 h. The resultant black precipitation is obtained through centrifugation followed by washing with alcohol thrice. The possible chemical reactions for the synthesis of $MnFe_2O_4$ NHSs are proposed as follows [15]:

$$CO(NH_2)_2 \rightarrow NH_3 + HCNO$$

$$NH_3 + H_2O \rightarrow NH_4^+ + OH^-$$

$$Mn^{+2} + 2OH^- \rightarrow Mn(OH)_2$$

$$Fe^{+3} + 3OH^- \leftrightarrow FeOOH + H_2O$$

$$Mn(OH)_2 + 2FeOOH \rightarrow MnFe_2O_4 + 2H_2O + H^+$$

During the reaction, urea decomposes into ammonia which is going to produce a large number of hydroxyl groups at high temperature through hydrolysis. These hydroxyl groups help in precipitating manganese and ferric ions of the precursor salts into their corresponding hydroxides in a form of colloid. Finally, the presence of both manganese hydroxide and iron oxide hydroxide in the reaction mixture enables to develop the phase of $MnFe_2O_4$. In order to evaluate the process of core excavation of $MnFe_2O_4$ NHSs, we have conducted time dependent synthesis of $MnFe_2O_4$ NHSs of average diameter of 100 nm at various reaction times of 6, 12, 18, and 24 h. A series of transmission electron micrographs of the resulting products, as shown in Figure 5.1.(a)−(d) indicates the distinct changes in the size, surface, and interior of the nanospheres with time. Initially, after a reaction time of 6 h, a nano−leaf like structure of primary $Mn(OH)_2$ and FeOOH nanocrystals with average length of 3 nm is observed as shown in Figure 5.1.(a) due to their orchid trigonal and monoclinic crystal lattice respectively. As the newly formed nano−leaf like structures are extremely nano in size and thermodynamically unstable, they aggregate all together to form a solid sphere of average diameter of 62 nm with rough surface as shown in Figure 5.1.(b) during 6−12 h of interval in order to reduce the surface energy. With a longer reaction time of 18 h, a hollowing effect is

noticed as shown in Figure 5.1.(c) and the solid sphere starts to form porous sphere of smooth surface with average size of approximately 90 nm. It is due to the volume reduction and hence increase in density because of the transformation of $Mn(OH)_2$ and FeOOH with lower density to denser $MnFe_2O_4$. After 24 h of reaction time, the distinct contrast between the margin and the interior of the spheres with average size of 100 nm as shown in Figure 5.1.(d) confirms the formation of NHSs with smooth surface. The underlying mechanism for the hollowing effect is Ostwald ripening [10] which involves a gradual outward migration of crystallites through a recrystallization process and the capping agent, oleylamine restricts the growth of nanocrystals, thus resulting the formation of NHSs of smaller diameter (~100 nm).

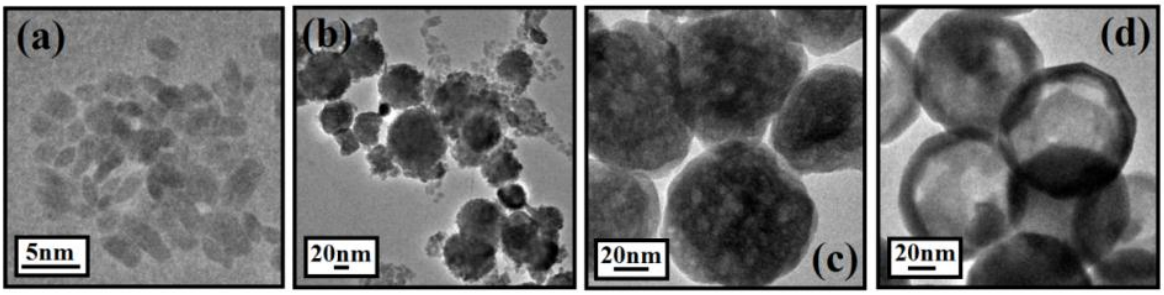

Figure 5.1. Formation mechanism of $MnFe_2O_4$ NHSs with average diameter of 100 nm and its representative transmission electron micrographs in four intermediate steps: (a) 6 h, (b) 12 h, (c) 18 h, and (d) 24 h.

A heat treatment at 500°C for 20 min is carried out to the as−prepared $MnFe_2O_4$ NHSs to remove the capping agent, oleylamine completely followed by cyclomixing with 0.5M disodium tartrate dihydrate for 12 h at room temperature. Removal of oleylamine is required because the presence of long hydrophobic chain in organic surfactant molecules over the surface of NHSs makes the system insoluble in water. The resulting mixture was centrifuged and the collected supernatant was passed through a syringe filter of 0.22 μm diameter to remove non−solubilised larger NHSs. The filtrate is termed as tartrate functionalized $MnFe_2O_4$ (T−$MnFe_2O_4$) NHSs solution. Next, the pH of the filtrate was adjusted from 7 to 12 by drop wise addition of 1M NaOH solution, and the resultant solution was heated at 70°C for 15 h under continuous stirring and the solution (fluorescence modified T−$MnFe_2O_4$ NHSs) became highly luminescent which is used for our studies.

The phase and morphology of the nanomaterials were characterized by X−ray diffraction (Rigaku Miniflex II desktop) using Cu Kα (λ=1.5418 Å) radiation, transmission electron microscope (TEM, TECHNAI G2 SF20 ST) and scanning electron microscope (SEM, FEI

Quanta-200 Mark-2). A JASCO Fourier transformed infrared (FTIR)−6300 spectrometer was used to confirm the attachment of tartrate ligand with $MnFe_2O_4$ NHSs. For FTIR measurement, powdered sample was mixed with KBr powder and pelletized. The background correction was made by using a reference of KBr pellet. The room temperature magnetic measurements of bare and functionalized $MnFe_2O_4$ NHSs were performed in a Lake Shore vibrating sample magnetometer (VSM) equipped with an electromagnet, capable of generating a field of up to 1.6 T at 300 K. In order to measure the UV−vis absorption of functionalized $MnFe_2O_4$ NHSs and the degradation of MB in presence of T−$MnFe_2O_4$ NHSs with spectroscopic precision, the spectra were recorded with a Shimadzu model UV−2600 spectrophotometer using a quartz cuvette of 1 cm path length. The characteristic fluorescence excitation and emission spectra were recorded on a Jobin Yvon Model Fluoromax−3 fluorometer. The comparative evaluation of photocatalytic performance of T−$MnFe_2O_4$ NHSs, $MnFe_2O_4$ NHSs, and bare tartrate for the degradation of aqueous solution of MB was performed using 8W UV lamp of wavelength 253 nm. A mixture of MB and T−$MnFe_2O_4$ NHSs/tartrate solutions in 1:1 (4.6 μM each) ratio was continuously stirred in the dark for 30 min in a quartz cuvette, maintaining pH ∼ 3. In case of solid $MnFe_2O_4$ NHSs, it follows the same procedure with addition of 0.01 gm of $MnFe_2O_4$ NHSs in the same concentration of MB solution. After this period of time, the UV light source was turned on and the cuvette was placed ∼ 2 cm apart from the light source. The absorbance of MB in the reaction mixture was measured time to time by the UV−vis spectrophotometer and the absorption peak at 663 nm was monitored to obtain the photocatalytic degradation efficiency. We added the same amount of MB (4.6 μM) to the solution after every cycle without further addition of catalyst for recyclability test. Finally, to evaluate the mechanism of MB degradation, we have carried out the UV−vis absorption study of MB solution in presence of T−$MnFe_2O_4$ NHSs under UV light of wavelength of 360 nm in addition to 253 nm as well as normal day light condition.

5.3. Results and Discussions

The XRD pattern of $MnFe_2O_4$ NHSs, as shown in Figure 5.2 confirms single phase, face centred cubic spinel structure (JCPDS card no. 10−0319) of $MnFe_2O_4$ and from the broadening of its Bragg reflection peaks, the average crystallite size of $MnFe_2O_4$ NHSs is found to be approximately 23 nm using Scherrer's Equation. Energy dispersive X−ray (EDX) spectroscopic analysis as shown in inset of Figure 5.2 confirms the absence of elemental

composition of the capping agent, oleylamine which may play significant role in determining the solubility of T−$MnFe_2O_4$ NHSs in water.

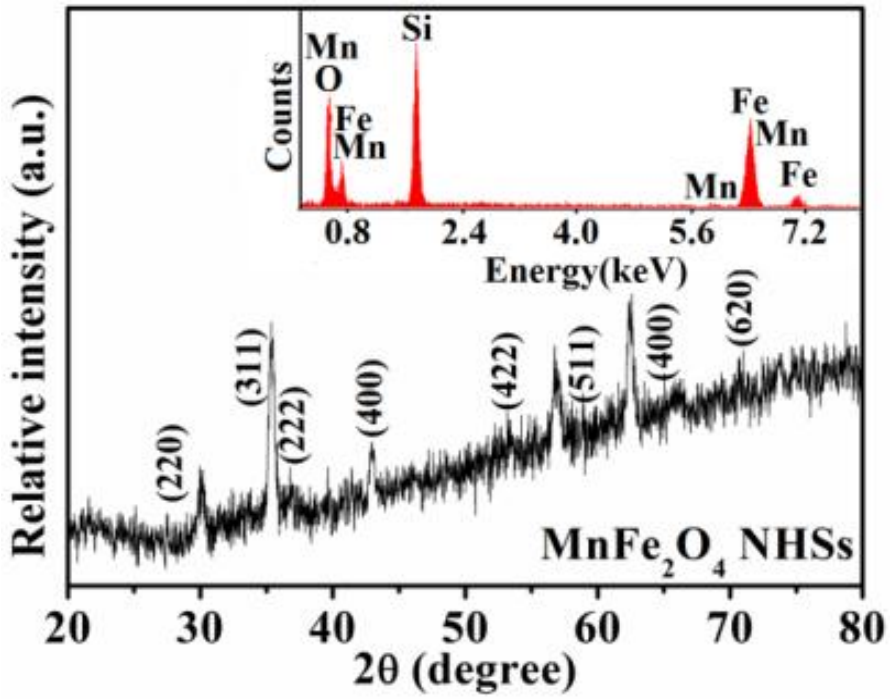

Figure. 5.2. (a) XRD pattern of $MnFe_2O_4$ hollow spheres of average diameter 100 nm. Inset exhibits the EDX spectrum indicating the presence of Mn, Fe, and O of $MnFe_2O_4$.

Figure 5.3.(a) demonstrates the TEM image of $MnFe_2O_4$ NHSs which are used for further surface modification in order to optical and catalytic studies. The dark margin and bright centre contrast of each nanostructure confirm the formation of NHSs. It is found that the particles are spherical in shape with a narrow size distribution and the average diameter is observed to be ~ 100 nm with shell thickness of the order of 7 nm. The structural property of an area selected by black rectangle of single $MnFe_2O_4$ NHS (Figure 5.3.(a)) is characterized by using the high−resolution TEM (HRTEM) as shown in Figure 5.3.(b), illustrating highly crystalline nature of the nanocrystals. The inter−planar distance is estimated to be 2.51 Å, which is in good agreement with the {311} planes of $MnFe_2O_4$. Figure 5.3.(c) shows the selected area electron diffraction (SAED) pattern of the same area of Figure 5.3.(a), indicating crystalline nature of as−synthesized NHSs. The SEM image of T−$MnFe_2O_4$ NHSs as presented in Figure 5.3.(d) confirms the attachment of tartrate ligand over the NHS's surface where the arrow head points out the broken part of the NHSs. The average diameter of T−$MnFe_2O_4$ NHSs is found to be of the order of 90 nm. Figure 5.3.(e) shows the EDX of

T−$MnFe_2O_4$ NHSs having elemental compositions of Mn, Fe, O, C, and Na which confirm the presence of both tartrate and $MnFe_2O_4$.

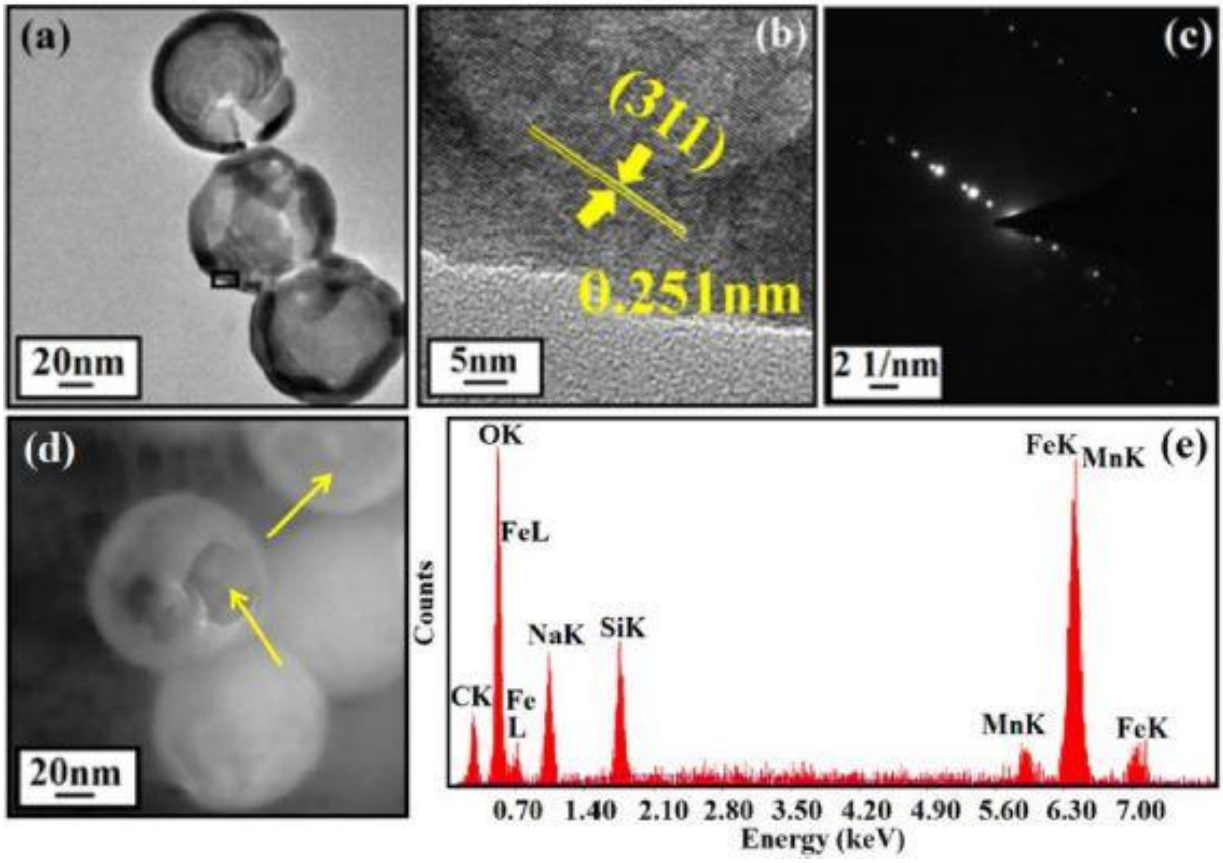

Figure 5.3. (a) TEM image of $MnFe_2O_4$ hollow sphere of average diameter 100 nm, (b) HRTEM image, (c) SAED pattern of the area selected by black rectangle as shown in the TEM image of $MnFe_2O_4$ NHSs, (d) SEM image, (e) EDX of T-$MnFe_2O_4$ hollow sphere of average diameter 90 nm.

In order to get the direct evidence of ligand functionalization onto the surface of NHSs, FTIR spectra (Figure 5.4) of tartrate, $MnFe_2O_4$ and T−$MnFe_2O_4$ NHSs have been carried out. The $MnFe_2O_4$ spectrum shows characteristic peaks at 580 and 696 cm^{-1}. The peak at 696 cm^{-1} is attributed to the stretching vibration mode of Mn–O for the tetrahedrally coordinated metal ions and the band at 580 cm^{-1} is assigned to the same for octahedrally coordinated metal ions [16]. However, T−$MnFe_2O_4$ NHSs exhibit those peaks with lower intensity probably because of high concentration of tartrate ligand. Pure tartrate has five peaks at 1070 cm^{-1}, 1128 cm^{-1} (arising due to C−OH stretching frequency) [17], 1428 cm^{-1}, 1629 cm^{-1} (attributing to the symmetric and asymmetric stretching modes of COO^-), and 3400 cm^{-1} (stretching vibrational mode of O−H bond) [18], which shift upon functionalization, clearly confirming the binding of ligands with NHSs surface.

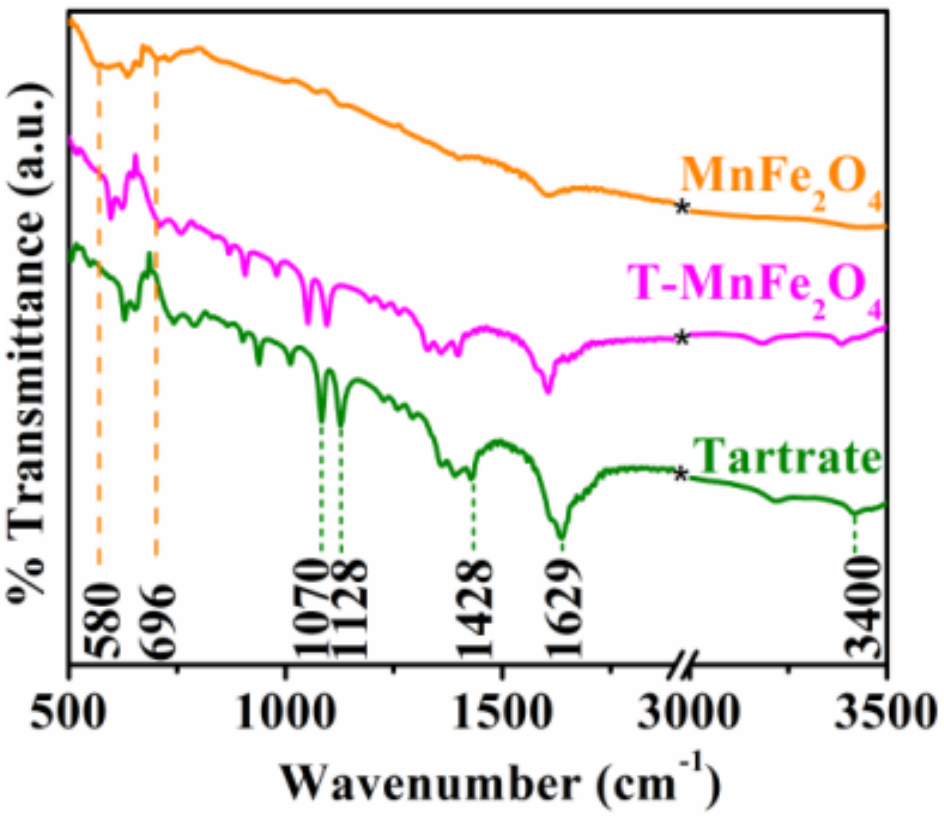

Figure 5.4. FTIR spectra of $MnFe_2O_4$ NHSs, T−$MnFe_2O_4$ NHSs, and tartrate.

Figure 5.5 shows the room temperature magnetic hysteresis loop of bare $MnFe_2O_4$ NHSs of average diameter of 100 nm whereas its inset exhibits the same for T−$MnFe_2O_4$ NHSs. The coercivity (Hc) and the saturation magnetization (Ms) of the parent $MnFe_2O_4$ NHSs are found to be 124 Oe and 37. 96 emu/g respectively, indicating their ferrimagnetic nature. Upon surface functionalization, their coercivity almost vanishes with significantly decreased saturation and remanence magnetizations which is a signature of superparamagnetic behaviour. Tartrate contains two σ-donor, hydroxyl (–OH) groups and two π-donor, carboxyl ($–COO^-$) groups which indicate that ligand must donate electrons to the transition metal ions of T−$MnFe_2O_4$ NHSs, leading to ligand to metal charge transfer which is also observed from the photoluminescence spectra as shown in Figure 7. Therefore, the decrease in M_s for T−$MnFe_2O_4$ NHSs is due to ligand to metal charge transfer (LMCT) transitions which appreciably quench the unpaired spins of Mn^{+2} [19]. This reduction in M_s decreases the spin−orbit coupling which is related to magnetocrystalline anisotropy energy (E_A) by the relation, $E_A = KV\sin^2\theta$, where K is the magnetocrystalline anisotropy constant which depends on the strength of spin−orbit coupling, V is the volume of a nanostructure, and θ is the angle between magnetization direction and magnetic easy axis of a crystallite. Therefore, reduced

spin−orbit coupling results in a decrease in magnetocrystalline anisotropy and hence H_c of the T−$MnFe_2O_4$ NHSs [20].

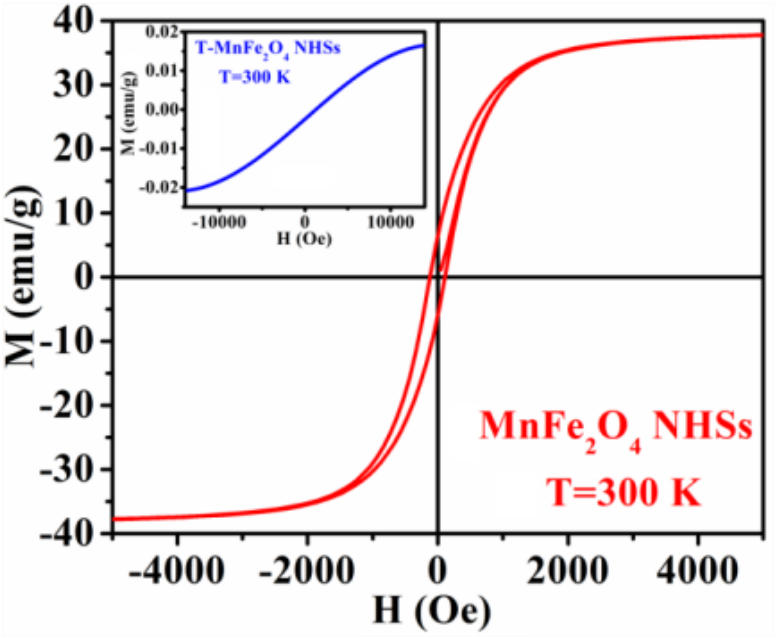

Figure 5.5. Field dependent magnetization graph of bare $MnFe_2O_4$ NHSs of average diameter 100 nm at 300 K. Inset shows the same for T−$MnFe_2O_4$ NHSs.

The surface electronic structure of nanomaterials changes significantly upon surface functionalization with organic ligands. In order to study the effect of surface functionalization, we have carried out UV−vis absorption measurements of bare tartrate, $MnFe_2O_4$, T−$MnFe_2O_4$ and fluorescence (fl.) modified T−$MnFe_2O_4$ NHSs. The comparative UV−vis absorption spectra as shown in Figure 5.6 indicate that there is a distinct absorption band ranging from 275−350 nm upon surface functionalization of $MnFe_2O_4$ NHSs with tartrate ligand. Since tartrate and $MnFe_2O_4$ NHSs do not exhibit any absorption in the UV−vis region, the broad band in case of T−$MnFe_2O_4$ NHSs is due to LMCT transition from highest occupied energy levels of tartrate to the lowest unoccupied energy levels of surface metal ions (Mn^{+2} and Fe^{+3}) of $MnFe_2O_4$ NHSs [21]. To increase the intensity of the absorption band of T−$MnFe_2O_4$ NHSs, it is further modified through heat treatment at ~70 °C for 15 h at pH~12 and the broad band of T−$MnFe_2O_4$ NHSs is found to split along with enhanced intensity in case of fl. modified T−$MnFe_2O_4$ NHSs solution. Generation of two absorption bands at around 295 and 334 nm are possibly due to enhanced interaction of the functional groups of tartrate at higher pH.

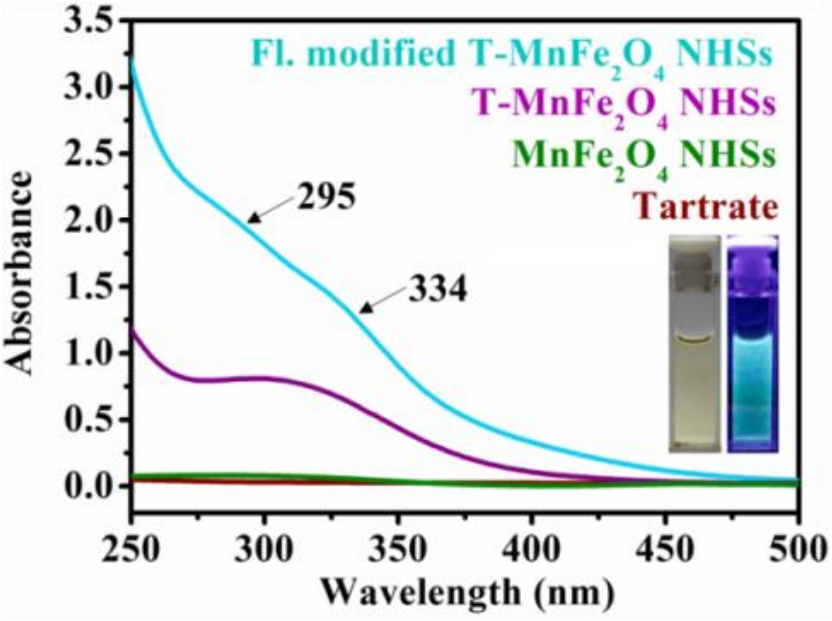

Figure 5.6. UV−vis absorption spectra of tartrate, $MnFe_2O_4$, T−$MnFe_2O_4$ and fl. modified T−$MnFe_2O_4$ NHSs. Inset exhibits the photographs of aqueous T−$MnFe_2O_4$ NHSs solution under visible and UV light respectively.

Upon getting knowledge about the UV−vis spectra of fl. modified T−$MnFe_2O_4$ NHSs solution, we have carried out their excitation and emission studies as depicted in Figure 5.7.(a) and (b). Figure 5.7.(a) shows the normalized emission spectra of fl. modified T−$MnFe_2O_4$ NHSs solution at 412, 492, 522 and 568 nm against excitation at four different wavelengths at 324, 395, 447 and 480 nm respectively whereas Fig. 7(b) exhibits the normalized excitation spectra of the same solution at different fluorescence maxima of 324, 393, 445 and 478 nm. According to the selection rule of atomic spectroscopy, there is no possibility of d−d transitions for Mn^{2+} (d^5) and Fe^{3++} (d^5) of $MnFe_2O_4$ since the transitions are both Laporte and spin forbidden [22]. However, there is a possibility for the existence of 3+ oxidation state of Mn at higher pH [23]. Tartrate, having two α−hydroxy carboxylate groups, is a strong field ligand and in presence of high−spin octahedral environment, the degeneracy of t_{2g} and e_g levels of Mn^{3+} (d^4) is lost due to Jahn−Teller distortion and caused to develop energy levels of $5B_{1g}$, $5A_{1g}$, $5B_{2g}$ and $5E_g$ with increasing energy [24]. Therefore, the first emission peak at 412 nm is due to LMCT from tartrate to the $Mn^{2+/3+}$ or Fe^{3+} and the peaks at 492, 522, and 568 nm are due to the d−d transitions [25] of $5B_{1g} \rightarrow 5E_g$, $5B_{1g} \rightarrow 5B_{2g}$ and $5B_{1g} \rightarrow 5A_{1g}$ respectively of surface Mn^{+3} ions of fl. modified $MnFe_2O_4$ NHSs. Multicolor fluorescence, arising due to different excitations of fl. modified T−$MnFe_2O_4$ NHSs solution is evident from the images of Figure 5.7.(c)−(e). It demonstrates that the off−white coloured

powder of fl. modified T−$MnFe_2O_4$ NHSs generate fluorescent colors like blue, green, and red upon excitations in the range of 340−380, 450−490 and 515−560 nm respectively, by using filters.

Size and morphology of the nanostructures play an important role in determining their catalytic activity [26]. In general, nanostructures with lower size exhibit efficient catalytic activity due to their higher surface area. Therefore, the double surface area of NHSs of average diameter of 100 nm must show better catalytic performance in contrast to their solid configuration. In addition to that the oxidation state of metal ion also determines their catalytic performance [27].

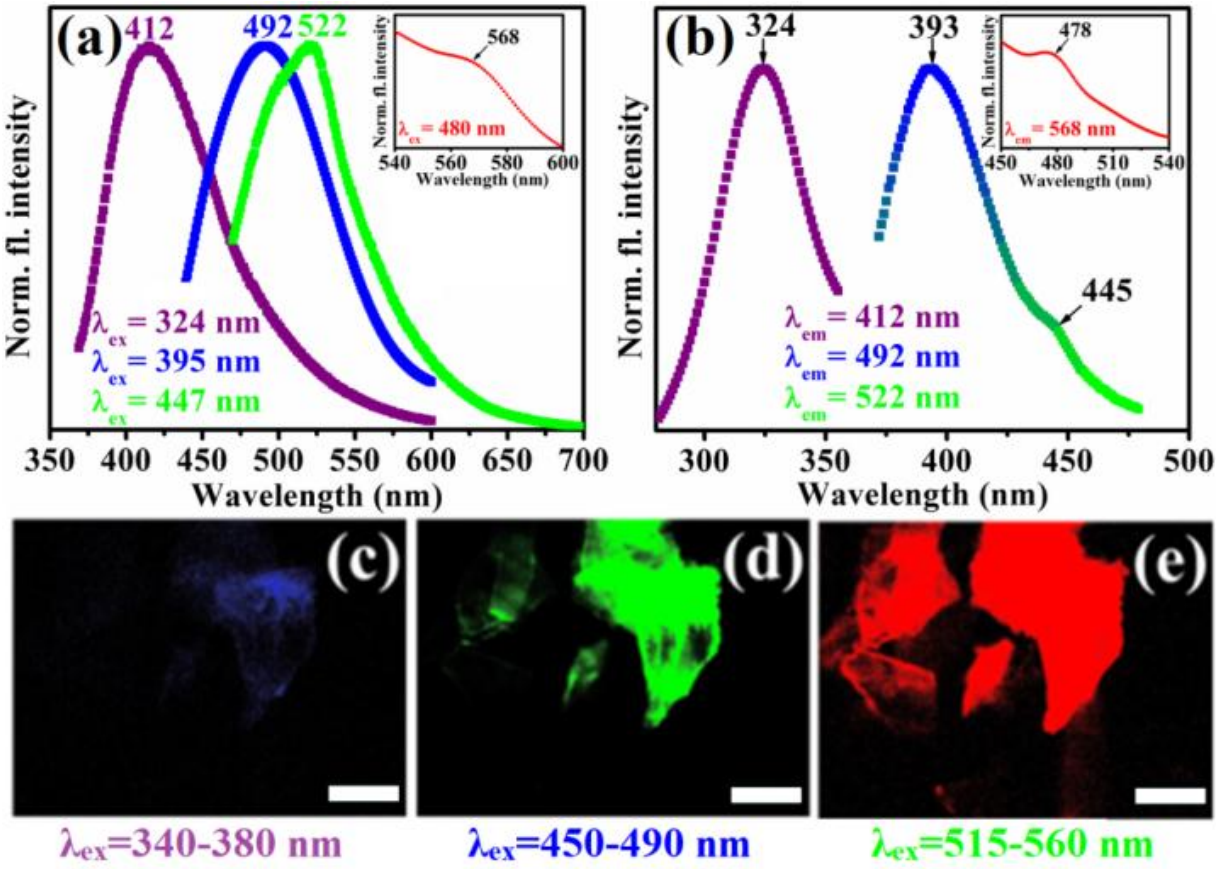

Figure 5.7. (a) Normalized steady−state fluorescence emission spectra at four different excitation wavelengths of 324, 395, 447 and 480 nm, (b) Normalized steady−state fluorescence excitation spectra at different emission wavelengths of 412,492, 522 and 568 nm of fl. Modified T−$MnFe_2O_4$ NHSs. Fluorescence microscopic images of the same NHSs powder under (c) UV, (d) blue and (e) green light irradiations. The scale bars in all the images are 500 μm.

Recently, significant efforts have been made to study the catalytic/photocatalytic performances of mixed valence nanostructures. Hence, in order to identify the catalytic

performance of mixed valance magnetic metal oxide with large effective surface area as well as to utilize the broad optical absorption band of T−$MnFe_2O_4$ NHSs throughout the UV−vis region, we have carried out the photocatalysis of textile dye, MB in presence of T−$MnFe_2O_4$ NHSs under UV light. Figure 5.8.(a) shows the excellent catalytic activity of T−$MnFe_2O_4$ NHSs for degradation of MB with time at pH~3 under UV light irradiation of wavelength 253 nm. The characteristic absorption at 663 nm has been chosen to monitor the photocatalytic degradation at room temperature. It demonstrates that the peak intensity at 663 nm changes significantly with time and the MB is found to degrade completely within 60 min of UV irradiation. Figure 5.8.(b) shows the rate of photocatalytic degradation of MB in the presence of bare tartrate, $MnFe_2O_4$ NHSs, T−$MnFe_2O_4$ NHSs under UV light of wavelength 253 nm and the degradation rate in presence of T−$MnFe_2O_4$ NHSs is maximum and found to fit excellently with a first order rate equation with kinetic rate constant (k) of 2.64×10^{-2} min^{-1}. It is noted that T−$MnFe_2O_4$ NHSs show good photoluminescence property upon UV excitation which may facilitates the photo induced electron transfer from T−$MnFe_2O_4$ NHSs to MB, resulting MB degradation only within 60 min. Lee et al. [28] have reported that electron transfer is associated with the MB degradation and enhanced interaction of MB with the double interfaces of T−$MnFe_2O_4$ NHSs further promote it. Guo et al. [29] have demonstrated the decomposition of MB dye in aqueous solution by $MnFe_2O_4$ NHSs having diameter in the range of about 170–220 nm as a catalyst and found 85% degradation of MB within 150 min. Therefore, surface modification of $MnFe_2O_4$ NHSs with tartrate ligand as in our case indeed plays important role in rapid degradation of MB. Photoluminescence study of T–$MnFe_2O_4$ NHSs already reveals the emergence of blue fluorescence under UV light irradiation, indicating the excitation of electrons from their valance band to the conduction band. Therefore, these excited electrons get the opportunity to react with the surface O_2 and H_2O of T–$MnFe_2O_4$ NHSs solution to generate superoxide anions ($O_2^{\cdot-}$) and hydroxyl ions ($OH^{\cdot}$) respectively which are responsible for the degradation of MB present in the aqueous solution of T–$MnFe_2O_4$ NHSs. The proposed reaction mechanism is as follows:

$$T\text{–}MnFe_2O_4 + h\gamma \rightarrow e_{CB}^{-} + h_{VB}^{+}$$

$$e_{CB}^{-} + O_2 \rightarrow O_2^{\cdot-}$$

$$O_2^{\cdot-} + MB \rightarrow Product$$

$$h_{VB}^{+} + H_2O \rightarrow HO^{\cdot} + H^{+}_{aq}$$

$$HO^{\cdot} + MB \rightarrow Product$$

In order to confirm the nature of MB degradation, we have carried out photocatalytic degradation of MB in presence of T-$MnFe_2O_4$ NHSs under UV light of another different wavelength of 360 nm and normal day light condition as shown in Figure 5.8.(c) and (d). The comparative study of photocatalytic degradation of MB in presence of T-$MnFe_2O_4$ NHSs under UV lights of wavelength 250 and 360 nm indicates that UV light influences MB degradation significantly. The decrease rate of MB concentration under UV light of wavelength 250 nm (~4.96 eV) is found to be faster than the MB degradation under UV light of wavelength 360 nm (~3.4 eV). In addition, no degradation is observed under normal day light condition which implies that MB decomposed through photocatalytic reactions under UV light. Since adsorption does not depend on the incident light [30,31], this MB degradation is practically due to catalysis instead of adsorption and T-$MnFe_2O_4$ NHS is photo-catalytically active material.

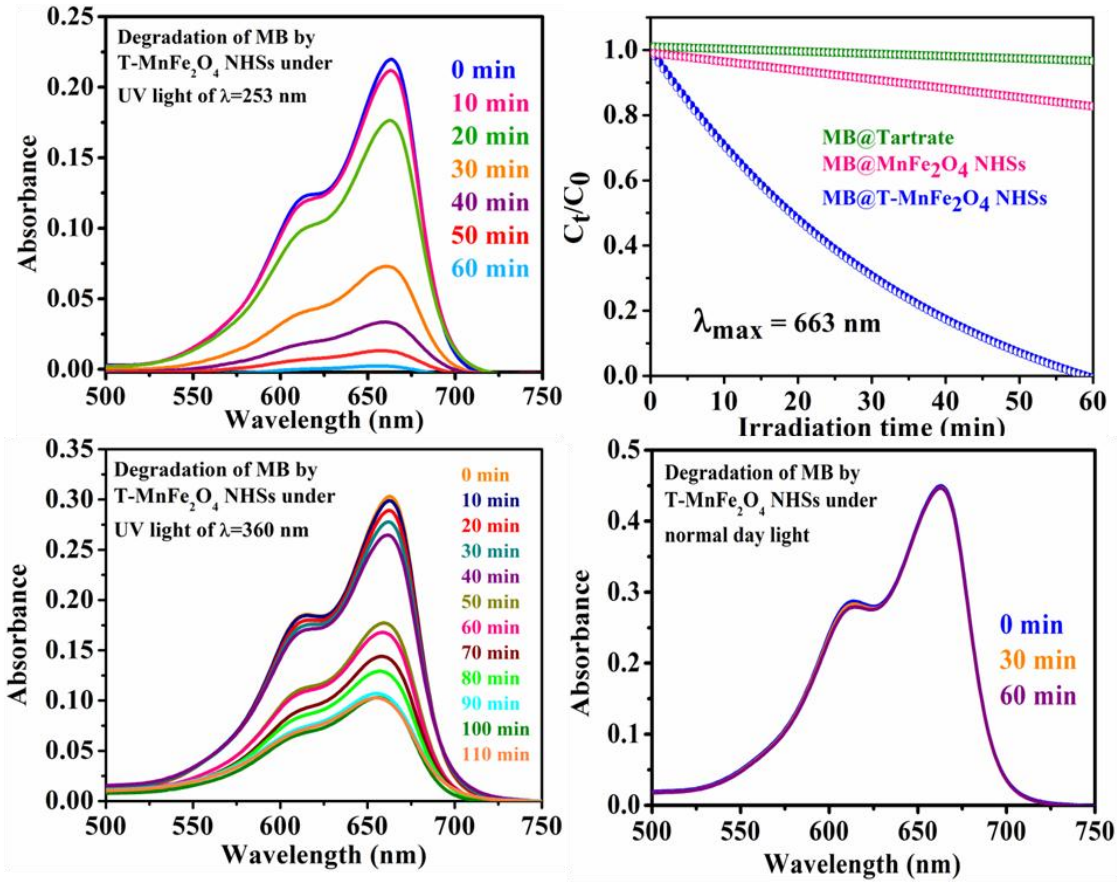

Figure 5.8. (a) UV−vis spectra of MB solution measured at different time in presence of T−$MnFe_2O_4$ NHSs and UV light of wavelength 253 nm, (b) Relative concentration of MB versus time, monitored at 663 nm in presence of T−$MnFe_2O_4$ NHSs/$MnFe_2O_4$ NHSs/bare tartrate under UV light of wavelength 253 nm. UV−vis spectra of MB degradation in presence of T−$MnFe_2O_4$ NHSs under (c) UV light of wavelength 360 nm, and (d) normal day light condition.

To confirm the stability of the high photocatalytic performance as well as for commercialization, the recycling experiments of T−$MnFe_2O_4$ NHSs under UV irradiation have been conducted. We have carried out five consecutive cycles as shown in Figure 5.9 which shows that the rate of the photocatalytic degradation remains almost constant, indicating the high stability of the catalyst. Since the photocatalytic properties of the T−$MnFe_2O_4$ NHSs rejuvenate after each cycle, it is very important for industrial applications.

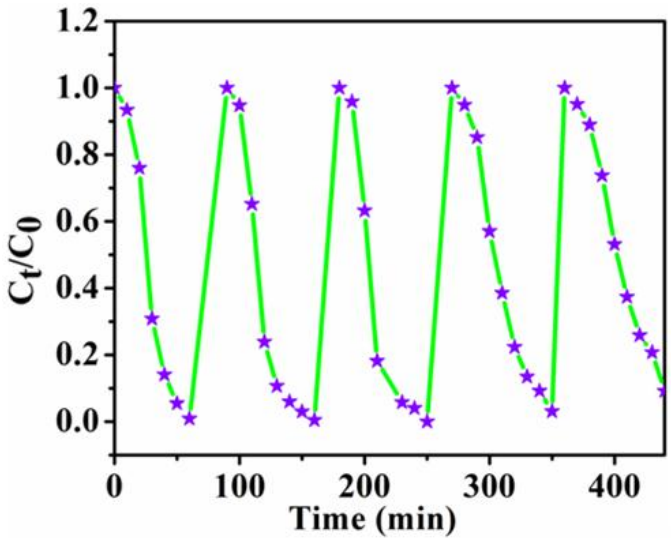

Figure 5.9. Reusability of T−$MnFe_2O_4$ NHSs in the degradation of MB under UV light of wavelength 253 nm over five cycles.

5.4. Conclusion

In summary, magnetic hollow nanospheres of $MnFe_2O_4$ having narrow size distribution and with average particle size of 100 nm have been successfully synthesized by self templated solvothermal method. Further, we have demonstrated that rational surface functionalization of these $MnFe_2O_4$ NHSs can modify their electronic structure through charge transfer from the organic ligand to the metal ion and therefore, enumerates wide range of multicolor fluorescence starting from blue, green, to red. Finally, we have utilized the large surface area of our developed magneto−fluorescent T−$MnFe_2O_4$ NHSs in monitoring the catalytic efficiency for the degradation of MB under UV light irradiation and it is found to exhibit excellent reusable photocatalytic performance which is beneficial for industrial applications. The T−$MnFe_2O_4$ NHSs developed in this work are potentially important for various applications such as photonics, separation, water treatment, bio−imaging, and drug delivery.

Bibliography

(1) U.I. Tromsdorf, N.C. Bigall, M.G. Kaul, O.T. Bruns, M.S. Nikolic, B. Mollwitz, R.A. Sperling, R. Reimer, H. Hohenberg, W.J. Parak, S. Förster, U. Beisiegel, G. Adam, H. Weller, Size and surface effects on the MRI relaxivity of manganese ferrite nanoparticle contrast agents, *Nano Lett.* **2007**, 7, 2422-2427.

(2) A.R.O. Rodrigues, J.M.F. Ramos, I.T. Gomes, B.G. Almeida, J.P. Araújo, M.J.R.P. Queiroz, P.J.G. Coutinho, E.M.S. Castanheira, Magnetoliposomes based on manganese ferrite nanoparticles as nanocarriers for antitumor drugs, *RSC Adv.* **2016**, 6, 17302-17313.

(3) I. Sandu, L. Presmanes, P. Alphonse, P. Tailhades, Nanostructured cobalt manganese ferrite thin films for gas sensor application, *Thin Solid Films* **2006**, 495, 130-133.

(4) B. Sahoo, S.K. Sahu, S. Nayak, D. Dhara, P. Pramanik, Fabrication of magnetic mesoporous manganese ferrite nanocomposites as efficient catalyst for degradation of dye pollutants, *Catal. Sci.Technol*. **2012**, 2, 1367-1374.

(5) F.K. Lotgering, Semiconduction and cation valencies in manganese ferrites, *J. Phys. Chem. Solids* **1964**, 25, 95-103.

(6) X. Wang, J. Feng, Y. Bai, Q. Zhang, Y. Yin, Synthesis, Properties, and Applications of Hollow Micro-/Nanostructures, *Chem. Rev*. **2016**, 116, 10983-11060.

(7) R. Rakshit, D. Sarkar, M. Pal, K. Serita, M. Tonouchi, K. Mandal, Acoustic vibration induced high electromagnetic responses of Fe_3O_4 nano-hollow spheres in the THz regime, *J. Phys, D: Appl. Phys*. **2015**, 48, 245301.

(8) J. Liu, T. Yang, D.-W. Wang, G.Q. (Max) Lu, D. Zhao, S.Z. Qiao, A facile soft-template synthesis of mesoporous polymeric and carbonaceous nanospheres, *Nat. Commun*. **2013**, 4, 2798.

(9) Z. Zhang, F. Zuo, P. Feng, Hard template synthesis of crystalline mesoporous anatase TiO_2 for photocatalytic hydrogen evolution, *J. Mater. Chem*. **2010**, 20, 2206-2212.

(10) X. Wang, F.L. Yuan, P. Hu, L.J. Yu, L. Bai, Self-assembled growth of hollow spheres with octahedron-like Co nanocrystals via one-pot solution fabrication, *J. Phys. Chem. C* **2008**, 112, 8773-8778.

(11) W. Wu, Q.G. He, C.Z. Jiang, Magnetic iron oxide nanoparticles: synthesis and surface functionalization strategies, *Nanosc. Res. Lett*. **2008**, 3, 397–415.

(12) S. Si, C. Li, X. Wang, D. Yu, Q. Peng, Y. Li, Magnetic Monodisperse Fe_3O_4 Nanoparticles, *Crys. Growth Des*. **2005**, 5, 391–393.

(13) D. Gerion, F. Pinaud, S.C. Williams, W.J. Parak, D. Zanchet, S. Weiss, Synthesis and Properties of Biocompatible Water-Soluble Silica-Coated CdSe/ZnS Semiconductor Quantum Dots, *J. Phy. Chem. B* **2001**, 105, 8861-8871.

(14) E.J. Bae, Y.-S. Min, U. Kim, W. Park, Single-walled carbon nanotube growth on glass, *Nanotechnol*. **2007**, 18, 15601-15605.

(15) P.M. Schaber, J. Colson, S. Higgins, D. Thielen, B. Anspach, J. Brauer, Thermal decomposition (pyrolysis) of urea in an open reaction vessel, *Thermochim. Acta* **2004**, 424, 131-142.

(16) H. Yanga, C. Zhanga, X. Shib, H. Hua, X. Duc, Y. Fangd, Y. Mad, H. Wua, S. Yanga, Water-soluble superparamagnetic manganese ferrite nanoparticles for magnetic resonance imaging, *Biomaterials* **2010**, 31, 3667-3673.

(17) N. Kaneko, M. Kaneko, H. Takahashi, Infrared and Raman spectra and vibrational assignment of some metal tartrates, *Spectrochim. Acta Part A* **1984**, 40, 33-42.

(18) V. Ramakrishnan, J.M.T. Maroor, IR and Raman studies of gel grown manganese tartrate, *Infrared Phys*. **1988**, 28, 201-204.

(19) B. N. Figgis, M. A. Hitchman, *Wiley-VCH, New York*, **2000**.

(20) D.A. van Leeuwen, J.M. van Ruitenbeek, L.J. de Jongh, A. Ceriotti, G. Pacchioni, O.D. Häberlen, N. Rösch, Quenching of Magnetic Moments by Ligand-Metal Interactions in Nanosized Magnetic Metal Clusters, *Phys. Rev. Lett.* **1994**, 73, 1432-1435.

(21) M.E. Bodini, L.A. Willis, T.L. Riechel, D.T. Sawyer, Electrochemical and spectroscopic studies of manganese(II), -(III), and -(IV) gluconate complexes. 1. Formulas and oxidation-reduction stoichiometry, *Inorg. Chem*. **1976**, 15, 1538-1543.

(22) J.E. Huheey, E.A. Keiter, R.L. Keiter, Inorg. Chem.: Principles of Structure and Reactivity, fourth ed., *Pearson Education, Singapore*, **2006**.

(23) T. Takashima, K. Hashimoto, R. Nakamura, Mechanisms of pH-Dependent Activity for Water Oxidation to Molecular Oxygen by MnO_2 Electrocatalyst, *J. Am. Chem. Soc.* **2012**, 134, 1519-1527.

(24) F. Aguado, F. Rodriguez, P. Núñez, Pressure-induced Jahn-Teller suppression and simultaneous high-spin to low-spin transition in the layered perovskite $CsMnF_4$, *Phys. Rev. B* **2007**, 76, 094417-094422.

(25) M. Matzapetakis, N. Karligiano, A. Bino, M. Dakanali, C.P. Raptopoulou, V. Tangoulis, A. Terzis, J. Giapintzakis, A. Salifoglou, Manganese Citrate Chemistry: Syntheses, Spectroscopic Studies, and Structural Characterizations of Novel Mononuclear, Water-Soluble Manganese Citrate Complexes, *Inorg. Chem*. **2000**, 39, 4044-4051.

(26) D. Majumder, I. Chakraborty, K. Mandal, S. Roy, Facet-dependent photodegradation of methylene blue using pristine CeO_2 nanostructures, *ACS Omega*, **2019**, 4, 4243-4251.

(27) S. Mostafa, F. Behafarid, J.R. Croy, L.K. Ono, L. Li, J.C. Yang, A.I. Frenkel, B.R. Cuenya, Shape-dependent catalytic properties of Pt nanoparticles, *J. Am. Chem. Soc.*, **2010**, 132, 15714–15719.

(28) S.-K. Lee, A. Mills, Novel photochemistry of *leuco*-Methylene Blue, *Chem. Commun*. **2003**, 18, 2366-2367.

(29) P. Guo, G. Zhang, J. Yu, H. Li, X.S. Zhao, Controlled synthesis, magnetic and photocatalytic properties of hollow spheres and colloidal nanocrystal clusters of manganese ferrite, *Coll. Surf. A* **2012**, 395, 168-174.

(30) M.T. Yagub, T.K. Sen, S. Afroze, H.M. Ang, Dye and its removal from aqueous solution by adsorption: A review, *Adv. Coll. Interf. Sci*. **2014**, 209, 172-184.

(31) G.W. Castellan, *Physical Chemistry, third ed., Addison-Wesley Publishing Company, Inc., Boston, United States*, **1964**.

Chapter 6

Effect of Bovine Serum Albumin on Tartrate Modified Manganese Ferrite Nano Hollow Spheres: Spectroscopic and Toxicity Study

In this chapter we have studied the interaction of bovine serum albumin (BSA) with T-$MnFe_2O_4$ NHSs using several spectroscopic techniques which suggest that the interaction occurs by an electrostatic mechanism. *In vitro* and *in vivo* toxicity studies reveal that the T-$MnFe_2O_4$ NHSs are benign. Furthermore, we have noticed that T-$MnFe_2O_4$ NHSs are also appearing to be an antimicrobial agent.

6. Effect of Bovine Serum Albumin on Tartrate Modified Manganese Ferrite Nano Hollow Spheres: Spectroscopic and Toxicity Study

6.1. Preamble

Magnetic nano hollow spheres (NHSs) have opened avenues for biomedical applications and diagnostics due to their dimensional similarities with biological molecules [1]. The cost-effectiveness, biocompatibility, non-toxicity, mechanical stability and large specific surface area of 3d transition metal oxides based NHSs demand their potential impact in clinical laboratory [2,3]. As for example, Hyeon et. al. developed a magnetite hollow nanocapsules which is utilized as multifunctional nanocarriers to deliver drugs and provide contrast for MRI [4]. Hence, the influence of NHSs to study the interaction with bio-macromolecules (serum albumin, protein, DNA, RNA and carbohydrate), encapsulation and drug delivery becomes a key area in chemical or bio medical fields. Recently, nano-sized hollow structures have gained tremendous attention because of their low density and enhanced coercivity [5]. Among the ferrites, $MnFe_2O_4$ NHSs show significant magnetization which is potentially useful for magnetic hyperthermia, magnetic imaging and drug delivery [6]. It is already reported that the particles, ranging from 10-200 nm are suitable for biomedical applications. After inoculation of the nano ordered magnetic particle into the blood for drug delivery or some other biomedical applications, they travel through blood which contains thousands of different proteins [7]. Thus the study of absorption/interaction of blood containing protein on the NHSs is very important. The aqueous phase insolubility, absence of inherent optical properties and the agglomerative nature of $MnFe_2O_4$ NHSs restrict their applications in biomedical field. To overcome the drawback of the NHSs, proper surface decoration with a biocompatible ligand is very essential. For example, Dong et al. synthesized and modified $Y_2O_3:Yb^{3+}/Er^{3+}$ hollow nanospheres with PEG which has very good potential in angiography due to the high contrast imaging and long blood circulation time [8]. Also, there are numerous reports on the effect of nanoparticles (NPs) to the macromolecules like DNA and proteins [9-12]. Elango et al. studied on the charge transfer complex of bovine serum albumin (BSA) with quinone and its influence on the ligand binding property [13]. Salis et al. have found that anions bind to the protein surface according to a Hofmeister series ($Cl^- < Br^- < NO_3^- < I^- < SCN^-$) [14]. Similarly, another group has used a photo-induced intramolecular

charge transfer (ICT) fluorescence probe to study the BSA in its native and thermal induced denatured states [15]. Different fluorescent probes also have been developed for studying microenvironment and protein binding sites but the study regarding microscopic origin of fluorescence emission spectra, changes in ligand to metal charge transfer transition (LMCT) due to the presence of ligand and metal ions, d-d transition of metal oxides in presence of protein have not yet been studied in detail [16-18]. Besides, most of the fluorescent probes are bulky in nature and non-magnetic. So, there is a limitation for applying fluorescent probes in many biological purposes. To overcome this problem, designing of new nano biocompatible fluorescent probes based on magnetic property is very essential.

For our current work, we have chosen BSA as our single preferred candidate which helps to maintain the colloidal osmotic pressure and pH of the blood [19]. BSA is a large globular protein that contains 583 amino acid residues [20]. The low cost, easy availability and well-known structure grow an interest to utilize BSA in a wide range [21-24]. This structure and behavior of BSA in aqueous medium helps researchers in finding the interaction of BSA with other proteins, urea, surfactants and nanomaterial using NMR, circular dichroism (CD), UV spectroscopy and fluorescence spectroscopy [25-28].

In the present case, we have synthesized magnetic $MnFe_2O_4$ NHSs and modified with tartrate to use for the biomedical applications. This is very necessary to understand the interaction property of T-$MnFe_2O_4$ NHSs with the protein to use the T-$MnFe_2O_4$ NHSs for biological purposes using the fluorescence and magnetic properties. We have deeply investigated the mechanistic origin of the increasing fluorescence intensity of T-$MnFe_2O_4$ NHSs in presence of BSA by several spectroscopic and other techniques. It is found initially that the tartrate is responsible for LMCT transition from tartrate ligand to the metal ion. But due to the interaction of T-$MnFe_2O_4$ with BSA, the protein enhanced the LMCT transition. BSA is also responsible for the intrinsic d-d transitions centered over Fe^{3+} ions in the NHSs. Addition of BSA into the aqueous solution of T-$MnFe_2O_4$ NHSs deforms the structure of BSA which has been investigated in details. Moreover, we have tried to find out the explanation of the relative fluorescence intensity variation like blue and green of bare T-$MnFe_2O_4$ NHSs and [BSA]-[T-$MnFe_2O_4$] in fluorescence microscope.

We have also examined the toxic effects of the developed nanomaterial both in cellline (RAW 264.7) as well as in rat model. Intriguingly, T-$MnFe_2O_4$ NHSs was found to be non-toxic in both the system we tested.

6.2. Experimental Section

6.2.1. Materials Used

The salts such as $MnCl_2.6H_2O$, $FeCl_3.6H_2O$, oleylamine and bovine serum albumin (BSA) (MW 66.5 kDa), Na_2HPO_4 and NaH_2PO_4 were purchased from Sigma Aldrich. Ethylene glycol, ethanol, disodium tartrate dihydrate and urea were purchased from Loba Chemie. Milli-Q water (Milli-Q Academic with 0.22μm Millipak R-40), DMEM (Hi-Media, India), fetal bovine serum (Gibco, USA) were used for the experiments. MTT, DMSO, Xylene, Paraffin, Eosin, Hematoxylin were purchased from Merck, India. 2´,7´-dichlorofluorescein diacetate (H2DCFDA) (Sigma, USA), CaspACE™ Assay System (Promega, USA) purchased. All the reagents are of analytical grade and used without further modification.

6.2.2. Synthesis and Functionalization of $MnFe_2O_4$ NHSs

In a typical synthesis of $MnFe_2O_4$ NHSs by solvothermal process, high temperature heat treatment of $MnCl_2.6H_2O$ and $FeCl_3.6H_2O$ have been done in presence of urea, oleylamine and ethylene glycol. The prepared $MnFe_2O_4$ NHSs were cyclomixed with 0.5 M disodium tartrate dihydrate solution. The resulting mixture was centrifuged and the collected filtrate is termed as tartrate functionalized $MnFe_2O_4$ (T−$MnFe_2O_4$) NHSs solution. The XRD patterns of the as-synthesized $MnFe_2O_4$ NHSs, EDX analysis, SEM image and TEM analysis of $MnFe_2O_4$ NHSs are shown in our previous report [29]. The TEM image shows the almost spherical shape of $MnFe_2O_4$ NHSs with average diameter of 100 nm.

6.2.3. What is Bovine Serum Albumin?

Bovine serum albumin (BSA) forms almost 55% of blood plasma protein which is derived from cows. It helps to maintain the colloidal osmotic pressure and pH of the blood. BSA is a large globular protein with a molecular weight of 66.5 kDa that contains 583 amino acid residues. It is a single polypeptide chain which is capable to bind with various small molecules, such as steroids, amino acids, metal ions, carbohydrates and other molecules. The secondary structure of BSA contains roughly 67% α-helix structure with six turns which is held by many hydrogen bonds between amino acids at different places in the chain and gives the shape a great stability. The tertiary structure is held by hydrogen bonds, disulphide bonds,

ionic bonds, hydrophobic and hydrophilic interactions. This structure consists of nine loops stabilized by 17 internal strong disulfide (S=S) bonds between 34 cysteine residues.

6.2.4. Preparation of Experimental Solution

1 mM stock solution of BSA was prepared by dissolving the BSA in 10 mM phosphate buffer (NaH_2PO_4 + Na_2HPO_4) at pH 7. Then it was kept at 4 °C for 3 hours to stable the solution. Further, the solution was diluted by adding the phosphate buffer of same concentration for carrying out the experiments. T-$MnFe_2O_4$ NHSs were used for the experiments without further changing the concentration. To carry out all the experiments for three times, T-$MnFe_2O_4$ NHSs solution was freshly prepared and phosphate buffer was used.
For biological studies, T-$MnFe_2O_4$ NHSs were mixed with Milli-Q water (Millipore, USA) to prepare different concentrations required for the experiments.

6.2.5. *In vitro* Analysis

In vitro cytotoxic effects of T-$MnFe_2O_4$ NHSs were investigated following our previous reports [30,31]. In brief, 1×10^6 macrophages (RAW 264.7; ATCC, USA) were cultured in six well culture vessel using DMEM medium supplemented with 10% fetal bovine serum and treated T-$MnFe_2O_4$ NHSs for 6 h at 37 °C in a humidified incubator maintaining 5% CO_2 level. After completion of treatment, cells were harvested by scarping, subjected to centrifugation at 3000×g for 5 min. Cell pellets were washed with PBS (100 mM, pH 7.0) for three times and cell viability was determined by MTT assay as demonstrated below.

6.2.6. MTT Assay

Cell viability of control and T-$MnFe_2O_4$ NHSs treated RAW 264.7 macrophages were determined by MTT (3-(4,5-Dimethylthiazol-2-yl)-2,5-Diphenyltetrazolium Bromide) assay following our previous reports [30,31]. Cells were treated with T-$MnFe_2O_4$ NHSs and harvested by centrifugation as depicted in the above. 200 µl of MTT solution (prepared in 100 mM PBS) was added to each cell pellet, mixed properly and incubated at 37°C for 1 h in dark. Cell suspension was centrifuged at 3000×g for 5 min, supernatant was discarded and purple coloured formazan crystal was further dissolved by the addition of 200 µl of DMSO. Colour intensity was measured spectrophotometrically at 495 nm using a plate reader (Bio-Rad, USA). Cell viability was determined using the following formula:

$$\%Cell\ viability = \frac{Absorbance\ of\ test\ sample}{Absorbance\ of\ control} \times 100$$

6.2.7. *In vivo* Analysis

Toxic effects of the T-$MnFe_2O_4$ NHSs were studied in a mammalian model (Wistar rat). All the animal related experiments were performed after obtaining an ethical clearance from CPCSEA (Reg. no.: 1819/GO/Ere/S/15/CPCSEA), Govt. of India. Three groups (n=6) of adult male rats (120±10 g) were exposed to T-$MnFe_2O_4$ NHSs (25µl/kg body weight mg and 100 µl/kg body weight) through intraperitoneal route for 7 days consecutively. All the experimental animals were provided with water and food *ad libitum*. After termination of the treatment, animals were euthanized and blood was collected through heart puncture. Haematological and biochemical parameters were determined following our earlier reports [30,32]. Besides, liver tissue was perfused with cold PBS (100 mM; pH 7.0) and histology was performed following Mukherjee et al [30]. In brief, liver tissue was cut in small pieces (5 mm × 5 mm), fixed in Bouin's fixative for 24 hours and alcohol gradation was performed. Tissues were treated with xylene, Xylene: paraffin (1:1) and embed in paraffin block to obtain thin section in Ultramicrotome (Weswox, India). Sections were deparaffinized using xylene, mounted on clear glass slide, subjected to staining with haematoxylin and eosin stain followed by the analysis using an optical inverted microscope (Dewinter, Italy).

6.2.8. Assay of Caspase

Activity of caspase-3 in T-$MnFe_2O_4$ NHSs treated macrophages was determined by the substrate-based colorimetric assay as depicted in our earlier reports [30,32].

6.2.9. Determination of Antimicrobial Activity

6.2.9.1. Antibacterial Activity

Antibacterial activity of T-$MnFe_2O_4$ NHSs was investigated by treating the culture of *Escherichia coli* (−ve bacterium) and *Bacillus subtilis* (gram +ve) following our earlier reports [31]. Briefly, bacteria were conducted in Luria-Bartoni (LB) broth (pH 7.0) for 24 h. After reaching the exponential growth phase, bacteria were separately treated with variable doses of T-$MnFe_2O_4$ NHSs and inhibition of microbial growth was monitored by determining

the turbidity (optical density; OD) of both control and treated microbes at 600 nm. All the experiments were performed in triplicate and replicated for at least three times.

6.2.9.2. Antifungal Activity

Antifungal activity of T-$MnFe_2O_4$ NHSs was investigated *in vitro* against a pathogenic fungus isolate *Pichia guilliermondii* (Genbank accession no.: KC771883) following the protocol described by Mukherjee et al [30]. In brief, *P. guilliermondii* was cultured in modified yeast potato dextrose (YPD) broth in presence of T-$MnFe_2O_4$ NHSs in different concentrations. Growth of control and treated fungi were monitored by measuring the turbidity at 600 nm against media control. Each data was collected from the experiments conducted in triplicate and repeated three times at least.

6.2.9.3. Statistical Analysis

All the experiments were performed in triplicate and repeated for three times at least. Data are given as mean ± S.D. Data were analyzed by Student's t-test and/or One-way ANOVA using Graphpad Prism 5.0. $p<0.05$ was considered as statistically significant.

6.2.10. Characterization

Magnetic measurements were carried out in a Lake Shore vibrating sample magnetometer (VSM).

The UV-visible (UV-vis) absorption spectra of tartrate modified $MnFe_2O_4$ NHSs solution along with BSA were taken on a Shimadzu UV-2600 spectrophotometer with a quartz cuvette of 1 cm path length. The steady-state fluorescence emission and excitation spectra of the same solutions were recorded on a Horiba Jobin Yvon Fluorolog fluorimeter. The Fluorescence anisotropy measurement was carried out in a Hitachi F-7000 Fluorescence Spectrophotometer. Fluorescence anisotropy is defined as

$$r = (I_{VV} - G.I_{VH})/(I_{VV} + 2G.I_{VH})$$

where I_{VV} and I_{VH} refer to the emission intensities obtained with the excitation polarizer oriented vertically and the emission polarizer oriented vertically and horizontally, respectively. The *G* factor is defined as

$$G = I_{HV}/I_{HH}$$

where the intensities I_{HV} and I_{HH} are the vertical and horizontal positions of the emission polarizer with the excitation polarizer being horizontal respectively. Time-resolved fluorescence spectra were carried out on a commercially available spectrophotometer (LifeSpec-ps) from Edinburgh Instruments, U.K. For the 320 nm laser source, the instrument response function (IRF) was 90 ps. The data were fitted using Igor Pro 6.34A data analysis software.

The circular dichroism (CD) spectra were recorded on JASCO J815 spectropolarimeter (Jasco International Co. Ltd, Hachioji, Japan) equipped with a Peltier temperature control system (model PTC-348WI). The instrument parameters for CD measurements were 50 nm/min, band width 1.0 nm, and sensitivity of 100 millidegree. The path length of the cuvette used was 1 cm. The concentration of BSA was fixed at 1 μM. The ellipticity values are expressed in terms of mean residue molar ellipticity (θ), in units of deg.cm^2.dmol^{-1}. Secondary structure calculations were performed by the software supplied by Jasco.

6.3. Results and Discussion

6.3.1. Magnetic Analysis of $MnFe_2O_4$ NHSs

To investigate the magnetic properties of $MnFe_2O_4$ NHSs, M-H hysteresis loops of the sample with maximum applied field of 14 kOe at 80 K and 300 K were carried out (Figure 6.1.(a)). At around room temperature (300K), H_C, M_R and M_S values of NHSs are found to be 128.7 Oe, 13.3 emu/g and 55.8 emu/g respectively, displaying the soft ferrimagnetic nature of $MnFe_2O_4$ NHSs. On lowering temperature (at 80 K), H_C = 163.8 Oe, M_R = 18.2 emu/g and M_S = 68.8 emu/g values of NHSs are increasing than 300 K as the increased value of magnetic anisotropy at lower temperature is preventing the orientation of magnetic spins in an applied field. Also reduced thermal fluctuation at 80 K helps to achieve higher magnetization in the sample.

Further, M-T curves of NHSs are measured in presence of 100 Oe field at 10 K interval within the temperature region of 80 K–400 K during both zero field cooled-heating (ZFCH) and FCH mode, are shown in Figure 6.1.(b). The separation gap between FCH and ZFCH curves is related to anisotropy energy barrier which is related to magneto-crystalline energy of the sample. Also split between FCH and ZFCH curves in the whole region 80–400 K indicates that blocking temperature (T_B) for this sample is situated above 400 K [33].

Moreover, it shows that $MnFe_2O_4$ NHSs with size 100 nm maintain cubic structural phase throughout 80–300K as no phase transtion cusp for ferrites i.e. Verway transition is found in this region.

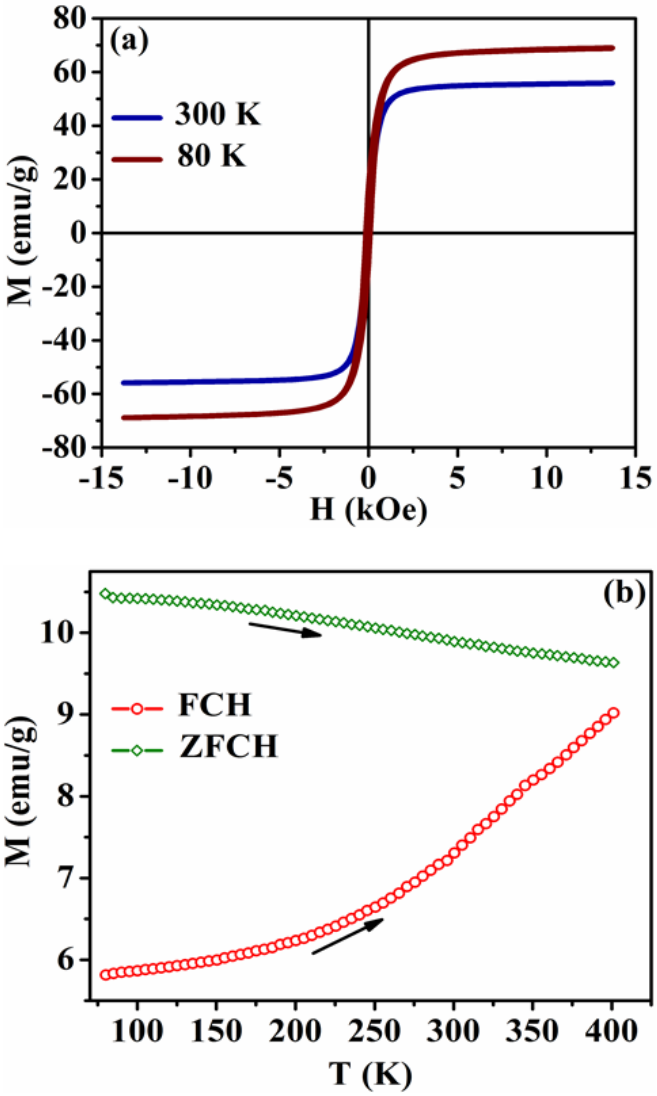

Figure 6.1. (a) M-H hysteresis loops at 300 K and 80 K and (b) Temperature (T) dependence of Magnetization (M) under ZFCH and FCH mode for $MnFe_2O_4$ NHSs.

To understand the dynamic nature of magnetization, magnetic relaxation property of the sample is measured. In Figure 6.2, after removal of aligning field of 14 kOe, variation of M with time is recorded. At first M sharply falls, then tries to retain it which reflects the influence of Neel and Brownian relaxation. The graph is fitted with $M(t) = M(0)e^{-t/\tau}$, where τ is relaxation time constant that represents ability to retain the magnetization as well as the interaction between magnetic spins.

The larger wall thickness of NHSs than it's crystallite or single domain size suggests non-existence of superspin state and also from the high value of T_B , strong interaction between super spins can not be expected around room temperature which is a possible reason behind the high value of τ = 1137 sec found here [34].

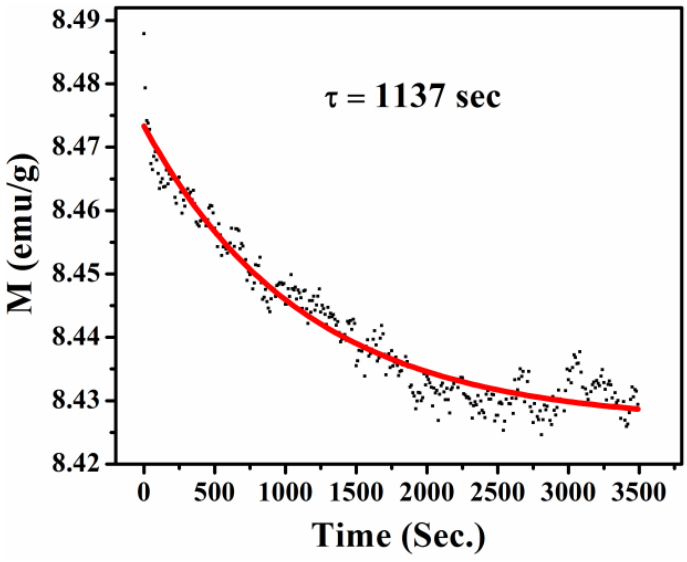

Figure 6.2. M vs. time curve at room temperature for $MnFe_2O_4$ NHSs.

6.3.2. UV-vis Absorption Study

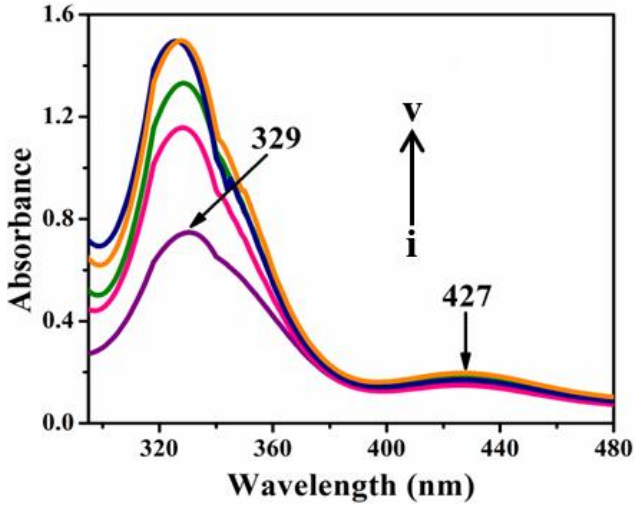

Figure 6.3. Absorbance titration profile of T-$MnFe_2O_4$ NHSs complex with increasing concentration of BSA of (i) 0.0, (ii) 0.266, (iii) 0.398, (iv) 0.530, (v) 0.660 μM. For 3 successive measurements calculated error is ±5%.

To study the protein sensing ability and changes in LMCT band as well as the d-d transition of the metal ion in presence of BSA, we investigated the UV-vis absorption profile of T-$MnFe_2O_4$ upon addition of increasing concentration of BSA which is shown in Figure 6.3. The absorption peak of T-$MnFe_2O_4$ NHSs at 329 nm is due to LMCT and that at 427 nm is assigned to d-d transition centered over Fe^{3+} ions in the NHSs. The absorption at 329 nm increases with a maximum blue shift of 5 nm on addition of BSA and clearly indicates the interactions between BSA and hydrophilic T-$MnFe_2O_4$ NHSs. A slight change in polarity in the hydrophilic environment of T-$MnFe_2O_4$ NHSs in presence of BSA is the reason behind the blue shift [35]. An increasing absorption at 427 nm on adding BSA also indicates more d-d transition due to decrement in t_{2g} and e_g level of d-orbitals centered over metal ion.

6.3.3. Fluorescence Emission Study

The evidence of the interaction of BSA to the T-$MnFe_2O_4$ NHSs was derived from fluorometric titration. When excited at 299 nm, BSA exhibits emission spectra at around 347 nm in Figure 6.4.(a). The addition of only 0.266 µM of BSA in the T-$MnFe_2O_4$ NHSs solution shows an emission spectrum at 378 nm against the excitation wavelength of 299 nm. The red shifted emission peak of BSA from 347 to 378 nm in presence of T-$MnFe_2O_4$ NHSs is due to the addition of BSA in the solution medium. Further, the addition of higher concentration of BSA resulted the solution medium less polar [36]. As a result, maximum blue shift of 10 nm (378nm to 368nm) along with the increase in intensity is observed when 0.660 µM BSA was added in the T-$MnFe_2O_4$ NHSs solution. This signifies slight change in polarity of the local environment of the fluorescent molecule as the environment becomes less polar due to the replacement of water molecules (ε=80) by less polar BSA. The difference between ground and excited states of BSA increases on reducing polarity of the environment resulting lower wavelength emission spectra (blue shift) and returning of more electrons to ground state (higher intensity). The tartrate ligand (charge, surface density and length) also plays a major role in determining the spectral changes [37]. In polar environment of the solution medium, T-$MnFe_2O_4$ NHSs are negatively charged due to the presence of tartrate ligand on the outer surface of $MnFe_2O_4$ NHSs. On adding BSA in the solution, a strong binding of tartrate ligand to the BSA takes place due to the formation of salt bridges between the negatively charged tartrate and the carboxylate ammonium type of lysine on the BSA surface. It is already established that BSA prefers to bind negatively charged surface of ligands [38]. Although BSA is negatively charged at pH 7 still it binds preferentially to

negatively charged tartrate which is somewhat puzzling. The isoelectric point of BSA is 4.6 which suggest that overall charge of BSA is negative but the attractive electrostatic interaction of 60 surface lysine groups with the tartrate moiety make this binding possible [39-41].

To explore the mechanistic origin of enhanced LMCT and d-d transition in presence of BSA, T-$MnFe_2O_4$ NHSs are excited at different wavelengths with increasing concentration of BSA at pH 7. Figure 6.4.(b) shows emission spectra in the range of 396-399 nm upon exciting the T-$MnFe_2O_4$ NHSs in presence of BSA at 329 nm. T-$MnFe_2O_4$ NHSs solution shows an emission spectrum at 396 nm but the increasing concentration of BSA in the medium, shifted emission wavelength (λ_{em}) to 401 nm with a red shift of 5 nm. The extended charge transfer from negatively charged BSA to tartrate to Mn^{2+}/Fe^{3+} ions causes an increment in fluorescence intensity. When T-$MnFe_2O_4$ NHSs are excited at 427 nm and it shows an emission spectrum at 496 nm as evident in Figure 6.4.(c). Further the increasing concentration of BSA results in the red shift of 13 nm (from 496 to 509 nm) with increasing fluorescence intensity. A strong electrostatic interaction between the BSA and the carboxylate group (COO^-) of tartrate ligand loose the ligand-metal interaction. It affects the d-d transitions of Fe^{3+} ions. As Mn^{2+} and Fe^{3+} both are d^5 system, they are Laporte and spin forbidden [40]. However, considerable d-d transitions of Fe^{3+} occur due to the relaxation of selection rules by spin orbit coupling and octahedral distortion [42]. The energy gap between t_{2g} and e_g of Fe^{3+} ion decreases and hence fluorescence intensity of d-d transition increases with addition of BSA in the solution medium [43,44]. These results strongly suggest the effect of BSA on the T-$MnFe_2O_4$ NHSs.

The binding affinity (K_{BH}) of the [BSA]-[T-$MnFe_2O_4$] complex was also determined from fluorometric titration of T-$MnFe_2O_4$ NHSs with increasing concentration of BSA using modified Benesi–Hildebrand equation

$$\frac{1}{\Delta F} = \frac{1}{\Delta F_{max}} + \frac{1}{(\Delta F_{max})K_{BH}} \times \frac{1}{[\mathrm{BSA}]}$$

where, ΔF is the difference in fluorescence intensity in presence and absence of BSA and [BSA] is the BSA concentration. The Benesi−Hildebrand association constant (K_{BH}) could be determined from the ratio of the intercept to the slope of the straight line of the plot of $1/\Delta F$ against 1/[BSA].

The calculated binding affinity value (K_{BH}) is estimated to be (1.06±0.32)x10^6 M^{-1} in Figure 6.4.(d) which is in good accordance with the binding constant value evaluated from the UV-vis absorption spectroscopic data.

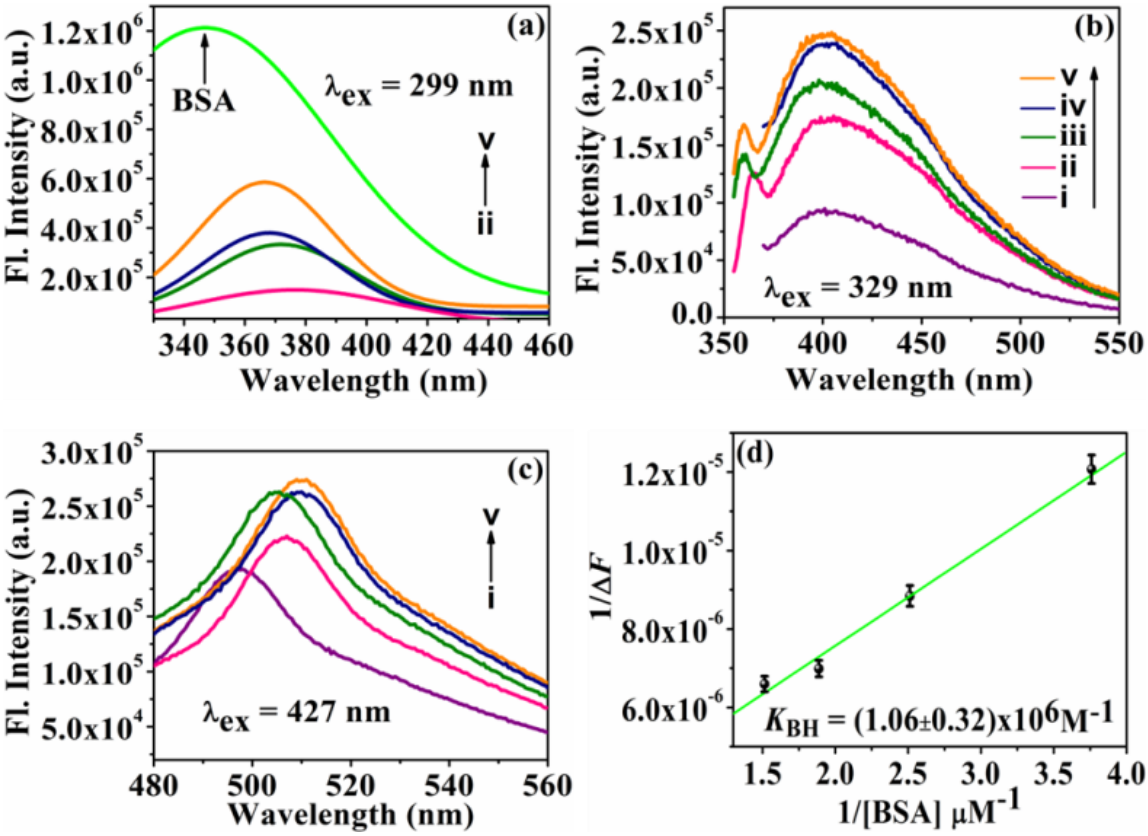

Figure 6.4. Fluorescence emission spectra of (a) BSA in phosphate buffer and BSA in increasing concentration of (ii) 0.266, (iii) 0.398, (iv) 0.530, (v) 0.660 μM at λ_{ex} = 299 nm in T-$MnFe_2O_4$ NHSs, (b)-(c) T-$MnFe_2O_4$ NHSs with increasing concentration of (i) 0.0, (ii) 0.266, (iii) 0.398, (iv) 0.530, (v) 0.660 μM BSA at λ_{ex} = 329 nm and 427 nm respectively. For 3 successive measurements calculated error is ±5% (d) Modified Benesie-Hildebrand plot for the complexation of BSA with T-$MnFe_2O_4$ NHSs from fluorescence data of λ_{ex} = 329 nm. Error bars are calculated from the standard deviation of 3 successive measurements.

To investigate whether BSA is attached only with T-$MnFe_2O_4$ NHSs, we performed the relative fluorescence intensity study of BSA in presence of water and tartrate separately. Figure 6.5 confirms that the relative fluorescence intensity of BSA is maximum with T-$MnFe_2O_4$ NHSs which is followed by H_2O and tartrate respectively.

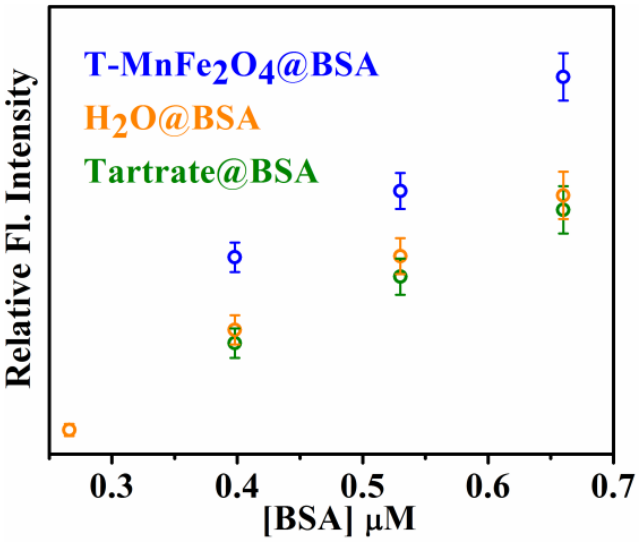

Figure 6.5. The comparative fluorescence intensity of BSA in presence of T-$MnFe_2O_4$ NHSs, H_2O and tartrate. Error bars are calculated from the standard deviation of 3 successive measurements for each case.

The continuous variation protocol (Job's plot) is carried out for the determining the stoichiometry of the complexation of [BSA]-[T-$MnFe_2O_4$]. The plot of difference fluorescence intensity (ΔF) at the wavelength maxima versus the mole fraction of the T-$MnFe_2O_4$ NHSs added revealed a single binding mode (Figure 6.6). Continuous variation analysis was done at 298.15 K (λ_{ex}= 329 nm). From the inflection point, mole fraction (χ) value was found to be 0.51. Thus, stoichiometry was estimated to be around 0.96.

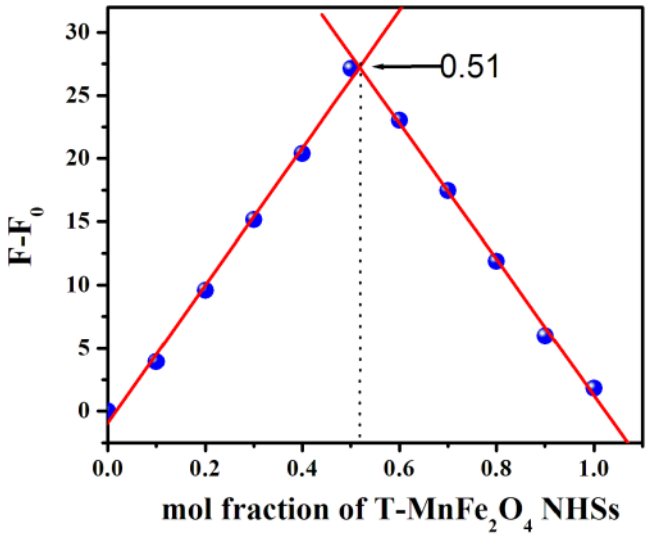

Figure 6.6. Job's plot depicting change in fluorescence intensity versus mole fraction of T-$MnFe_2O_4$ NHSs.

6.3.4. Steady State Fluorescence Anisotropy Study

Steady state fluorescence anisotropy measurement is a useful experiment to know how the surrounding environment imposes motional restriction on the fluorophore [45]. It also gives the information about the fluorophore in liquid media where the fluorophore can rotate freely but the increase in the rigidity in the environment surrounding the fluorophore can causes an enhancement in the anisotropy value [46]. Figure 6.7.(a) depicts the change in the anisotropy value of T-$MnFe_2O_4$ NHSs with an increasing concentration of BSA in phosphate buffer medium. The figure reveals that with the addition of BSA (0.660 μM) in the medium, the fluorescence anisotropy increases from 0.029 to 0.084 monotonically before leveling off. This fact clearly indicates that substantial restriction on free motion of T-$MnFe_2O_4$ NHSs is imposed with the addition of BSA. This happens due to the binding of BSA with T-$MnFe_2O_4$ NHSs.

The binding constant of the [BSA]-[T-$MnFe_2O_4$] can be estimated using Ingersoll and Strollo method [47]

$$\frac{1}{f_B} = 1 + \frac{1}{K_b[\mathrm{BSA}]}$$

where K_b is the apparent binding constant of the [BSA]-[T-$MnFe_2O_4$]. f_B corresponds to the fractional fluorescencence contribution of T-$MnFe_2O_4$ NHSs bound to BSA:

$$f_B = \frac{r - r_F}{R(r_B - r) + (r - r_F)}$$

where the anisotropy value of free T-$MnFe_2O_4$ and [BSA]-[T-$MnFe_2O_4$] are denoted by r_F and r_B respectively. The correction factor R is the ratio of intensity of [BSA]-[T-$MnFe_2O_4$] and T-$MnFe_2O_4$ NHSs. The double reciprocal plot of $1/f_B$ versus 1/[BSA] is shown in Figure 6.7.(b) which is a straight line and from the slope K_b value is estimated to be $(1.21\pm0.21)\times10^6$ M^{-1} which is in good agreement with the value obtained from the spectrofluorometric titration experiment. Thus the fluorescence anisotropy study suggests the strong binding affinity of T-$MnFe_2O_4$ NHSs to BSA and this method is feasible to find out the binding constant [48].

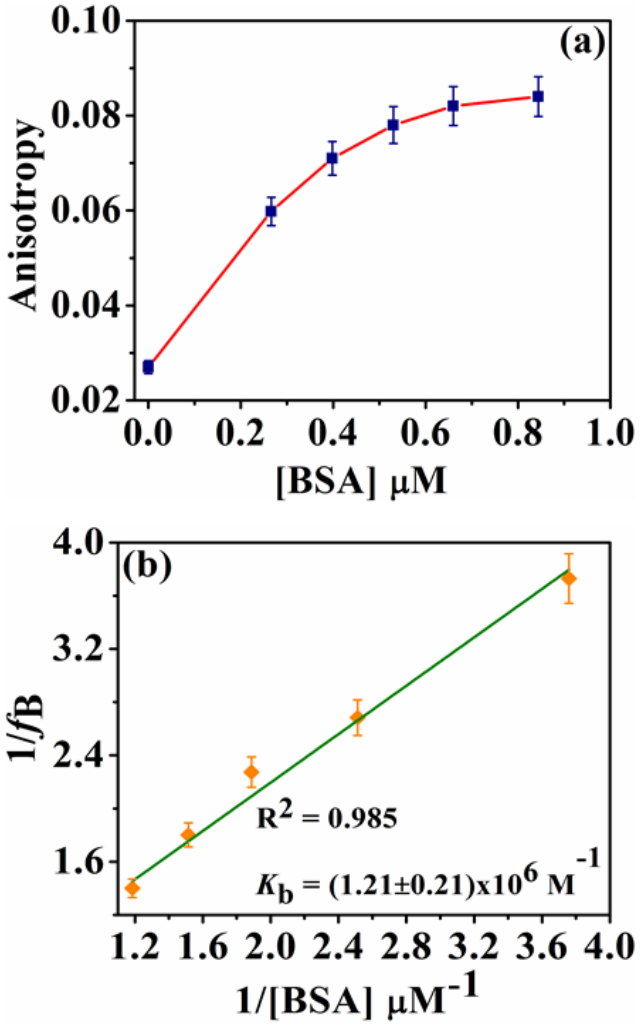

Figure 6.7. (a) Variation of steady state fluorescence anisotropy of T-$MnFe_2O_4$ NHSs as a function of BSA concentration. λ_{ex} = 329 nm and λ_{em} = ~396 nm for T-$MnFe_2O_4$ NHSs. (b) $1/f_B$ vs 1/[BSA] plot to evaluate the binding constant for the complexation of BSA with T-$MnFe_2O_4$ NHSs. Error bars are calculated from the standard deviation of 3 successive measurements.

6.3.5. Fluorescence Microscopic Imaging

Further, to understand the fluorescent intensity difference of T-$MnFe_2O_4$ NHSs and [BSA]-[T-$MnFe_2O_4$], fluorescence microscopic images are obtained. Figure 6.8.(a) and (b) indicate the fluorescent colors such as blue and green upon exciting the T-$MnFe_2O_4$ NHSs under UV and blue light irradiation respectively. Intensity of the same fluorescent colors (blue and green) increases noticeably with the addition of only 0.398 μM of BSA into the T-$MnFe_2O_4$ NHSs solution which is illustrated in Figure 6.8.(c) and (d) respectively. The main reason for increasing intensity of [BSA]-[T-$MnFe_2O_4$] is due to the extended charge transfer through the formation of salt bridge between BSA and tartrate ligand of T-$MnFe_2O_4$ NHSs which we

have discussed earlier. During this experiment, we fixed the excitation wavelengths at 340-390 (for UV) and 460-495 (for blue) nm for generating blue and green fluorescence of the sample respectively.

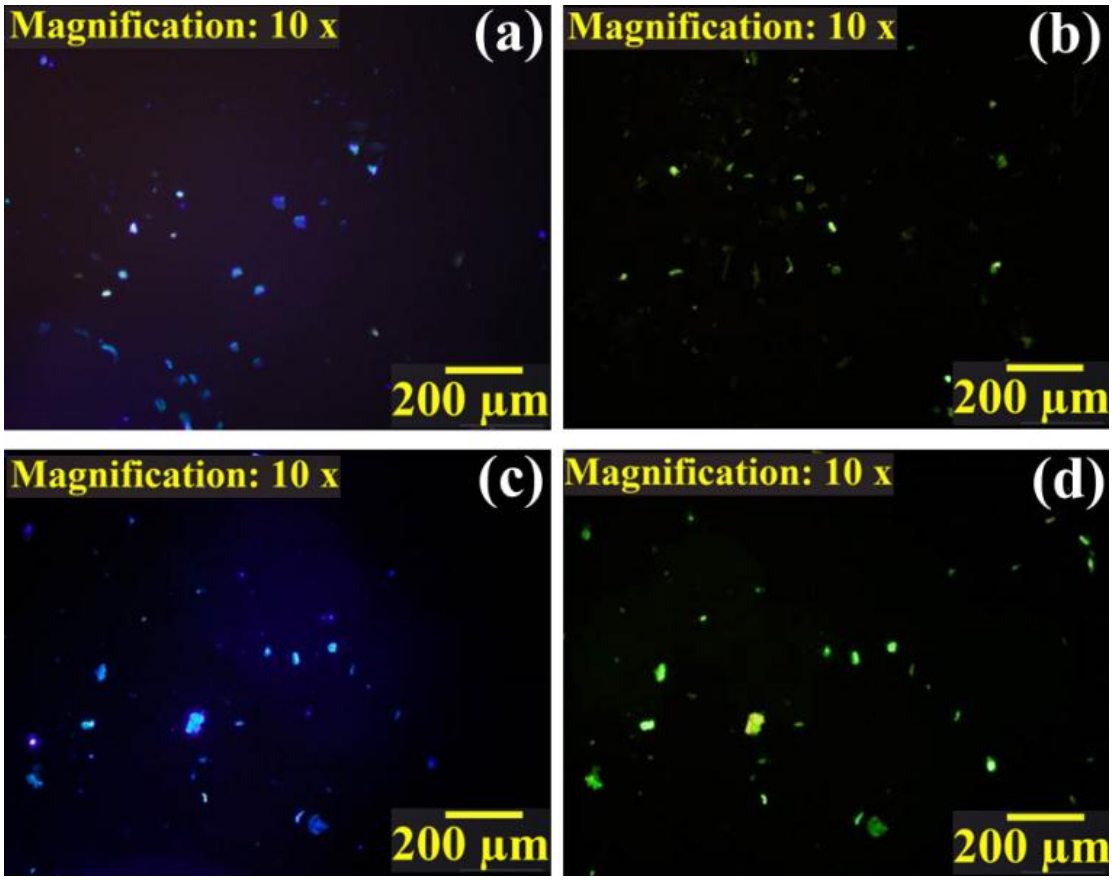

Figure 6.8. Fluorescence microscopic images of T-$MnFe_2O_4$ NHSs under (a) UV and (b) blue light irradiation. The higher fluorescence intensity of [BSA]-[T-$MnFe_2O_4$] NHSs is observed under (c) UV (d) blue light irradiation. The scale bars in all the images are 200 µm.

6.3.6. Effect of pH in Fluorescence Intensity

A series of emission spectra (357-498 nm) of [BSA]-[T-$MnFe_2O_4$] were recorded in the pH ranging from 3 to 10 against the excitation wavelength (λ_{ex}) of 329 and 427 nm and are shown in Figure 6.9.(a) and (b) respectively. In two cases, maximum intensity is observed at basic medium (pH 10), followed by acidic (pH 3) and neutral (pH 7) medium. The difference in fluorescence intensity in different pH range is explained by a simple schematic (Scheme 6.1).

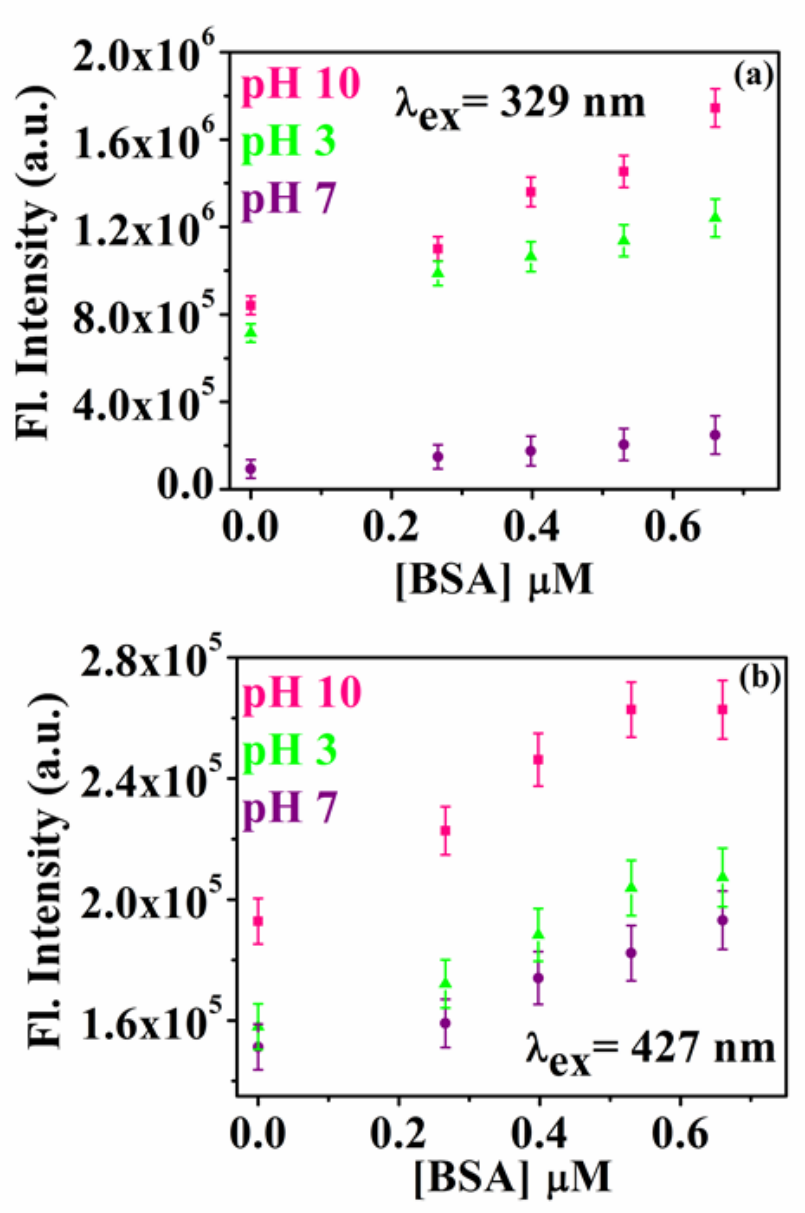

Figure 6.9. pH titration of T-$MnFe_2O_4$ NHSs with increasing concentration of BSA of (i) 0.0, (ii) 0.266, (iii) 0.398, (iv) 0.530 and (v) 0.660 μM at (a) λ_{ex} = 329 nm and (b) λ_{ex} = 427 nm. Error bars are calculated from the standard deviation of 3 successive measurements for each case.

The plausible complexation of metal unit by the tartrate in neutral medium (pH 7) is shown in Scheme 6.1.(A-C). Dissolving of tartrate into water medium maintains the equilibrium of the system and the complex formation drives the reaction forward. Chelation of $MnFe_2O_4$ NHSs is favorable in aqueous medium by tartrate for having a binding site; α- hydroxy carboxylate group [49,50]. Further, addition of sodium hydroxide (pH 10) in T-$MnFe_2O_4$ NHSs, the carboxylic acid (-COOH) group converted into carboxylate ($-COO^-$) group in Scheme 6.1.(D) and the bond rearrangement (Scheme 6.1.(F)) helps to donate more electrons to the metal

ions. Now the addition of increasing concentration of BSA in the T-$MnFe_2O_4$ NHSs is strongly influenced by the pH and the electrostatic interaction of BSA with the T-$MnFe_2O_4$ complex gets more favorable. Due to addition of hydrochloric acid (pH 3) in the T-$MnFe_2O_4$ NHSs, -COOH group gets protonated (Scheme 6.1.(E)) and the bond rearrangement forms the resonance structure (Scheme 6.1.(G)) which donates electrons to the metal ions but unlike the basic medium. For the formation of chelate complex in acid medium, tartrate ligand gets hydrolysis over the –COOH group but the chelate formation in basic medium is successively more stable rather in acid medium [51,52]. As a result, T-$MnFe_2O_4$ NHSs and [BSA]-[T-$MnFe_2O_4$] in basic medium show better fluorescence intensity rather in acid medium against the excitation wavelength of 329 and 427 nm. Finally, the minimum fluorescence intensity of T-$MnFe_2O_4$ NHSs at pH 7 (Scheme 6.1.(C)) can be explained on the basis of nucleophilicity of C=O, C-OH and C-O^- groups. As the nucleophilicity of C=O is much lower comparing with the C-OH and C-O^-, the electron donation from C=O to the metal ions is less. As a result, the fluorescence intensity of T-$MnFe_2O_4$ NHSs and [BSA]-[T-$MnFe_2O_4$] is lowest in neutral medium comparably with the basic and acidic medium against the excitation wavelength of 329 and 427 nm.

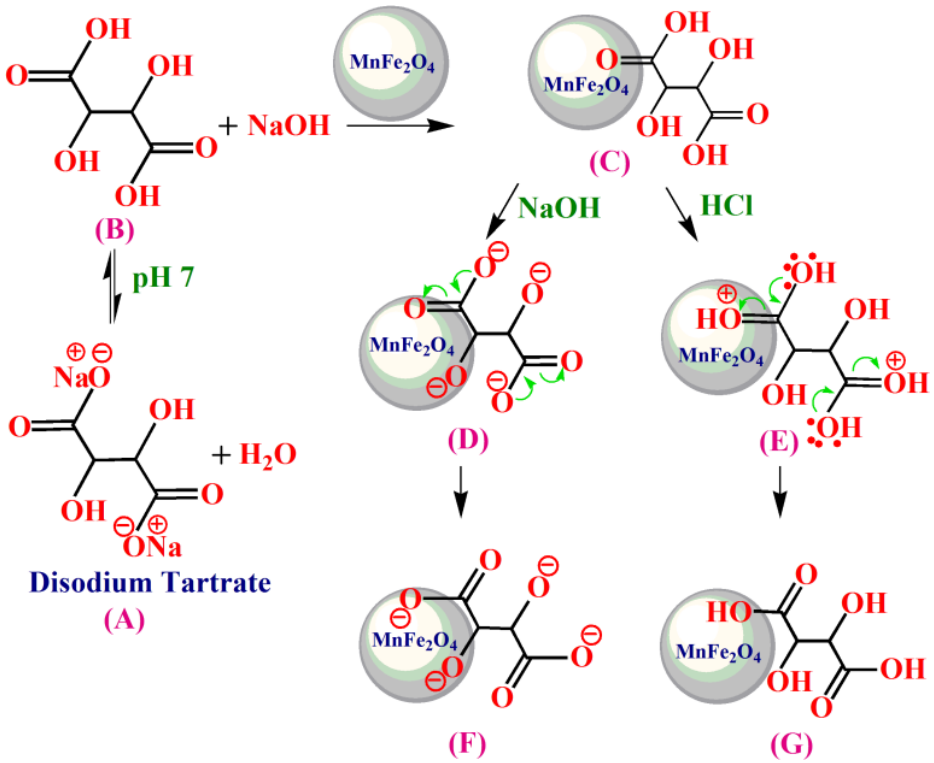

Scheme 6.1. The plausible formation process of T-$MnFe_2O_4$ framework in neutral, basic and acidic medium.

6.3.7. Temperature Dependent Fluorescence Study

Temperature dependent fluorescence was also carried out at five different temperatures (296.15 K, 298.15 K, 301.15, 304.15 K and 306.15K) to evaluate the thermodynamic parameters (ΔG, ΔH and ΔS) for the formation of adduct between BSA and T-$MnFe_2O_4$ using the classical Van't Hoff equation

$$\ln K = -\frac{\Delta H^0}{RT} + \frac{\Delta S^0}{R}$$

where, K is the association binding constant corresponding to various temperatures and R is the gas constant (8.314 J K^{-1} mol^{-1}). The standard state enthalpy changes ($\Delta H°$) can be calculated from the slope of the Van't Hoff plot ln$K$ versus 1/T, the standard molar entropy change ($\Delta S°$) can be calculated from the intercept and standard molar Gibbs energy ($\Delta G°$) can be estimated from the following relationship

$$\Delta G° = \Delta H° - T\Delta S°$$

The binding constants are calculated from the fluorescence titration of the complex T-$MnFe_2O_4$ NHSs with BSA (as described earlier) at the five different temperatures 296.15K, 298.15 K, 301.15 K, 304.15 K and 306.15 K respectively. Some marginal decrease in the binding constant values was observed and from these values the Van't Hoff plot ln K versus 1/T was constructed (Figure 6.10).

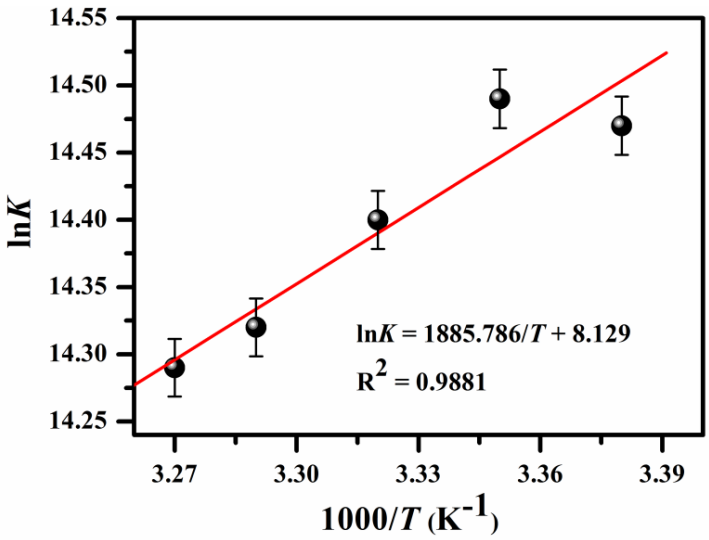

Figure 6.10. Van't Hoff plot for the binding of BSA with T-$MnFe_2O_4$ NHSs. Error bars are calculated as the standard deviation of 3 successive measurements.

Table 6.1. Binding constants (*K*) and relative thermodynamic parameters for the binding reaction between BSA and T-$MnFe_2O_4$ NHSs at pH 7.

Complex	*T*(K)	*K* (10^6 M^{-1})	ΔG° / kJ mol^{-1}	ΔH° / kJ mol^{-1}	ΔS° / J mol^{-1}
T-$MnFe_2O_4$ NHSs	296.15	1.92±0.01	-35.69	-15.68	67.58
	298.15	1.98±0.01	-35.83		
	301.15	1.81±0.01	-36.03		
	304.15	1.66±0.01	-36.23		
	306.15	1.61±0.01	-36.37		

The value of the thermodynamic parameters was listed in Table 6.1. The negative value of $\Delta H°$ indicates that the interaction process is exothermic in nature. Negative binding free energy and positive entropy also imply that the BSA binding process is thermodynamically favorable [53,54]. Moreover, slightly decreasing value of rate constant upon increasing temperature implies that the interaction between the BSA and T-$MnFe_2O_4$ NHSs becomes weak.

6.3.8. Time Resolved Fluorescence Decay Study

Time resolved fluorescence measurement is a very useful and sensitive technique to study and predict the effect of the microenvironment surrounding a fluorescent molecule. We have measured the fluorescence lifetime of T-$MnFe_2O_4$ NHSs in presence of different concentration of BSA.

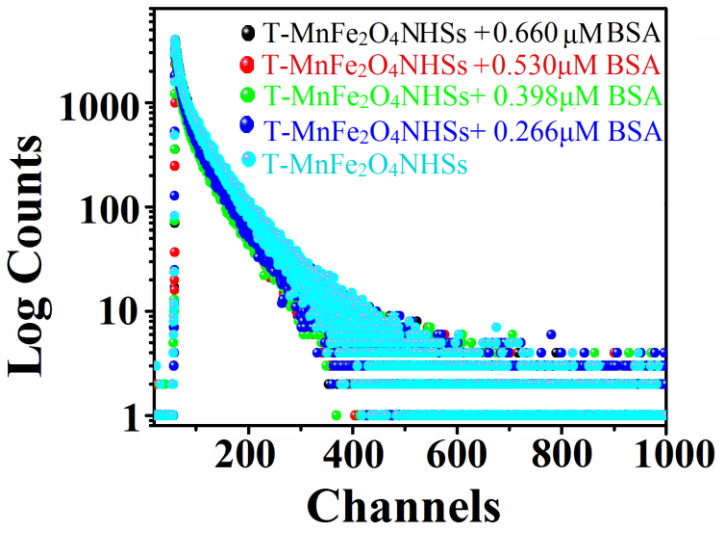

Figure 6.11. Fluorescence decay profile of T-$MnFe_2O_4$ NHSs (5 µM) in presence of increasing concentration of BSA (0-0.660 µM).

The nanosecond lifetime decay study of T-$MnFe_2O_4$ NHSs (5 μM) in absence and presence of BSA (0-0.660 μM) were recorded at an excitation wavelength of 320 nm whereas the emission wavelength was at 400 nm. A comparative decay profile is depicted in Figure 6.11 and the average fluorescence lifetime (τ_{av}) for biexponential decay curve was obtained from the equation

$$\tau_{av} = \tau_1 a_1 + \tau_2 a_2$$

where τ_1 and τ_2 are the two relaxation time constants with normalized pre-exponential factors a_1 and a_2 respectively. The biexponential fitting of the decay processes provides the parameters which are given in Table 6.2. As for BSA, the shorter lifetime is independent of any structure, association of the tryptophan structure in the excited state and the longer lifetime component is attributed to the interaction between the BSA and the surrounding microenvironment of the medium. The fluorescence lifetime (τ_{av}) thus refers to the average time of a molecule which stays in its excited state before emitting a photon. The τ_{av} values are found to be higher in presence of BSA than the native complex. This increase in lifetimes of T-$MnFe_2O_4$ NHSs in presence of BSA is due to the decreased non-radiative rates in the BSA environment [55]. Interestingly, the addition of BSA leads to a further increase in lifetime signifies the better interaction of the T-$MnFe_2O_4$ NHSs with the BSA [56]. This is in compliance with the steady state fluorescence titration as described earlier.

Table 6.2. Lifetime values of fluorescence decay of compound (5 μM) in presence of increasing concentration of BSA (0-0.660 μM). χ^2 represents the goodness of fit. Errors are calculated as the standard deviation of 3 successive measurements.

T-$MnFe_2O_4$ NHSs	**BSA (μM)**	**Lifetime (ns)**					χ^2
		τ_1	τ_2	a_1	a_2	τ_{av}	
5 μM	0	0.44±0.03	3.56±0.07	0.68	0.32	1.42±0.07	1.04
	0.266	0.65±0.02	3.96±0.06	0.66	0.34	1.79±0.04	1.05
	0.398	0.68±0.09	4.13±0.08	0.65	0.35	1.89±0.03	1.07
	0.530	0.69±0.10	4.65±0.09	0.64	0.36	2.11±0.21	1.03
	0.660	0.71±0.05	4.90±0.08	0.65	0.35	2.17±0.11	1.06

6.3.9. Circular Dichroism Study

Circular dichroism (CD) spectrometry is an important tool for the quantification of the conformational changes in the secondary structure of BSA after absorbed onto nanoparticle complex [57]. The structural and conformational change of BSA in presence of T-$MnFe_2O_4$ NHSs was measured by the circular dichroism (CD) spectra in the far-UV region (190−260 nm) at room temperature in absence and in presence of T-$MnFe_2O_4$ NHSs (Figure 6.12).

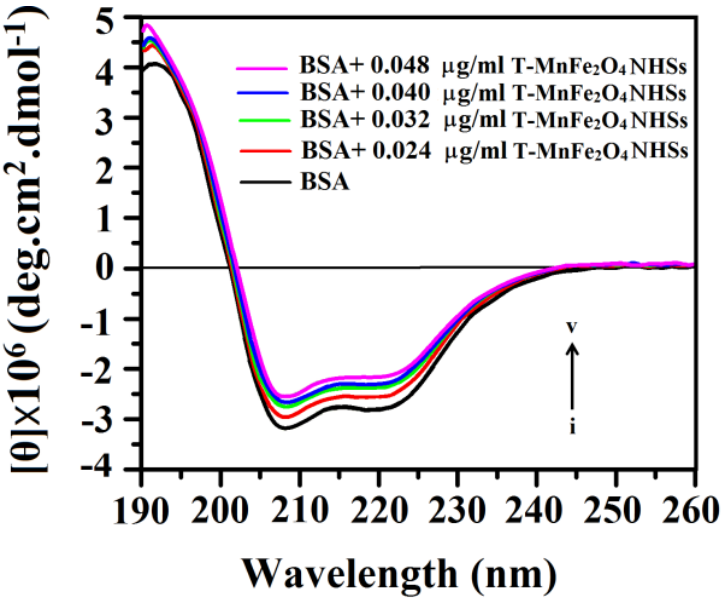

Figure 6.12. CD spectra of BSA in presence of different concentration of T-$MnFe_2O_4$ NHSs in phosphate buffer at pH 7 and T = 298 K.

Two negative bands in the UV region of pure BSA at 208 and 222 nm have been assigned as the n → π* transition due to the peptide bond of α-helix. The CD spectra of BSA with different concentrations of T-$MnFe_2O_4$ NHSs were collected after baseline by CD spectra of only the corresponding T-$MnFe_2O_4$ NHSs concentration. Using the following equation, the observed CD results were first converted into mean residue ellipticity (MRE) according to the following equation

$$\text{MRE (deg cm}^2\text{ dmol}^{-1}) = \frac{\theta_{obs}}{c_p n l \times 10}$$

Where, C_p is the concentration of BSA in μM, θ_{obs} is the observed ellipticity in mdeg, l is the path length in cm (here 1 cm), and n is the number of amino acid residues of protein (583 for BSA).The α-helix contents of BSA had been calculated from MRE values at 208 nm using the following equation [58]

$$\% \, \alpha - \text{helix} = \frac{-\text{MRE}_{208} - 4000}{33000 - 4000} \times 100$$

The estimated α-helicity content of native BSA in phosphate buffer at pH 7 and T = 298 K was found to be 56.1% and in presence of T-$MnFe_2O_4$ NHSs the intensity of α-helix gradually decreases with increasing concentration of nano complex. The % of the helical content changes from ~56.1 to ~49.3 (±3%) at 0.024 μg/ml T-$MnFe_2O_4$ NHSs, to ~45.2 (±3%) at 0.032 μg/ml T-$MnFe_2O_4$ NHSs, to ~44.8 (±3%) at 0.040 μg/ml T-$MnFe_2O_4$ NHSs and to ~41.9 (±3%) at 0.048 μg/ml T-$MnFe_2O_4$ NHSs is shown in Table 6.3. The results indicate that the conformational changes of BSA were observed after absorbed onto T-$MnFe_2O_4$ NHSs surface but the secondary structure of BSA retains predominantly its α-helix character, the shape of the peaks and the maximum peak position remained almost the same.

Table 6.3. The *α*-helical content (±3%) of BSA for three successive measurements in different concentration of T-$MnFe_2O_4$ NHSs.

Conc. of T-$MnFe_2O_4$ NHSs (μg/ml)	**% of α-helix**
0	56.1
0.024	49.3
0.032	45.2
0.040	44.8
0.048	41.9

6.3.10. T-$MnFe_2O_4$ NHSs are Non-toxic

The most important trait of a therapeutic nanomaterial is its non-toxic nature. It means that a nanomaterial can only explore for biological application if it possesses no noxious effect on human or other mammals. Herein, T-$MnFe_2O_4$ NHSs were tested in *in vitro* model i.e. RAW 264.7 macrophages and animal model i.e. rat.

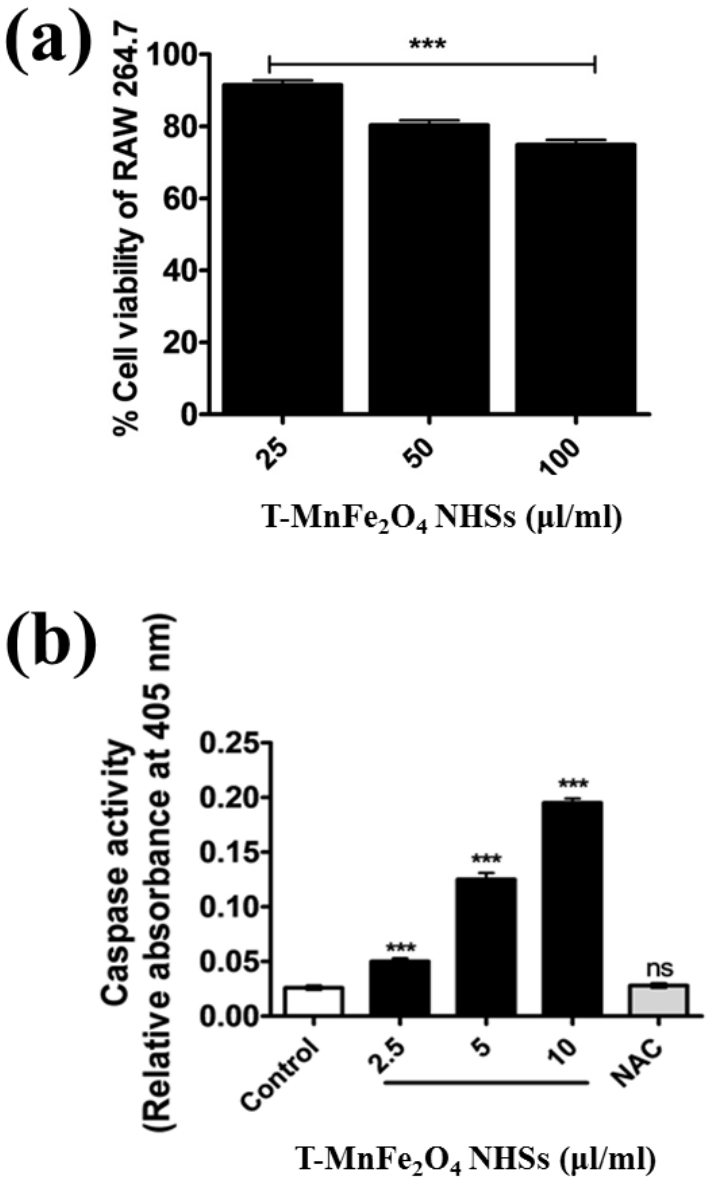

Figure 6.13. (a) MTT assay showing cell viability of RAW 264.7 macrophages. (b) Caspase activity in T-$MnFe_2O_4$ NHSs treated macrophage cells in vitro.

RAW 264.7, a mouse cell line of macrophage (an immune cell) was selected as a model for testing the toxicity of T-$MnFe_2O_4$ NHSs (Figure 6.13.(a)). An ideal nanotherapeutic (anticancer or antimicrobial) should not induce any adverse effect on the immune cell system of the recipient. Treatment of macrophage culture with T-$MnFe_2O_4$ NHSs did not induce any sign of cytotoxicity even after 24 h of incubation (Figure 6.13(a)). Cell viability study using MTT assay revealed no significant degree of cell death in T-$MnFe_2O_4$ NHSs treated cells (Figure 6.13.(a)). However, at the highest dose minute level (~18%) of cell death was observed (Figure 6.13.(a)). We have analyzed whether such death is normal or due to toxicity of T-$MnFe_2O_4$ NHSs**.** Our experimental data on caspase-3 activity clearly revealed that

upregulation of caspase-3 activity leads to such cell death (Figure 6.13.(b)). Caspase-3 activation is a hall mark of programmed cell death i.e. apoptosis and such phenomenon is observed in presence of most of the exogeneous stressors. On other side, necrosis is the abnormal cell death process. Herein, sign of apoptosis suggests that the minute percentage death in macrophages were due to normal cell death process i.e. apoptosis but not due to necrosis (Figure 6.13.(b)). Interestingly, the cytotoxic dose of T-$MnFe_2O_4$ NHSs was (CC_{50} 200.25µl/ml) more than 10 folds higher than that of the treatment doses.

After observing the benign nature of T-$MnFe_2O_4$ NHSs in vitro, we conducted *in vivo* **e**xperiments in rat model. Data obtained from the *in vivo* toxicity analysis study corroborate with the *in vitro* experiment. Peritoneal macrophages of T-$MnFe_2O_4$ NHSs treated animals were devoid of any significant level of cell death (Figure 6.14(a)). No toxic alteration in the histological architecture of the liver tissue indicates the benign nature of T-$MnFe_2O_4$ NHSs (Figure 6.14.(b)). Liver is a key organ in mammalian body system that governs important physiological processes like digestion, metabolism and detoxification. Toxic agent that enters into the mammalian circulation is known to affect liver function by inducing structural damages. In this study, T-$MnFe_2O_4$ NHSs caused no alteration in the tissue histology of rat liver tissue. Alongside this, other critical hepatic markers like the transaminases (SGPT and SGOT) and ALP were also normal. SGPT and SGOT are crucial determinants of liver function as they are important for maintaining the metabolism. On other side, ALP maintains membrane integrity. Therefore, changes in the level of these enzymes are indicative of disruption of liver function. But, T-$MnFe_2O_4$ NHSs treatment did not induce any changes in these enzymes and also the serum proteins (albumin and globulin) in the rat (Figure 6.14.(c) and (d)). Unchanged levels of conjugated and unconjugated bilirubin (Figure 6.14.(e) and (f)) also support earlier observations and demonstrate the non-toxic nature of T-$MnFe_2O_4$ NHSs.

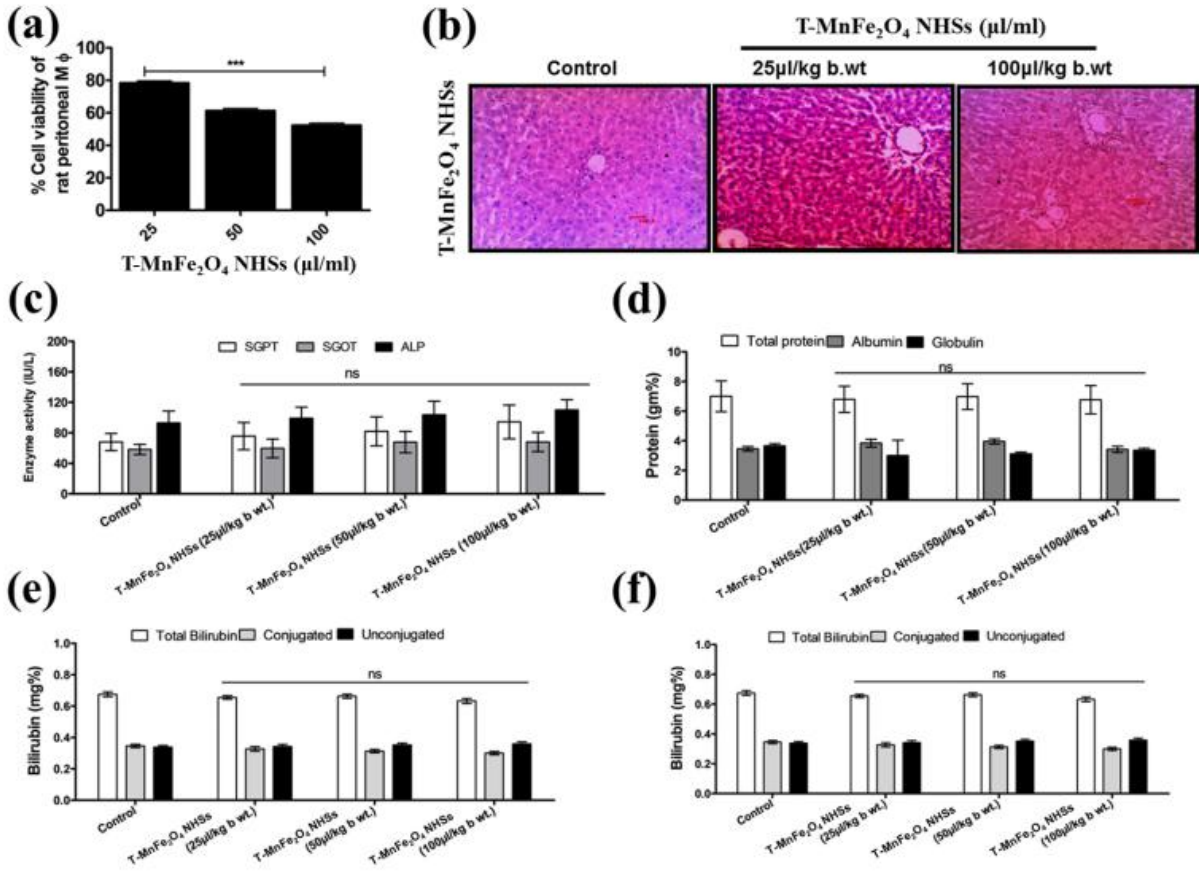

Figure 6.14. (a) MTT assay showing cell viability of rat peritoneal macrophages. (b) Histology showing the architecture of liver tissues in rat treated with T-MFO-HS. Changes in the levels of (c) hepatic enzymes, (d) serum proteins, (e) and (f) serum bilirubin in T-$MnFe_2O_4$ NHSs treated rat.

Furthermore, we also studied the haematological parameters like the counts and percentages of different W.B.C like neutrophils, eosinophils, basophils, monocytes and lymphocytes and all were in the normal range in T-$MnFe_2O_4$ NHSs treated animals (Figure 6.15(a) and (b)). We also noticed no change in the level of haemoglobin, the important blood parameter (Figure 6.15.(c)). All these data collectively revealed that T-$MnFe_2O_4$ NHSs are non-toxic nanomaterial under the experimental conditions used in this study. Herein, we adopted an acute toxicity (short term) schedule and therefore chronic toxicity (long term) study is particularly required to facilitate the biological applications of the nanomaterials in future. Moreover, detail pharmacokinetics studies (absorption, serum retention time, bioavailability, excretion) are also required before designing any application directly related to human use.

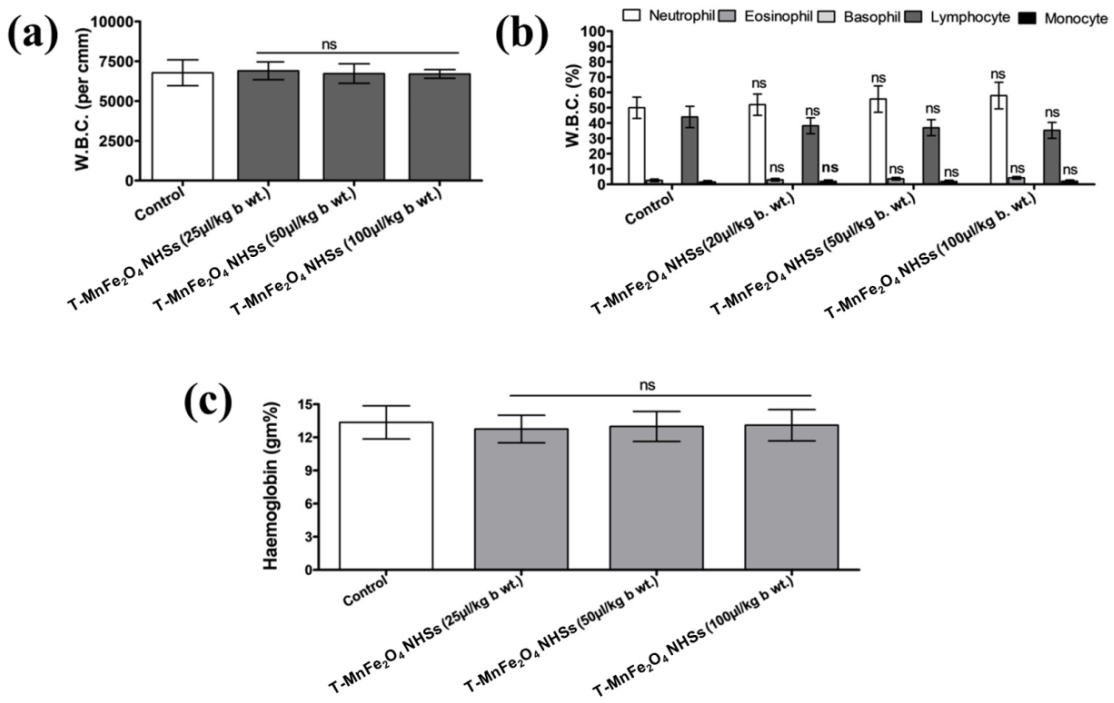

Figure 6.15. Analysis of the haematological parameters in T-$MnFe_2O_4$ NHSs treated rat. Changes in (a) W.B.C. count, (b) %W.B.C, and (c) Haemoglobin in rat blood treated with T-$MnFe_2O_4$ NHSs.

6.3.11. T-$MnFe_2O_4$ NHSs Possesses Antibacterial and Antifungal Activities

Antimicrobial activities i.e. lethal effect on bacteria and fungus are considered to be the major desirable properties of smart nanoparticles. In this connection, previous literatures have demonstrated that iron-based nanomaterials do exert lethal action against bacteria and fungi [59]. But, most critical issues are the toxic effect on the host and high dose [60]. Interestingly, the study depicts that the nanocomposite T-$MnFe_2O_4$ NHSs is non-toxic (Figure 6.16) and this has prompted us to study whether this nanomaterial could have any antimicrobial action or not. We found excellent antibacterial and antifungal activities T-$MnFe_2O_4$ NHSs *in vitro* (Figure 6.16). T-$MnFe_2O_4$ NHSs were found to cease the growth of both gram -ve (*E. coli*) and gram +ve (*B. subtilis*) bacteria (Figure 6.16) with calculated minimum inhibitory concentration (MIC) of 5.5 µg/ml and 5.8 µg/ml respectively for *E. coli* and *B. subtilis*. Moreover, we have also determined a strong antifungal activity of T-$MnFe_2O_4$ NHSs against *P. guilliermondii*, an opportunistic fungal pathogen that infects human (Figure 6.16). The calculated MIC for the antifungal activity of the Ag-NPs was found to be 3.45µg/ml.

Considering the antimicrobial actions of T-$MnFe_2O_4$ NHSs can be explored in future further for its activity against clinical isolate of pathogenic bacteria and fungi.

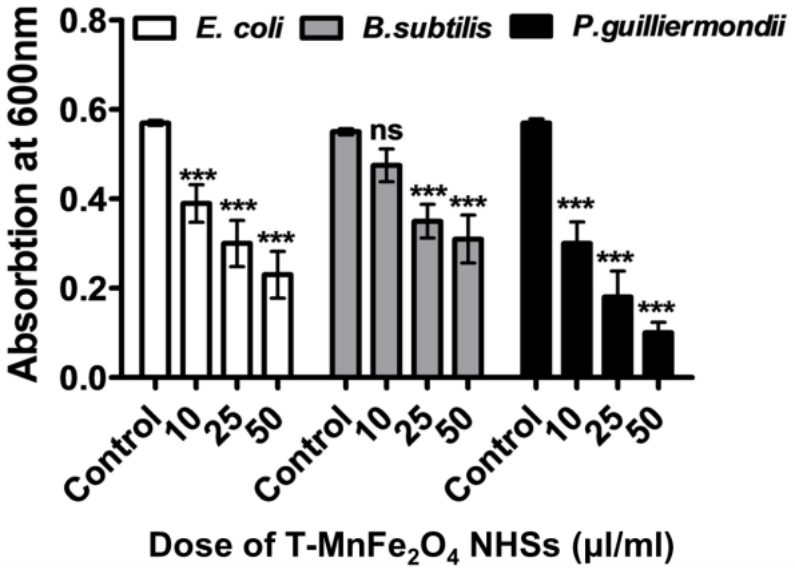

Figure 6.16. Antibacterial and antifungal activities of T-$MnFe_2O_4$ NHSs *in vitro.*

6.4. Conclusion

We have explored the effect of BSA towards the fluorescence intensity of $MnFe_2O_4$ NHSs due to the d-d transition corresponding to the d-orbital energy level splitting of Fe^{3+} ions. The association between BSA and T-$MnFe_2O_4$ NHSs has been clearly demonstrated by the UV-vis and fluorescence spectral change. The steady state anisotropy study also confirms the interaction between BSA and T-$MnFe_2O_4$ NHSs. The surface modification strategy of $MnFe_2O_4$ NHSs with tartrate ligand develops inherent multicolour fluorescence covering blue, cyan and green and enhances the intensity of same colours due to the addition of BSA. The negative value of the standard state enthalpy change reveals that the interaction of BSA to the T-$MnFe_2O_4$ NHSs is exothermic in nature. The higher fluorescence lifetime of T-$MnFe_2O_4$ NHSs in presence of higher concentration of BSA reveals that a strong electrostatic interaction is occurring between the BSA and microenvironment of the medium. The CD spectra confirm the T-$MnFe_2O_4$ NHSs induced conformational change of BSA in terms of decrease of the α-helix content in BSA. The other important traits of T-$MnFe_2O_4$ NHSs are its non-toxic nature in mammalian body system and ability of killing microorganisms. We hope that our study is potentially important to open new door for designing new biomolecular detection agents and nanomedicines.

Bibliography

1) M. Szekeres, E. Illés, C. Janko, K. Farkas, I. Y. Tóth, D. Nesztor, I. Zupkó, I. Földesi, C. Alexiou, E. Tombácz, Hemocompatibility and biomedical potential of poly (gallic acid) coated iron oxide nanoparticles for theranostic use, *J. Nanomed. Nanotechnol.* **2015**, 6, 252.

(2) J.-H. Oh, J.-S. Lee, Salt concentration-induced dehybridisation of DNA–gold nanoparticle conjugate assemblies for diagnostic applications, *Chem. Commun.* **2010**, 46, 6382-6384.

(3) K. An, T. Hyeon, Synthesis and biomedical applications of hollow nanostructures, *Nano Today* **2009**, 4, 359-373.

(4) Y. Piao, J. Kim, H. B. Na, D. Kim, J. S. Baek, M. K. Ko, J. H. Lee, M. Shokouhimehr, T. Hyeon, Wrap–bake–peel process for nanostructural transformation from β-FeOOH nanorods to biocompatible iron oxide nanocapsules, *Nat. Mater.* **2008**, **7**, 242.

(5) X. Wang, J. Feng, Y. Bai, Q. Zhang, Y. Yin, Synthesis, properties, and applications of hollow micro-/nanostructures, *Chem. Rev.* **2016**, 116, 10983-11060.

(6) Q. Song, Z. J. Zhang, Controlled synthesis and magnetic properties of bimagnetic spinel ferrite $CoFe_2O_4$ and $MnFe_2O_4$ nanocrystals with core–shell architecture, *J. Chem. Soc.* **2012**, 134, 10182-10190.

(7) S. Chen, X. Hao, X. Liang, Q. Zhang, C. Zhang, G. Zhou, S. Shen, G. Jia, J. Zhang, Inorganic nanomaterials as carriers for drug delivery, *J. Biomed. Nanotechnol.* **2016**, 12, 1-27.

(8) L. Dong, D. An, M. Gong, Y. Lu, H. L. Gao, Y. J. Xu, S. H. Yu, PEGylated upconverting luminescent hollow nanospheres for drug delivery and in vivo imaging, *Small* **2013**, 9, 3235-3241.

(9) S. Dyawanapelly, D. D. Jagtap, P. Dandekar, G. Ghosh, R. Jain, Assessing safety and protein interactions of surface-modified iron oxide nanoparticles for potential use in biomedical areas, *Colloids Surf. B Biointerf.* **2017**, 154, 408-420.

(10) S. R. Saptarshi, A. Duschl, A. L. Lopata, Interaction of nanoparticles with proteins: relation to bio-reactivity of the nanoparticle, *J. Nanobiotechnology* **2013**, 11, 26.

(11) P. Wang, X. Wang, L. Wang, X. Hou, W. Liu, C. Chen, Interaction of gold nanoparticles with proteins and cells, *Sci. Technol. Adv. Mater.* **2015**, 16, 034610.

(12) X. Li, M. Chen, W. Yang, Z. Zhou, L. Liu, Q. Zhang, Interaction of bovine serum albumin with self-assembled nanoparticles of 6-O-cholesterol modified chitosan, *Colloids Surf. B Biointerf.* **2012**, 92, 136-141.

(13) A. Satheshkumar, K. P. Elango, Spectroscopic and molecular docking studies on the charge transfer complex of bovine serum albumin with quinone in aqueous medium and its influence on the ligand binding property of the protein, *Spectrochim. Acta A Mol. Biomol. Spectrosc.* **2014**, 130, 337-343.

(14) L. Medda, B. Barse, F. Cugia, M. Boström, D. F. Parsons, B. W. Ninham, M. Monduzzi, A. Salis, Hofmeister Challenges: Ion Binding and Charge of the BSA Protein as Explicit Examples, *Langmuir* **2012**, 28, 16355-16363.

(15) S. Ghosh, S. Jana, D. Nath, N. Guchhait, Fluorescent probing of protein bovine serum albumin stability and denaturation using polarity sensitive spectral response of a charge transfer probe, *J. Fluores.* **2011**, 21, 365-374.

(16) A. Chakraborty, S. Ghosh, S. Kar, D. N. Nath, N. Guchhait, Dual emission from (E)-3-(4-methylamino-phenyl)-acrylic acid ethyl ester (MAPAEE) and its application as fluorescence probe for studying micellar and protein microenvironment, *J. Mol. Struct.* **2009**, 917, 148-157.

(17) A. Mallick, B. Haldar, N. Chattopadhyay, Spectroscopic Investigation on the Interaction of ICT Probe 3-Acetyl-4-oxo-6,7-dihydro-12H Indolo-[2,3-a] Quinolizine with Serum Albumins, *J. Phys. Chem. B* **2005**, 109, 14683-14690.

(18) S. Ghosh, S. Jana, N. Guchhait, Domain Specific Association of Small Fluorescent Probe trans-3-(4-Monomethylaminophenyl)-Acrylonitrile (MMAPA) with Bovine Serum Albumin (BSA) and Its Dissociation from Protein Binding Sites by Ag Nanoparticles: Spectroscopic and Molecular Docking Study, *J. Phys. Chem. B* **2012**, 116, 1155-1163.

(19) J. Hankins, The role of albumin in fluid and electrolyte balance, *J. Infus. Nurs.* **2006**, 29, 260-265.

(20) S. Chandrasekaran, N. Sudha, D. Premnath, I. V. Enoch, Binding of a chromen-4-one Schiff's base with bovine serum albumin: capping with β-cyclodextrin influences the binding, *J. Biomol. Struct. Dyn.* **2015**, 33, 1945-1956.

(21) S. Medina, J. Blankenburg, J. Olson, C. Landes, S. Link, Adsorption of a protein monolayer via hydrophobic interactions prevents nanoparticle aggregation under harsh environmental conditions, *ACS Sustain. Che. Eng.* **2013**, 1, 833-842.

(22) X. M. He, D. C. Carter, Atomic structure and chemistry of human serum albumin, *Nature* **1992**, 358, 209.

(23) B. Jachimska, K. Tokarczyk, M. Łapczyńska, A. Puciul-Malinowska, S. Zapotoczny, Structure of bovine serum albumin adsorbed on silica investigated by quartz crystal microbalance, *Colloids Surf. A Physicochem. Eng. Asp.* **2016**, 489, 163-172.

(24) D.-H. Tsai, F. W. DelRio, A. M. Keene, K. M. Tyner, R. I. MacCuspie, T. J. Cho, M. R. Zachariah, V. A. Hackley, Adsorption and conformation of serum albumin protein on gold nanoparticles investigated using dimensional measurements and in situ spectroscopic methods, *Langmuir* **2011**, 27, 2464-2477.

(25) S. Jana, S. Ghosh, S. Dalapati, N. Guchhait, Exploring structural change of protein bovine serum albumin by external perturbation using extrinsic fluorescence probe: spectroscopic measurement, molecular docking and molecular dynamics simulation, *Photochem. Photobiol. Sci.* **2012**, 11, 323-332.

(26) A. E. Ledesma, D. M. Chemes, M. de los Angeles Frías, M. d. P. G. Torres, Spectroscopic characterization and docking studies of ZnO nanoparticle modified with BSA, *Appl. Surf. Sci.* **2017**, 412, 177-188.

(27) C. Henoumont, L. Vander Elst, S. Laurent, R. N. Muller, Study of non-covalent interactions between MRI contrast agents and human serum albumin by NMR diffusometry, *JBIC, J. Biol. Inorg. Chem.* **2009**, 14, 683-691.

(28) N. Shahabadi, M. Hakimi, T. Morovati, S. Hadidi, K. Moeini, Spectroscopic investigation into the interaction of a diazacyclam-based macrocyclic copper(ii) complex with bovine serum albumin, *Luminescence* **2017**, 32, 43-50.

(29) I. Chakraborty, R. Rakshit, K. Mandal, Synthesis and functionalization of $MnFe_2O_4$ nano−hollow spheres for novel optical and catalytic properties, *Surf. Interfaces* **2017**, 7, 106-112.

(30) S. Mukherjee, N. Joardar, S. Mondal, A. Schiefer, A. Hoerauf, K. Pfarr, S. P. S. Babu, Quinolone-fused cyclic sulfonamide as a novel benign antifilarial agent, *Scientific Reports* **2018**, 8, 12073.

(31) D. Ghosh, S. Dhibar, A. Dey, S. Mukherjee, N. Joardar, S. P. S. Babu, B. Dey, Graphene oxide dispersed supramolecular hydrogel capped benign green silver nanoparticles for anticancer, antimicrobial, cell attachment and intracellular imaging applications*J. Mol. Liq.* **2019**, 282, 1-12.

(32) A. S. Ray, N. Joardar, S. Mukherjee, C. H. Rahaman, S. P. Sinha Babu, Polyphenol enriched ethanolic extract of Cajanus scarabaeoides (L.) Thouars exerts potential antifilarial activity by inducing oxidative stress and programmed cell death, *PLOS ONE* **2018**, 13, 0208201.

(33) B. Aslibeiki, P. Kameli, M. H. Ehsani, H. Salamati, G. Muscas, E. Agostinelli, V. Foglietti, S. Casciardi and D. Peddis, *J. Magn. Magn. Mater.* **2016**, 399, 236-244.

(34) B. Aslibeiki, P. Kameli, H. Salamati, M. Eshraghi, T. Tahmasebi, Superspin glass state in $MnFe_2O_4$ nanoparticles, *J. Magn. Magn. Mater.* **2010**, 322, 2929-2934.

(35) V. Kalidasan, X. L. Liu, T. S. Herng, Y. Yang, J. Ding, Bovine serum albumin-conjugated ferrimagnetic iron oxide nanoparticles to enhance the biocompatibility and magnetic hyperthermia performance, *Nano-Micro Lett.* **2016**, 8, 80-93.

(36) R. Jin, D. Song, H. Xiong, L. Ai, P. Ma, Y. Sun, Magnetic core/shell Fe_3O_4/Au nanoparticles for studies of quinolones binding to protein by fluorescence spectroscopy, *Luminescence* **2016**, 31, 499-506.

(37) A. Chaudhary, A. Gupta, S. Khan, C. K. Nandi, Morphological effect of gold nanoparticles on the adsorption of bovine serum albumin, *Phys. Chem. Chem. Phys.* **2014**, 16, 20471-20482.

(38) S. H. Brewer, W. R. Glomm, M. C. Johnson, M. K. Knag, S. Franzen, Probing BSA binding to citrate-coated gold nanoparticles and surfaces, *Langmuir* **2005**, 21, 9303-9307.

(39) A. Tkachenko, H. Xie, S. Franzen, D. L. Feldheim, *Assembly and Characterization of Biomolecule-Gold Nanoparticle Conjugates and Their Use in Intracellular Imaging*, Springer, Humana Press, **2005**.

(40) J. E. Huheey, E. A. Keiter, R. L. Keiter, O. K. Medhi, Inorganic Chemistry, Pearson Ed.; India, Singapore, **2006**.

(41) L. M. Martínez-Prieto, E. A. Baquero, G. Pieters, J. C. Flores, E. de Jesús, C. Nayral, F. Delpech, P. W. N. M. van Leeuwen, G. Lippens, B. Chaudret, Monitoring of nanoparticle reactivity in solution: interaction of l-lysine and Ru nanoparticles probed by chemical shift perturbation parallels regioselective H/D exchange, *Chem. Commun.* **2017**, 53, 5850-5853.

(42) J. Jung, M. Matsubara, T. Arima, J. He, Y. Kaneko, Y. Tokura, Optical magnetoelectric effect in the polar $GaFeO_3$ ferrimagnet, *Phys. Rev. Lett.* **2004**, 93, 037403.

(43) J. Weber, W. Koehl, J. Varley, A. Janotti, B. Buckley, C. Van de Walle, D. D. Awschalom, Quantum computing with defects, *Proc. Natl. Acad. Sci.* **2010**, 107, 8513-8518.

(44) Q. Yu, H. He, L. Gan and Z. Ye, The defect nature of photoluminescence from a porous silicon nanowire array, *RSC Adv.* **2015**, 5, 80526-80529.

(45) J. R. Lakowicz, J. R. Lakowicz, Principles of Fluorescence Spectroscopy, Springer, New York, USA Springer, New York, USA **2006**, 353−381.

(46) P. Kundu, S. Ghosh and N. Chattopadhyay, Exploration of the binding interaction of a potential nervous system stimulant with calf-thymus DNA and dissociation of the drug–DNA complex by detergent sequestration, *Phys. Chem. Chem. Phys.* **2015**, 17, 17699-17709.

(47) C. M. Ingersoll, C. M. Strollo, Steady-State Fluorescence Anisotropy to Investigate Flavonoids Binding to Proteins, *J. Chem. Educ.* **2007**, 84, 1313−1315.

(48) M. Sasmal, R. Bhowmick, A. S. Musha Islam, S. Bhuiya, S. Das, M. Ali, Domain-Specific Association of a Phenanthrene–Pyrene-Based Synthetic Fluorescent Probe with Bovine Serum Albumin: Spectroscopic and Molecular Docking Analysis, *ACS Omega* **2018**, 3, 6293-6304.

(49) H. H.-M. Yeung, A. K. Cheetham, Phase selection during the crystallization of metal–organic frameworks; thermodynamic and kinetic factors in the lithium tartrate system, *Dalton Trans.* **2014**, 43, 95-102.

(50) P. Manning, Tartrate complexes of the rare-earth elements: I. The d-, dl-, and meso-tartrate complexes of Tb and Eu, *Can. J. Chem.* **1963**, 41, 2557-2565.

(51) H.-L. Chan, H.-Q. Liu, B.-C. Tzeng, Y.-S. You, S.-M. Peng, M. Yang, C.-M. Che, Syntheses of ruthenium (II) quinonediimine complexes of cyclam and characterization of their DNA-binding activities and cytotoxicity, *Inorg. Chem.* **2002**, 41, 3161-3171.

(52) T. Cifuentes, J. Cayupi, C. Celis-Barros, G. Zapata-Torres, R. Ballesteros, R. Ballesteros-Garrido, B. Abarca, C. Jullian, Spectroscopic studies of the interaction of 3-(2-thienyl)-[1, 2, 3] triazolo [1, 5-a] pyridine with 2, 6-dimethyl-β-cyclodextrin and ct DNA, *Org. Biomol. Chem.* **2016**, 14, 9760-9767.

(53) T. D. SMITH, Chelates formed by Tin(11) with citric and tartaric acids, and their interaction with certain transition-metal ions, *J. Chem. Soc. Chem.* **1965**, 2145-2150.

(54) R. E. Hamm, C. M. Shull Jr, D. M. Grant, Citrate complexes with iron (II) and iron (III), *J. Am. Chem. Soc.* **1954**, 76, 2111-2114.

(55) B. Ojha, G. Das, Salt concentration-induced dehybridisation of DNA–gold nanoparticle conjugate assemblies for diagnostic applications, *Chem. Commun.* **2010**, 46, 2079-2081.

(56) D. Sarkar, Probing the interaction of a globular protein with a small fluorescent probe in the presence of silver nanoparticles: spectroscopic characterization of its domain specific association and dissociation, *RSC Adv.* **2013**, 3, 24389-24399.

(57) S. Roy, T. K. Das, Interaction of biosynthesized gold nanoparticles with BSA and CTDNA: A multi-spectroscopic approach, *Polyhedron* **2016**, 115, 111-118.

(58) J. Kuchlyan, N. Kundu, D. Banik, A. Roy, N. Sarkar, Spectroscopy and fluorescence lifetime imaging microscopy to probe the interaction of bovine serum albumin with graphene oxide, *Langmuir* **2015**, 31, 13793-13801.

(59) P. Nehra, R. P. Chauhan, N. Garg, K. Verma, Antibacterial and antifungal activity of chitosan coated iron oxide nanoparticles*Br. J. Biomed. Sci.* **2018**, 75, 13-18.

(60) Q. Feng, Y. Liu, J. Huang, K. Chen, J. Huang, K. Xiao, Uptake, distribution, clearance, and toxicity of iron oxide nanoparticles with different sizes and coatings, *Scientific Reports* **2018**, 8, 2082.

Chapter 7

Conclusion and Scope for Future Work

This chapter gives an overall conclusion of the work described so far and the scopes for further work in this specific field.

7.1. Epilogue

In this thesis, we have mainly focused our work on the synthesis of transition metal oxide ($MnFe_2O_4$) based magnetic nanostructures (nanoparticles (NPs), and nano hollow spheres (NHSs)) by wet chemical and solvothermal synthesis procedures followed by functionalization with small organic ligands (tartrate, malate, and citarte) to make efficient the nanostructures for biological applications.

First, our intension was to use three biocompatible ligands like tartrate, malate, and citrate for functionalization the surface of $MnFe_2O_4$ NPs. The small organic ligands (tartrate, malate, and citrate) have different numbers of α-hydroxy carboxylate group along with steric effect which may have different surface chemistry, optical and magnetic responses. Interestingly, we noticed that tartrate modified $MnFe_2O_4$ NPs show better fluorescence property comparing with malate and citrate modified $MnFe_2O_4$ NPs due to the presence of maximum number of α-hydroxy carboxylate group in tartrate ligand. It indicates that α-hydroxy carboxylate moiety plays a key role to generate intrinsic fluorescence in functionalized $MnFe_2O_4$ NPs. Moreover, the comparative magnetic study of T-$MnFe_2O_4$, M-$MnFe_2O_4$ and C-$MnFe_2O_4$ NPs reveals that the ligand that induces largest splitting of d-orbital energy levels of surface transition metal ions results in nethermost enhancement of coercivity and upmost decrement of magnetization of bare $MnFe_2O_4$ NPs. Finally, T-$MnFe_2O_4$ NPs were used for DNA binding and nuclease activity studies which clearly indicate that T-$MnFe_2O_4$ NPs bind and stabilize the DNA helix due to intercalation and induce cleavage on plasmid DNA. Next we noticed that although citrate is a bulky ligand still the surface modification of NPs with citarte ligand shows very good multifluorescent colors (covering blue, cyan, green and red) due to ligand to metal charge transfer transition (LMCT) and d-d transitions. We have explored the origin of multicolor fluorescence properties through LMCT transition from the citrate ligand to the lowest unoccupied energy level of Mn ions and d-d transitions over Mn ions present in the NPs. The pristine and surface modified magneto fluorescent Mn_2FeO_4 nanoparticles are tested against protein adsorption and satisfactory results are obtained. The catalytic activities of citrate functionalized $MnFe_2O_4$ NPs for the degradation of MB (a model water contaminant under UV light) and BR (a biologically harmful pigment) are investigated and competent performance is observed. Later, we synthesized $MnFe_2O_4$ nano hollow spheres (NHSs) by solvothermal process. Surface by volume ratio is high for NHSs comparing with NPs which has a positive effect on optical and magnetic properties. T−$MnFe_2O_4$ NHSs show better catalytic efficiency for the degradation of MB under UV light irradiation. For biological

applications of the sample, association between BSA and T-$MnFe_2O_4$ NHSs has been clearly demonstrated by the UV-vis and fluorescence spectral change. The higher fluorescence lifetime of T-$MnFe_2O_4$ NHSs in presence of higher concentration of BSA reveals that a strong electrostatic interaction is occurring between the BSA and microenvironment of the medium. The CD spectra confirm the T-$MnFe_2O_4$ NHSs induced conformational change of BSA in terms of decrease of the α-helix content in BSA. The other important traits of T-$MnFe_2O_4$ NHSs are its non-toxic nature in mammalian body system and ability of killing microorganisms. We hope that our study is potentially important for diagnostics and therapeutics to environmental remediation.

7.2. Scope for Future Work

Our developed $MnFe_2O_4$ NPs and NHSs may be very useful for drug delivery with the help of external magnetic field. By tuning the size of the NSs, we can get our desired applications. Cell viability test of the NSs is also very essential for the biological applications. As the NSs are nontoxic and show multi fluorescent color, it may be useful for bio imaging. We can tune the magnetic property of the metal oxide by changing the size of the NHSs and measure the T_2 contrast ability for MRI application.

The solid state emission from the modified nano complex can be used for security, sensing and lighting etc. Tunable emission features can be developed by changing the metal and the ligand. The change in the structural pattern can result in significant emissive properties, colors and quantum yields.

Magneto-fluorescent nano materials can be used as a protein sensor also. We have already established from fluorescence spectroscopy and microscope that our prepared nano complex binds easily with protein and increases fluorescence intensity. This can be helpful to detect the protein in a sample.

Finally, these nanostructures and their applications can correlate between chemistry, biology and nanotechnology. The stated plan in this proposal will require a deep analytical as well as computational study. These materials can have excellent functionalities for next generation MRI contrast agents, sensors, cancers and in many other biological fields.